The water vapour corrosion of uranium niobium alloys

C. Coe
Interface Analysis Centre
University of Bristol

A thesis submitted for the degree of
Doctor of Philosophy
October 2016

~55000 words

This thesis is dedicated to my late mum Silvana Kenney who throughout my PhD has provided me with moral support, comfort and encouragement.

Abstract

Low temperature water vapour corrosion of uranium niobium alloys (3 wt% and 6 wt% niobium) and the base metals were investigated. It was found that the alloys exhibited slower corrosion rates than the two base metals, confirming the enhancement of corrosion resistance. However, the UNb6 alloy exhibited similar reaction rates to the UNb3 alloy, which was unexpected as it has previously been shown that an increase in niobium content leads to an increase in corrosion resistance.

Secondary ion mass spectrometry (SIMS) was carried out on the corroded samples though, due to the thickness of the oxides, only limited information on the mechanism could be derived. Nevertheless, complementary atom probe tomography (APT) analysis was able to provide a more detailed picture of the corroded structure and allowed some key information related to the mechanism to be elucidated. In particular, for uranium metal after exposure to air (or D_2O), uranium hydride (or deuteride) was clearly detected using APT. The presence of hydride is of great significance for the mechanism. For niobium metal, hydride was also detected by both SIMS and APT. This has previously been seen and it has been suggested that the hydride is involved in the oxide formation, similar to Baker's proposed mechanism for uranium.

Energy dispersive x-ray spectrometry (EDX) of Transmission electron microscopy (TEM) sections and APT analysis of corroded alloy samples showed clear phase separation in the UNb6 samples. This phase decomposition is most likely due to ageing as the UNb6 material is at least 30 years old. Previous work has shown ageing to have an effect on UNb alloys, leading to an increase in strength but a decrease in both ductility and corrosion resistance. This age decomposition of the material could possibly explain the unexpected kinetic results, as any phase separation could lead to the alloy having niobium depleted regions (as seen by APT and EDX), which means the material would react in a similar manner to that of pure uranium, i.e. significantly faster.

This work clearly demonstrates the importance of the corrosion resistance of UNb alloys as compared to pure uranium; however, it is highly important for the alloy to remain in its metastable phase in order to retain this resistance. If the material undergoes transformation to the two-phase mixture (either through heating or ageing) then the material will revert back to reaction kinetics of pure uranium and thus lose this enhancement.

Acknowledgements

The author would like to thank all staff and students at the IAC for their help and support. Thanks also to colleagues at AWE for their help, support and backing of the project.

Special mention is offered to:

- Peter Heard for his help on ion beam related matters
- Joseph Glascott for his suggestions, advice and encouragement
- Scott Bazley for his advice and continuous encouragement.
- My family for providing support at home

AUTHORS DECLARATION

I declare that the work in this dissertation was carried out in accordance with the Regulations of the University of Bristol. The work is original except where indicated by special reference in the text and no part of the dissertation has been submitted for any other degree. Any views expressed in the dissertation are those of the author and in no way represent those of the University of Bristol. The dissertation has not been presented to another University for examination either in the United Kingdom or overseas.

SIGNED:…….. DATE:…….

Contents

List of figures

List of tables

1 Chapter one – introduction and literature review

1.1 Introduction

Uranium metal and its oxides have become synonymous with nuclear energy applications. Metallic uranium was used as the fuel material in the world's first fission reactors but was subsequently replaced by uranium dioxide (UO_2), which now forms the basis for fuel within the current generation of fission power reactors. Due to its inherently reactive and pyrophoric nature, legacy uranium remaining from first generation nuclear reactors now poses a significant challenge for both safe long-term storage and future disposal. Consequently, understanding the mechanism by which uranium reacts with moisture at the atomic scale is essential for underpinning predictions of the ageing of stored legacy materials and informing the design of future storage and waste handling facilities.

The addition of niobium to uranium metal enhances its corrosion resistance. However, the exact method behind this enhanced resistance is not fully understood. UNb is a two phase mixture of orthorhombic α-U and bcc γ-Nb phase. When quenched from the γ phase Nb is retained in a metastable martensitic phase which improves the corrosion resistance and ductility of the alloy. This enhanced corrosion resistance is of significance with regards to the long term storage of uranium where moisture may be present thus creating the possibility of hydrogen production which, in turn, could lead to a pyrophoric risk through the formation of hydride and has the potential of causing an explosion if exposed to oxygen/air. The corrosion of the alloy is significant in determining if there are any detrimental changes to the material with age as the UNb alloy is known to undergo significant phase changes with temperature and age[1].

Currently, the mechanism of the water vapour reaction (with and without oxygen present) with uranium, niobium and UNb alloys remains under debate. There have been a number of studies on the kinetics and mechanism of the reaction for uranium, with varying hypotheses being proposed[2–6]. For niobium the literature is limited with the majority of studies focussing on the higher temperature reactions due to niobium being used inside super conducting radio frequency (SRF) cavities, within particle accelerators[7]. For the alloys there have been a

number of investigations into the effect of alloying on the corrosion resistance of uranium, with the alloying element and the weight percentage of the element being studied[8–12].

In the following section a reminder of basic oxidation and corrosion for metals and alloys is presented together with a literature review of relevant studies conducted on uranium, niobium and UNb alloys.

1.2 Oxidation and corrosion theory

Oxidation is a thermodynamic process aiming at optimally reducing Gibbs free energy (G). This may be defined as:

$\Delta G = \Delta H - T\Delta S$

where H is enthalpy (the standard heat of the reaction), T is temperature and S is entropy, (the measure of the molecular disorder of the system). For a reaction to occur spontaneously, ΔG must be negative as the system seeks to achieve minimum free energy. For nearly all metals within an oxygen containing environment $\Delta G<0$, i.e. the metal oxide is the most stable form. Table 1.1 lists the Gibbs free energy values for the main uranium and niobium oxides.

Table 1.1 Gibbs free energy of formation for the main uranium and niobium oxides[13,14]

Oxide	**ΔG kJ mol^{-1} (at 298.15 K)**
UO_2	-1031.833
U_4O_9	-1069.125
U_3O_7	-1080.572
U_3O_8	-1123.157
UO_3	-1140.420
NbO	-414.986
NbO_2	-779.864
Nb_2O_5	-911.045

Oxidation proceeds via addition of oxygen atoms to the surface of the material. The weight of the material usually goes up in proportion to the amount of material that has become oxidised. This weight increase (Δm) can be monitored continuously with time (t).

Two types of behaviour are usually observed, the first is linear oxidation with:

$\Delta m = k_L t$

where k_L is a kinetic constant. The rate is directly proportional to time.

The second type of oxidation behaviour is parabolic with:

$(\Delta m)^2 = k_P t$

where k_P is another kinetic constant.

Figure 1.1 shows the rate curves for linear and parabolic oxidation. The linear weight loss is observed for very volatile materials where the oxide evaporates as soon as it is formed, thus offering no barrier at all to oxidation. Oxidation therefore proceeds at a rate that is proportional to time and the material loses weight because the oxide is lost.

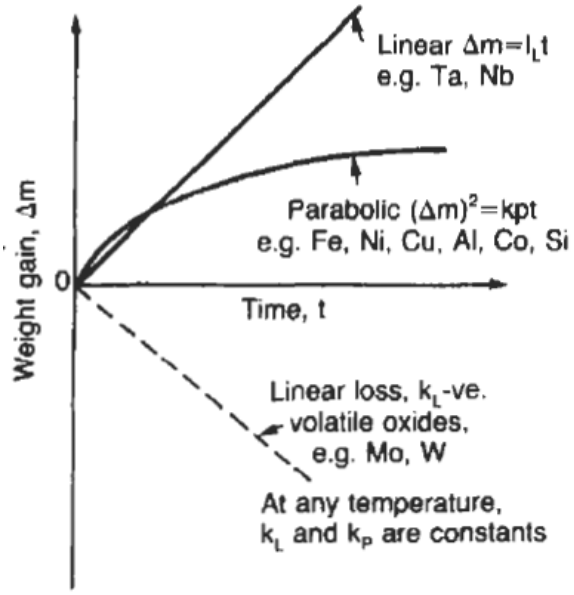

Figure 1.1 Measurements of oxidation rates[15]

A linear reaction rate tends to describe a reaction controlled by either diffusion through the gas phase, surface reaction or an interface step. For linear oxidation, as the oxide film thickens, it develops cracks or partly lifts away from the material so that the barrier between material and oxide does not become any more effective as oxidation proceeds. If the volume of oxide is much less than that of the material, it will crack to relieve the strain. If the volume is much greater, the oxide will tend to release the strain energy by breaking the adhesion between material and oxide and springing away, see Figure 1.2.

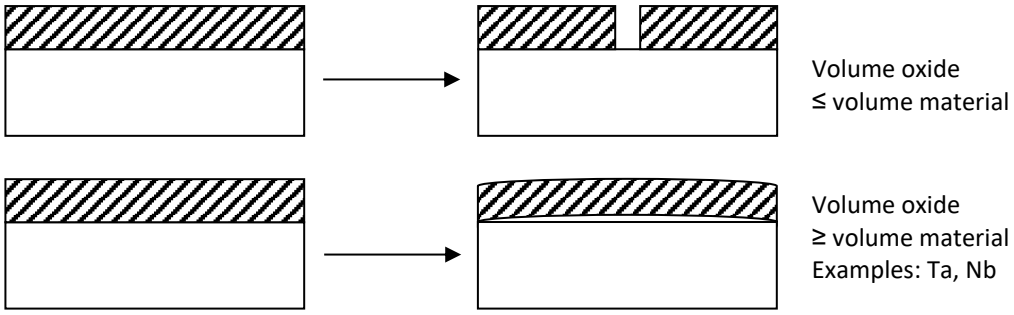

Figure 1.2 Breakdown of oxide films, leading to linear oxidation behaviour[15]

For a parabolic reaction rate, the reaction of metal plus oxygen:

$M + O \longrightarrow MO$

is really split into two steps. First the metal forms an ion, releasing electrons, eg:

$M \longrightarrow M^{2+} + 2e^-$

These electrons are then absorbed by oxygen to give an O ion:

$O + 2e^- \longrightarrow O^{2-}$

Either the M^{2+} and the two electrons diffuse outward through the film to meet the O^{2-} at the outer surface or the oxygen diffuses inwards (with two electron holes) to meet the M^{2+} at the inner surface. The kinetics of the reaction are usually limited by diffusion through the forming oxide layer, initially displaying a fast rate of reaction which slows with oxide growth, see Figure 1.3.

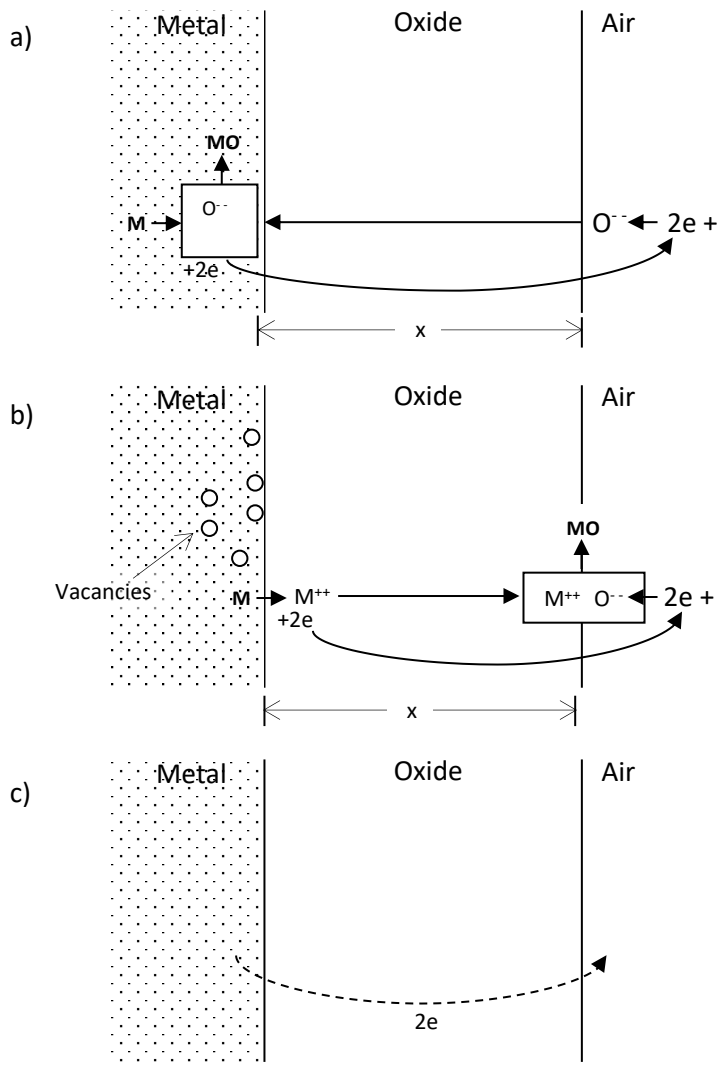

Figure 1.3 Schematic of how oxide layers grow to give parabolic oxidation behaviour, a) M^{2+} diffuses very slowly in oxide, the oxide grows at the oxide-metal interface, b) O^{2-} diffuses very slowly in oxide, oxide grows at the oxide-gas interface, vacancies form between the metal and oxide, c) electrons move very slowly, the oxide can grow (slowly) at metal-oxide interface or oxide-gas interface depending on whether M^{2+} diffuses faster than O^{2-} or not, reproduced from reference[15]

Oxidation rates follow Arrhenius' law, where K is a rate constant and can be thought of as the number of collisions leading to a reaction per second.

$$K = Ae^{\left(\frac{-E_a}{RT}\right)}$$

where A is a proportionality constant, E_a is the activation energy, T is temperature and R is the universal gas constant.

Each alloy component has a different affinity for O_2. Therefore, the rates will be affected and simple kinetic rate equations are often inappropriate to describe alloy oxidation. The second

(minor) component may enter the oxide film, affecting the lattice defect structure, or may accumulate as metal or oxide beneath the main oxide film. If O_2 diffuses into the alloy in atomic form, precipitation of the oxide of the less noble metal may occur as an internal oxide. There are two classes of alloys. Class one is where only one of the elements oxidises and class two is where both alloying elements oxidise simultaneously[16].

Figure 1.4 shows the various options for oxidation of an alloy AB, where B the less noble metal exclusively oxidises. In this case the content of element B within the alloy plays a role in how the oxide forms externally or internally within a matrix of A.

Figure 1.4a: B is a minor element and oxidises internally, BO particles in a matrix of A

Figure 1.4b: B is a minor element and oxidises externally, a single layer of BO above alloy matrix depleted in B

Figure 1.4c: B is a major element and oxidises internally, non-oxidisable material A is dispersed in BO

Figure 1.4d: B is a major element and oxidises externally, non-oxidisable material A is in an A-enriched zone beneath the BO scale

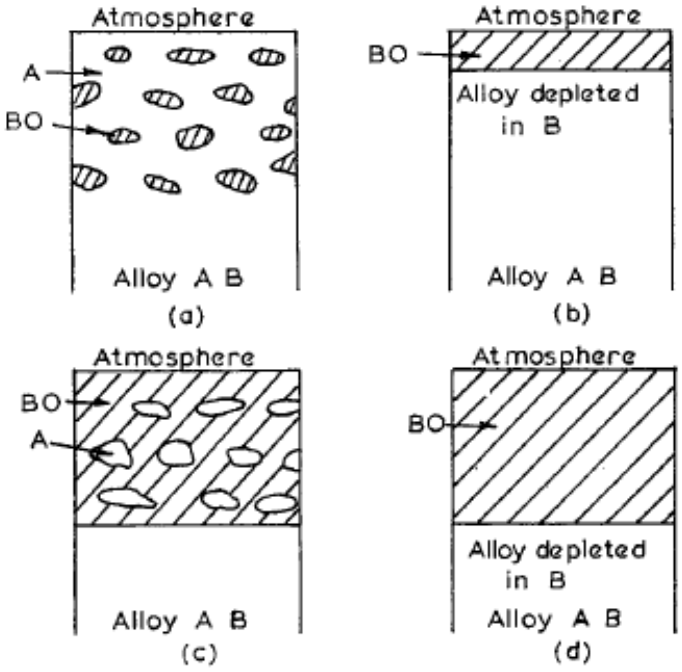

Figure 1.4 Schematic representation of modes of oxidation of alloy AB of variable composition, where B is the less noble metal and oxidises exclusively, reproduced from reference[16].

Figure 1.5 shows the various options for oxidation of an alloy AB, where both alloying elements oxidise simultaneously. Again, the content of element B within the alloy plays a role as does the solubility of the oxides within one another.

Figure 1.5a: A and B oxidise to give a single solid solution (A,B)O

Figure 1.5b: A and B oxidise to form compound ABO_2 within a matrix of AO

Figure 1.5c: AO and BO are insoluble in each other; B is a minor component and an internal oxide of BO lies beneath a mixed layer of AO and BO

Figure 1.5d: AO and BO are insoluble in each other; B is a major component and so no internal oxidation would be observed

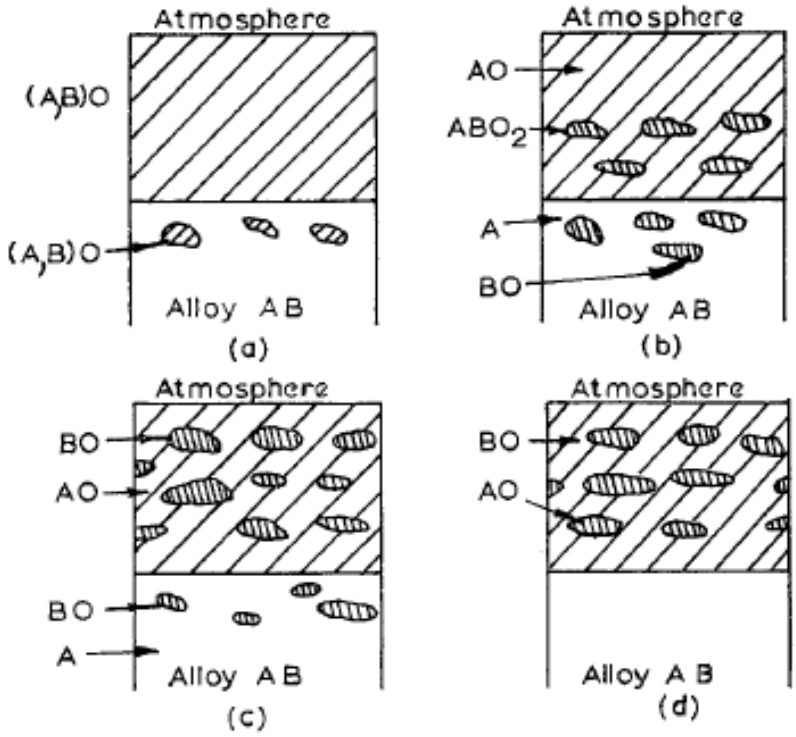

Figure 1.5 Schematic representation of modes of oxidation of alloy AB of variable composition, where B is the less noble metal and both metals oxidise simultaneously, reproduced from reference[16].

1.3 Literature review

1.3.1 Uranium

The uranium-oxygen system is complex with a number of possible oxidation states (4+ to 6+) and stoichiometries.

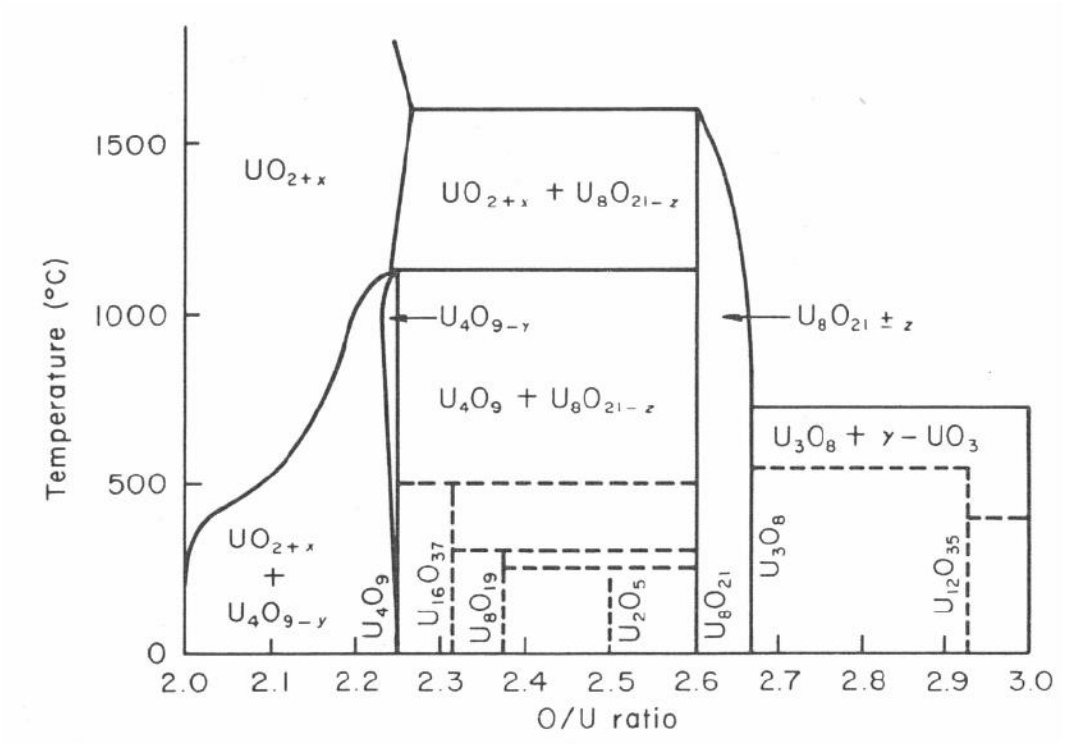

Figure 1.6 Phase diagram of the uranium-oxygen system, reproduced from reference[17]

The most common forms of uranium oxide are triuranium octoxide (U_3O_8) and uranium dioxide (UO_2). Both of these oxide forms are solids that have low solubility in water and are relatively stable over a wide range of environmental conditions. Because of their stability, uranium oxides are generally considered the preferred chemical form for storage or disposal.

Uranium reacts with oxygen according to the equation:

$U + ((2+x)/2)O_2 \rightarrow UO_{2+x}$

In oxygen at temperatures up to 200 °C the oxide formed is hyperstoichiometric uranium dioxide with x in the range 0.2 to 0.4 while at higher temperatures, above 275 °C, U_3O_8 is also formed[18].

The water vapour reaction also produces hyperstoichiometric uranium dioxide but with a lower x value, between 0 and 0.1[18].

$U + (2+x)H_2O \rightarrow UO_{2+x} + (2+x)H_2$

The addition of oxygen to the water vapour reaction leads to a more highly oxidised product than with pure water vapour, with x in the same range as for pure oxygen (0.2 to 0.4). In

saturated water vapour, the presence of oxygen may oxidise uranium to the trioxide $UO_3.0.8H_2O$.

The rate of reaction is strongly dependent on the nature of the uranium surface, i.e. on the thickness, adherence and stoichiometry of the surface oxide layer[18].

1.3.1.1 Kinetics

Oxidation of a clean surface is a two-stage process in which the reaction rate is limited by diffusion of oxygen or oxygen-containing species through a coherent product layer formed on the surface. During an initial parabolic stage, the rate at constant temperature decreases progressively as the thickness of the product layer increases. This is followed by a pseudo-linear rate due to repeated spallation of material.

Ritchie[19] conducted a review of the rates for reactions up to 300 °C and provided linear rate laws for various conditions, dry air, water vapour and water vapour plus oxygen at 100% relative humidity (RH) and 2-90% RH. Table 1.2 shows the rate for each of the conditions.

Table 1.2 Linear reaction rates determined by Ritchie[19].

Exposure	Temperature (°C)	Rate (mg U cm^{-2} h^{-1})
Uranium-dry air	40 - 300	6.9×10^8 exp (-18300/RT)
Uranium-water vapour (100% RH)	20 - 100	3.2×10^8 exp (-13800/RT)
Uranium-oxygen-water vapour (100% RH)	25 - 100	4.6×10^9 exp (-17800/RT)
Uranium-oxygen-water vapour (2-90% RH)	40 - 130	4.8×10^{13} exp (-25000/RT)

It has been previously shown[4] that the reaction rate for water vapour is faster than that for dry oxygen/air. It has been suggested that the rate determining step is the transport of the oxygen-containing species to the metal though the thin layer of adherent metal oxide via interstitial mechanism.

The rate of the uranium oxygen reaction was shown[19] to depend on the pressure aligned with the Langmuir isotherm, in that the reciprocal of the rate bears a linear relationship to the reciprocal of oxygen pressure. Above a certain limiting pressure, it was found that any further increase had little or no effect on the rate. For the water vapour reaction, sigmoidal dependence was found for the reaction rate on relative humidity at 75 °C and 100 °C. When

oxygen is added to the water vapour reaction, a much slower rate is seen and very little hydrogen is evolved. Below 100 °C it was found that the rate is independent of relative humidity between 2-90% but the rate increases with humidity from 90-100%, likely due to a change in mechanism[6,19].

1.3.1.2 Mechanism – water vapour

The free energy of formation of UO_2 is lower than that of H_2O, meaning that water will oxidise uranium to UO_2. The underlying mechanism by which the reaction of uranium with water vapour proceeds, whether in the presence of oxygen or not, has been a longstanding topic of debate[4,6,20–22]. Although anionic diffusion is agreed upon, several reaction mechanisms have been proposed with different dominant diffusing species and pathways through the oxide to the oxide-metal interface. Both Baker[2,3] (using gas chromatographic analysis of reaction products) and Allen[23] (using X-ray photoelectron spectroscopy) claim the diffusing species to be OH^- for the uranium water reaction, in cases both with and without oxygen present. However, Weirick[22] (using thermogravimetric and gas spectrometric measurements) and Haschke[4,5] (using microbalance and pressure-volume temperature methods) contest that the diffusing species is O^{2-}. In some cases it is suggested that uranium hydride is formed during the reaction, as an intermediary species or co-product, forming either as a continuous layer or at discrete locations. The formation of uranium hydride has been proposed as a reason for the increased oxidation rate as compared to dry oxygen.

The mechanism proposed by Baker[2,3] and Allen[23] is firstly based on the dissociation of water to OH^- at the oxide surface:

$H_2O \rightarrow H^+(\text{hydrated}) + OH^-$ (at oxide surface)

OH^- species then diffuse to the metal-oxide interface, where they subsequently react with the metal to yield UO_{2+x} and molecular hydrogen:

$U + 2OH^- \rightarrow UO_2 + H_2 + 2e^-$

The hydrogen produced by both uranium oxidation and water dissociation can also react with the metal to form uranium hydride, which Baker proposes can subsequently react with additional water to form uranium dioxide and hydrogen:

$6H\cdot + 2U \rightarrow 2UH_3 + 4H_2O \rightarrow 2UO_2 + 7H_2$

Baker[2,3] poses three possibilities for the formation of uranium hydride: (1) it is a product of reaction between free hydrogen and uranium metal; (2) it is an intermediate in the oxidation of uranium by water; (3) hydride and oxide are alternate products of reaction. Kondo[20,24] proposed a hydride fracture mechanism where uranium hydride is formed as an intermediate product. It is a two stage mechanism; initially very thin oxide and hydride films are formed and grow to some critical thickness before stage two proceeds (see below). The mechanism for stage two is similar to that proposed by Baker, with the hydrogen from water dissociation reacting with the uranium to form hydride, which in turn reacts with the oxygen ion (OH^-/O^{2-}) to form oxide. These product layers then undergo a fracture and healing process.

1) Oxide gas interface:
Adsorbed water + electrons → Hydrogen + hydroxyl ion
2) Metal hydride interface:
Uranium + hydrogen → Uranium hydride
3) Hydride oxide interface:
Uranium hydride + oxygen ion → Uranium oxide + hydrogen + electrons

Other studies (including those by Weirick[22] and Haschke[4,5]) contest that since no UH_3 is detected, the diffusing species is unlikely to be OH^-, and thus it is more likely that both oxygen and water react directly with the uranium, in the form:

1) $U + O_2 \rightarrow UO_2$
2) $U + 2H_2O \rightarrow UO_2 + 2H_2$

Haschke[4,5] states that the product formed is the same as in dry air oxidation, i.e. UO_2. The mechanism involves water chemisorbing as hydroxide on to the oxide at low temperatures showing rate enhancement. At high temperatures the water desorbs and the enhancement terminates. The enhanced rate is determined by the OH^- concentration. With the lattice oxide concentration remaining constant, the concentration of OH^- is proportional to the square root of the water vapour pressure. The OH^- ions react with electrons to form O^{2-} and hydrogen atoms. Half of the O^{2-} formed is used to replace those reacted during the OH^- formation and

the remainder enters interstitial sites, migrates as clusters and reacts. The product hydrogen atoms combine to form H_2, which leads to desorption.

1.3.1.3 Mechanism – water vapour plus oxygen

The addition of oxygen, even in very low quantities (~100 vppm), to water vapour is known to have a marked effect on the reaction kinetics and hence the mechanism. Reported experimental findings include the amount of inhibition produced by oxygen to be directly proportional to the $H_2O_{(v)}$ pressure, the generation of hydrogen is reduced to very low levels and oxygen is linearly consumed with time in the oxygen-inhibited U-H_2O reaction in a constant volume system[21].

Again there is much debate on the diffusing species, be it OH^- [2,3], O^{2-} [21,22] or a combination[6], and how oxygen inhibits the reaction with water vapour. There are three main scenarios for the role of oxygen:

1) Reducing H_2O dissociation at the surface by preferential adsorption of oxygen
2) Impeding OH^- diffusion by blocking adsorption sites
3) Promoting surface recombination of water

Baker[2,3] suggests that OH^- is the diffusing species and that the oxygen is consumed through conversion to water thus preventing the evolution of hydrogen. He suggests that the inhibition is due to the direct adsorption of water on the oxide being prevented by a chemisorbed layer of oxygen. He proposes the following reaction scheme for the water vapour plus oxygen reaction:

$O_{2(g)} + 2e^- \rightarrow 2{}^{G}O_S^-$

$H_2O_{(g)} \rightarrow H_S^+ + OH_S^-$

${}^{G}O_S^- + H_S^+ \rightarrow {}^{G}OH_S$

where ${}^{G}O$ signifies a species derived from oxygen gas and subscript s indicates surface-adsorbed species.

OH_S^- diffuses to the uranium-uranium oxide interface and reacts liberating H· which diffuses to the solid-gas interface to form water:

$H\cdot + {}^{G}OH_S \longrightarrow H_2{}^{G}O_{(g)}$

Haschke[4] agrees with Baker that the oxide is formed from the water and that the oxygen combines with hydrogen to form water. However, he proposes the route of this exchange to be via a water catalysed cycle with the product hydrogen associating with atomic oxygen to form O_2 at the oxide surface, and not by a process involving dissociation of H_2O into the elements as proposed by Baker[2,3]. Kondo[20,24] also agrees that there is an interaction of oxygen and active hydrogen. However, in this scheme the hydrogen is released from the oxidation of uranium hydride and not the dissociation of water. This then leads to a shortage of hydrogen supply and thus retards the proposed hydride fracture mechanism, producing an inhibitory effect on the rate of oxidation.

Both Colmenares[21] and Weirick[22] propose O^{2-} as the diffusing species, with Colmenares[21] proposing that a layer of chemisorbed oxygen forms on top of the surface oxide, which then blocks the transport of OH^- but not that of oxygen. The oxygen is able to diffuse through the uranium oxide coherent layer to react with the metal at the metal-oxide interface to form the UO_2 oxide product. Weirick[22] proposed that in the initial stages of the reaction, a different mechanism operated which was essentially the same as the pure water vapour reaction (direct reaction with H_2O) and that a change of mechanism occurred after about 24 h, after which reaction was directly with O_2, and no exchange occurred. Winer[25], using X-ray photoelectron spectroscopy (XPS), also postulated that the inhibition of the $H_2O(v)/U$ reaction by oxygen is due to preferential chemisorption of oxygen species on the surface, blocking water molecules and thus the transport of hydroxyl ions.

McGillivray[6] studied the reaction of uranium with water vapour with and without oxygen present using both gravimetric microbalance measurements and Secondary ion mass spectrometry (SIMS). He reported the diffusing species to be both OH^- and O^{2-} when uranium is in the presence of both water and oxygen, but that oxygen preferentially absorbs on the oxide surface, thus limiting the water dissociation process. The depth profile studies showed that the initial oxide product is highly enriched in the isotope from H_2O and that the content of isotope from O_2 progressively increases with depth. It has been found that oxidation proceeds by reaction of H_2O with O_2, transforming into both H_2O and oxide product meaning that each H_2O

reacted is replaced, keeping the concentration constant. The composition of the oxide layer is thus controlled by the rates of competing oxidation and reduction reactions:

$H_2{}^{18}O + e^- \rightarrow {}^{18}OH$ and/or $({}^{18}O)^{2-}$ (at surface)

$U^{4+} + 2({}^{18}OH)^- \rightarrow U({}^{18}O)_2 + 2H^+$

$({}^{16}O)_2 + 4e^- \rightarrow 2({}^{16}O)^{2-}$ (at surface)

$U^{4+} + 2({}^{16}O)^{2-} \rightarrow U({}^{16}O)_2$

1.3.1.4 Summary of uranium literature

For uranium, a multitude of research has been carried out. However, fundamental information on the mechanism remains debated, such as the diffusing species, if and how hydrogen is involved, e.g. is hydride formed, and how the addition of oxygen to the water vapour reaction leads to a reduction in rate.

- Literature opinions of the diffusing species differ:
    - OH^- as diffusing species (Baker, Ritchie, Allen, Colmenares)
    - O^{2-} as diffusing species (Haschke, Weirick)
    - Both (McGillivray)
- H_2 production can occur via three possible routes: (1) at the oxide gas interface; (2) the oxide metal interface; and (3) through reaction of hydride with water. Opinions differ on how many and which routes:
    - Only one route – at the oxide gas interface (Haschke)
    - Two routes – Oxide metal interface (Kondo)
    - All three routes (Baker)
- Opinion differs on whether hydride forms during the water vapour reaction:
    - Hydride formed (Baker, Kondo)
    - Hydride not produced (Ritchie, Colmenares, Haschke)
- How O_2 inhibits the U-H_2O reaction is also debated:
    - Reducing H_2O dissociation and impeding OH^- diffusion in oxide (Colmenares, Weirick, Winer)
    - Promoting surface recombination of species to reform water (Baker, Haschke, Kondo)
    - Reducing H_2O dissociation at the surface and recombination (McGillivray)

1.3.2 Niobium

Niobium forms oxides with the oxidation states +5 (Nb_2O_5), +4 (NbO_2) and +3 (Nb_2O_3), as well as with the rarer oxidation state +2 (NbO). Most commonly encountered is the pentoxide, precursor to almost all niobium compounds and alloys.

Niobium has a high melting point and a low vapour pressure. It has good ductility and a low neutron cross-section. However, at high temperatures, above 400 °C, it has very low oxidation resistance, meaning that the initial protective film is supplanted by a scale which offers little to no protection from further rapid oxidation.

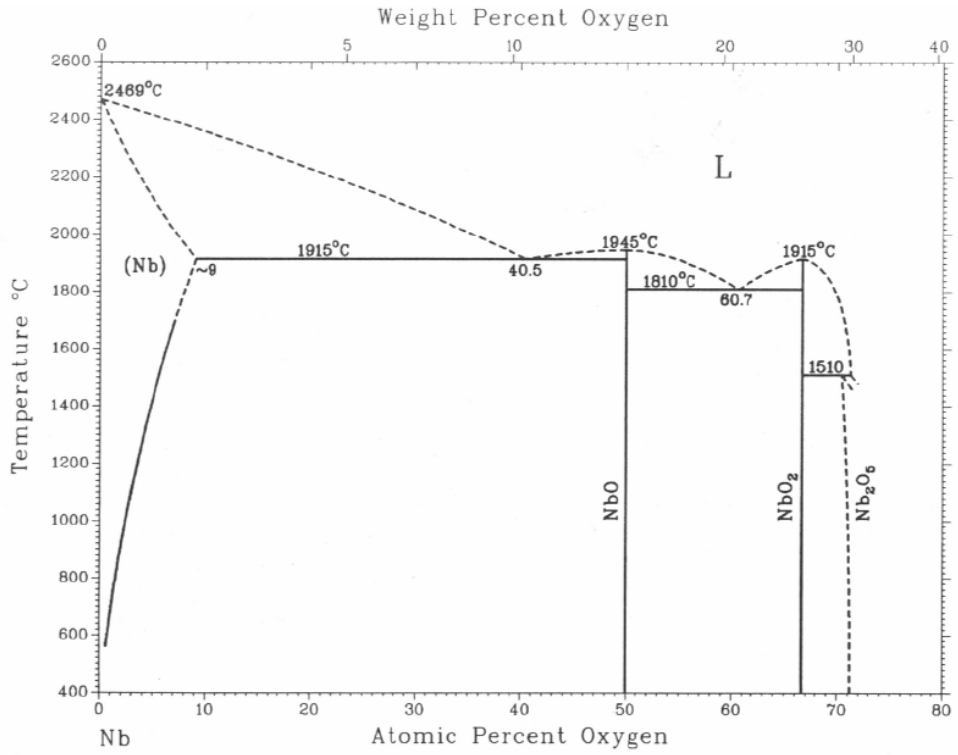

Figure 1.7 Phase diagram for niobium and oxygen[17]

Niobium is used for superconducting radio frequency cavities, which are central components of high energy and high intensity particle accelerators. During fabrication of these cavities it has been found that small atoms such as oxygen and hydrogen reside as interstitial atoms in niobium's bcc structure and then go on to form niobium oxides and hydrides. For the superconducting industry these oxides and hydrides are believed to be responsible for

reducing the quality factor (Q). The Q-factor is a dimensionless parameter that describes how under-damped an oscillator or resonator is and characterises a resonator's bandwidth relative to its centre frequency[7]. For this study the Q-factor is not relevant. However the principal and mechanism of oxide and/or hydride formation is likely to be similar.

1.3.2.1 Kinetics – oxygen

Many workers[26,27] have investigated the oxidation of niobium (in oxygen/air), and the relevant features of its behaviour have been summarised by Argent and Phelps[27] , see Table 1.3. A possible scheme to explain the change in oxidation behaviour with temperature was also provided. It assumes that oxygen is adsorbed on the outer oxide surface and that it subsequently dissociates and is incorporated in the scale. At low temperatures the potential sites for oxygen absorption are all occupied, meaning the rate-controlling process is the diffusion of anions through a coherent layer, and therefore parabolic growth law is observed.

As the temperature is increased (above 400 °C) the oxide layer reaches a limiting thickness at which the scale cracks. Between 400 °C - 450 °C the surface becomes completely covered by a layer of absorbed oxygen, leading to a linear but pressure-independent rate. As the temperature is increased further (up to 600 °C) the surface of the oxide is no longer saturated with absorbed oxygen and the temperature dependence of the rate decreases. The rate of oxidation depends on the square root of the oxygen pressure. The outer scale breaks down owing to a change in density from amorphous Nb_2O_5 to α-Nb_2O_5. From 600 °C -675 °C the surface area of the scales and the absorption per unit area decrease rapidly and give a decreasing rate of oxidation with increasing temperature, and absorption becomes the rate-controlling factor.

The temperature range of 675 °C - 800 °C sees the rate depend on the oxygen concentration in the gas phase, with diffusion through the inner oxide once again the determining factor, and a pressure dependence of square root. Finally, between 850 °C - 1050 °C the niobium is largely saturated with oxygen and the oxides are near stoichiometric, with β-Nb_2O_5 forming.

Below 250 °C Cabera and Mott[26] suggested that the rate changed from log to inverse log with increase in time and, therefore, oxide thickness.

Table 1.3 Characteristic features of the oxidation of niobium[27].

	Temperature range °C					
	250 - 400	**400 - 450**	**450 - 600**	**600 - 675**	**675 - 850**	**850 - 1050**
Growth law	Parabolic	Parabolic changing to linear	Parabolic changing to linear	Linear	Linear	Linear
Temperature dependence of oxidation rate	Positive	Positive	Positive	Negative	Positive	Positive
Pressure dependence	Independent	Independent	$P^{½}$	P^{1}	$P^{½}$	Not known
Oxide type	Amorphous + α-Nb_2O_5	Amorphous + α-Nb_2O_5	α-Nb_2O_5	α-Nb_2O_5	α-Nb_2O_5	β-Nb_2O_5
Oxide character	Adherent film showing temper colours	Adherent dark film	Cream oxide some spalling at temperature Maximum specific surface at 450°C	Cream oxide, slight spalling Decreasing specific surface →	Light grey oxide changing to dark grey with increasing temperature No spalling	Cream oxide. No spalling at temperature but spalls on cooling
Deviations from stoichiometry	Not known	Changes from anion deficient at 400°C to apparent cation deficiency at 450 °C	Apparently cation deficient. Approaches stoichiometry at 550 °C	Increasing anion deficiency	Anion deficient returning to stoichiometry at 800 °C	Not known

1.3.2.2 Kinetics – water vapour

There is limited literature on the kinetics of the corrosion of Nb by water vapour and the majority of studies have been conducted at much higher temperatures to the ones used within this study. As previously stated, at higher temperatures niobium's oxidation resistance is lowered, which leads to cracking of the protective oxide film.

Blackburn[28] conducted a short review on the niobium water vapour reaction. He found that the previous studies had varied opinions on the kinetics before transition (below 400 °C).

Protective (parabolic) oxidation was found by Gulbransen and Andrew[29,30], Inoye[31], Cathcart[32] and Bridges and Fassell[33], while Klopp, Simms and Jaffee[34] reported the kinetics to be linear.

Blackburn[28] found that for experiments conducted between 250 °C – 350 °C the slope of the curve was close to 0.5 while measurements between 200 °C – 225 °C and 400 °C – 750 °C had a slope closer to 0.33. Two sample preparation methods were used, experiments conducted at 250 °C – 500 °C were prepared by abrasion with a blast of alumina powder while experiments conducted at the other temperatures (200 °C – 250 °C and >500 °C) were prepared by mechanical polishing. When the data were plotted by surface treatment, the mechanically-polished samples show a slope of 0.33 while the blast samples show a slope closer to 0.5 for temperatures up to 350 °C before changing to a slope of 0.33 for the 350 °C – 750 °C temperature range. A clear change in reaction kinetics was seen above 750 °C, where a decrease in the rate constant was seen. This temperature is associated with breakaway oxidation and the formation and growth of Nb_2O_5.

Passier[35] found that the reaction at high temperatures (800 °C – 1000 °C) was slow compared to the reaction in oxygen. In 13.2 hPa water vapour the rate was linear after a short period of decreasing rate. The apparent E_a increases from 39 to 93 kJ mol^{-1} when water vapour increases from 2.6 to 65.8 hPa. The pressure influence was shown to be important and could be fitted by a homographic law:

$$K_1 = \frac{AP_{H_2O}}{1 + BP_{H_2O}}$$

where A (mg cm^{-2} h^{-1} hPa^{-1}) and B (hPa^{-1}) are constants.

Blackburn[28] found that at low temperatures the rate of oxidation of niobium in water vapour was similar to that in oxygen. The main difference was the temperature required for breakaway oxidation to occur. For water vapour, this temperature was much higher (750 °C) than for oxygen (450 °C), leading to a much slower nucleation and growth rate of Nb_2O_5. This means the oxide on niobium remains protective for a longer period when exposed to water vapour over oxygen.

Inoye[31] found that the addition of water vapour to oxygen accelerates the reaction at 400 °C but not at higher temperatures. The reaction being slower in water vapour than oxygen is the opposite of that found for uranium. The addition of water vapour to the oxygen reaction also has the adverse effect in accelerating the rate. It is therefore anticipated that the differences in the kinetics for each of the bulk metals (U and Nb) will have an impact on the reaction of the alloy.

1.3.2.3 Mechanism

Kubaschewski[36] reported that at 330 °C the oxide formed from oxygen is amorphous Nb_2O_5 with some sub-oxides. As the temperature increases the suboxides decompose and the X-ray pattern for Nb_2O_5 sharpens. At 500 °C small blister like cracks start forming and increase with time. Above 500 °C the spalling and cracking becomes pronounced and at 1250 °C there is a non-adherent layer that easily flakes off.

There have been varying results in identifying these sub-oxides. Phelps, Gulbransen and Hickman[37] were able to definitively identify NbO as one of the low-temperature products of oxidation. In the oxygen studies by Hurlen[38], which covered the temperature range of 100 °C – 1000 °C, neither NbO, NbO_2 nor Nb_2O_5 were found below the breakaway point (750 °C), although in some cases two oxides, designated NbO_x and NbO_y, were detected. The NbO_x phase has also been seen by Brauer and Müller[39], who assigned it to Nb_2O.

From Passier's[35] water vapour study, a compact adherent oxide was formed which consisted of monoclinic NbO_2. This was contrary to what was expected. Based on thermodynamic calculations, see

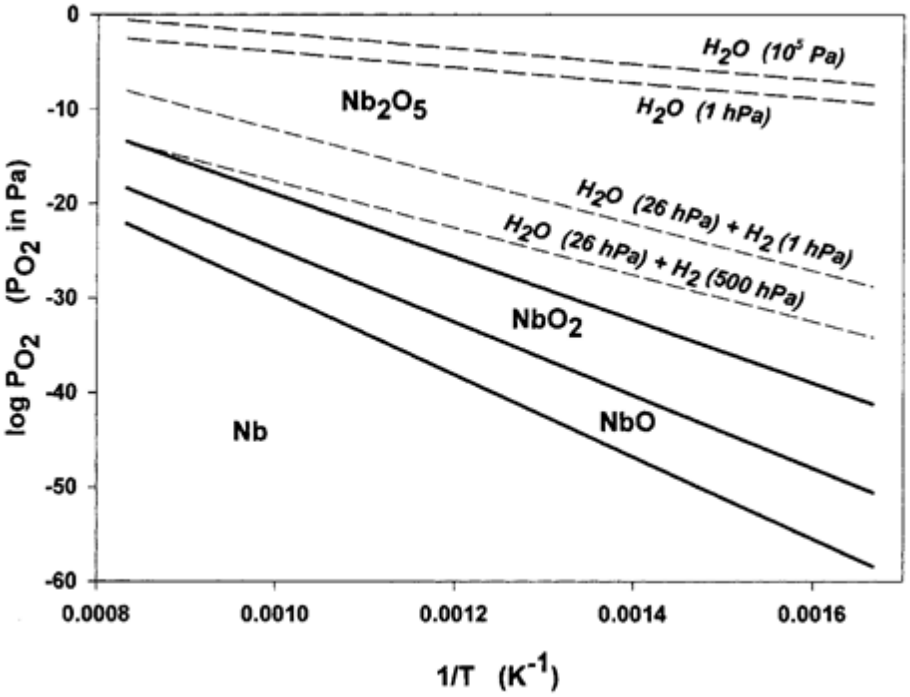

Figure 1.8, Nb_2O_5 should have been present. This result, however, was consistent with previous literature[40,41]. Gold markers, deposited by dc sputtering, showed that the new oxide is formed at the oxide-metal interface and arises therefore via transport of oxygen vacancies. He proposed a model in which the limiting step was the surface reaction of oxygen incorporation into the oxide scale without formation of any hydroxide defects.

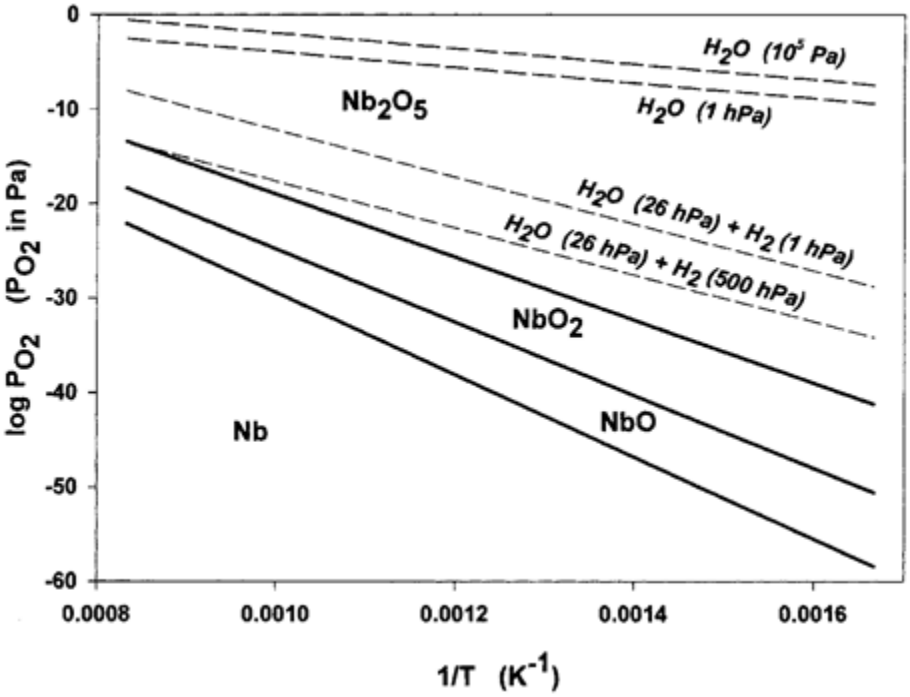

Figure 1.8 Stability domains as functions of temperature and oxygen pressure of metallic niobium and its oxides. Solid lines, limits of phase-stability domains, dashed lines O_2 partial pressures in equilibrium with H_2O (short dash) and H_2O/H_2 (long dash)[35].

Sheasby[42,43] used SIMS to look at the oxidation of niobium using ^{18}O. He found that the ^{18}O was found in the oxide layers adjacent to the metal. At 700 °C a layered structure is formed due to the continual cracking and oxide re-growth. At a slightly lower temperature of 600 °C it was found that Nb_2O_5 was either growing from the NbO layer or directly from the metal which resulted in much faster kinetics. The ^{18}O distribution demonstrated that oxygen, and not niobium, was the mobile species agreeing with Passier's[35] observations.

Wu[44] also used SIMS to look at the niobium oxide structure. He investigated the effect of sample preparation, buffered chemical polishing (BCP) and buffered electro polishing (BEP) and also utilised argon bombardment to slowly etch through the oxide layers. The sputtering was slowed to allow good signal:noise ratios of each ion of interest. Samples treated using BEP were found to have a thin layer of niobium suboixde remaining, while for samples treated using BCP the strongest peaks were for the metal Nb^+.

Blackburn[28] found that the mechanism of the low-temperature oxidation of niobium is similar in oxygen and water vapour. Before the transition to breakaway oxidation, the reaction involves solution of oxygen in the metal and formation of NbO and NbO_2 on the surface. Since

NbO_2 grows at a linear rate which is less than the total oxidation rate, it must grow at the NbO-NbO_2 interface offering no barrier to the penetration of gaseous oxygen or water to the NbO surface. The cubic or parabolic rate which accounts for the bulk of the oxidation arises from dissociation of oxygen and the simultaneous formation of NbO.

Cathcart[32], say that breakaway oxidation (in both oxygen and water vapour) is due to mechanical stress in the film, which leads to cracks and blisters and then subsequent breakdown of protection. The rate is linear due to continual cracking and healing. Hurlen[45], state that the breakaway is due to the nucleation and growth of Nb_2O_5. Blackburn agrees with the latter, showing that NbO_2 is present before the Nb_2O_5 phase appears.

Ford[46,47] investigated the hydride formation as well as possible suppression of these detrimental effects by a change to the preparation process. It was found that adsorption of hydrogen from the gas phase is exothermic and hydrogen becomes anionic. Adsorption into lattice vacancies is preferred over interstitial sites, as a single vacancy can accommodate six hydrogen atoms and then additional hydrogen can be found in nearby interstitial sites. This implies that a vacancy can serve as a nucleation centre for a hydride phase. Attachment of an oxygen ion to a lattice vacancy is substantially stronger than for hydrogen. Thus, the concentration of oxygen in the bcc lattice can have a strong impact on the ability of hydrogen to form detrimental phases, e.g. a hydride. The oxygen atoms have been found to migrate into the vacancies previously occupied by hydrogen, thus preventing further hydrogen atoms returning to the sites and reducing the opportunity of nucleation and growth of a hydride phase.

Kim[48] investigated the hydrogen and oxygen interstitials in niobium using atom probe tomography. He found that the oxide layer was 0-10 nm in depth and contained NbO, NbO_2 and Nb_2O_5. This was then followed by a small niobium metal layer, approximately 5nm before entering into a relatively thick, 40 nm, niobium hydride layer. It was found that residual gases within the system were not responsible for these chemical analyses and therefore the oxides and hydride formed were from reaction.

1.3.2.4 Summary of niobium literature

For niobium there is limited literature on the water vapour reaction under the experiment conditions relevant to this study (<70 °C). The literature suggests a clear breakaway region at 750 °C possibly associated with the nucleation and growth of Nb_2O_5. Previous analysis on the oxidised material reveals the oxidation to be via anionic diffusion with oxide forming at the oxide metal interface, therefore the same mechanism as with uranium. Suboxides (NbO and NbO_2) have been seen by some researchers in addition to the most stable oxide Nb_2O_5. The Nb_2O_5 has been found to form from both these suboxides and directly from reaction with exposed metal (due to cracking). There is also clear evidence of hydride formation, suggesting the possible involvement of OH^- in the mechanism.

- Kinetic rate laws:
    - Parabolic (250 °C – 400 °C) moving to linear (400 °C – 600 °C) for oxygen (Cabera)
    - Slope of 0.33 for polished samples (200 °C – 250°C and >500 °C) and blasted samples (350 °C – 750 °C) (Blackburn)
    - Slope of 0.5 for blasted samples (<350 °C) (Blackburn)
    - Homographic rate law 800 °C – 1000 °C (Passier)
    - Reaction slower in water than oxygen (opposite to uranium)
    - Addition of water vapour to oxygen reaction accelerates rate (up to 400 °C)
- Structure:
    - Lower oxide NbO present (Phelps, Gulbransen, and Hickman)
    - Lower oxides NbO_x and NbO_y (Hurlen, Brauer)
    - Niobium hydride found between the oxides and the bulk metal (Kim, Ford)
- Mechanism before breakaway oxidation:
    - Oxide formed at oxide-metal interface
    - Solution of oxygen in the metal and formation of NbO and NbO_2 on the surface
- Breakaway mechanism
    - Nucleation and growth of Nb_2O_5 on NbO_2 (Blackburn, Hurlen)
    - Mechanical stress leads to cracking of the oxide (Cathcart)
    - Occurs at higher temperature with water vapour than oxygen (Blackburn)

1.3.3 Uranium niobium alloys

Transition metal elements are added to uranium to improve physical, mechanical and corrosion properties. Uranium alloys can exhibit age-hardening responses due to the complete solubility in the body centred cubic (bcc) γ-U phase at high temperatures but virtual insolubility in the low temperature phase (α-U). This study focuses on the uranium niobium alloy system with the phase diagram shown in figure 1.9. Niobium has been found to significantly increase uranium's corrosion resistance. Initially however the alloys exhibit poor resistance due to segregation, it is only after heat treatment followed by quenching to room temperature that the alloys show improved corrosion resistance. This rapid cooling results in niobium supersaturated metastable phases including α', α'' and γ^0. The α' phase is martensitically-formed orthorhombic α, whereas the α'' and γ^0 phases are monoclinically-distorted α' and tetragonally-distorted γ respectively. At ambient temperature, the α' phase exists over the concentration range 0-8 at% Nb, the α'' phase over the 9-15 at% Nb range and the γ^0 phase over the 16-20 at% Nb range. At >20 at% Nb, the metastable (niobium supersaturated) γ phase is retained[1].

Table 1.4 contains the free energies of formation of UO_2 and the three niobium oxides, and Table 1.5 lists the equilibrium ratio of water vapour to hydrogen pressure for the formation of the oxides, calculated from these free energies. These increase in the order UO_2 < NbO < NbO_2 < Nb_2O_5, with the relative affinity of the metals for the formation of these oxides increasing in the reverse order. It is therefore predicted that uranium should be oxidised first to UO_2, followed by the oxidation of niobium to NbO, NbO_2 and Nb_2O_5 in that order. In addition, the ability of uranium metal to reduce the niobium oxides should limit their formation at the oxide-metal interface[17].

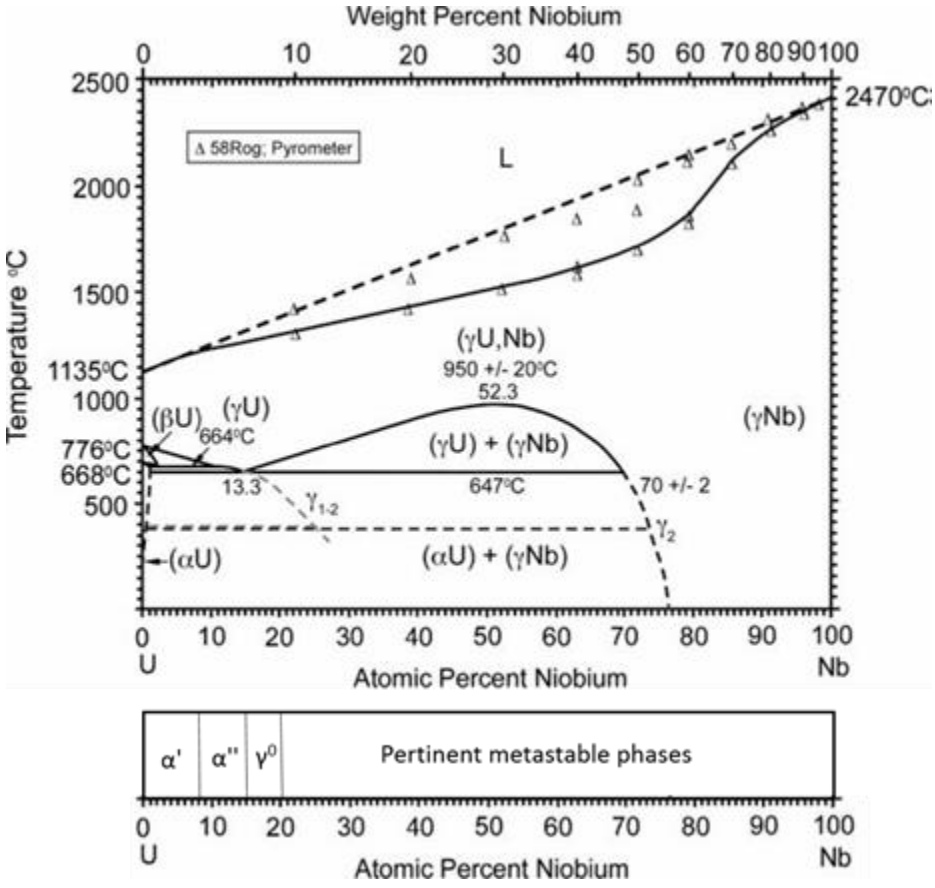

Figure 1.9 UNb phase diagram[1,49].

Table 1.4 Free energies for the formation of uranium and niobium oxides from H_2O for the temperature range relevant to this thesis (20 °C – 75 °C)[17].

Temperature (K)	Free energy (kJ mol^{-1})			
	UO_2	NbO	NbO_2	Nb_2O_5
298.15	-575	-163	-282	-623
300.00	-575	-163	-282	-623
400.00	-566	-163	-282	-623

Table 1.5 Equilibrium ratio of H_2O to H_2 pressure in formation of uranium and niobium oxides from H_2O for the temperature range relevant to this thesis (20 °C – 75 °C)[17].

Temperature (K)	PH_2O/PH_2			
	UO_2	NbO	NbO_2	Nb_2O_5
298.15	4.55E-51	2.35E-29	1.95E-25	1.47E-22
300.00	9.62E-51	3.66E-29	2.87E-25	2.07E-22
400.00	1.10E-37	1.90E-21	1.61E-18	2.00E-16

Low temperature ageing of UNb alloys (<20 at% Nb) has been found to result in increased strength levels, but with this comes ductility loss and a reduction in its corrosion resistance[1]. The term ageing is used to describe specific physical mechanisms by which the microstructure

and properties evolve as a function of time for a given temperature and local environment. Therefore, long term storage of the material may lead to ageing and could change the material in ways that will adversely affect its performance, in this instance its corrosion resistance. The compositional inhomogeneity of the material will also have an impact, due to areas of differing local Nb content having different initial mechanical properties and ageing rates. This means that the material may corrode differently to that of a compositionally homogeneous UNb alloy. Studies have been conducted to investigate the ageing of UNb alloys, with various decomposition mechanisms such as chemical redistribution, spinodal decomposition and order-disorder transformation being proposed[1,49]. The materials used in this study are 3 and 6 wt% Nb and therefore fall within the metastable phases of α' and α'' respectively. The alloys used within this study have an age of >15 years. They have been stored at low temperatures (below 60 °C) but in the presence of moisture. Due to this age of material it is possible than some form of ageing/decomposition may have occurred and it is likely to have an impact on the corrosion rates.

1.3.3.1 Kinetics

Magnani's[8] experiments demonstrated that UNb alloys have a slower oxidation rate when compared to pure uranium, with the oxide thickness decreasing with increasing niobium content. Younes[50], using Auger and XPS, also demonstrated the alloy (6 wt% Nb in this case) to show slower oxidation rate than uranium, while pure niobium oxidised at a much lower rate than both the uranium and alloy.

In contrast, Fu[10] demonstrated using XPS that the initial (<10 nm) thin oxide film grew faster on the alloys than the base metals. This showed that the growth of the initial thin film cannot be part of the corrosion resistance mechanism. This can only occur subsequently during the growth of thicker (>10 nm) oxide films, which is supported by the work of both Magnani[8] and Younes[50]. It was also demonstrated by Kelly[11] that the oxidation rate decreased with increasing niobium content, for the range of alloys studied (2-8 wt% Nb).

For pure uranium, the rate of oxidation is faster by water than oxygen, which may be due to diffusion to the oxide-metal interface being easier for OH^- than O^{2-}. This was not the case for

pure niobium and it appears not to be the case for the alloy with Manner[51] using XPS and secondary neutral mass spectrometry (SNMS), showing oxidation to be much slower with D_2O rather than O_2.

Yang[52] conducted experiments on UNb alloy containing 2.5 wt% niobium in air. He found three regimes:

1) Below 80 °C a parabolic rate law is followed with an activation energy of 74.7 kJ mol^{-1}

2) 100 °C – 150 °C, there are two stages with a transition point from diffusion controlled reaction to a rate controlled by surface reaction

3) > 150 °C linear kinetics with activation energy of 31.5 kJ mol^{-1}

These regimes are similar to those seen for niobium and uranium, with the linear kinetics being associated with some form of continual cracking and healing mechanism of the no longer protective oxide.

1.3.3.2 Mechanism

The actual mechanism behind this enhanced resistance is uncertain and the oxidation of UNb alloys has only been studied by a few investigators. A number of investigators have shown the oxides formed during oxidation agree with the thermodynamics, with UO_2 initially forming, followed by an NbO sub-layer at the oxide-metal interface, then NbO_2 and finally Nb_2O_5 with longer exposure times[10,50]. Manner[9] using XPS found that the oxidation state of niobium is dependent on the exposure temperature. Exposure of 500 L (Langmuirs) at 227 °C produced a change of approx. 0.5 eV which is still characteristic of a clean Nb surface, while at 27 °C the same exposure produced peaks characteristic of Nb_2O_5.

The two proposed corrosion resistant mechanisms of UNb alloys are therefore[17]:

1) Nb forms a very thin second-phase oxide (Nb_2O_5) that protects the underlying metal by acting as an oxygen diffusion barrier. UNb is not more corrosion resistant than pure uranium metal until a critical density of Nb_2O_5 has been formed and it is the deficiency of Nb_2O_5 at the start that results in faster initial oxidation of UNb than pure U.

2) Dissolution of Nb in UO_2 lattice modifies electronic structure of oxide, resulting in slower oxygen transport through lattice. A mixed oxide is formed and the presence of niobium within the oxide acts as a diffusion barrier to interstitial oxide or hydroxide ions.

Manner[9] suggests the resistance is due to either the accumulation of Nb lowering reactivity of uranium at the metal-oxide interface or the formation of a critical density of Nb_2O_5 which acts as a diffusion barrier. Both of these proposals would lead to a depletion of Nb in the outer oxide, which was not detected by Manner[9]. Fu[10] however did observe niobium depletion and interpreted this result as a thin Nb_2O_5 layer forming at the oxide-metal interface which acted as a diffusion barrier to slow oxide growth, thus supporting Manner's proposal.

Niobium depletion in the outer oxide could only occur if the oxide grew by migration of metal ions across the oxide from the metal to the oxide-gas interface, with uranium ions moving much faster than niobium ions. This could only occur during the initial growth of the thin film. Both Manner and Fu were using XPS which has a low analysis depth range, meaning that only the initial film may have been analysed and, therefore, depletion in niobium is plausible. However, the depletion may not be relevant to the corrosion resistance which is only apparent in the growth of thick oxide films.

Magnani[8] studied the corrosion of UNb alloys with thick oxide films (>10 nm). Growth of these films is via thermal diffusion of interstitial oxide or hydroxide ions across the oxide film from the oxide-gas interface toward the metal. Niobium depletion at this stage is not possible as diffusion of U^{4+} and Nb^{5+} to form separate oxide layers (UO_2 and Nb_2O_5 respectively) would be too slow. It was suggested that a mixed oxide is formed containing a UO_2 fluorite structure with a proportion of U^{4+} being replaced by Nb^{5+} and addition of compensating interstitial O^{2-} ions. The addition of these interstitial oxygen ions would be responsible for slowing the oxidation by impeding the passage of other mobile O^{2-} ions.

1.3.3.3 Summary of uranium niobium literature

For UNb alloys there is again limited open literature available. Published work shows the rate of corrosion (after an initial thin film is produced) to be significantly slower than uranium. However, it does not provide a definitive mechanism for this enhanced resistance. There are

a number of mechanisms postulated with varying opinions on niobium depletion at the surface or oxide-metal interface and the formation of diffusion barriers being reported.

- Pressure dependence (McGurk):
    - Initial oxidation is parabolic with formation of a protective oxide (NbO)
    - Followed by a transition to linear facilitated by formation of porous Nb_2O_5
- Oxides formed (McGurk)
    - Relative affinity for formation of oxides in order:
      $UO_2 > NbO > NbO_2 > Nb_2O_5$
    - UO_2 formed first, followed by NbO suboxide at oxide-metal interface, NbO_2 and Nb_2O_5 formed after longer exposures
- Nb depletion vs enrichment
    - Metal – enriched in Nb at oxide-metal interface (Magnani)
    - In acidic solutions niobium enrichment in the oxide was seen (Kelly)
    - Depletion of Nb in the outer oxide (Fu)
- Reason for resistance
    - Interstitial O ions slow oxidation by impeding passage of other mobile O^{2-} ions (Magnani)
    - Formation of Nb oxide layer at oxide-metal interface – acts as diffusion barrier for U ions (Manner, Fu, Kelly)
    - Accumulation of metallic niobium, lowering the activity of uranium at the oxide-metal interface (Manner)

1.4 Aims of this study

The kinetics in both water vapour and water vapour plus oxygen are generally agreed upon for uranium. However, the mechanism remains unanswered. Anionic diffusion is agreed upon with OH^- or O^{2-} (or both) as the diffusing species. There is still much debate over the exact mechanism and whether a thin hydride layer is formed. For niobium the kinetic data are limited, with the majority of work being conducted at much higher temperatures due to niobium's use in the superconducting industry. Information on the oxides formed through oxidation with water vapour is limited, with the majority of previous work looking into oxygen

as the oxidative species. For the alloy system the kinetic data are limited and information on the mechanism and how niobium enhances the corrosion resistance is conflicting.
The work presented in this thesis is focussed on determining the mechanism of the water vapour reaction for uranium, niobium and the alloys. The key information sought after are the diffusing species and the presence of any intermediates formed along the way (e.g. hydride) as these provide an insight into the mechanism. For the alloys the role of the niobium and/or its oxides in the enhancement of corrosion resistance for uranium is the focus.

The alloys studied were 3 wt% and 6 wt%, these will be referred to as UNb3 and UNb6 respectively. There were two exposures studied, water vapour and water vapour plus oxygen. Exposures were conducted in sealed cells, with the pressure (assumed to be due to hydrogen evolution) being monitored throughout. The kinetic data were collected and analysed. However, this was incidental to the mechanistic study. For niobium and the alloys, the reaction has previously been shown to be relatively slow. Therefore, these reactions are deemed long term (months-years). The uranium reaction has been shown to be significantly faster (weeks-months).

Isotopically-labelled waters ($D_2{}^{16}O$ and $H_2{}^{18}O$) were used sequentially to allow depth profile analysis by SIMS. The use of the labelled oxygens should help determine the location of the freshly-formed oxide and the use of deuterium should also help confirm the diffusing species and whether any hydride was formed. When oxygen is added to the system, the use of labelled oxygen will help determine how the oxide forms, and from which molecule.

To further investigate the corrosion mechanism, atom probe tomography (APT) was conducted on samples that were exposed to air and D_2O vapour in air. ATP is a 3D atomic scale microscopy technique suited to the study of nanoscale structures, interfaces and elemental gradients in materials. For uranium, ATP was used to clarify the mechanism of water-driven uranium corrosion by unambiguously determining, or refuting, the presence and location of hydride within the corrosion product formed. For niobium, ATP was used to investigate the oxide structure and for the alloys APT was used to investigate the niobium distribution within the alloy and how the material undergoes initial oxidation.

The main aims of the thesis are shown here as bullet points. For each of the materials studied there were a number of key pieces of information sought. These highlighted key points will then be referred back to in the conclusions section to determine which aims were met.

- Uranium-water vapour reaction
    - Investigate mechanism of the reaction
        - Determine diffusing species
        - Determine if any hydride is formed
- Niobium-water vapour reaction
    - Investigate the rate kinetics of the reaction
        - Pressure and temperature dependencies
        - How addition of oxygen effects the rate kinetics
    - Investigate the mechanism of the reaction
        - Determine diffusing species
        - Determine oxide structure
- UNb alloy-water vapour reaction
    - Investigate the rate kinetics of the reaction
        - Pressure and temperature dependencies
        - How addition of oxygen effects the rate kinetics
    - Investigate the mechanism of the reaction
        - Determine diffusing species
        - Determine oxide structure
        - Determine niobium distribution within the alloy
            - Mechanism for enhanced resistance

2 Chapter two – analytical techniques

The key information to be derived from this study is on the mechanism of the water vapour reaction. Identification of the corrosion products and oxide structures was vital. It is also vital to know the degree of homogeneity of the alloys as this would have an impact on the corrosion resistance.

There were three different analytical techniques utilised during this study. The form of analysis was either sample imaging, focussing on the visual confirmation of the microstructure of the material, or mass composition, providing elemental confirmation of the reacting species and the resulting corrosion products.

For sample imaging both scanning electron microscopy (SEM) and atom probe tomography (APT) were used. The SEM was coupled with an energy dispersive x-ray (EDX) detector which allowed elemental analysis of the surface, providing key information on the corrosion products and, for the alloys, information on the metal constituents.

Mass composition utilised the analytical technique of secondary ion mass spectrometry (SIMS). This was used to analyse the corroded surface, providing chemical identification of the products. SIMS was able to differentiate isotopes allowing mechanistic information to be derived. APT also provided some mass composition, which allowed elemental compositions to be derived from the surface.

2.1 Scanning electron microscope (SEM)

Scanning electron microscopy (SEM) scans a sample surface with a focused electron beam producing images with information about the sample's topography and composition. The basic components of a scanning electron microscope are the electron column, consisting of an electron gun and a lens system, the electron collector and the viewing system. Figure 2.1 shows a schematic of a typical SEM system.

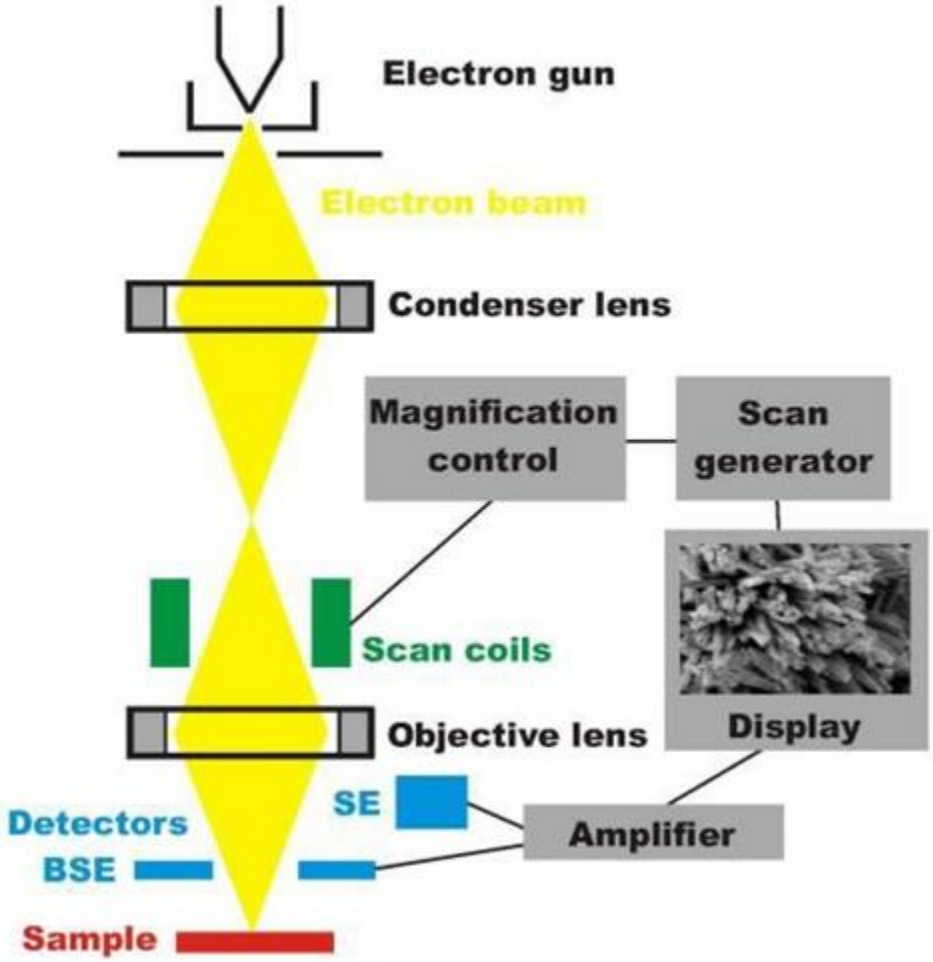

Figure 2.1 Schematic of SEM system[53].

2.1.1 Electron beam generation and manipulation

An SEM is required to operate under vacuum to allow the electron beam to travel unimpeded. The electron gun generates electrons and accelerates them down the column. The electron gun consists of three components: 1) a tungsten filament or LaB_6 crystal to generate the electrons; 2) the Wehnelt cap which controls the electron flow; and 3) the anode plate (positively charged) which draws the electrons down the column forming the electron beam.

A series of electromagnetic lenses are used to focus the electron beam because otherwise the spot size produced is too large to generate a sharp image. Condenser lenses are used first which adjust the beam diameter (spot size) and intensity. Beneath these are objective lenses which focus the beam and enable beam rastering.

2.1.2 Beam interaction, imaging and analysis

Resolution of the image is determined by a number of factors:

- **Accelerating voltage:** A greater accelerating voltage leads to increased depth penetration of the primary beam, which can be a positive or negative, depending on the aim of the investigation. However, the accelerating voltage also causes a greater interaction volume which decreases the resolution.
- **Spot size:** This is the diameter of the 'spot' when the electron beam impinges the surface of the sample. Decreasing the spot size enables greater resolution and decreases probe current. Increasing spot size decreases resolution and increases beam current.
- **Volume of interaction:** The volume inside the specimen in which interactions occur while being struck with an electron beam. This volume depends on Atomic number of the material being examined; Accelerating voltage being used and Angle of incidence for the electron beam.
- **Sample composition:** The primary electron depth of penetration and therefore volume of interaction (size and shape) is affected by composition. Depth of penetration and interaction volume decreases with increasing atomic number.

Once the electron beam enters the sample target area a multitude of reactions occur which enable imaging and analysis techniques to be performed. These include secondary electrons, backscattered electrons, X-rays, Auger electrons and cathodoluminescence.

Secondary electrons (SE): SE are low energy (<50 eV) electrons and generally escape from the surface layer (<10 nm). Secondary electron (SE) emission is due to inelastic interactions. The SE are used to show morphology and topography of the surface. The angle of SE emission is affected by the angle of incidence. The contrast in the image is dominated by the so-called edge effect: more secondary electrons can leave the sample at edges leading to increased brightness there (see Figure 2.2). This then provides vital information on the topography of the surface.

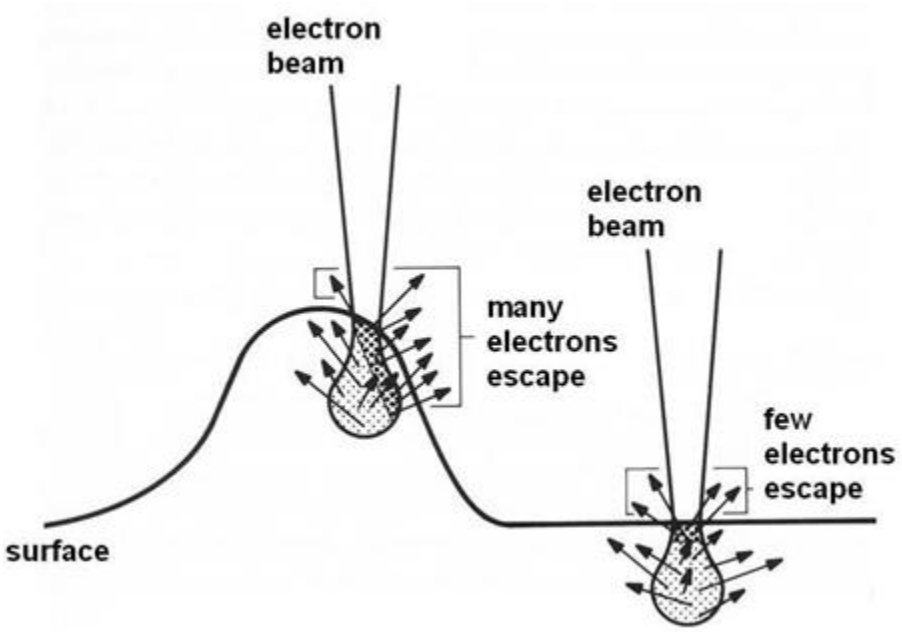

Figure 2.2 Schematic showing how secondary electrons relay topographic information[53].

Backscatter electrons (BSE): BSE are returning high energy (>50 eV) primary electrons and escape from a more moderate depth (10 – 100nm) in the sample. BSE result from elastic interactions between primary electrons and the target specimen. BSE are used to illustrate contrast in composition for multiphase samples, and to carry out crystallographic analysis.

Analysis of an area of interest can either be via a raster of the electron beam across the surface to form an image or the beam can be kept static to obtain analysis at one position. Two pairs of electromagnetic deflection coils are used to sweep the beam across the specimen (beam rastering). The first set deflects the beam off the optical axis of the microscope and the second bends the beam back onto the axis at the pivot point of the scan.

2.1.3 Electron detection

To produce the image, the ejected SE and BSE require detection. The signal generated from the specimen is acquired by the detector and processed to produce an image or spectrum. SE detection is commonly carried out using an Everhart-Thornley detector (scintillator-photomultiplier system). Semiconductor detectors are used to collect BSE and are usually positioned in an annular arrangement[53–55].

SEMs often have secondary detectors which use some of the other signals generated to provide further information about the sample including chemical compositions (using energy dispersive x-ray spectroscopy (EDX)) or crystalline structure and crystal orientations (using electron backscatter diffraction (EBSD))[54,55]. EDX is discussed in more detail in section 2.2.

2.2 Energy dispersive x-ray spectroscopy (EDX)

EDX was used in this study to determine elemental composition of the materials pre and post water vapour exposure. For the base metals it was used to visually examine the degree of oxidation after water vapour exposure. For the alloys, it was again used to look at oxidation. However, it was also used in order to investigate the niobium distribution, to see if it changed with oxidation. This information would aid in understanding how the addition of niobium to uranium leads to an enhanced corrosion resistance.

EDX is a micro elemental analysis technique used in conjunction with SEM to provide element composition information and the distribution of those elements. The technique utilises an electron beam to bombard a surface. The X-rays emitted are at a characteristic energy for each element and therefore can provide composition information.

Backscattered electron images in the SEM display compositional contrast that results from different atomic number elements and their distribution. EDX allows those particular elements to be identified and their relative proportions (atomic % for example).

Initial EDX analysis usually involves the generation of an X-ray spectrum from the entire scanned area of the SEM. Two basic types of X-rays are produced on inelastic interaction of the electron beam with the specimen atoms in the SEM:

- Characteristic X-rays result when the beam electrons eject inner shell electrons of the specimen atoms.
- Continuum (Bremsstrahlung) X-rays result when the beam electrons interact with the nucleus of the specimen atoms.

Continuum X-rays represent the background on which the characteristic X-ray peaks are imposed and therefore the characteristic X-rays used for elemental identification need to be

differentiated from them. Continuum X-rays result when beam electrons interact with the coulomb (electrical) field of the nucleus of the specimen atom. On interaction, the beam electron loses energy that can be given off as continuum X-rays. The distribution of this energy loss is continuous and not characteristic of the specimen atomic number. The intensity of the continuum background increases with probe current, atomic number and accelerating voltage

The characteristic X-ray lines are named according to the shell in which the initial vacancy occurs and the shell from which an electron drops to fill that vacancy. To ionise an atom, the incoming electron or ionising radiation must possess a minimum amount of energy. That energy is the binding energy of the particular inner shell electron, which is a specific, characteristic energy for each electron in the atom. The X-ray energy for a specific transition is the difference between the outer shell and inner shell electron energies.

There are four different modes of analysis – qualitative, quantitative, elemental mapping and line profile analysis. Only the first three modes were utilised with qualitative analysis showing which elements are present; quantitative analysis shows the relative concentration of each element and elemental mapping shows the distribution on the sample of these elements[56].

2.2.1 Limitations of quantitative analysis

In quantitative EDX microanalysis in SEM, the mass fractions or weight percent's of the elements present in the sample are calculated. The spectra are processed to remove Bremsstrahlung X-rays and spectral artefacts, and then the Characteristic X-rays are compared with data measured from standard reference materials. In so called Standardless Quantitative analysis, or semi-quantitative analysis, the spectra are compared with data collected from standards in the factory of the manufacturer of the EDS system and stored with the system software. In fully Standardised Quantitative analysis the spectra from the standards are collected on the same instrument as the spectra from the sample being analysed, which allows for more accurate analyses[57].

In this thesis, standardless quantitative analysis was carried out and therefore the values obtained have a high degree of error and are therefore only used as a rough estimate for niobium concentration within the alloys and not for oxide content and determining stoichiometry.

For standardised quantitative analysis, the samples must be flat and polished. Samples should also be homogeneous, 'bulk' not porous or thin films on a substrate, otherwise the matrix correction procedures will not work correctly, see figure 2.3.

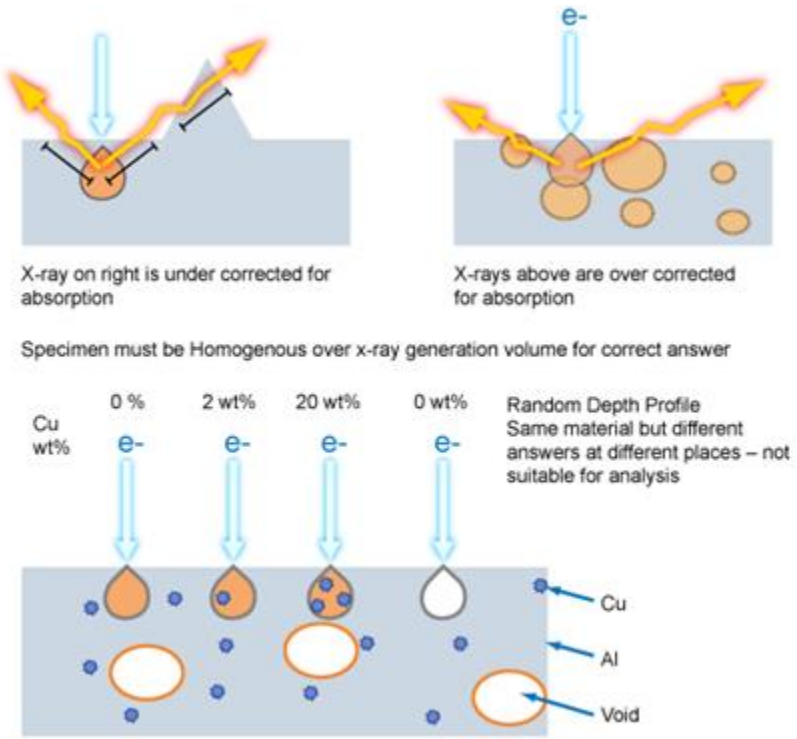

Figure 2.3 Displaying the requirement for a flat homogenous void free surface.

Some of the limitations of quantitative EDX analysis are listed below:

- Light elements (Z < 11) cannot be routinely analysed by EDX.
- Carbon is the most commonly used coating material for non-conductive samples and cannot be analysed if the sample is carbon coated.
- Many minerals contain oxygen bonded with a range of cations. It is common practice to calculate the amount of oxygen in the sample by measuring the percentages of the

cations and calculating oxygen by stoichiometry. This generally is more accurate than analysing for oxygen.

- Calculating oxygen by stoichiometry requires knowledge of the valence state of the cations to which it is bonded. This information is not available from EDS analysis
- Some samples may contain structurally bound water or carbonate. Complete analyses of these samples cannot be derived by EDX analysis.

2.2.2 Concentration calculation

The K ratio is the ratio of the intensity (number of X-ray counts) in the filtered peak for an element of interest in the sample to the intensity in the filtered peak for the standard assigned to that element:

$K = I^{sample}/I^{std}$

It is expected that the concentrations of the element in the sample and the standard are related to the measured X-ray intensities, so the concentration of the element of interest in the sample can be approximated by the K ratio multiplied by the concentration of the element in the standard, which is known:

$C^{sample} = K \times C^{std}$

This calculation however comes with a number of associated error as every element in the sample has an effect on the measured X-ray intensity of every peak in the X-ray spectrum. That is, the measured intensity depends on the composition of the whole sample. Therefore, to calculate the concentrations of the elements in the sample matrix corrections need to be applied to the raw intensities to allow for differences in composition between the sample and the standard.

There are three parts to the matrix corrections based on:

- Z - differences in mean atomic number,
- A - differences in absorption of X-rays, and
- F - differences in the production of secondary X-rays, or X-ray fluorescence.

The matrix corrections are therefore commonly known as ZAF corrections.

2.2.2.1 Atomic number correction, Z

There are two parts to the atomic number correction:

1) Backscattering component

2) Stopping power component.

As the mean atomic number of the sample increases the number of electrons that are backscattered (backscatter coefficient) also increases, and this is what gives rise to contrast in backscattered electron images. The electrons that are backscattered are ejected from the sample and cannot generate X-rays from it, so if the sample has a different mean atomic number than the standard a correction to the measured X-ray intensity must be made.

The stopping power is the rate of energy loss by the incident electrons per unit of mass penetrated in the sample, and it decreases with increasing mean atomic number, Z. The mass penetrated increases with increasing Z, and more X-rays are generated from samples with higher Z. The stopping power correction has the opposite sense to the backscatter correction, and the sum of the two corrections makes up the mean atomic number correction, Z.

2.2.2.2 Absorption correction, A

X-rays generated within the sample travel in all directions through it, and may be absorbed within it. X-rays are either absorbed within the sample or they pass through it – they do not gradually lose energy as electrons do. In the energy range for X-rays generated in the SEM, X-ray absorption is most commonly due to the photo-electric effect. This means that if the energy of the Characteristic X-ray is equal to the ionization energy of an electron shell of an atom in the sample, there is a strong probability that the X-ray photon will be absorbed and a photo-electron will be generated. The probability of the X-ray being absorbed is dependent on the other elements in the sample and their ionization energies.

The probability of the X-ray being absorbed also depends on the distance that it travels through the sample before it escapes and enters the X-ray detector. The path length of the X-ray through the sample is given by z cosec ψ where z is the depth in the sample from which

the X-ray is generated and ψ is the takeoff angle of the detector. The absorption correction factor is given by μ cosec ψ where μ is the Mass Absorption Coefficient (MAC).

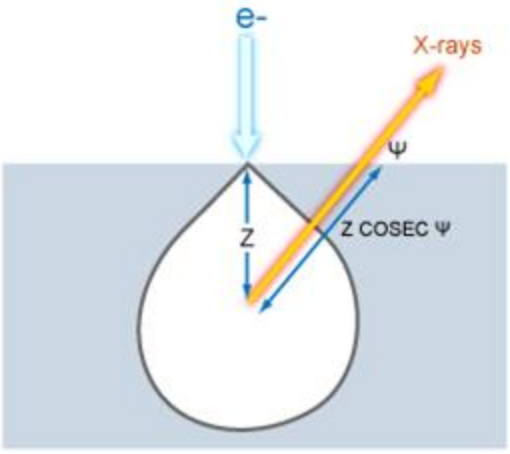

Figure 2.4 The distance travelled through the sample by an X-ray photon generated at depth z is z cosec Ψ, where Ψ is the takeoff angle of the X-ray detector.

In general, MACs increase as the energy of the absorbed X-ray decreases so corrections for low Z elements are large while those for high Z elements are smaller. Also, high Z elements tend to be strong absorbers so large corrections are required for low Z elements in a matrix containing high Z elements.

2.2.2.3 Mass absorption coefficients

Mass absorption coefficients are stored as a matrix of numbers of absorption of a particular X-ray line (the emitter) by an absorber

2.2.2.4 Fluorescence correction, F

The X-rays produced in the sample by the electrons of the primary beam have the potential to produce a second generation of X-rays. This process is known as secondary fluorescence, or just fluorescence. Fluorescence occurs when Characteristic X-rays produced by the primary-beam electrons from one element in the sample have an energy greater than the critical ionization energy of an electron shell in another element present in the sample.

2.2.2.5 Corrected concentration calculation

The calculation of the concentration of an element in a sample must therefore take account of the differences in composition between the sample and the standard. A ZAF factor can be calculated that takes account of the stopping power, backscattering coefficient, absorption and fluorescence effects.

$C^{sample} = K \times C^{std} \times (ZAF^{sample}/ZAF^{std})$

The ZAF factor for the standard can be calculated from its composition, which is known, but the composition of the sample needs to be known before the ZAF factor can be calculated. As the composition of the sample is not known, an iterative technique is used, with an initial composition calculated from the measured K ratio. The ZAF factor for this composition is calculated and the composition of the sample is recalculated, and the process repeated until there is no change in the calculated composition.

2.3 Focused ion beam (FIB)

FIB systems are similar to SEMs but instead of electron guns they use a focused beam of ions, in this case gallium ions. A number of systems are now dual-beam meaning they have both an electron beam and an ion beam.

By using a low beam current they can be used for imaging and with a high beam current they are used for site specific sputtering or milling. Sputtering is a process where an atom is ejected from the surface of a sample as it's bombarded by high energy particles.

The primary ion beam hits the surface of the sample and sputters material either as secondary ions, neutral atoms or secondary electrons. When the beam rasters across the surface of the sample, the signals from the ions or electrons can be collected. At low beam currents, only a small amount of material is sputtered while at higher currents a large amount of material can be sputtered away allowing precision milling of the sample[58]. This technique was required in order to prepare tips for atom probe analysis. Atom probe analysis requires needle-shaped specimens with a tip radius of 20-100 nm. The precision milling ability of a FIB was therefore

required to prepare these samples. Detailed information on the sample preparation of the atom probe samples by FIB is found in section 3.5.

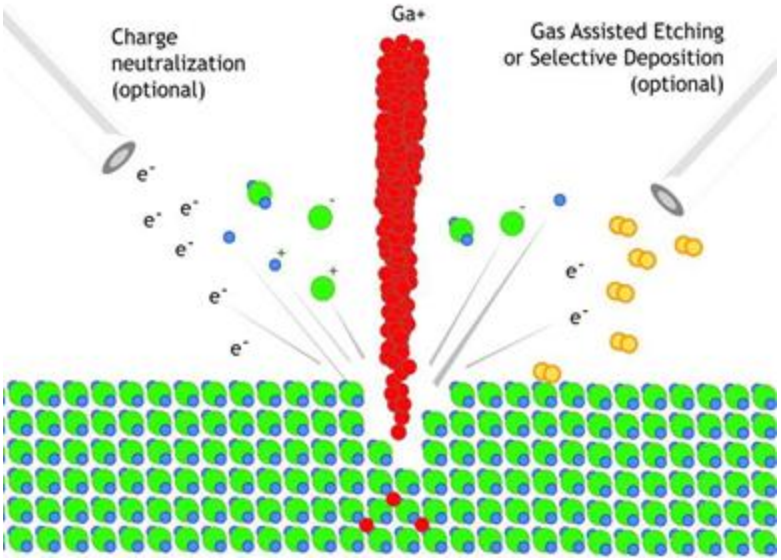

Figure 2.5 Schematic of FIB process[58].

2.4 Secondary ion mass spectrometry (SIMS)

In this study isotopically-labelled water and oxygen were used. SIMS has the ability to differentiate between isotopes. Changes in these isotopes can be seen as a function of depth using depth profiling, thus highlighting any changes in reacting species and corrosion product, providing an insight to the mechanism of the water vapour reaction.

SIMS is the mass spectrometry of ionised particles which are emitted when a surface is bombarded by energetic primary particles, such as gallium. The emitted particles can be electrons, neutral species in the form of atoms or molecules, or ions either atomic or cluster. The majority of the emitted species are neutral. However it is only the secondary ions (atomic and/or clusters) that are detected and analysed, producing a mass spectrum of the surface[59].

SIMS instruments vary depending on the type of primary source and mass spectrometer used. There are four types of beam – electron bombardment, plasma, surface ionisation and field ionisation. In the instrument used for this work, field ionisation was the primary particle source using a gallium liquid metal ion source, whereby a thin skin of liquid gallium is allowed

to flow over a fine tungsten tip in the region of a very high extraction field. The effect of distorting the skin towards the exit ring leads to the setting up of a cone and ball structure of liquid gallium on the probe tip. Primary ions of the metal are stripped away from the plasma ball, creating an ion beam.

For the mass analyser, there are three varieties: magnetic sector; quadrupole; and time of flight. The instrument in this study used a magnetic sector mass analyser, whereby the ions are extracted from the sample using a high extraction potential. Upon negotiating a magnetic field, a charged particle experiences a field force in a direction orthogonal to the direction of magnetic flux and its original axis of travel, generating a circular pathway. The degree of force experienced and the radius of path are directly related to its velocity. All ions are accelerated to a fixed potential before entering the magnetic field. Thereby, they can be readily separated according to mass via the following equation:

$$R = \frac{1}{B}\left(\frac{2mv}{z}\right)^{1/2} \qquad (2)$$

where R = radius of curvature, m/z = mass to charge ratio, B = magnetic field and v = accelerating potential.

A double sector instrument incorporates an electrostatic sector to combat resolution degradation effects that can occur with higher masses. This permits a small energy band of ions to be selected and focussed on to the entrance slit of the magnet for analysis, allowing the positional sense of the secondary ions to be retained throughout analysis. Secondary ion images can be projected in real time onto a fluorescent screen or directly into computer software via a position sensitive detector[59]. Figure 2.6is a schematic of a SIMS instrument.

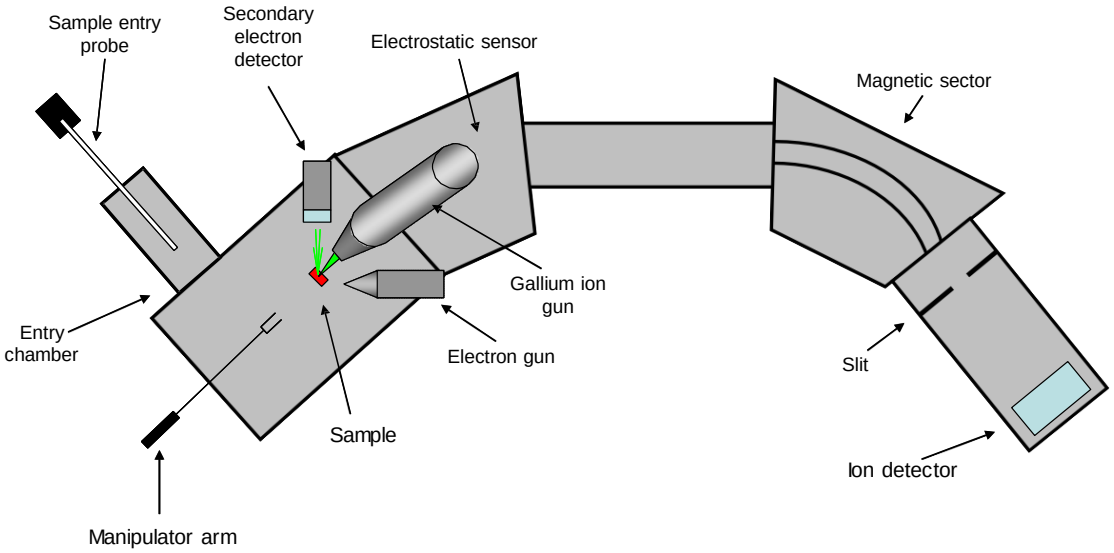

Figure 2.6 Schematic of a SIMS instrument, showing the various components, including the gallium ion gun (beam), the electrostatic sector to combat resolution degradation, the magnetic sector to allow separation due to m/z ratio and the ion detector.

The instrument could be operated in a number of ways depending on the information that was desired. Most analyses began by acquiring a mass spectrum to ascertain the composition of the sample. Having identified the masses of interest the ion count could be collected spatially to produce an ion map, or a depth profile could be produced to see how composition varied with depth. In this work only depth profiling was performed after the initial mass spectra were acquired.

2.4.1 Mass spectra

SIMS can be used to produce mass spectra of a sample surface from a defined area or region by scanning a range of m/z ratios (e.g. 0-300 amu) and continuously monitoring the ion signal. Spectra can be acquired for positive or negative ions but not at the same time. This is useful in determining what elements are present based on their relative mass unit. This can then be used to create ion maps or depth profiles. A low beam current, usually ~0.1 nA, is used to reduce the degree of etching of the surface. Figure 2.7 shows an example spectrum obtained from a UNb3 sample after a water vapour experiment, highlighting the oxygen and hydroxyl species, and chlorine species which are from the salt solution used ($MgCl_2$). It can be seen that SIMS was able to differentiate between the isotopes of oxygen and hydrogen from the water

vapour. However, for certain masses there were more than one possible assigned ion or ion cluster. More detail on this can be found in section 3.4.

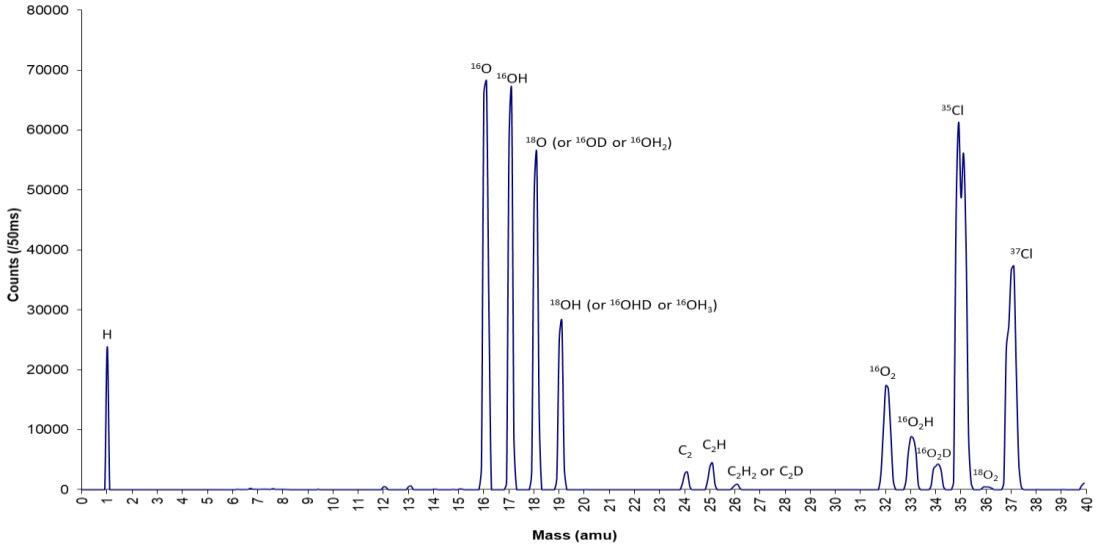

Figure 2.7 Negative mass spectrum 0-40 amu of UNb3 coupon from water vapour experiment at 30 mbar and 45 °C.

2.4.2 Depth profiling

From the spectra, accurate mass values for the elements of interest are obtained. These masses can then be followed (profiled) as a function of time. A depth profile utilises the beam current to etch away at the surface and allow the detector to analyse the elemental composition. The beam current, magnification, dwell time and etch time can all be varied depending on the surface and thickness of the material to be analysed. As the surface is etched away the intensity of the elements pre-selected are recorded and a profile produced, an example is shown in Figure 2.8.

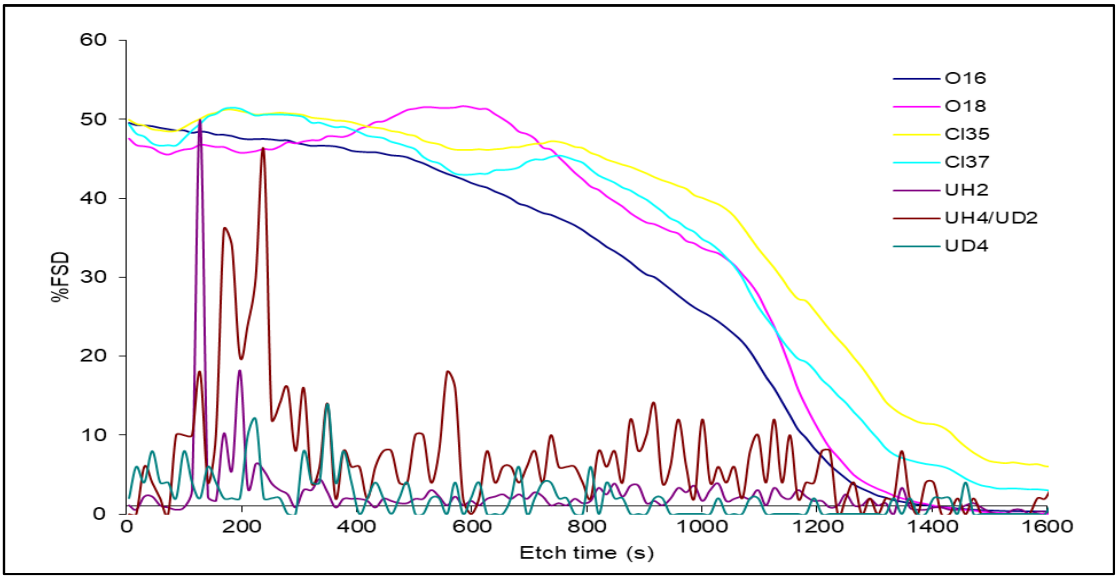

Figure 2.8 Negative depth profile of a UNb3 coupon exposed to water vapour at 30 mbar and 45 °C. The parameters were a 3 nA beam current and x5000 magnification.

2.4.3 Ion mapping

SIMS can be used to image a material's surface to look for any interesting features such as defects, etc. It can also be used to produce ion (elemental) maps, allowing the location of a particular element (or isotope) to be determined. The signal intensity is recorded as a function of the beam position as it scans the surface, producing a 2D image showing the spatial distribution of the chosen mass. As the scanning area does not change, different masses can be chosen and the surface elemental composition can be determined. Ion mapping can also be used as a function of time/depth. As the area is not changed, the surface will slowly etch away and a picture of elemental composition as a function of depth can be revealed. Figure 2.9 shows an ion map highlighting the UO^+ ion.

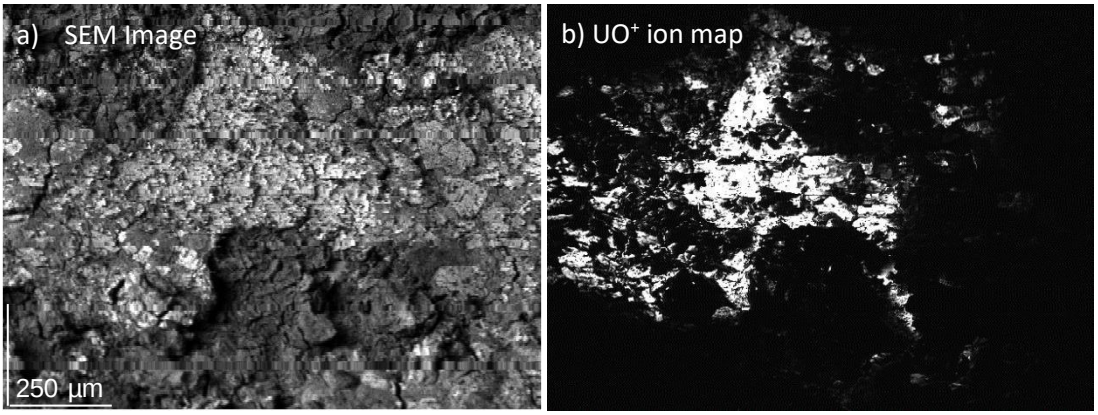

Figure 2.9 Images of spalled uranium coupon from water vapour experiment at 30 mbar and 45 °C, a) SEM image, b) Ion map highlighting UO^+ ion location (white). Images taken at x100 mag, 25.0kV and 1nA.

2.5 Atom probe tomography

Atom probe tomography was used to study the initial oxidation of the metals and alloys. This technique allows the structure of a material to be visually reconstructed, displaying the location of individual atoms. For this study, APT was utilised to look at the oxide structure of uranium and niobium after water vapour exposure, in an attempt to look for a hypothesised hydride layer. For the alloys, APT has the ability to visually demonstrate the locations of each alloying element, allowing confirmation of homogeneity or phase separation. For UNb alloy, it is of great interest to see how the niobium aids in the corrosion resistance, whether through the formation of a protective oxide barrier or due to formation of a mixed oxide as previously surmised.

Atom probe tomography (APT) is a 3D atomic scale microscopy technique suited to the study of nanoscale structures, interfaces and elemental gradients in materials. Advances in the technique[60], particularly the introduction of laser-pulsing[61,62] and the development of advanced focused ion beam (FIB) lift-out techniques for specimen preparation[63,64] have opened up APT to a wider range of less conductive and/or brittle materials. Figure 2.10 shows a schematic of atom probe microscopy.

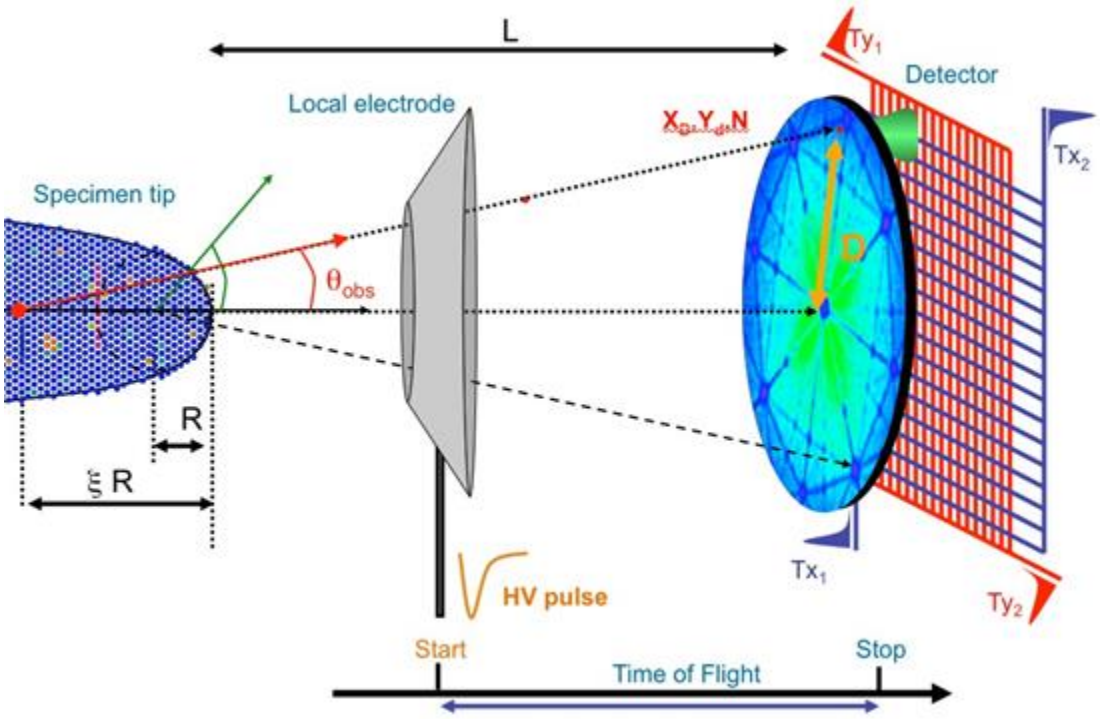

Figure 2.10 Schematic representation of atom probe microscopy.

APT utilises a needle-shaped specimen with a tip radius of 20-100 nm. The technique exploits the effect of an intense electric field upon which is superimposed an ultrafast voltage or laser pulse, for the highly controlled field evaporation of individual ions from the surface of the specimen. There are two different mechanisms to trigger the evaporation:

1) Increase the electric field at a constant temperature (voltage mode)

2) Increase the temperature while the electric field is kept constant (laser mode)

The use of a local electrode enables lower voltages to be used to provide this critical field. Specimen fracture is associated with the very intense electrostatic pressure due to the applied electric field needed to produce field evaporation. Therefore, the local electrode helps reduce the fracture potential. The use of the local electrode also increases the field of view by masking out the ions with high angle trajectories, which would otherwise contribute to noise.

The tip apex is about 100 nm across while the detector is about 100 mm across. The projected image of atoms therefore has a magnification of about one million times. At this magnification, interatomic distances become easy to resolve with modern detector technology. Each detected ion can be directly correlated to the pulse by which they were

evaporated, enabling their time-of-flight and hence their elemental identification. A position-sensitive detector records the hit position of individual ions. From the position at which each ion strikes the detector and the sequence of evaporation, a straightforward reverse-projection algorithm can be used to precisely reconstruct its original location in 3D within the specimen.

In this study laser pulsing mode was utilised where the energy of laser pulses was kept constant throughout the experiment, and the DC voltage was varied to achieve the desired evaporation rate. The probability of evaporation events per pulse is kept deliberately small. This is both to suppress the formation of multiple simultaneous hits, which are difficult for single particle detectors to encode, and to reduce the field-induced stress on the specimen to lessen the risk of fracturing.

By using pulsed evaporation, the time-of-flight for each instance of the specimen evaporation can be measured. The time-of-flight, t_{flight}, of an ion is defined as the time between the application of the pulse that prompts the field evaporation and when the detection system measures the impact. The time of flight of the ion is directly related to its kinetic energy E_c, and can be used to measure several parameters related to its motion.

$$E_c = \frac{1}{2} m v^2 \tag{2}$$

where m is the mass and v is the velocity, which in turn is calculated from:

$$v = \frac{L}{t_{flight}} \tag{3}$$

where t_{flight} is the time-of-flight and L is the flight length between the specimen and the detector[61–64].

Further details on the sample preparation required for atom probe tomography and the post analysis of the data to create a 3D reconstruction of the tip can be found in section 3.5.

3 Chapter three – experimental procedures

3.1 Water vapour corrosion pots

3.1.1 Sample preparation

3.1.1.1 Materials

There were four materials used in this work, uranium, niobium, UNb3 (containing 2.68 wt% niobium) and UNb6 (containing 6 wt% niobium). The uranium metal and uranium niobium alloys were provided by AWE, while the niobium coupons were from Goodfellow metals.

The uranium coupons were from low temperature rolled uranium sheet that was cut into square coupons, 12 mm^2 x ~1 mm thick coupons. Typical impurities are shown in Table 3.1.

Table 3.1 Impurity data for uranium[65]*.*

Impurity	Concentration by weight (ppm)
C	50
Fe	22
Al	4
Ni	17
Si	2
Cr	2

The niobium had a purity of 99.9%. The coupons were circular discs 10 mm in diameter by 1 mm thick. Typical impurities are shown in Table 3.2.

Table 3.2 Impurity data for niobium, values provided by Goodfellow metals.

Impurity	Concentration by weight (ppm)
Al, Ca, Co, Cr, Cu, Fe, Mg, Mn, Mo, Ni, Si, Sn, Zr, H	<10
B	2
Ta	255
Ti	20
W	<100
C	25
N	35
O	230

Both the UNb3 and the UNb6 coupons were produced using the vacuum induction melting process, with heat treatments ranging between 700-850 °C followed by water quenching. The heat treatment undertaken kept the alloys within the α-U + γ-Nb phase, with the associated metastable niobium phases α' (UNb3) and α'' and γ^0 (UNb6)[66]. Figure 3.1 shows the phase diagram for UNb alloys and Table 3.3 contains impurity information on the alloys.

Table 3.3 Impurity data for alloys[66].

Impurity	Concentration by weight (ppm)
C	100
Si	73
Fe	50
Zr	<50
Zn	<50
Ti	<50
Cr	<50
Cu	25
Ni	25
Ca	<25

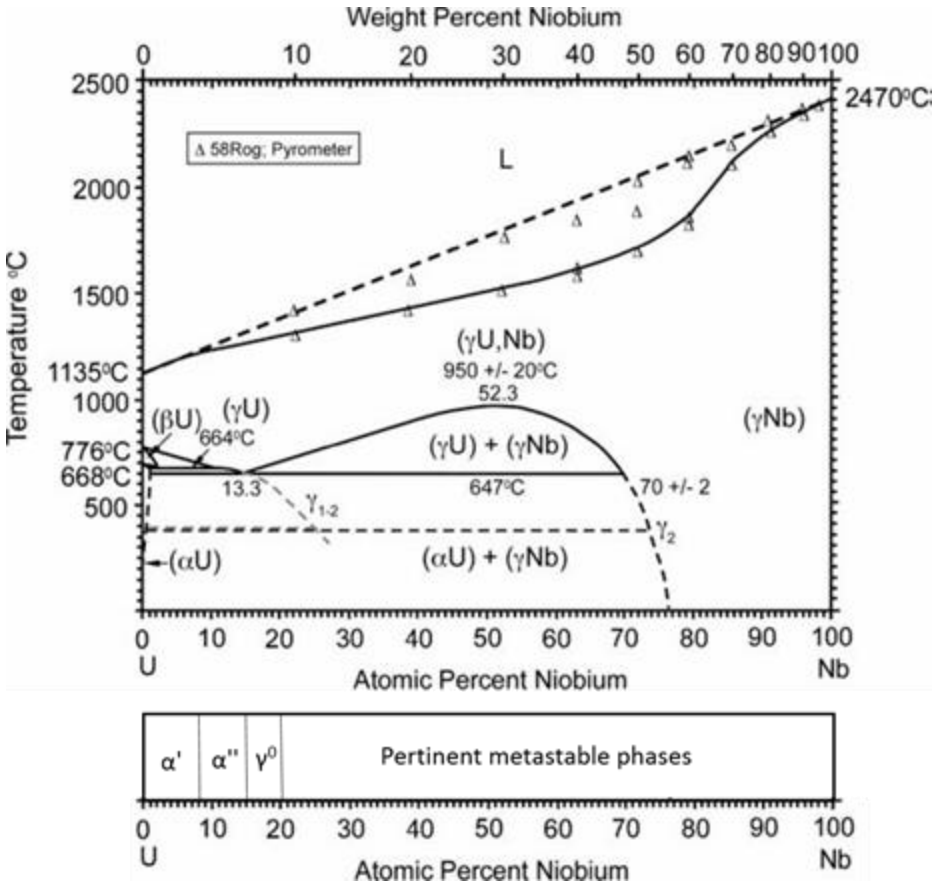

Figure 3.1 UNb phase diagram[1,49].

3.1.1.2 Mechanical polish

All materials were prepared in the same way to ensure consistency and repeatability. All samples were mounted onto a stub using carbon stickers. Each sample was polished using a succession of silicon carbide grit papers from p320 to p1200 on both sides and all edges. The samples were hand polished using water as a lubricant. Once a mirror-like surface was achieved the sample was washed in ethanol. The sample was then either ready to be placed in a reaction cell, see section 3.1.2, or taken for analysis by EDX or ATP, see sections 3.2 and 3.5 respectively. Exposure to the atmosphere was kept to a minimum.

3.1.2 Equipment and procedure

Experiments were carried out in sealed reaction pots, with a salt solution contained in a ceramic crucible at the bottom of the cell and the coupon in a stainless steel sample holder suspended over the crucible. The reaction cells were assembled as shown in Figure 3.2.

The pots had a pressure transducer attached to one side, allowing pressure changes within the cell to be recorded. On the other side of the cell was a valve, this enabled the cell to be easily connected up to a gas handling rig to allow any residual gas within the cell to be evacuated. As the cell contained a liquid solution, it was necessary to use liquid nitrogen in order to freeze the solution and avoid any liquid being pumped through and damaging the gas handling rig. A cycle of freeze-pump-thaw was undertaken to remove any trapped gas or impurities from the salt solution.

Saturated salt solutions were used to create constant water vapour pressures at each temperature. Relative humidity values for salts were obtained from Greenspan[67] and are shown in Table 3.4. The equation below was used to calculate the expected water vapour pressure in mbar for a chosen salt at a specific temperature in degrees celsius.

$$P = \frac{1000}{760} \times 7.16 \times 10^{8} \times \left(\frac{RH}{100}\right) \times \exp\left(\frac{-10200 \times 4.184}{8.31451 \times (T + 273.15)}\right) \text{ mbar} \qquad (1)$$

Table 3.4 Theoretical water vapour pressures available from salt solutions at the temperatures of interest.

Salt	Temperature (°C)	RH%	Pressure (mbar)
Sodium chloride (NaCl)	30	75.1	31.4
Magnesium chloride ($MgCl_2$)	45	31.1	28.9
Potassium fluoride (KF)	55	20.6	31.3
Lithium chloride (LiCl)	70	10.8	32.3
Potassium fluoride (KF)	70	21.7	65.3
Sodium chloride (NaCl)	70	75.1	225.6
Pure water	70	100.0	300.6

For the niobium water vapour experiments, both temperature and pressure were investigated. Previous work had been carried out on uranium and UNb alloys showing them to have a $(P_{H_2O})^{½}$ pressure dependence[12]. Therefore, for uranium, UNb3 and UNb6 only the temperature dependence was investigated, with all experiments being conducted at approximately 30 mbar. This pressure was found to provide a range of temperatures accessible using a variety of salts. The experimental conditions are listed in Table 3.5. These are the desired pressures and temperatures. The actual starting pressures and mean temperatures for each experiment may vary due to temperature changes within the laboratory and/or impurities within the salt solutions from either the water or salts. Errors are calculated based on transducer and thermocouple accuracy.

Table 3.5 Desired pressures and temperatures for the water vapour experiments for U, Nb and UNb alloys

	Temperature			
Material	**30 °C**	**45 °C**	**55 °C**	**70 °C**
Nb	31 mbar	29 mbar	31 mbar	32 mbar
				65 mbar
				226 mbar
				301 mbar
U	31 mbar	29 mbar	31 mbar	32 mbar
UNb3	31 mbar	29 mbar	31 mbar	None
UNb6	31 mbar	29 mbar	31 mbar	None

The reacted coupons were analysed using SIMS in order to obtain isotopic depth profiles. Therefore, the experiments were conducted using isotopically-labelled water ($D_2{}^{16}O$ then $H_2{}^{18}O$).

a)

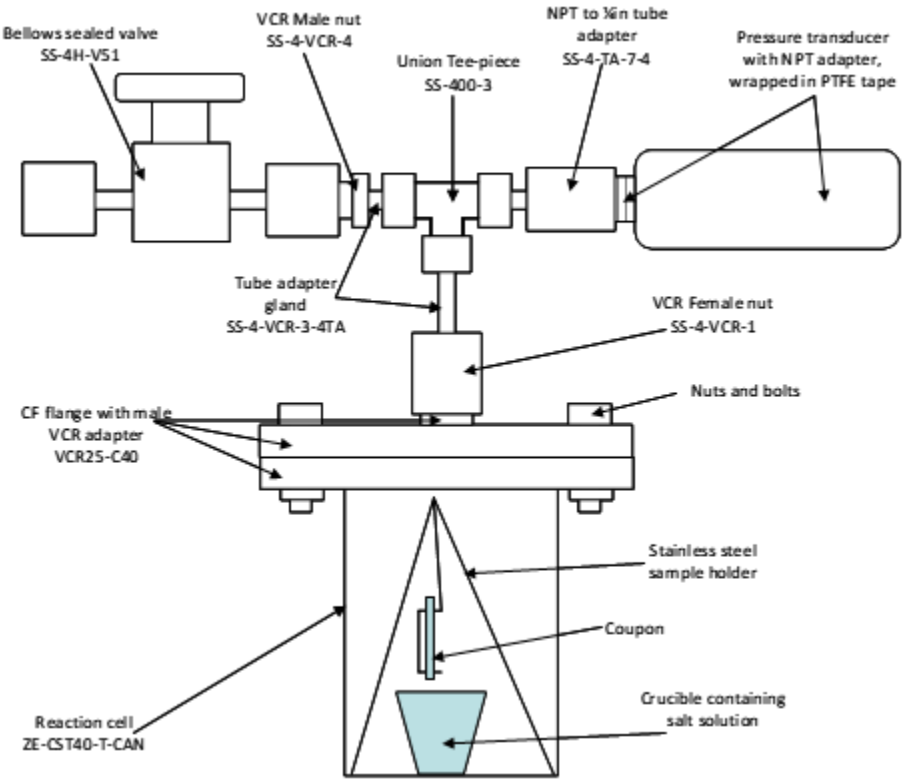

b)

Figure 3.2 Reaction cell set up, a) schematic, b) photograph.

The appropriate saturated salt solution was prepared in a ceramic crucible and placed within the corrosion cell. The cell was gasket-sealed and attached to a gas handling rig where it went through three freeze-pump-thaw cycles, obtaining a minimum vacuum of $1x10^{-5}$ mbar each

time. On the third and final thaw, the cell was removed from the gas handling rig and the polished sample mounted in the sample holder was loaded into the cell. The cell was then evacuated once more, isolated from the gas handling rig and placed in the appropriate oven. Thermocouples were placed within each oven in order to record the temperature throughout the experiment. Once the cell was placed in the oven, the data logging software (orchestrator) was started. This software recorded both the temperature and pressure of the experiment, with recordings taken once every hour.

Once the experiment with the first salt solution (using $D_2{}^{16}O$) had finished, the reaction cell was removed from the oven and attached to gas handling rig for cooling and evacuation. The new salt solution (using $H_2{}^{18}O$) was then loaded, the cell evacuated and the experiment was restarted.

When the second water exposure experiment had finished, the cell was removed and the gas evacuated. The cell could then be opened and the reacted coupon could be analysed using SIMS. Once SIMS analysis was complete the reacted coupon was then available for further analysis by EDX.

3.1.2.1 Water vapour plus oxygen

For uranium, the addition of oxygen to the water vapour reaction has been shown to inhibit the evolution of hydrogen and reduce the rate until the oxygen is fully depleted[3,4,6,22]. In contrast, for niobium, the addition of oxygen to the water vapour reaction has been shown to increase the rate in comparison to the pure oxygen reaction[31]. The addition of oxygen to the water vapour reaction was investigated for UNb3 and UNb6 using isotopically-labelled water and oxygen to allow the oxidising species and mechanism to be examined. Experiments on uranium and niobium were also performed as references. A pressure of 30 mbar and a temperature of 55 °C were used to conduct the experiments. These conditions have already been used for water vapour only experiments and therefore allowed comparison. The experiments were duplicated to allow different H/O isotope combinations, as shown in Table 3.6. Again, these are desired pressures and temperatures. The actual starting pressures and mean temperatures will be reported in the results sections.

Table 3.6 Combined water vapour plus oxygen experiments conducted at 55 °C.

		Water		Oxygen	
Material	**Temperature (°C)**	**Form**	**Pressure (mbar)**	**Form**	**Pressure (mbar)**
Nb	55	$H_2{}^{18}O$	31	$^{16}O_2$	10
U					
UNb3					
UNb6					
Nb	55	$D_2{}^{16}O$	31	$^{18}O_2$	10
U					
UNb3					
UNb6					

The initial procedure was similar to that of water vapour, but in this instance the oxygen was added after the coupon had been loaded and the cell evacuated. With the frozen cell isolated from the rest of the rig, oxygen was added to the gas handling rig. Using baratrons the pressure of oxygen in the rig was monitored. The cell line was slowly opened, allowing oxygen to be added to the cell. Using the baratron to monitor the pressure carefully, the cell line was left open until the required pressure of oxygen had been obtained. Once obtained the cell was immediately isolated and the oxygen left in the gas handling rig was evacuated. The cell was then removed and placed in the appropriate oven and the Orchestrator data logger was started.

When the experiment had finished, the cell was removed and the gas evacuated. The cell could then be opened and the reacted coupon could be analysed using SIMS.

3.1.3 Corrosion pot data collection and analysis

Outputs from all the pressure gauges and thermocouples (located in the ovens) were fed into a data logger (Datascan 7320) that was linked to a PC. This allowed P-T data to be recorded and displayed in real time using Orchestrator software. The data was then exported for further processing e.g. rate calculation, which assumes that the increase in pressure is solely due to the evolution of H_2 from the water vapour reaction. The use of saturated salt solutions ensures that, at constant temperature, the water vapour partial pressure also remains constant. By knowing the exact volume of the vessel, the surface area of the coupon and the

recorded pressure change the corrosion rate can be calculated. The amount of gas is obtained from the pressure change using the ideal gas equation.

The rate is presented in the form of mmol H_2 cm^{-2} s^{-1}. Two methods are used to calculate the rate; the mean of these two values is then taken. The volume of gas is obtained from the pressure change using the ideal gas equation. The first method takes change in volume of gas (in terms of mmol H_2 cm^{-2}) over the change in time (in seconds). The second method uses the Microsoft Excel TREND function. The TREND function returns values along a linear trend. It fits a straight line (using the method of least squares) to the arrays of known_y (volume of gas) against known_x (time). It returns the y-values along that line for the array of new_x values that are specified.

3.2 Energy dispersive x-ray spectroscopy (EDX)

3.2.1 Equipment

The field emission gun scanning electron microscope (FEGSEM) instrument was a Zeiss Sigma high definition field emission SEM with EBSD and EDX; backscattered electron and variable pressure detectors, a three axis micromanipulator and in-situ argon sputter cleaning. This instrument was used to collect EDX data on each of the materials pre and post water vapour reaction.

Figure 3.3 Photograph of FEGSEM.

3.2.2 Sample preparation

Two sets of exposures were analysed, pre-exposure and post-exposure to water vapour. For each exposure, a coupon of uranium, niobium, UNb3 and UNb6 were analysed. For the pre-exposure experiments, the coupons were prepared as in section 3.1. The post-exposure samples were loaded into the instrument directly from the corrosion cell. There would be some inevitable, albeit minimal, air exposure during transfer from the corrosion cell to the instrument (<5 min).

Data acquisition was kindly conducted by Peter Martin from the Interface Analysis Centre (IAC), University of Bristol.

3.3 Focussed ion beam (FIB)

3.3.1 Equipment

A dual beam system was used containing both ion and electron columns. This instrument was a FEI Helios NanoLab 600 with three-axis micromanipulator, platinum deposition and force measurement. Figure 3.4 shows a photograph of the instrument. This instrument was used to produce atom probe tomography (APT) lift outs. The ability to use SEM to image while using the FIB to mill is essential for in-situ sample preparation for atom probe. Discussion on the sample preparation for APT is in section 3.5.

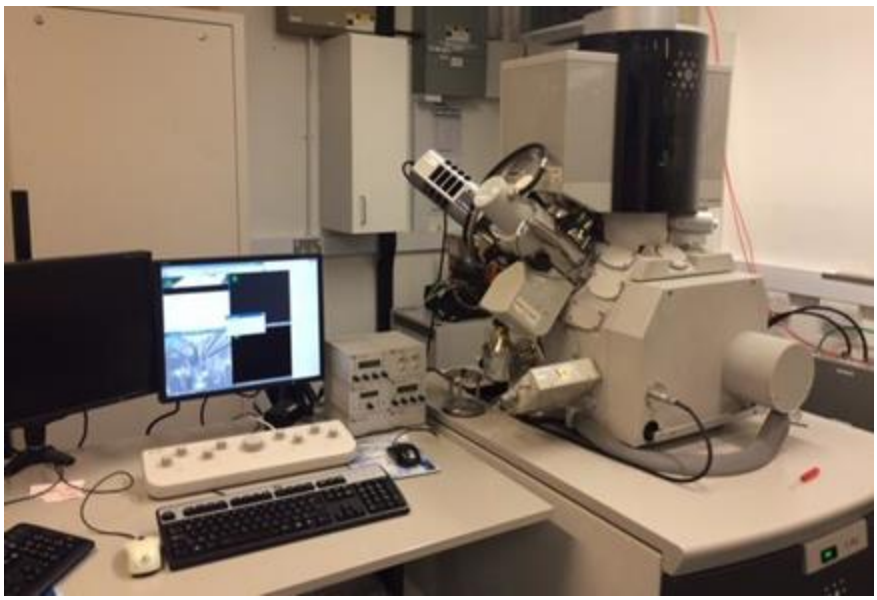

Figure 3.4 Photograph of dual beam system.

3.4 Secondary ion mass spectrometry (SIMS)

3.4.1 Equipment

SIMS analysis was carried out using a magnetic sector instrument. It uses an FEI gallium ion gun operated at 25 keV. The beam current (1 or 3 nA) is controlled using an electronically variable aperture. The instrument is coupled to a VG model 7035 double focusing magnetic sector analyser and the detector used to collect the secondary ions was a Everhart-Thornley detector. Figure 3.5 shows a photograph of the SIMS instrument used in this study.

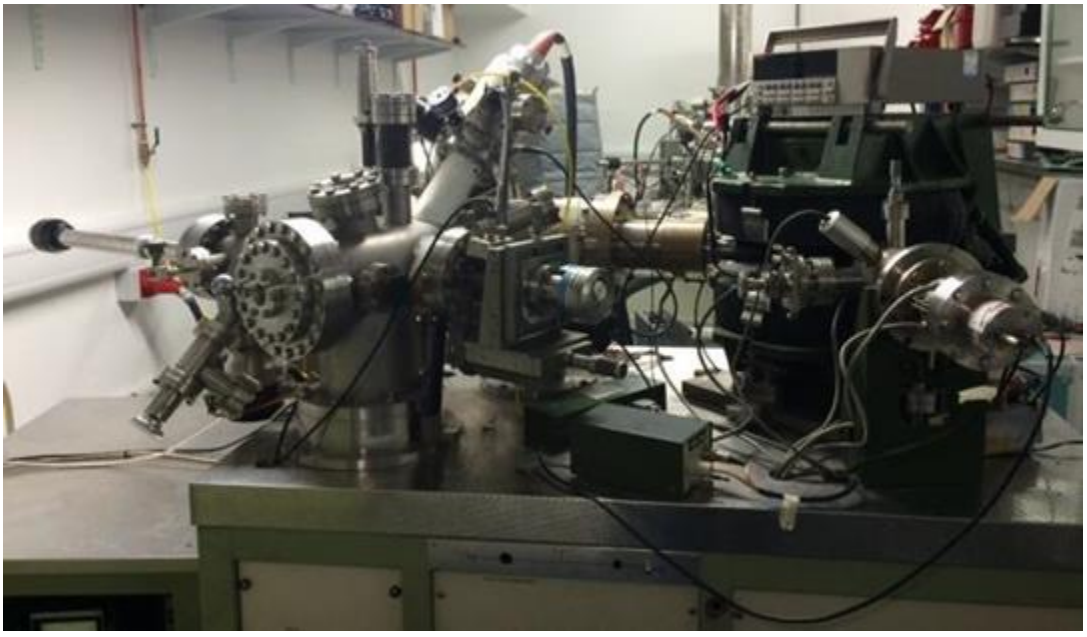

Figure 3.5 Photograph of magnetic sector SIMS instrument.

3.4.2 Sample preparation

All samples that underwent water vapour corrosion (see section 3.1) were analysed by SIMS. Once the corrosion experiment was complete the samples were loaded immediately into the SIMS instrument for analysis. There would be some inevitable, albeit minimal, air exposure during transfer from the corrosion cell to the instrument (<5 min).

The focal point of the analysis was on isotopic depth profiles, using the oxygen and hydrogen isotopes from the waters used in the reaction. Before a depth profile can be conducted the accurate ion masses need to be established using the mass spectrum mode of SIMS. Initially three wide scans were conducted, with mass ranges of 0-100, 100-200 and 200-300 amu. A

step size of 0.05 and a magnification of 1000 were used unless otherwise stated. Additional scans were then run to focus in on smaller ranges to allow more accurate readings of mass values, such as 0-40 to allow closer inspection of the oxygen isotopes, 90-140 for niobium and 225-285 for uranium. The main ions of interest for both positive and negative modes are listed in Table 3.7.

Table 3.7 Ions of interest in both positive and negative modes.

Negative mode		**Positive mode**	
M/Z	**Species**	**M/Z**	**Species**
1	H	93	Nb
2	H_2, D	94	NbH
16	^{16}O	95	NbH_2, NbD
17	^{16}OH	109	$Nb^{16}O$
18	$^{16}OH_2$, ^{16}OD, ^{18}O	110	$Nb^{16}OH$
19	$^{16}OH_3$, ^{18}OH	111	$Nb^{16}OH_2$, $Nb^{16}OD$, $Nb^{18}O$
94	NbH	113	$Nb^{18}OD$
95	NbH_2, NbD	125	$Nb^{16}O_2$
239	UH	127	$Nb^{16}O_2H_2$, $Nb^{16}O_2D$, $Nb^{16}O^{18}O$
240	UH_2, UD	129	$Nb^{16}O_2D_2$, $Nb^{18}O_2$
242	UH_4, UD_2	238	U
246	UD_4	239	UH
262	$U^{16}OD_4$, $U^{18}OD_3$	240	UH_2, UD
		254	$U^{16}O$
		255	$U^{18}OH$
		256	$U^{16}OH_2$, $U^{16}OD$, $U^{18}O$
		266	$Nb_2{}^{16}O_5$
		270	$U^{16}O_2$
		271	$U^{16}O_2H$
		272	$U^{16}O_2H_2$, $U^{16}O_2D$, $U^{16}O^{18}O$
		274	$U^{16}O_2D_2$, $U^{18}O_2$
		276	$Nb_2{}^{18}O_5$

3.4.3 Data analysis

Depth profile data is collected in the form of % full scale deflection (FSD), where the values are normalised with respect to the maximum recorded value. The depth profiles were plotted as %FSD since the count rate of different species varies by orders of magnitude. However, relative contributions from ^{16}O and ^{18}O ionic species were compared by analysing and plotting absolute counts rather than full scale deflection.

For the % oxygen profiles, the % oxide was calculated by summing up the absolute counts for all of the oxygen containing ions, then using the maximum number of counts (over the etch time) to represent 100%. The %oxide was then calculated for each data point as a function of this maximum 100% value. The intensity was then seen to increase or decrease as a function of etch time/depth and thus oxide thickness. The oxygen concentration for the two isotopes (^{16}O and ^{18}O) were calculated by summing up all ions containing the isotope and dividing this by the total oxygen content. This then allowed the ratio of ^{16}O:^{18}O to be determined.

3.4.4 Stopping range of ions in matter (SRIM)

SRIM is a software package that has been used to determine individual sputter rates for ions of interest within a target following bombardment by energetic primary particles (in this case gallium ions). It models the interaction between ions and atoms, i.e. the beam and the sample[68].

In this study sputter rates were calculated for U and O from a uranium oxide (UO_2) target and for Nb and O from a niobium oxide (Nb_2O_5) target. It was found that sputter rates obtained for O were approximately four times larger than those for U and Nb, indicating that O is preferentially removed from UO_2 and Nb_2O_5 respectively. Nevertheless, it is reasonable to assume that the etch rate of the oxide (i.e. number of UO_2/Nb_2O_5 clusters removed per gallium ion) will be determined by the sputter rate of U and Nb. This is because the preferential removal of O atoms simply changes the stoichiometry, rather than the thickness, of the oxide.

The calculated values from SRIM gave a sputter ratio for UO_2 of 4.65 molecules per ion and for Nb_2O_5 of 2.17 molecules per ion.

The etch depth is calculated from the beam current, scan area (magnification) and ion yield (which takes into account the sputter rate and the volume occupied by a molecule):

Etch rate (nm s^{-1}) = (Ion yield × Beam current)/Scan area

The etch rate can then be used to determine the depth of a profile and therefore related to the corresponding oxide thickness of the corroded samples.

3.5 Atom probe tomography (APT)

3.5.1 Equipment

Analysis was performed using a Cameca local electrode atom probe (LEAP) 3000X HR atom probe, with a pulsed green laser (532 nm). The laser was set at a frequency of 160 kHz, to prevent wraparound of the heavy (thus, slow in terms of time-of-flight techniques) uranium atoms into the beginning of the next pulse, and a laser power of 0.5 nJ. Specimens were cooled to -223 °C and kept at a vacuum better than 3×10^{-11} mbar. Evaporation rate varied between 0.1 and 0.5%. Figure 3.6 shows a photograph of the instrument. Data acquisition was kindly performed by Dr Tomas Martin from Oxford Materials, University of Oxford.

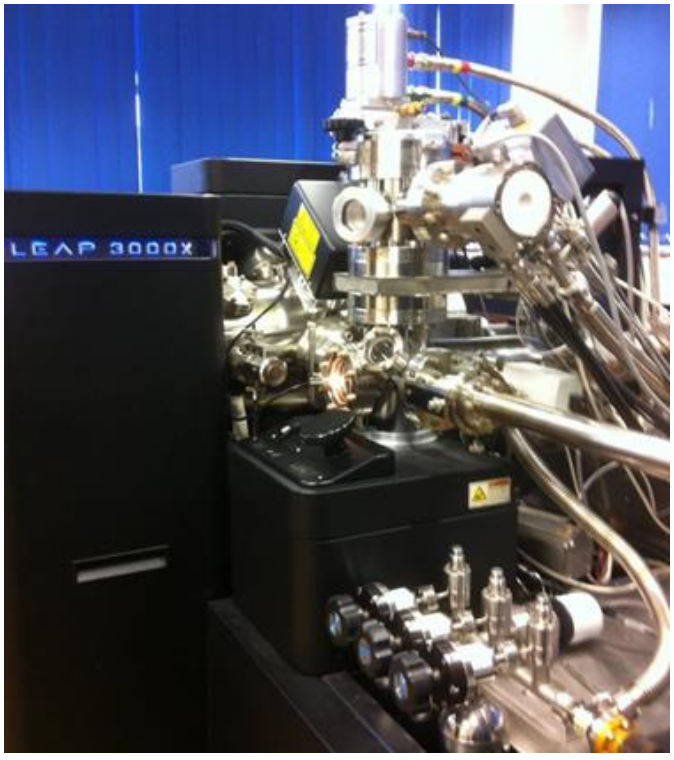

Figure 3.6 Photograph of atom probe instrument.

3.5.2 Sample preparation

All material (U, Nb, UNb3, UNb6) was polished (see section 3.1) before exposure to:

1) Air at room temperature for an hour

2) D_2O vapour at room temperature for two hours

After exposure the coupons were loaded into the dual beam system for specimen preparation.

Specimen preparation for the atom probe is challenging and time consuming. There are specific requirements that must be met in order to obtain successful data from the specimen:

- Radius at specimen tip 50-150 nm with the feature of interest within 100 nm of the apex; required in order to produce the high field necessary
- Smooth surface to reduce fracture probability
- Circular cross section as asymmetric cross sections will lead to blade-shaped specimens that distort the ion trajectories toward the detector
- Sufficient specimen length and tip clearance to allow sufficient analysis and reduce fracture probability
- Appropriate shank angle, low taper angle enables significant depth before maximum voltage reached

The in-situ FIB method of Thompson[63,64] was followed with the exception of the application of a protective capping layer. It was found that due to the large size of the specimen atoms compared to the Ga^+ ions, the damage from the ion beam was minimal. Furthermore, the presence of a protective layer of platinum had a detrimental effect on atom probe yield, as fracture could occur at the interface between the platinum and uranium or niobium. It was therefore decided to carry out the in-situ lift out and, thus, annular milling on a strip with no protective cap.

Trench milling was carried out around a rectangle of material approximately 2 µm wide and 20 µm in length (Figure 3.7a). The first trench was cut along the length of this rectangle at a 30° angle (22° stage tilt toward the ion column axis) with respect to the surface of the sample. The trench was drawn with the width x as 4 µm, the length y as 27 µm, and the cut depth z as

7 µm. A beam current of 6.5 nA was used; this minimised the time required to cut through. The stage was then concentrically rotated 180° and a trench of the same size was cut on the opposite side of the rectangle. The 30° cuts allow a wedge (shown in Figure 3.8) to be cut. The shape of the liftout is important for providing sufficient area to place platinum down when attaching the specimen to the pre-fabricated silicon tip.

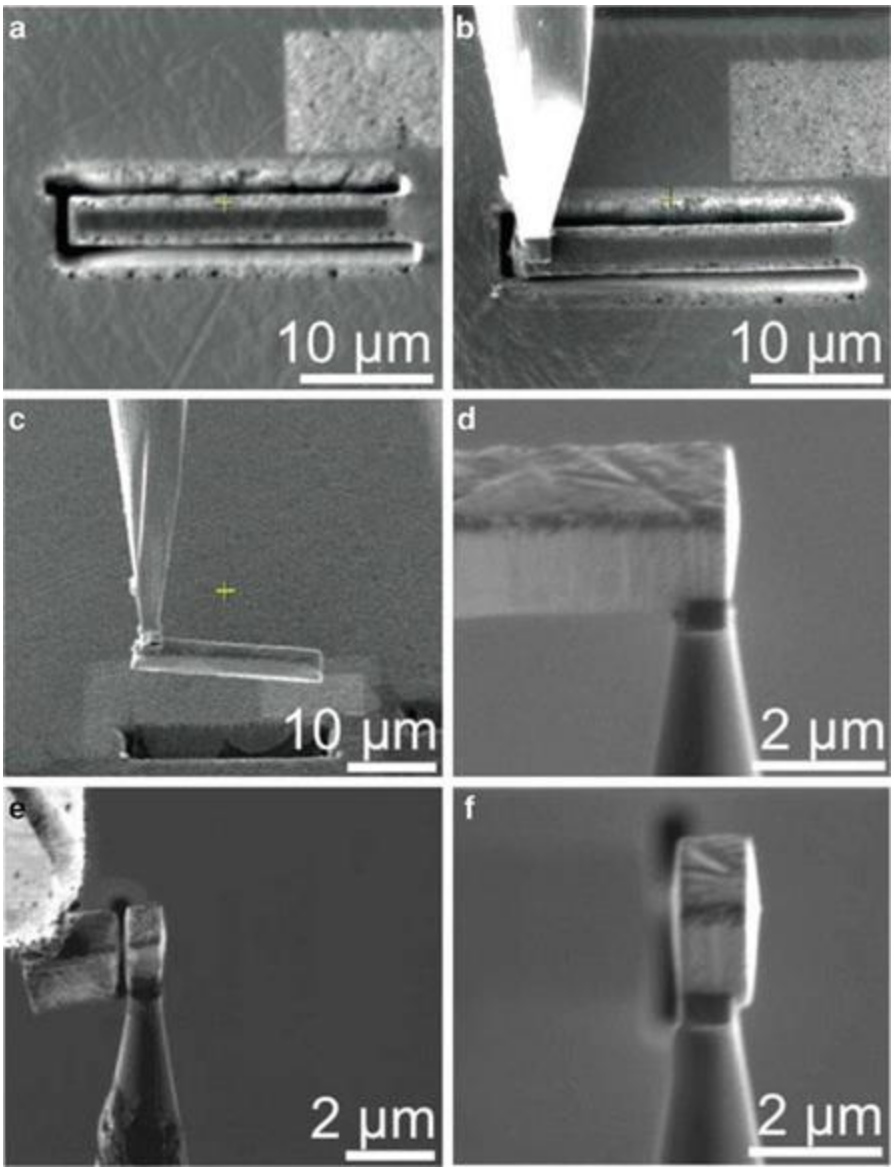

Figure 3.7 SEM images of liftout procedure[63].

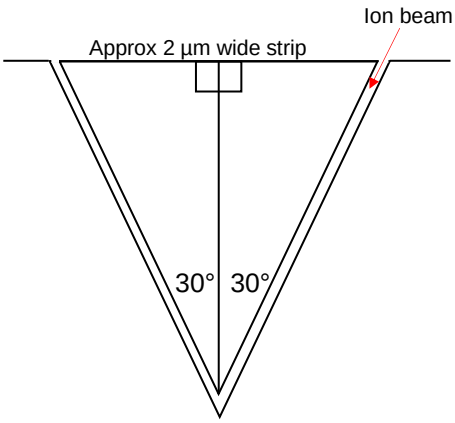

Figure 3.8 Schematic showing the initial trench cuts.

The stage was then returned to 0° and a mill cut made at one end of the wedge, with a 2.7 nA beam current and 5 µm deep cut being used, (Figure 3.7a). The micromanipulator system is then required. The needle is brought in and attached to the free end of the wedge using ion-induced platinum deposition; a beam current of 26 pA is used and a rectangle of platinum 0.5 µm deep is put down, (Figure 3.7b). The other end of the wedge is now cut free; again a 2.7 nA beam current and 5 µm deep cut are required. The needle can now carefully be lifted up and out of the way with the strip of material securely attached (Figure 3.7c).

The microtip of pre-fabricated silicon tips is then loaded into the dual beam system. Microtips were supplied by Cameca. They provide 36 tips with three fiducials. Figure 3.9 shows an SEM image of a microtip.

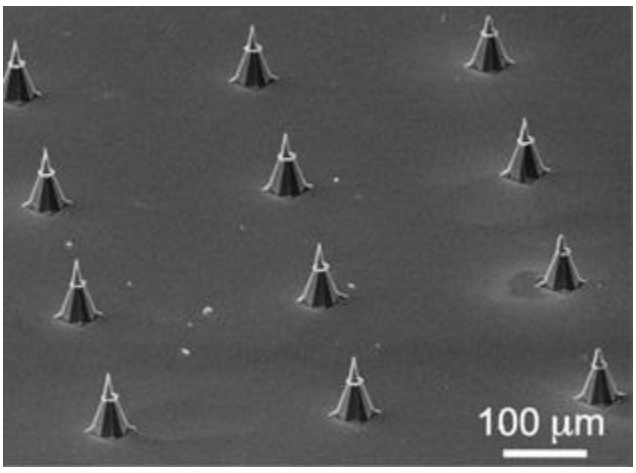

Figure 3.9 SEM image of pre-fabricated silicon microtips from Cameca.

The needle with the strip attached is then moved back in and aligned with the first available tip (Figure 3.7d). Once aligned with the flat top of the tip platinum deposition is used to fill in the gap between the wedge and the microtip post, a 26 pA beam current is used and a deposit 0.5 µm deep is used. Once the wedge is secure the ion beam is used to cut free the remaining wedge (2.7 nA and 20 µm deep) (Figure 3.7e). The needle and strip are then moved and aligned with the next available post and the process repeated until there is no more wedge left to attach. The needle is then moved out and the stage is rotated 180° and platinum is deposited on the opposite side of each attached wedge for enhanced stability.

Once all required samples have been lifted out and attached to individual posts the process of sharpening into tips using annular milling is then conducted. As previously mentioned the requirement is for a tip apex of between 50-100 nm. Annular milling uses a circular/doughnut cutting shape with varying outer and inner diameters. Figure 3.10 shows a schematic of the process and Table 3.8 shows the recipe followed for each of the prepared tips.

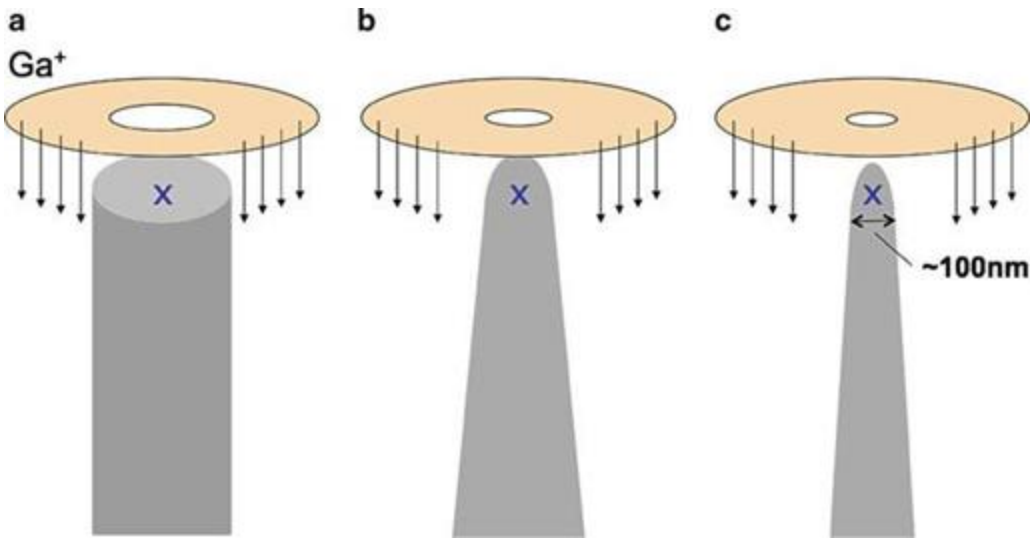

Figure 3.10 Schematic of annular milling process taken from reference[63].

Table 3.8 Recipe for annular milling procedure.

Beam current	Outer diameter (µm)	Inner diameter (µm)	Depth (µm)	Approximate time cutting (min)
0.44 nA	7	3	5	10
0.44 nA	6	2	5	5
0.26 nA	3.5	1.5	5	3
0.26 nA	2.5	1	5	3
90 pA	2	0.5	5	2
90 pA	1.5	0.25	5	1

A final polish was then carried out at a much lower energy of 5 keV and a 71 pA beam current. This polish was carried out using a circle of 7 µm outer and 0 µm inner diameters. The polish is conducted under close observation for approximately one minute, making sure that the area of interest is not polished away.

SEM images of each of the tips are taken to aid in the atom probe data analysis and reconstruction. Figure 3.11 shows two SEM images, one from a UNb6 sample and one from a uranium sample.

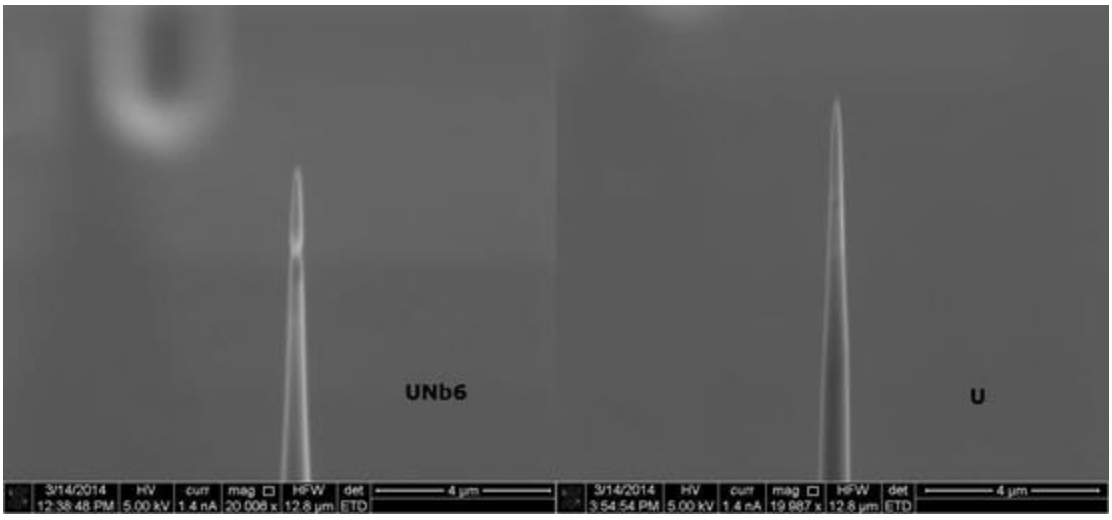

Figure 3.11 SEM images of two prepared tips.

3.5.3 Data analysis

The data collected are a sequence of atomic coordinates and mass-to-charge state of each ion collected. The reconstructed volume is a truncated cone in which the radius increases during the experiment due to the taper angle of the needle-shaped specimen. The x and y atomic coordinates are derived from x and y positions of the impact of each ion on the position sensitive detector. The z coordinate is estimated from the order in which atoms are collected, assuming uniform field evaporation over the surface of the specimen[69–71].

Integrated visualisation and analysis software (IVAS) was used. The input file created by the atom probe experiment (*.RHIT) contains the voltage, detector coordinates (XD, YD) and the time-of-flight for each individual ions recorded during the experiment. The reconstruction process utilises specimen-specific parameters (such as field factor kf and image compression

ξ) and the instrument-specific parameters (such as detection efficiency ε) to produce an output file that contains the 3D position (x, y, z) and mass-to-charge-ratio (z) for each individual atom in the 3D space.

The IVAS Cal/Recon Wizard guides the user through a series of steps which facilitates the conversion of raw RHIT data into reconstructed positions and chemical identities. These steps include:

- Select ion sequence range
- Select detector region of interest (ROI)
- ToF corrections
- Mass calibration
- Ranged-ion assignment
- Reconstruction

The first step is to choose an appropriate subset of the raw data for processing. This is done by selecting an ion collection range and a real region of interest (ROI). By using the voltage vs. ion sequence number plot (Figure 3.12), any non-uniformity during the evaporation process (such as contamination, fracturing or the start of the acquisition) can be removed.

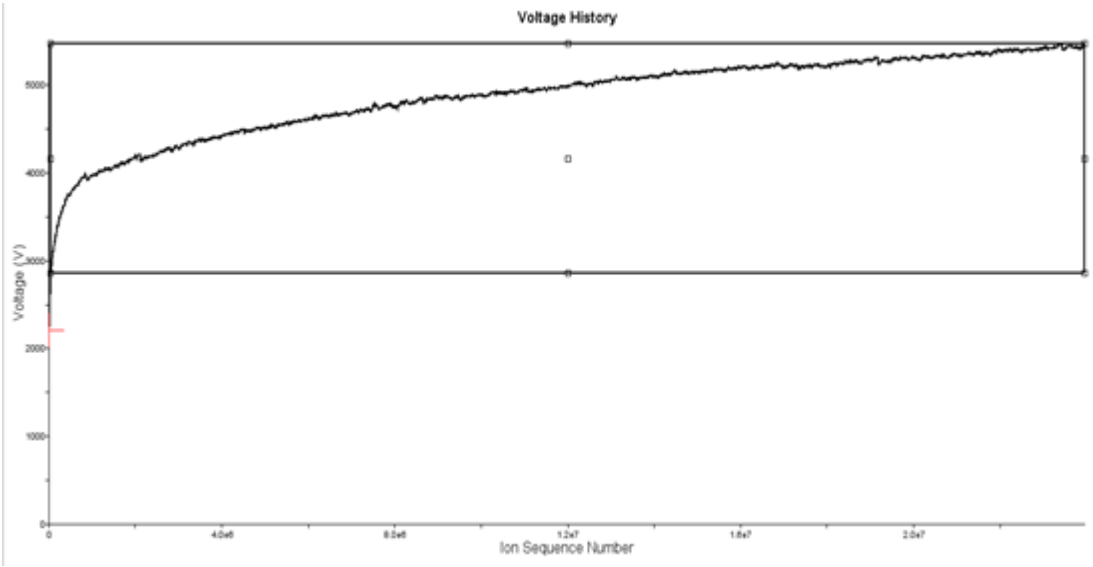

Figure 3.12 An appropriate continuous range of voltages is selected in the IVAS Cal/Recon Wizard by adjusting the voltage box overlay to capture the appropriate region of the Voltage vs. Ion Sequence curve.

Removing any rough edge regions in the data is very important as this improves the accuracy of the reconstruction since the algorithms utilise the selected ROI to calculate the depth increment (Figure 3.13).

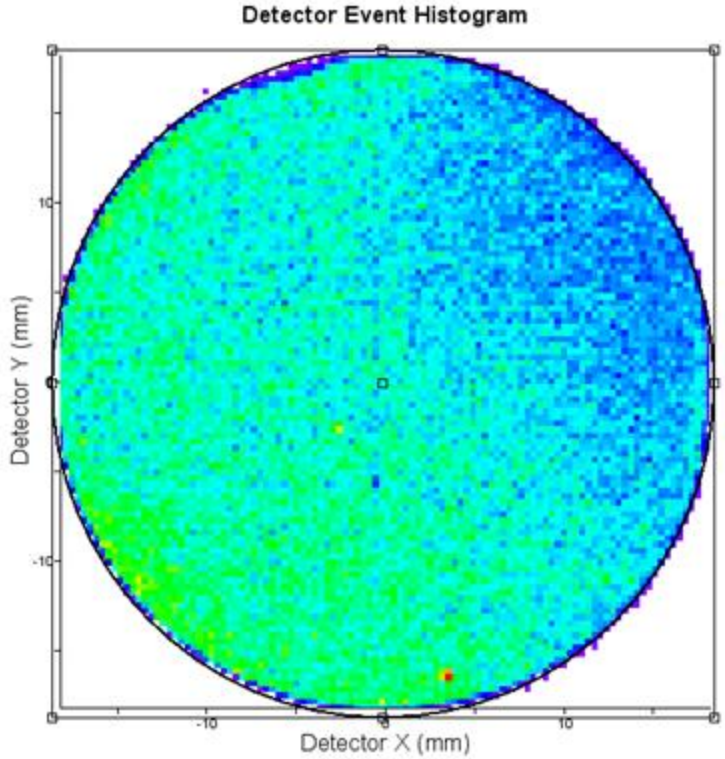

Figure 3.13 An appropriate elliptical detector area is selected in the IVAS Cal/Recon Wizard by adjusting the hit overlay to capture the appropriate region of ion hit-map on the detector.

IVAS conducts ToF corrections and calibrations before producing a mass spectrum, allowing chemical identities and volumes to be assigned for each ion type. The process of ranging is critical as this determines the actual nature of the atoms in the final 3D dataset. Any areas not selected in the ranging process will be treated as "noise" and are ignored from the reconstruction process (Figure 3.14).

Finally, each ion is reconstructed by assigning it with a 3D position using the tip profile reconstruction method. An SEM image of the pre-LEAP-analysis tip profile is used. The stage tilt is corrected and then an imaging scale factor is defined to relate pixel dimensions to nanometres. Profile tracers are used to define the shape of the tip, as shown in Figure 3.15. Most important is the uppermost tracer which defines the initial tip radius of the reconstruction. Although a reconstruction profile and defined volume are created as deep

into the sample as the traces are drawn, the reconstruction will only fill this volume up to the point that all the ions collected are used[69–71].

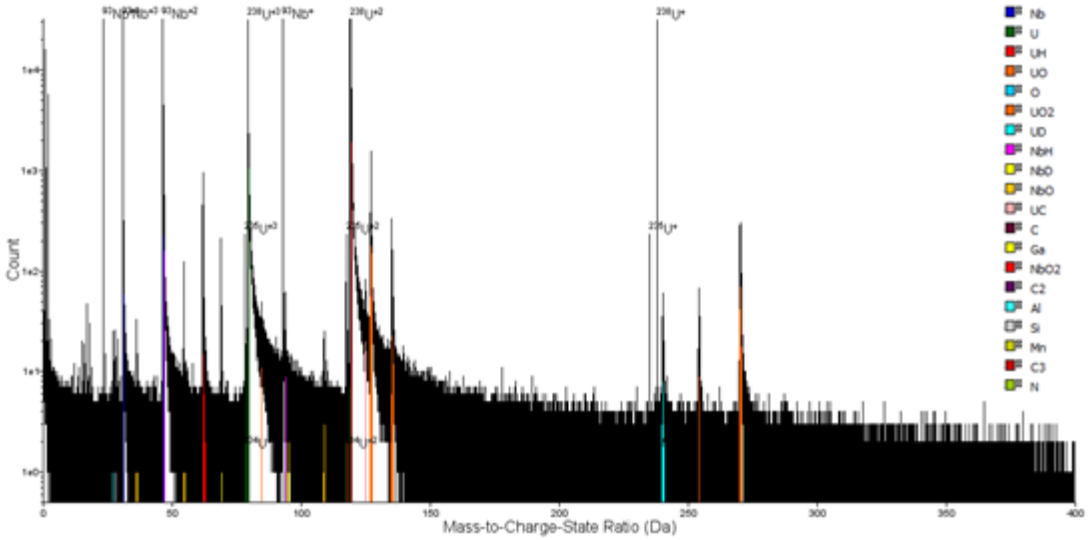

Figure 3.14 Mass spectrum showing ranges selected during the data processing.

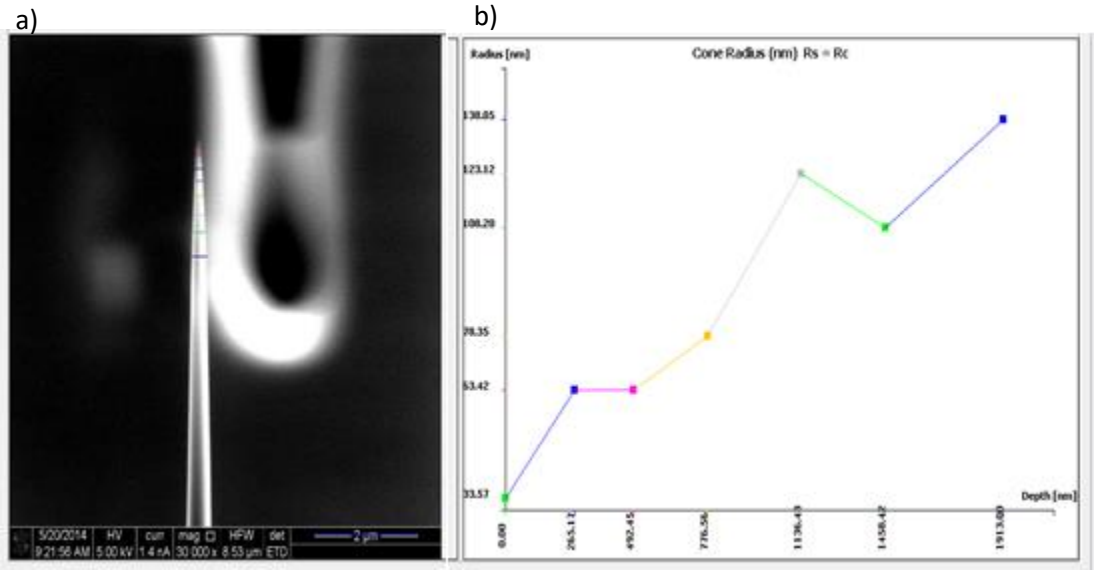

Figure 3.15 The IVAS Cal/Recon Wizard allows users to define the reconstruction radius evolution based on the actual tip profile. (a) By measuring various portions of the tip (coloured profile tracer lines), (b) a radius evolution function is defined. The field evaporated end form of this tip enables accurate determination of the initial radius, R, in relation to the other tip measurements.

At the end of the process, the ROOT and POS files are created so that the reconstructed data is available for further quantitative analyses or visualisation such as:

- Displaying only certain atoms

- Creating an “isosurface” to identify volumes of high concentrations of certain atoms, such as a cluster or a precipitate
- Creating a “region of interest” volume and determining the elemental composition of the selected volume
- Creating a 1D concentration profile and plotting the composition graph
- Creating a 2D concentration profile across a precipitate phase to illustrate the element distribution

4 Chapter four – results of uranium water vapour reaction

The reaction of uranium with water vapour has been studied previously. However, the mechanism of the reaction remains inconclusive. There is a debate over the formation of any hydride and also how the addition of oxygen inhibits the water vapour reaction.

In this study the reaction of uranium metal with $D_2{}^{16}O$ vapour followed by $H_2{}^{18}O$ vapour was conducted in order to investigate the mechanism by way of isotopic changes using SIMS, with the key aims being to determine the diffusing species and if hydride formation occurs. The addition of oxygen to the water vapour reaction has also been studied, again using isotopic water and oxygen to allow SIMS depth profiling to reveal mechanistic information on the role oxygen plays in inhibiting the reaction.

Atom probe analysis was also conducted to study the initial oxidation of uranium metal with exposure to water vapour. Atom probe analysis produces a 3D reconstruction of the nano-structure of the material, which will provide chemical composition information and help determine hydride formation.

In addition, uranium metal was studied to provide a baseline for the study of the uranium niobium alloys. Both the kinetic and mechanistic data should provide an insight into the alloy system as well as a standard, end-member material for comparison.

Much of the text and many of the figures from the atom probe section (section 4.4) were taken directly from the paper published in Scientific Reports under the title 'Atomic-scale studies of uranium oxidation and corrosion by water vapour'[72]*.*

4.1 Material characterisation using EDX

EDX was used to provide elemental information of the material pre and post water vapour exposure, allowing the extent of oxidation to be visually recorded.

4.1.1 EDX of freshly polished uranium surface

Figure 4.1 shows the SEM image of a polished uranium coupon pre exposure to any water vapour. The coupon was polished manually using silicon carbide (SiC) paper with grits 320 - 1200. From the micrograph it can be seen that there are clear polishing marks and scratches as well as some regions of imperfections on the surface.

Figure 4.2 shows an EDX spectrum of the polished uranium coupon. The main elements present are uranium and oxygen, as expected.

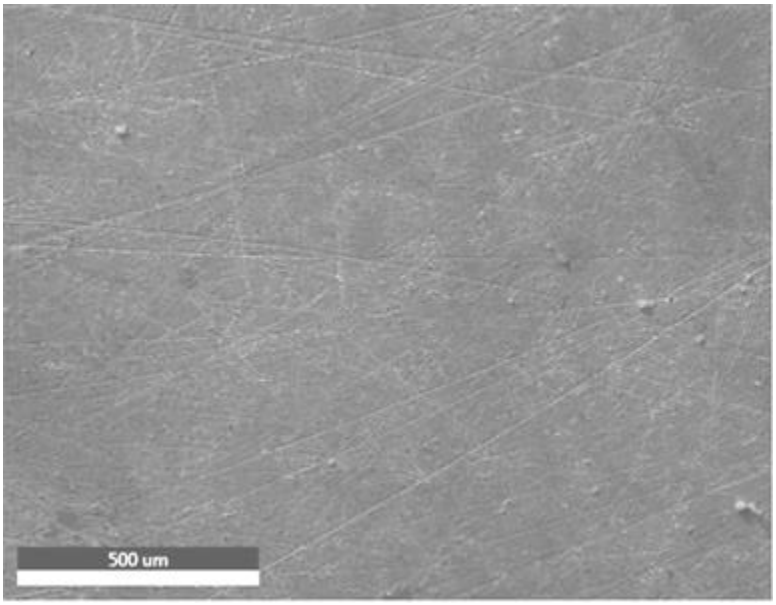

Figure 4.1 SEM image of a polished uranium coupon.

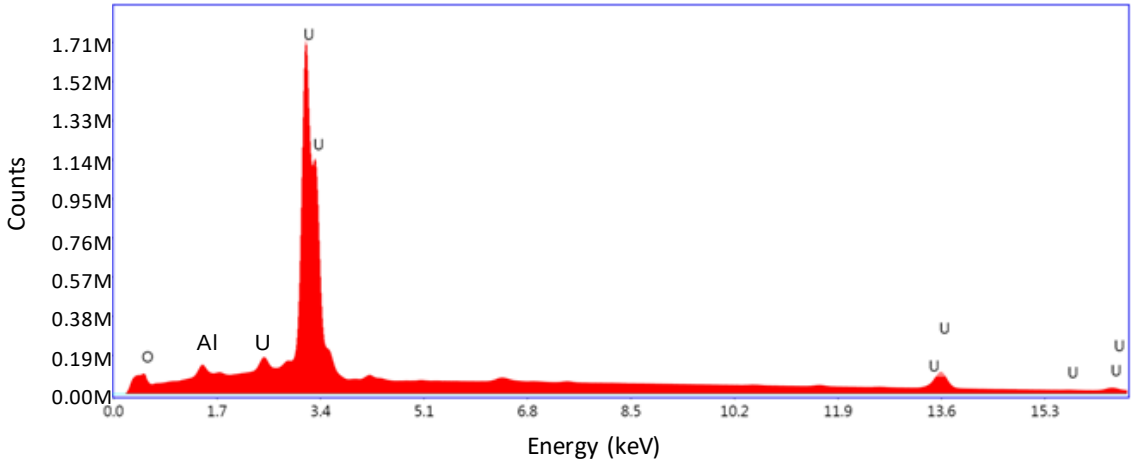

Figure 4.2 Spectrum from EDX analysis on polished uranium surface.

The elemental maps are shown in Figure 4.3, with yellow and green representing uranium and oxygen respectively. From Figure 4.3, it can be seen that the majority of the surface is uranium with oxygen distributed throughout.

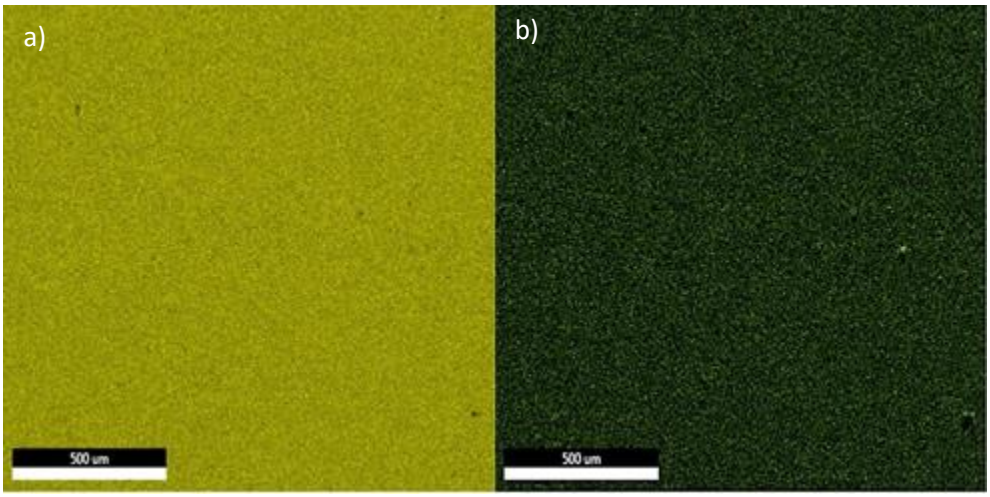

Figure 4.3 EDX elemental analysis of the polished uranium surface, a) uranium in yellow, b) oxygen in green.

4.1.2 EDX of uranium surface after water vapour exposure

Figure 4.4 shows an SEM image and a photograph of a uranium coupon after exposure to water vapour at 55 °C for 879 hours. From the SEM image (figure 4.4a) it can be seen that the topography of the sample is a lot rougher that that seen in figure 4.1 for the freshly polished surface. From the photograph (figure 4.4b) it can be seen that the material has spalled drastically with an entire coherent layer of oxide being separated from the coupon. Spallation of the material will both affect the kinetics of the reaction and the analysis by SIMS. The majority of the uranium samples displayed thick oxides with some spallation evident. However, this was the only sample that showed a detached oxide layer.

Figure 4.5 presents the spectral analysis of the surface with elemental analysis for uranium and oxygen shown in Figure 4.6.

4.1.3 Summary

The analysis shows how the topography and (gross) composition of the surface of the samples change as a result of the exposures given. The impact of these changes on the kinetics and SIMS will be discussed in sections 4.2 and 4.3 respectively.

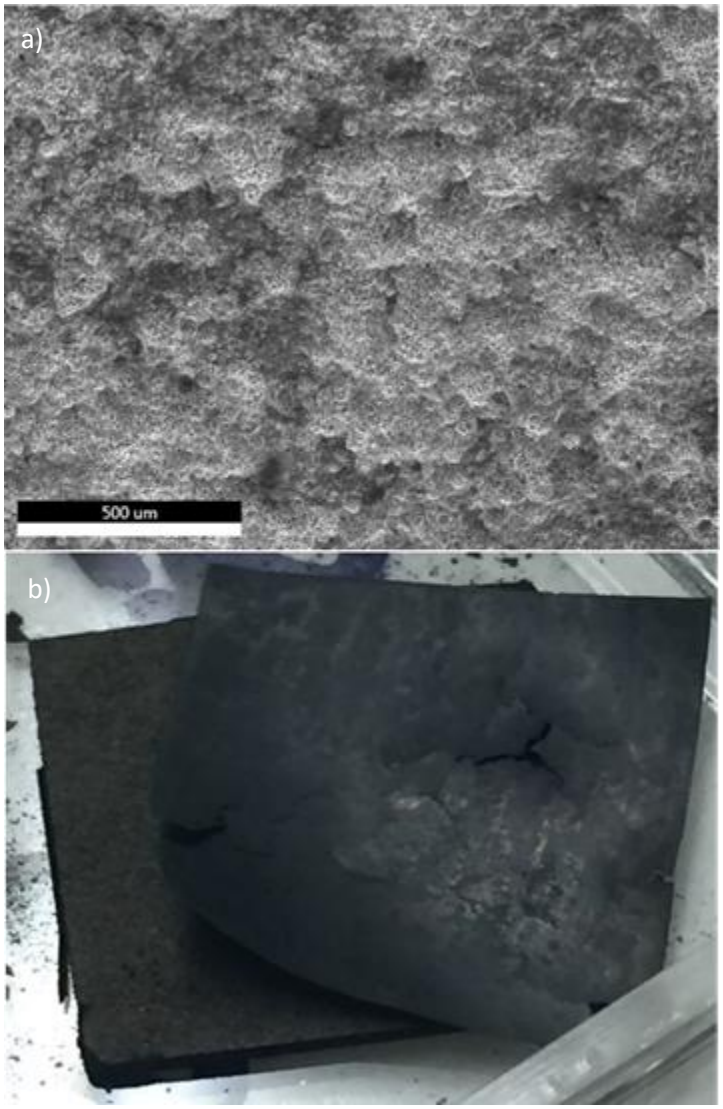

Figure 4.4 Corroded uranium coupon from the experiment conducted at 55 °C with a water vapour pressure of 30 mbar, a) SEM image of the surface, b) photograph of the oxidised surface showing a detached intact oxide layer of a 12 mm² coupon.

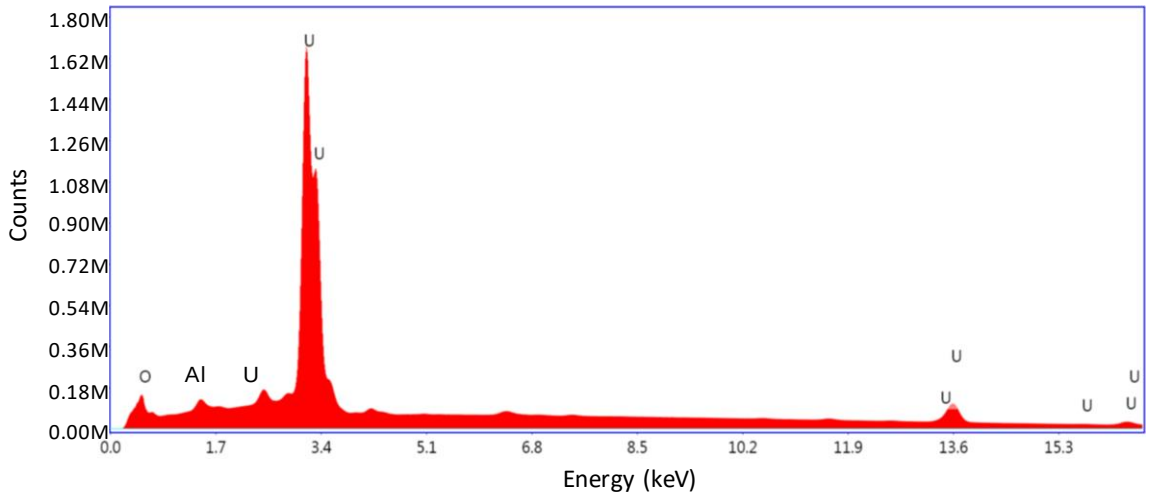

Figure 4.5 Spectrum of EDX analysis of the corroded surface.

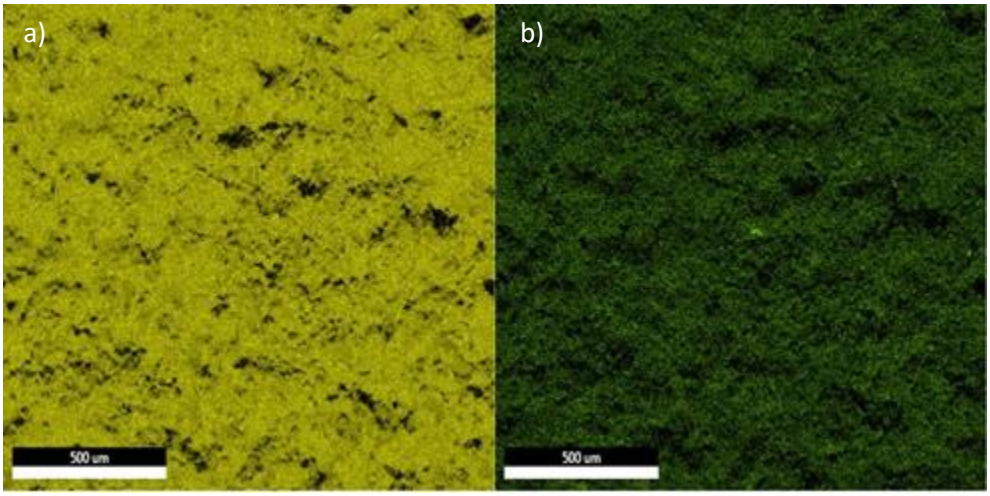

Figure 4.6 EDX elemental analysis of the corroded uranium coupon, a) yellow uranium, b) green oxygen.

4.2 Corrosion kinetics

Water corrosion experiments on uranium were conducted at four different temperatures. The pressure dependence has previously been shown to be $P_{(H_2O)}^{½}$ [4,6,21] for the range of temperatures investigated in this study. Therefore, only one vapour pressure of ~30 mbar was used throughout. Comparable pressures of ~30 mbar could be produced using various salt solutions over the desired temperature range. These were long-term experiments, with the length of exposure varying from a couple of weeks to over a year.

The kinetic data are presented from both the $D_2{}^{16}O$ reaction and the subsequent $H_2{}^{18}O$ reaction. For the $H_2{}^{18}O$ experiment, the initial surface oxide has already been formed through the $D_2{}^{16}O$ reaction. Therefore, the reaction kinetics should be linear and consistent with the final $D_2{}^{16}O$ rate.

Errors associated with the thermocouples (Type K) and the transducers should be noted. For the thermocouple the accuracy is ±2.2 °C or ±0.75%, whichever is greater. For the transducers there a few factors addressed in its performance rating:

- Long term drift ±0.1% span/annum
- Accuracy ±0.25%
- Thermal error 1% (0 °C to 70 °C), 2% for 40 to 250 mbar ranges (0 °C to 50 °C)

When experimental data referring to temperature or pressure are presented and discussed the associated errors will be highlighted.

The desired temperatures were 70 °C, 55 °C, 45 °C and 30 °C, the actual temperatures varied slightly due to changes in the room temperature of the laboratory. The pressure values are only theoretical/predicted values calculated from an equation by Greenspan[67]. Therefore, changes in temperature and impurities within the water will impact the actual pressure.

Table 4.1 Theoretical water vapour pressures available from salt solutions at the temperatures of interest.

Salt	Temperature (°C)	RH%	Pressure (mbar)
Sodium Chloride (NaCl)	30	75.1	31.4
Magnesium chloride ($MgCl_2$)	45	31.1	28.9
Potassium fluoride (KF)	55	20.6	31.3
Lithium chloride (LiCl)	70	10.8	32.3

For the 30 °C experiment, the reaction cells were placed in the open laboratory rather than within an oven. This meant that the temperature varied quite significantly throughout seasonal changes. It also meant that the temperature was lower than desired, with the temperature average being ~22°C ±2.2 °C. The lower temperature therefore affects the starting pressure of the experiment. For this temperature the predicted starting pressure is 19.9 mbar which is reasonably close to the actual starting pressure of 18.63 mbar.

The actual average temperatures and starting pressures (once at temperature of experiment) of the uranium $D_2{}^{16}O$ corrosion experiments were:

- 69.54 ±2.2 °C experiment starting pressure of 36.37 mbar ±0.39%
- 57.37 ±2.2 °C experiment starting pressure of 23.11 mbar ±0.52%
- 45.00 ±2.2 °C experiment starting pressure of 41.47 mbar ±0.93%
- 21.98 ±2.2 °C experiment starting pressure of 18.63 mbar ±0.44%

The actual average temperatures and starting pressures of the uranium $H_2{}^{18}O$ experiments were:

- 56.85 ±2.2 °C experiment starting pressure of 27.78 mbar ±0.63%
- 45.56 ±2.2 °C experiment starting pressure of 41.76 mbar ±0.94%

- 27.98 ±2.2 °C experiment starting pressure of 21.66 mbar ±0.49%

There was an issue of a leak within the cell for the 70 °C $H_2{}^{18}O$ experiment and therefore the kinetic data are not presented.

It can be seen for both of the nominal 45 °C experiments that the starting pressure is consistently higher than the theoretical value. This possibly suggests that there was an issue with the salt (either due to impurities or not being fully saturated) or that oxygen was present within the system, leading to an increase in starting pressure. Oxygen presence is unlikely due to the freeze, pump and thaw process that the reaction cells undergo in order to remove residual gases from the system. If it was the case that the salt solution was not fully saturated, then a much higher water vapour pressure of 96 mbar would be expected, (at 45 °C the pressure of pure water vapour is approximately 96 mbar). This vapour pressure is significantly higher than the starting pressures stated above, suggesting that saturation was not the issue here. This therefore leaves one option of salt purity ($MgCl_2$) as the issue.

For the reaction with water vapour plus oxygen, previous work has shown the oxygen to inhibit the evolution of hydrogen and reduce the reaction rate[3,6]. The experiments with water vapour plus oxygen were carried out at a desired temperature of 55 °C and with the desired starting pressures of 40 mbar (30 mbar water vapour and 10 mbar oxygen). Both isotope regimes were investigated – $D_2{}^{16}O$ + $^{18}O_2$, actual temperature of 61.55 ±2.2 °C and pressure of 33.14 ±0.75 mbar (24.14 mbar water + 9 mbar oxygen) and $H_2{}^{18}O$ + $^{16}O_2$, actual temperature of 57.62 ±2.2 °C and pressure of 36.89 ±0.83 mbar (27.89 mbar water + 9 mbar oxygen). The reason for the reduced starting pressure is most likely due to salt impurities and temperature fluctuations.

4.2.1 Reaction with sequential water vapour exposure

Example data are presented for some of the experiments, in figures 4.7-4.10 with all of the rate data being presented in Table 4.2 and plotted in Figure 4.11. The plots are representative for all of the data and are presented in two formats, firstly a plot showing the pressure (mbar) and temperature (°C) data for the exposure and secondly the amount of hydrogen evolved (mmol H_2 cm^{-2}) and the corresponding rate (mmol H_2 cm^{-2} s^{-1}) for that reaction.

Figure 4.7 shows the pressure and temperature data from the experiment at 57.80 °C (mean temperature) and a $D_2{}^{16}O$ water vapour pressure of 23.11 mbar (starting pressure). As can be seen the pressure increases over the length of exposure, from 23.11 mbar up to 111 mbar (transducer maximum). The temperature can be seen to fluctuate by a few degrees 55-58 °C. The fluctuations are due to changes in temperature within the laboratory, there is no form of regulation such as air conditioning; therefore, the temperature of the laboratory varies throughout the year. Any change in temperature is taken into account when calculating the amount of hydrogen evolved.

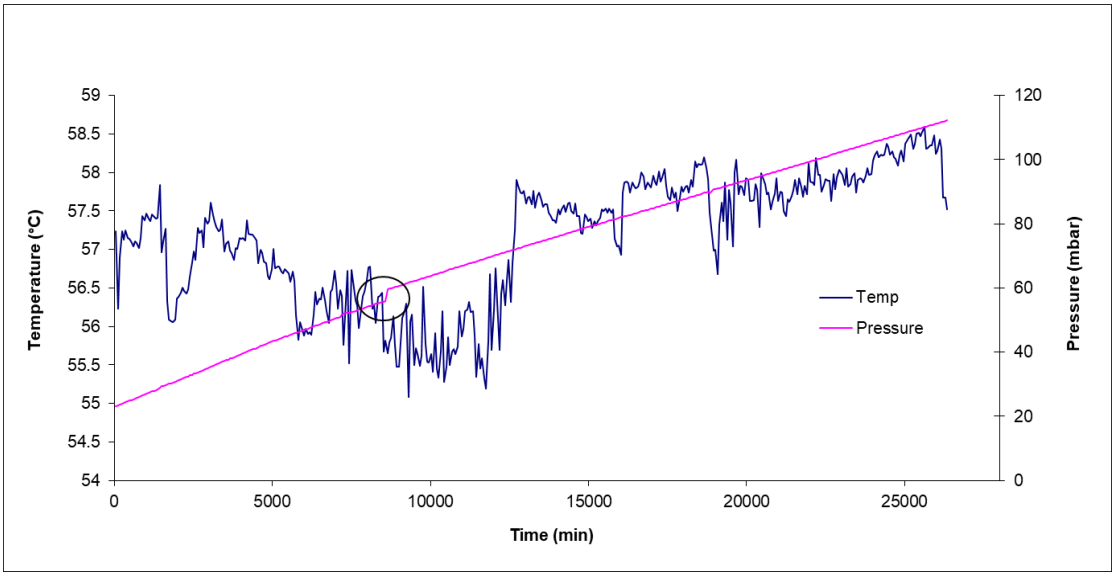

Figure 4.7 Pressure and temperature graph for the uranium at 57.37 °C and 23.11 mbar $D_2{}^{16}O$ experiment.

In figure 4.7 there is a region (circled area) where the pressure appears to jump, from 55 to 59 mbar in the space of one hour. The temperature appears stable over this period so there is no obvious reason for this jump however one possibility is a spallation event, similar to the one shown in figure 4.4.

When the pressure data are converted into the amount of hydrogen evolved (see section 3.1 for details), it can be seen that there are a couple of distinct regions, either side of the previously mentioned jump in pressure seen in Figure 4.7. Figure 4.8 shows the hydrogen evolved as a function of time in minutes. The rates are marked up on the plot, these are calculated as described in section 3.1 and are in terms of mmol H_2 cm^{-2} s^{-1}. The rates vary

slightly, with the initial rate being slightly faster. However, this initial rate is likely to be less stable as the reaction is in the early stages and may not have reached the linear kinetics regime. Therefore it is the rate of the second stage that is carried forward.

Figure 4.9 and Figure 4.10 show the data from experiment at 21.98 °C and 18.63 mbar water vapour pressure using $D_2{}^{16}O$. The reaction cell was placed within the open laboratory and not in an oven therefore the average temperature is closer to 23 °C than 30 °C (ranges from 19 to 25 °C). Figure 4.9 highlights a couple of regions (A and B) where the data scan unit was not recording; the calculations for rate were taken after these periods as shown in Figure 4.10.

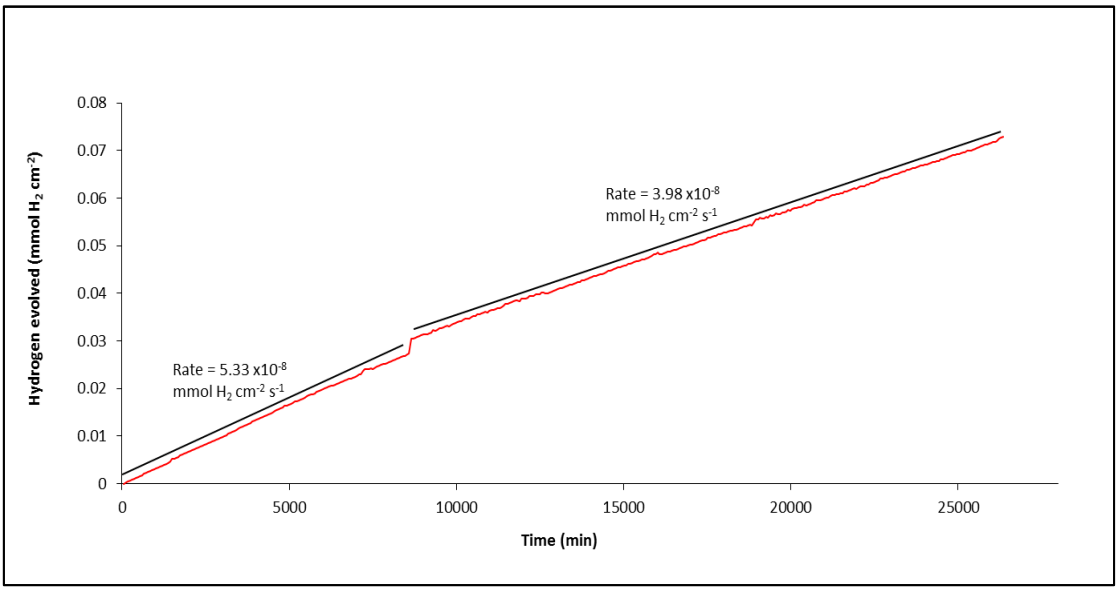

Figure 4.8 The amount of hydrogen evolved for the uranium at 57.37 °C and 23.11 mbar $D_2{}^{16}O$ experiment.

Figure 4.11 shows the calculated rates for all of the uranium $D_2{}^{16}O$ experiments. The rate is expressed in terms of mmol H_2 cm^{-2} s^{-1} $mbar^{-0.5}$. There is reasonable correlation between the data, showing that as temperature is increased so does the corrosion rate.

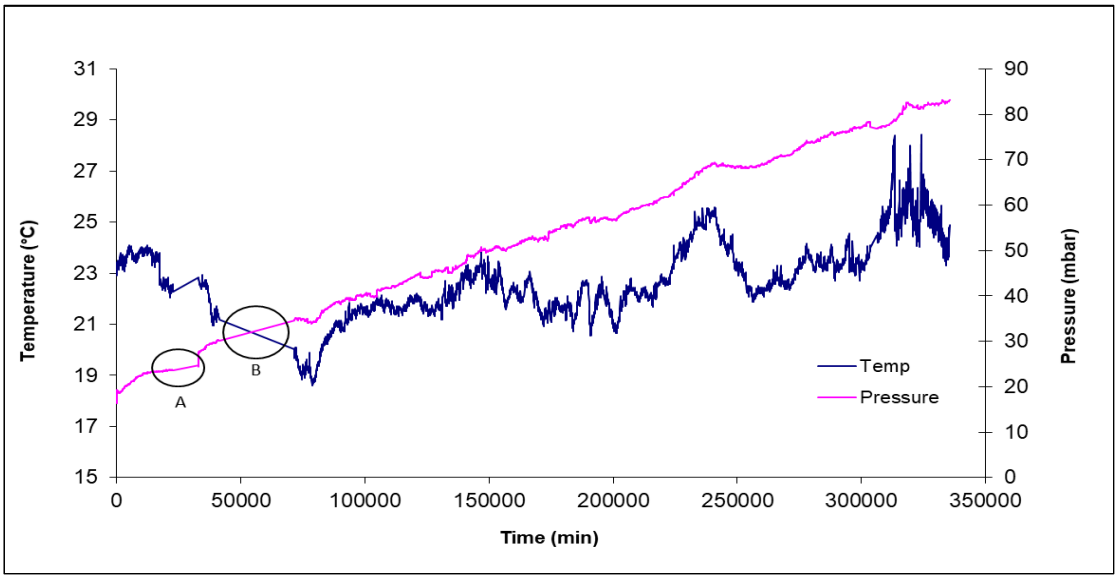

Figure 4.9 Pressure and temperature graph for the uranium at 21.98 °C and 18.63 mbar $D_2{}^{16}O$ experiment.

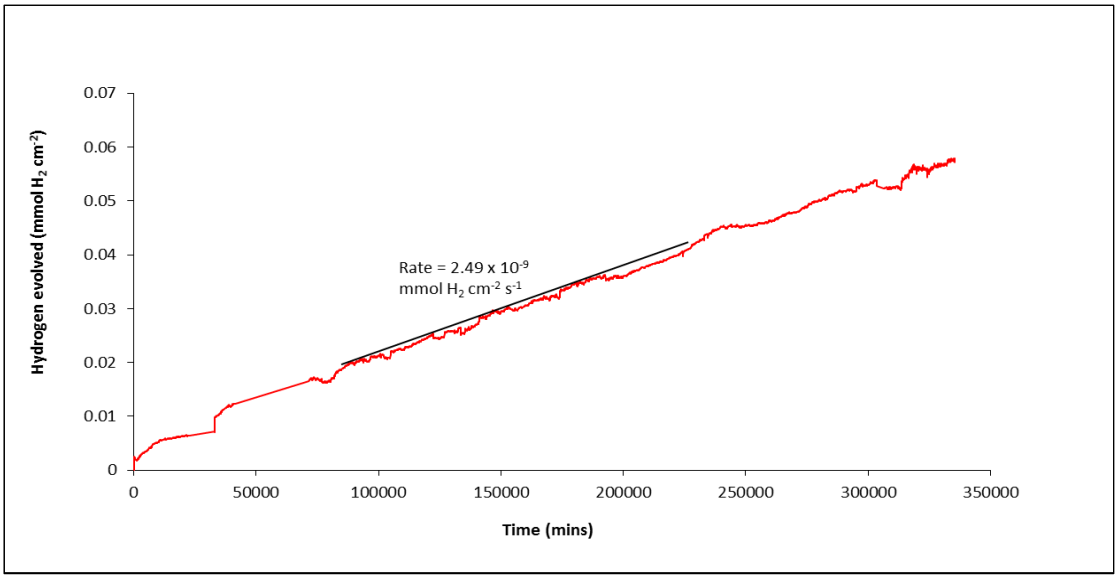

Figure 4.10 The amount of hydrogen evolved for the uranium at 21.98 °C and 18.63 mbar $D_2{}^{16}O$ experiment.

Table 4.2 Rate data for all uranium $D_2{}^{16}O$ experiments at the desired starting pressure of 30 mbar.

Average temperature		1000/T (K^{-1})	Starting pressure (mbar)	Rate (mmol H_2 cm^{-2} s^{-1})	Rate (mmol H_2 cm^{-2} s^{-1} $mbar^{-0.5}$)
°C	K				
69.54	342.75	2.92	36.37	9.29E-08	1.54E-08
57.37	330.95	3.02	23.11	3.98E-08	8.28E-09
45.00	318.15	3.14	41.47	2.20E-08	3.42E-09
21.98	295.13	3.39	18.63	2.49E-09	5.77E-10

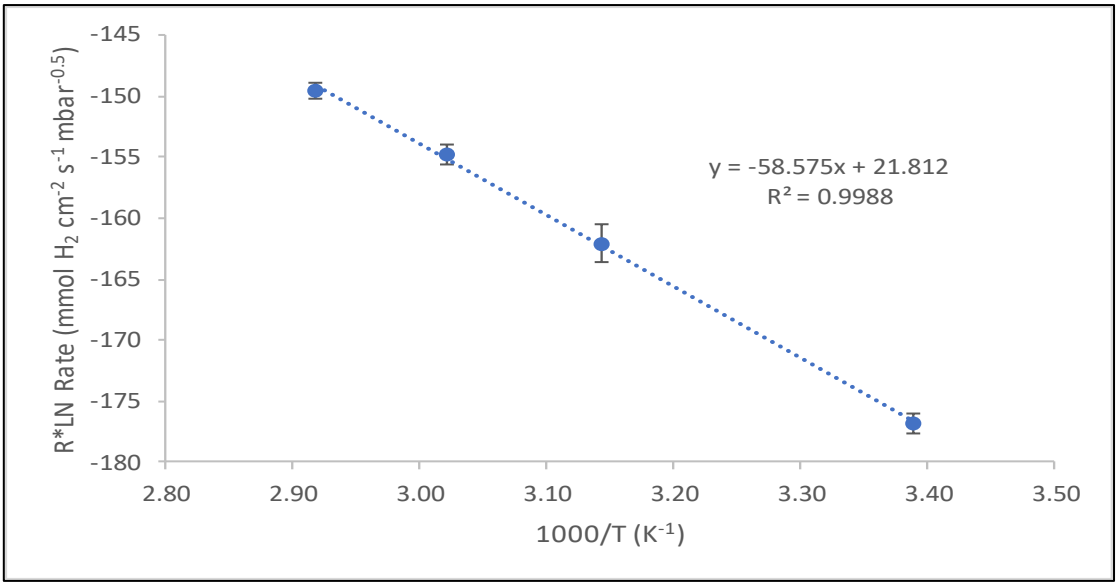

Figure 4.11 Graph displaying rate data for all uranium $D_2{}^{16}O$ 30 mbar experiments – 69.54 °C, 57.37 °C, 45.00 °C and 21.98 °C. The error bars are calculated from the transducer %accuracy and are not an indication of confidence in the data.

The experimental rates for the $D_2{}^{16}O$ experiments can be compared to values from previous studies. Hilton[18] reviewed the rates of the uranium-water vapour reaction at temperatures between 20 – 302 °C. He derived an average linear rate constant:

$$\frac{K_l}{P^{0.5}} = 9.76 \times 10^5 exp\left(\frac{-46.6 \pm 0.7}{RT}\right) \text{mg U cm}^{-2}\ \text{h}^{-1}\ \text{kPa}^{-0.5} \qquad (1)$$

Where the activation energy is in kJmol^{-1}, p is water vapour pressure in kPa, *T* is temperature in kelvin and *R* is the gas constant in J mol^{-1} K^{-1}.

The rates in this study are expressed in terms of mmol H_2 cm^{-2} s^{-1} mbar$^{-0.5}$. Therefore, this equation of Hilton is converted to:

$$\frac{K_l}{P^{0.5}} = 2.28 \times 10^3 exp\left(\frac{-46.6 \pm 0.7}{RT}\right) \text{mmol H}_2\ \text{cm}^{-2}\ \text{s}^{-1}\ \text{mbar}^{-0.5} \quad (2)$$

Where the activation energy is in kJmol^{-1}, p is water vapour pressure in mbar, *T* is temperature in kelvin and *R* is the gas constant in J mol^{-1} K^{-1}.

This equation has been used to derive rate values for the conditions of this study.

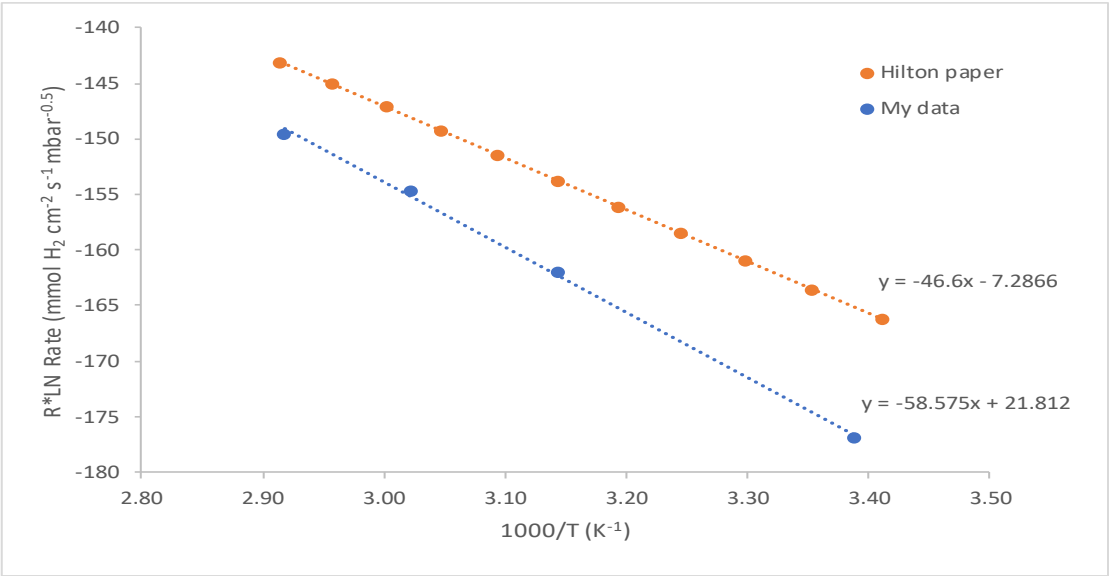

Figure 4.12 Graph comparing data for the $D_2{}^{16}O$ reaction with uranium with average linear rate calculated derived by Hilton[18].

As can be seen in Figure 4.12, the experimental rates are slower than those previously reported by Hilton[18]. However, the general trend of an increase in temperature increasing the rate is similar.

An activation energy of 58.58 kJ mol^{-1} has been calculated; this value is higher than those previously calculated by Hiltons[18] review (46.6 kJ mol^{-1}), Glascott[73] (40.7 kJ mol^{-1}) and Colmenares[21] (41.72 kJ mol^{-1}). However, it is within the range reported by Baker[2,33] (50-71 kJ mol^{-1}) who conducted water vapour experiments on uranium between 35-240 °C. It must be noted that in this work there are only four data points and therefore more data is required to allow a more comprehensive comparison to previous work.

A factor that could affect the corrosion rates is that of the metal purity. It has previously been shown that inclusion (carbide or nitride) water reactions appeared to occur more vigorously than the concurrent uranium-water reactions. The uranium used in this study is low carbon. Therefore, the rate should be slower than with high carbon material. This idea, however, can only be surmised as not all of the purities are known. However it could partly explain the conflicting data[21,74]. Another possibility is the ingress of O_2 within the reaction cell. Oxygen has been shown to inhibit the water vapour reaction, producing significantly slower rates[3,75].

When the rate data from the $D_2{}^{16}O$ reactions are compared to the $H_2{}^{18}O$ counterparts it can be seen that the rates appear faster with $H_2{}^{18}O$, see Table 4.3 and Figure 4.13. There is also a significant difference in activation energy for the two regimes.

Table 4.3 Rate data for all uranium $H_2{}^{18}O$ experiments.

Temperature		1000/T (K^{-1})	Starting Pressure (mbar)	Rate (mmol H_2 cm^{-2} s^{-1})	Rate (mmol H_2 cm^{-2} s^{-1} $mbar^{-0.5}$)
(°C)	(K)				
56.85	330.95	3.02	27.78	4.23E-08	8.03E-09
45.56	318.15	3.14	41.76	6.33E-08	9.80E-09
27.98	301.13	3.32	21.67	2.29E-08	4.92E-09

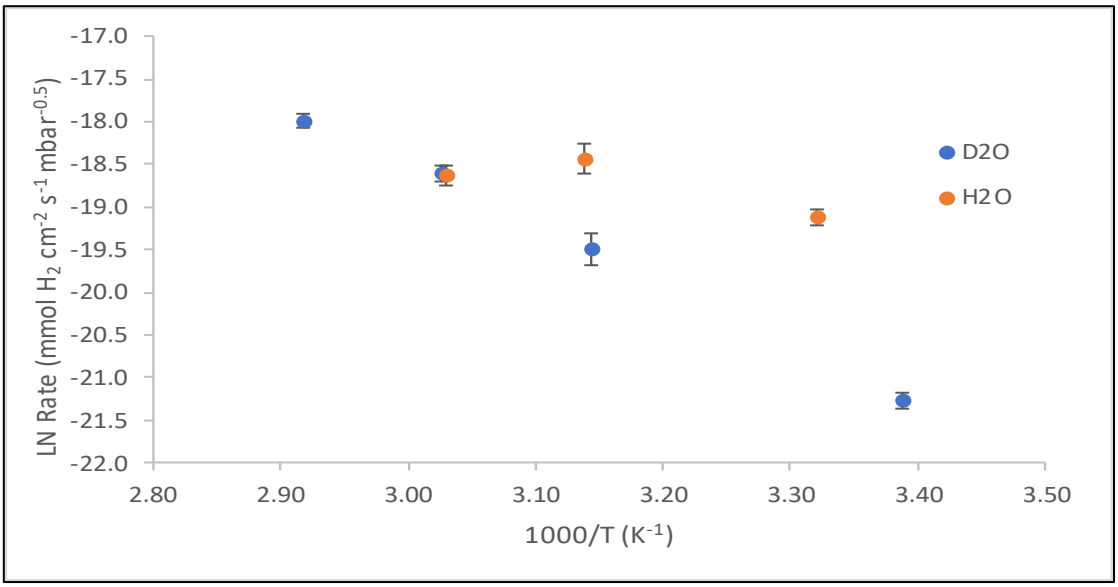

Figure 4.13 Graph comparing the uranium data for the $D_2{}^{16}O$ with the $H_2{}^{18}O$ experiments. The error bars are calculated from the transducer %accuracy and are not an indication of confidence in the data.

One possible scenario for the difference is due to the different reaction species, i.e. an isotopic effect. However, as there is not a consistent difference between the rates, this is unlikely.

Another possibility is for a contaminant of some form (most likely oxygen) to be present in both the $D_2{}^{16}O$ and $H_2{}^{18}O$ reactions, which causes slower rates when compared to previous work.

The difference between the two water rates in this study therefore could be due to varying amounts of the contaminant; $D_2{}^{16}O$ water is of a lower purity than $H_2{}^{18}O$. Therefore, the contamination level could be higher. However, in the water vapour plus oxygen reaction it has previously been shown that oxygen is preferentially consumed so the effect of oxygen contamination slowing the rate would be short lived[74].

If an Arrhenius plot of all of the data ($D_2{}^{16}O$ and $H_2{}^{18}O$ rates) is produced, the derived activation energy of 44.39 kJ mol^{-1} is closer to those reported previously[21,73]. The correlation value however is poor (R^2 = 0.69) with divergence increasing with increasing temperature.

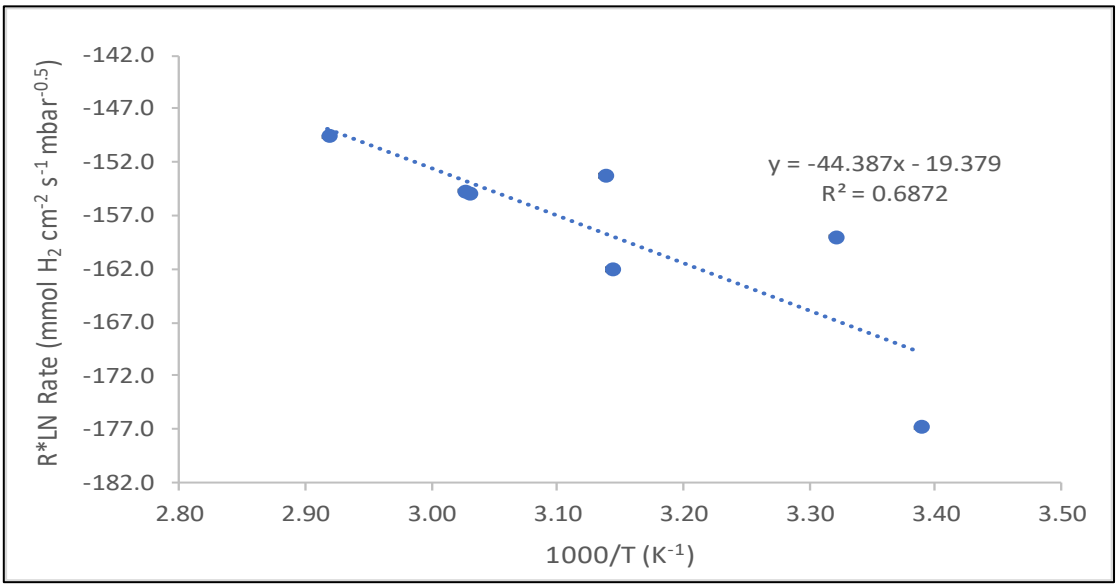

Figure 4.14 Arrhenius plot for all data ($D_2{}^{16}O$ and $H_2{}^{18}O$ exposures).

4.2.2 Reaction with water vapour plus oxygen

Previous work has shown the uranium corrosion rate to be inhibited by the addition of oxygen to the water vapour reaction; however, the mechanism remains unknown [4,5,21]. The different isotopic combinations were used in order to allow enhanced SIMS analysis of the oxide once reacted to try and establish the mechanism. The kinetics were collected and the same assumptions and calculations were applied as for the water vapour experiments. All experiments were conducted at a desired temperature of 55 °C and the desired pressure of water vapour was 30 mbar using potassium fluoride as the salt. A pressure of approximately 10 mbar of oxygen was added, making the starting pressure of an experiment approximately 40 mbar. However, the actual starting pressures and average temperatures vary slightly:

$H_2{}^{18}O + {}^{16}O_2$ experiment:

- 57.73 °C experiment starting pressure of 36.89 mbar (27.89 mbar H_2O + 9 mbar O_2)

$D_2{}^{16}O + {}^{18}O_2$ experiment:

- 61.53 °C experiment starting pressure of 33.14 mbar (25.14 mbar H_2O + 8 mbar O_2)

Figure 4.15 and Figure 4.16 show the pressure/temperature and rate data respectively for the uranium with $H_2{}^{18}O + {}^{16}O_2$ experiment. The temperature was seen to fluctuate dramatically ranging from 38 °C up to 70 °C. The data were also seen to show repetition suggesting a possible issue with the thermocouple reading with noise influencing the data. Therefore, the average temperature of 57.62 °C was used for the rate calculations. The pressure can be seen to increase from ~38 mbar up to ~48 mbar before decreasing back down to 38 mbar. The variation in pressure could be related to the varying temperature but this is not known due to the thermocouple error or it is due to the oxygen being consumed (so a decrease in pressure is seen). Once fully consumed, hydrogen will be evolved and the pressure increases[74].

The variation in pressure is very different to the water vapour only experiments which saw a continual increase in pressure even when there were thermocouple issues, suggesting that oxygen does impact the reaction. The addition of oxygen had a dramatic effect and appeared to reduce the rate to a very low value that is too small to be accurately measured. Therefore the rates presented should be taken as a rough and dubious approximation and are solely there to demonstrate the difference between water vapour only and the water vapour plus oxygen reactions.

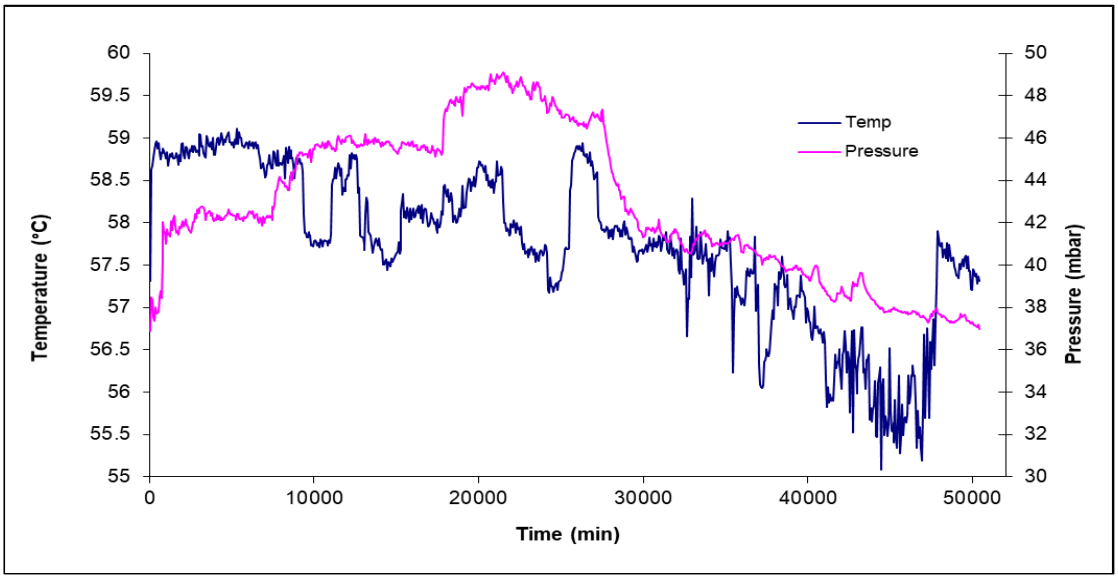

Figure 4.15 Pressure and temperature graph for the uranium at 57.62 °C and 36.89 mbar $H_2{}^{18}O$ + $^{16}O_2$ experiment.

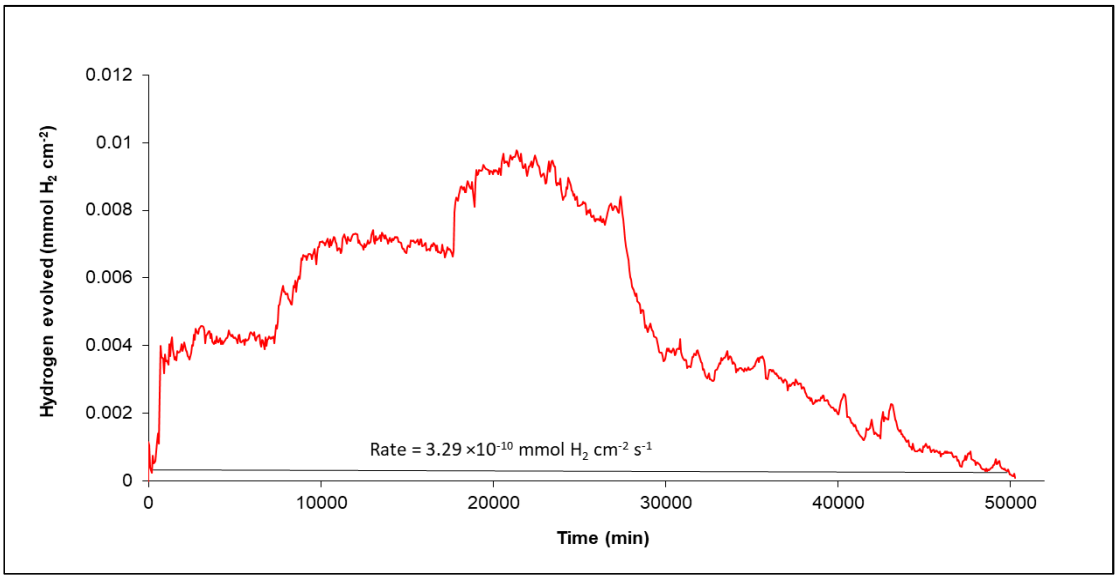

Figure 4.16 Volume of gas and rate graph for the uranium at 57.62 °C and 36.89 mbar $H_2{}^{16}O$ + $^{16}O_2$ experiment.

The temperature data from the $D_2{}^{16}O$ + $^{18}O_2$ experiment are less noisy. However, readings are slightly higher than desired, ranging from 59-65 °C, with an average of 61.55 °C. The oven itself was showing a temperature of ~55 °C. Therefore, this suggests an issue with the thermocouple. There are also a few regions where the pressure appears very noisy and shows an increase of ~10 mbar for a period before returning back to the starting pressure. This possibly suggests an error with the pressure transducer. However, without accurate temperature data this cannot be confirmed as the change in pressure could be related to a change in temperature.

If this is compared to the uranium 55 °C with 23.11 mbar of water vapour and no oxygen, over the course of 26000 minutes the pressure had increased from 23.11 mbar to 111 mbar. The rate is difficult to calculate due to the fluctuations but it can be speculated.

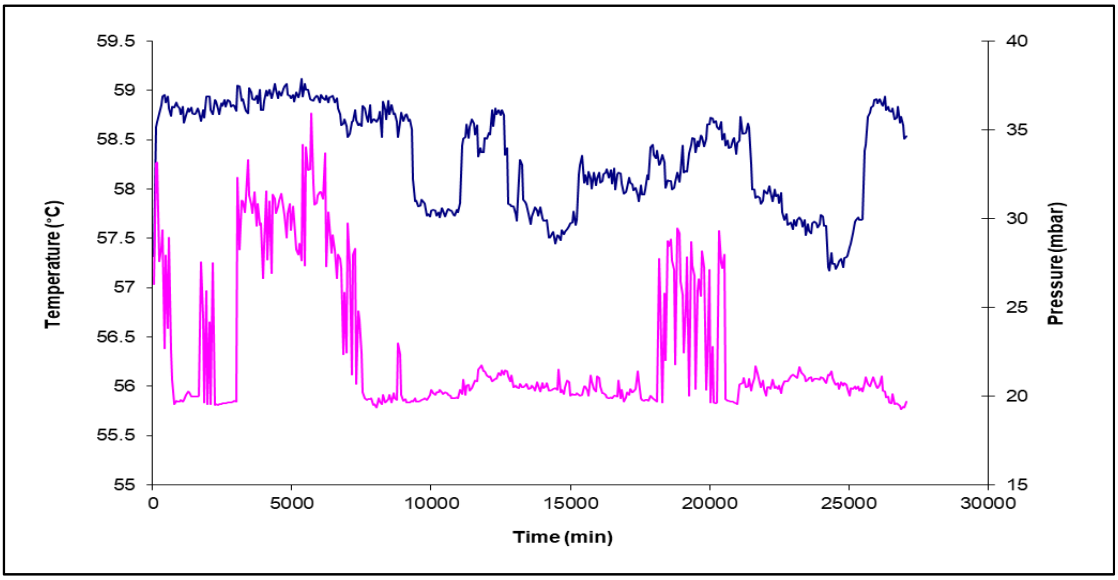

Figure 4.17 Pressure and temperature graph for the uranium at 61.53 °C and 33.14 mbar $D_2{}^{16}O$ + $^{18}O_2$ experiment.

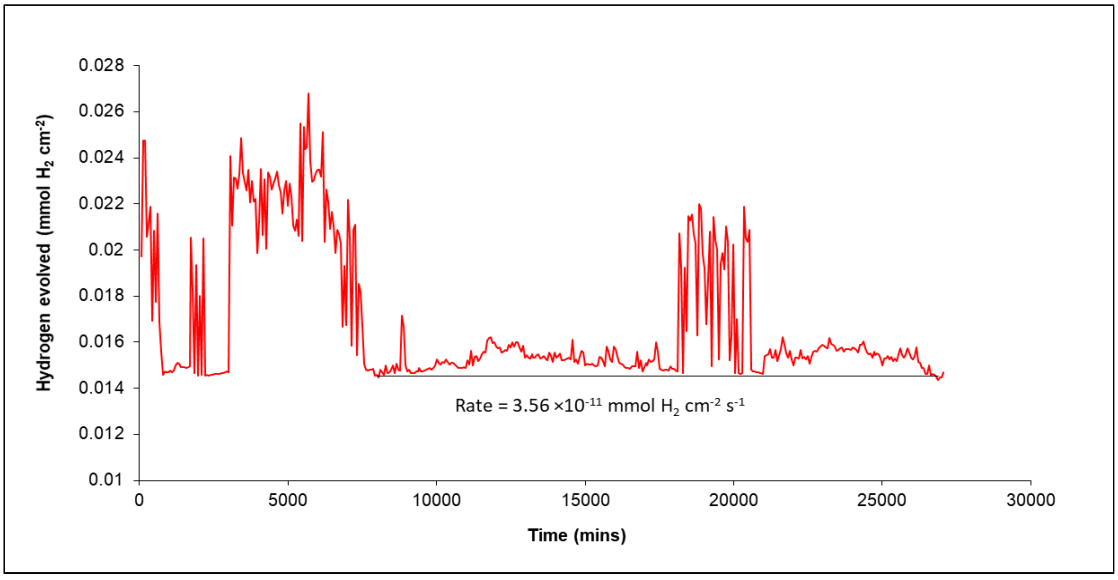

Figure 4.18 Amount of hydrogen evolved for the uranium at 61.55 °C and 33.14 mbar $D_2{}^{16}O$ + $^{18}O_2$ experiment.

A comparison of water vapour with and without oxygen data is presented in Figure 4.19 and Table 4.4. From Figure 4.19 the difference can be clearly seen with both the water vapour and oxygen experiments having significantly lower rates than the corresponding water vapour only experiment. This data are in agreement with previous literature [5,21] showing the addition

of oxygen to the water vapour reaction dramatically reduces the corrosion rate. Previous work has shown no hydrogen will evolve while oxygen remains in the system. Once the oxygen is depleted, the reaction will return to the kinetics of the water vapour reaction. This experiment was stopped prior to this change to allow for SIMS analysis of the initial oxide.

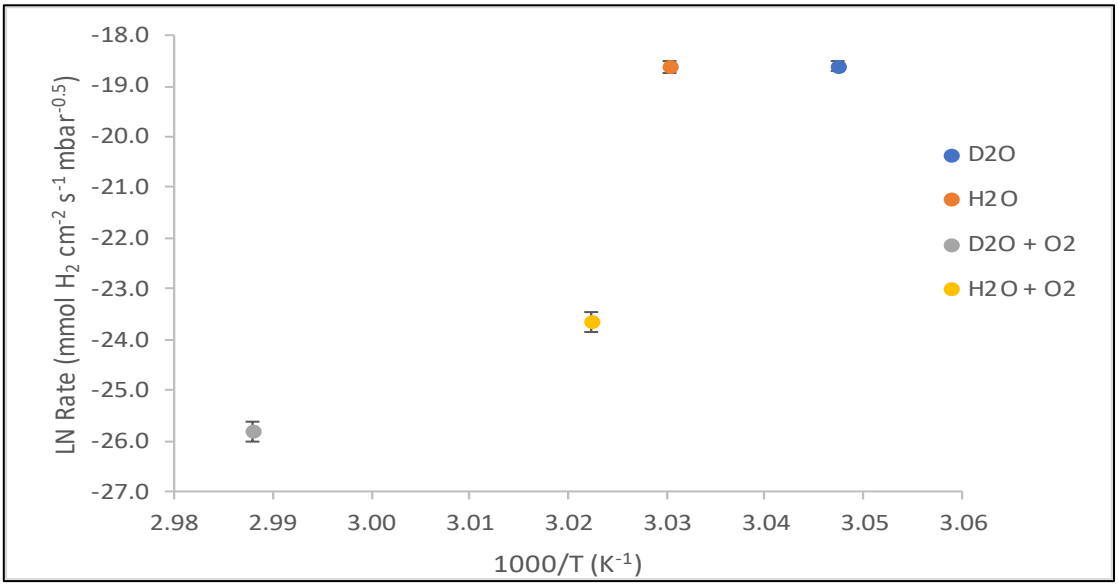

Figure 4.19 Graph comparing the rate data for uranium + water vapour experiments with uranium + water vapour + oxygen experiments conducted at approximately 55 °C. The error bars are calculated from the transducer %accuracy and are not an indication of confidence in the data.

Table 4.4 Comparison of rate data from the water vapour plus oxygen experiments.

Exposure mixture		Temperature		1000/T (K^{-1})	Starting Pressure (mbar)	Rate (mmol H_2 cm^{-2} s^{-1})
Water	Oxygen	(°C)	(K)			
$D_2{}^{16}O$	$^{18}O_2$	61.53	334.70	2.99	33.14	3.56E-11
$H_2{}^{18}O$	$^{16}O_2$	57.62	330.77	3.02	36.89	3.29E-10

Figure 4.20 is an Arrhenius plot reproduced from Haschke[4] which clearly shows the change in kinetics for the dry air, water vapour and the water vapour plus oxygen reactions. It clearly demonstrates that the reaction with water vapour is faster than the dry air reaction, and more importantly that the addition of oxygen to the water vapour reaction produces linear kinetics somewhere between the two end-member corrosion regimes.

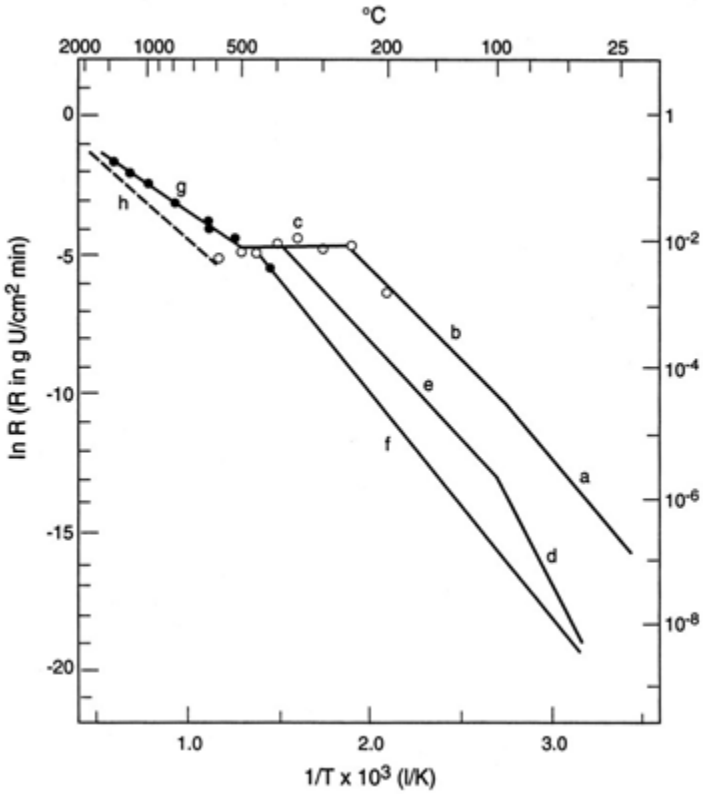

Figure 4.20 Arrhenius data for corrosion of uranium in dry air (filled circles) and water vapour at 760 torr (open circles). Curves a, b, and c describe the corrosion rate in water at saturation pressures, curves d and e indicate the rate in humid air at a nominal water pressure of 40 torr, curve f show the rate in dry air and curves g and h describe the rates in dry/humid air during autothermic reaction and binary oxides. The process is described by the hypothetical isothermal conditions, respectively. Figure reproduced from reference[4].

4.2.3 Summary

The kinetic data from the uranium experiments show slightly slower rates than previous literature. However, the general trend is the same and the results show good correlation with each other. The activation energy calculated for the water vapour reaction is higher than most previously determined [21,73] but similar to that of Baker[2,3]. Residual oxygen or impurities within the water system are a possible reason for the reduced reaction rates. There is also the purity of the uranium metal which has an effect on the corrosion rate, with low carbon material (as used here) displaying slower corrosion rates than high carbon material[74].

For the water vapour plus oxygen reaction a significantly slower rate as compared to the pure water vapour reaction was seen. This is in agreement with previous literature[3,18].

4.3 SIMS analysis of corroded samples

After the samples had been exposed to both of the water vapours and sufficient rate data had been collected, the reacted coupons were then analysed by SIMS. The use of the isotopic oxygen and hydrogen in the waters allowed some mechanistic information to be deduced from SIMS depth profiling of the oxide surface.

Any change in the oxygen ion yields during the profile provided fundamental information on the diffusing species and the reactions. For the water vapour experiments initially $D_2{}^{16}O$ was used followed by a switch to $H_2{}^{18}O$. Therefore, changes from ^{16}O and ^{18}O containing ions are key. If the ^{18}O peak is detected before the ^{16}O peak, this implies that the fresh oxide is formed at the oxide-gas interface and uranium ions diffuse outwards. The alternative is for ^{18}O peak to be detected after the ^{16}O peak, implying anionic diffusion, with the oxygen species diffusing inwards and the fresh oxide forming at the oxide-metal interface. The latter is the commonly agreed route. However, the oxygen containing species remains disputed. Therefore, the presence of any hydroxyl species will be significant in helping determine whether OH^{-} [2,3] or O^{2-} [4,22] are the diffusing species. SIMS was also used to look for any hydride present, as again this has been hypothesised[2,3,20,24] and relates to the mechanism. The use of deuterated water allows the investigation into any hydroxyl/hydride formation to be unambiguous as there will be residual hydrogen within the SIMS chamber that could contaminate the surface.

In the depth profiles presented oxygen 18 is represented by a "*" symbol.

4.3.1 Analysis after exposure to sequential water vapour

The kinetic data have been used to provide an estimate of the oxide thickness for each of the samples. Table 4.5 shows the oxide thickness from each of the water vapour exposures. Stopping Range of Ions in Matter (SRIM) has been used in order to calculate sputter yields for uranium and oxygen in UO_2 (Stopping range of ions in matter (SRIM)section 3.4.4). From this sputter yield a depth can be determined for each profile, presented later in **Error! Reference s ource not found.**. Therefore, from the estimated thickness derived from the kinetic data and the etch depth calculated from SRIM, it is possible to determine whether the oxide metal interface has been reached during the profiles.

Table 4.5 Calculated oxide thickness values for all of the uranium experiments. The total time includes the exposure to both $D_2{}^{16}O$ and $H_2{}^{18}O$. This value can then be compared to the etch depths of SIMS analysis.

Temperature (°C)	Water	Exposure time (hours)	Time to grow 1 µm UO_2 (hours)	Thickness of UO_2 (µm)
69.54	$D_2{}^{16}O$	414	24.3	17.04
-	$H_2{}^{18}O$	-	-	-
Total				**17.04**
57.37	$D_2{}^{16}O$	439	56.8	7.73
56.85	$H_2{}^{18}O$	440	53.3	8.26
Total				**15.98**
45.00	$D_2{}^{16}O$	179	102.5	1.75
45.56	$H_2{}^{18}O$	165	35.6	4.63
Total				**6.83**
21.98	$D_2{}^{16}O$	8607	906.1	9.50
27.98	$H_2{}^{18}O$	1801	98.5	18.29
Total				**27.79**

Table 4.6 Etch depths calculated using SRIM, a sputter yield of 4.65 was used.

Average Temperature (°C)	Mode of SIMS	Length of depth profile (seconds)	Gun current (nA)	Magnification	Etch Depth (µm)
69.54	positive	3019.0	3.1	x5000	11.6
	negative	3901.0	3.1	x3000	5.4
57.17	positive	1801	3.1	x5000	6.9
	negative	736.0	3.1	x2000	0.5
45.28	positive	3087	3.1	x5000	11.8
	negative	7208	3.1	x2000	4.6
24.98	positive	11655	3.1	x5000	44.6
	negative	8534	3.1	x5000	32.7

However, as shown by the estimate of oxide thickness (Table 4.5), all of the experiments suggest that the oxide is no longer coherent and is instead within the spallation region, >0.05 µm[65]. This is evidenced by the loose black oxide seen on all of the samples. The thickness can therefore only be used as a very rough estimate and not treated quantitatively. More accurate

thickness measurements could be undertaken directly using atomic force microscopy (AFM) or FIB measurement of a cross section.

With a surface that has undergone spallation, the oxide distribution and thickness is likely to be varied. This means that during depth profiling of different regions on the same sample, the oxide intensities and compositions may vary. Even for a coherent oxide there would be a non-uniform oxide thickness which would mean that profiles collected on the same sample may show significant variability in oxide ion yield.

It must be noted that due to the use of the hydrogen and oxygen isotopes at the same time there is the possibility of overlapping species (these were highlighted in table 3.7). An assumption is made as to which species is more likely to be present based on sensitivity values, however there is a strong caveat over the data that further analysis would be required to accurately determine the oxygen isotopes and any exchanges that take place. One possible way to overcome this would be to only investigate one isotope at a time, such as $H_2{}^{16}O$ then $H_2{}^{18}O$ or $H_2{}^{16}O$ then $D_2{}^{16}O$.

Figure 4.21 shows the negative depth profile and the percentage oxygen fractions from this profile for the experiment at 45 °C and 41.47 mbar. From the depth profile (figure 4.21a) it can be seen that there is a clear oxygen peak, with the dominant oxygen ion as O-16. The O-18 ion peak is present in the same region but with a much lower intensity. The percentage profile of oxide intensity and relative isotope ratios is shown in Figure 4.21b. It shows approximately a 70:30 ratio of oxygen-16 to oxygen-18. After approximately 2000 s (depth ~1.27 µm) the majority of the oxide intensity has diminished to <10% and after 4000 s (depth ~2.55 µm) the oxygen intensity is virtually zero, suggesting that the depth profile is through the oxide. From Table 4.5 an estimated oxide thickness for this experiment based on the reaction rate was 6.83 µm.

Figure 4.22 shows a depth profile in positive mode for the uranium experiment at 45.00 °C and 41.47 mbar. From this profile it can be seen that the oxides containing O-16 and O-18 ions are nearly identical throughout the profile. There are clear steps/regions of oxide in the

profile, as the coupon had undergone spallation. It is likely that these peaks are due to different thicknesses of oxide as the profile etches deeper into the coupon.

a)

b)

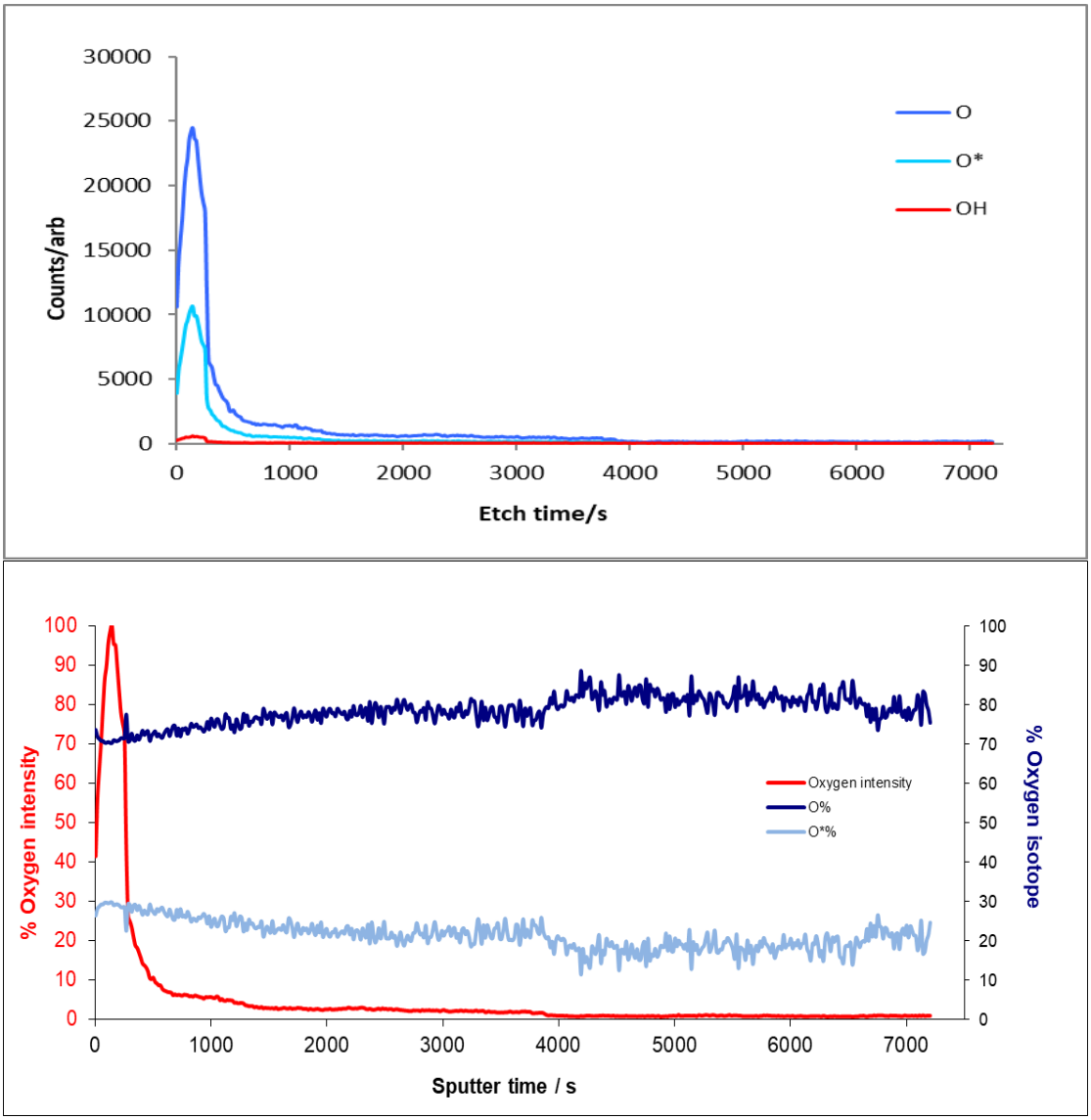

Figure 4.21 SIMS data for 45 °C 41.47 mbar experiment, a) negative depth profile, b) % oxygen fractions calculated from the negative depth profile.

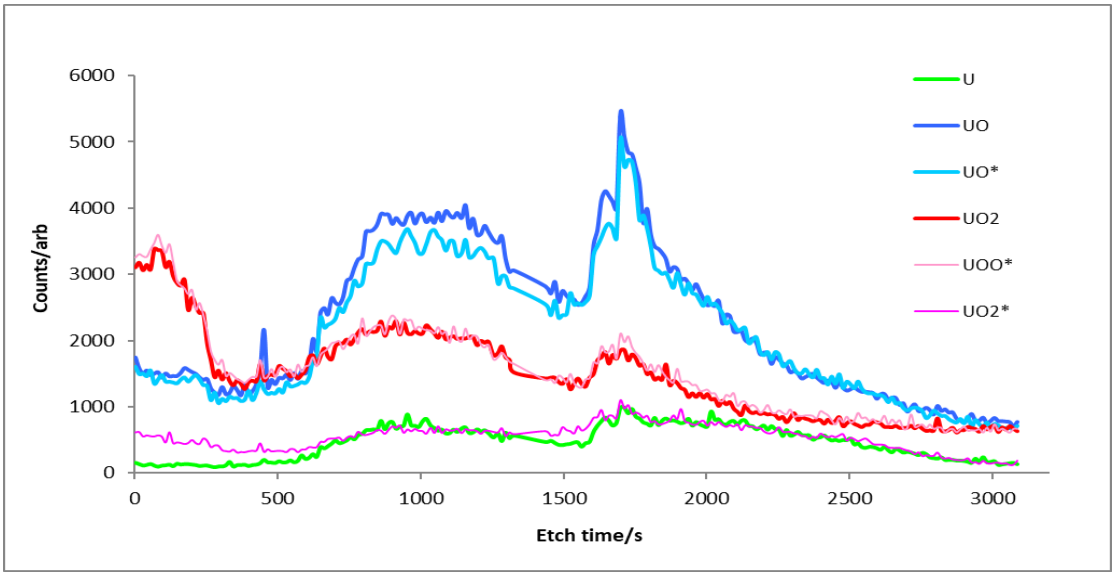

Figure 4.22 Positive depth profile of uranium experiment at 45 °C and 41.47 mbar.

Figure 4.23 uses the data from the depth profile in figure 4.22 to construct profiles showing the % oxide fractional composition as a function of oxygen isotopes (figure 4.23a) and oxygen containing molecular ions (figure 4.23b). From figure 4.23a it can be seen that O-16 is the dominant ion with ~60% however between 2000 and 2500 second etch time the profiles move closer to 50:50 before returning back to 60:40 with O-16 dominating again. This etch time equates to a depth of 7.6 -9.5 µm. According to the estimated oxide thickness (table 4.5), this depth should be through the oxide-metal interface. $H_2{}^{18}O$ was the second water vapour exposure. Therefore a rise in O-18 at the oxide-metal interface, suggests that anionic diffusion species is occurring with the oxygen containing species, diffusing through to the metal, which conforms with previous studies[74]. From figure 4.23b it can be seen that the profiles for UO and UO* are the same and there appears to be a change in oxide composition from UO_2/UOO* to UO/UO* at 500 second etch time which equates to 2 µm in depth. Near the end of the profile a possible second crossover can be seen, with the oxide looking to revert back to UO_2/UOO*.

Figure 4.24 shows SIMS data for the uranium experiment at 21.98 °C and 18.63 mbar. Figure 4.24a shows a depth profile in positive mode; Figure 4.24b presents the % fractional composition of the oxygen isotopes and figure 4.24c shows the % fractional compositions of the individual molecular ions. In figure 4.24a it can be seen that the UO ion has the highest intensity, followed by U and UO_2* and UO_2. The UO_2* is replaced by UO_2 at approximately

1800 seconds. Figure 4.24b shows that O-16 is the dominant oxygen isotope throughout the profile with UO the dominant species in figure 4.24c. In figure 4.24c a change over from UO_2* to UO_2 can be seen to occur at 1800 seconds and then possibly reverting back at 11000 seconds.

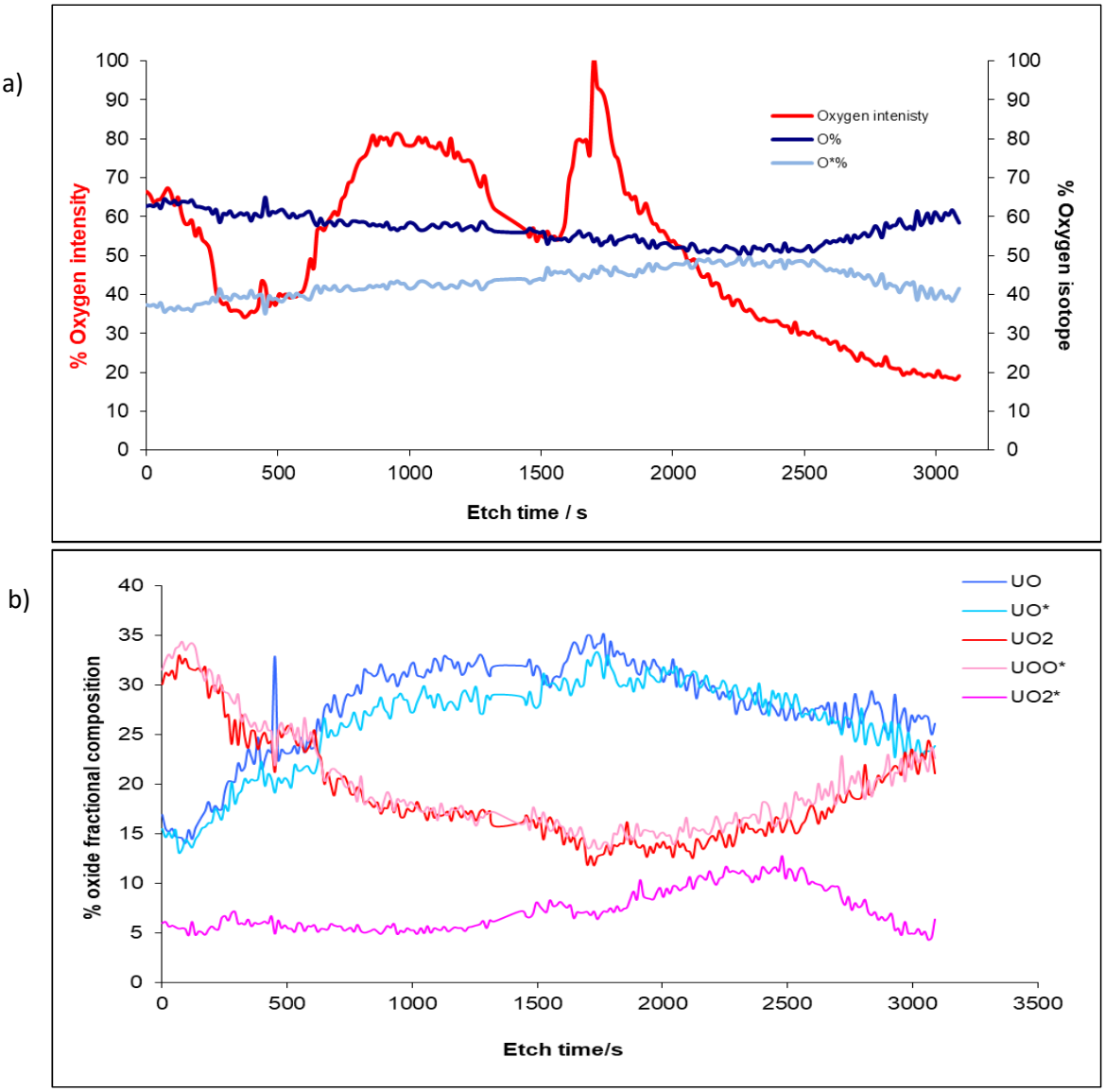

Figure 4.23 Profile showing % fractional composition for the uranium experiment at 45 °C and 41.47 mbar using data from the positive depth profile in figure 4.22, a) with respect to oxygen isotopes, b) with respect to molecular ions of interest.

Figure 4.25 shows a negative SIMS depth profile for the uranium experiment at 30 °C and 30 mbar. Figure 4.25a shows a depth profile in negative mode and figure 4.25b presents the % fractional composition of the oxygen isotopes. It can be seen that the dominant ion in the negative profile is O-16 and this is more evident in figure 4.25b where the % fractional composition of oxygen-16 is approximately 70-80%.

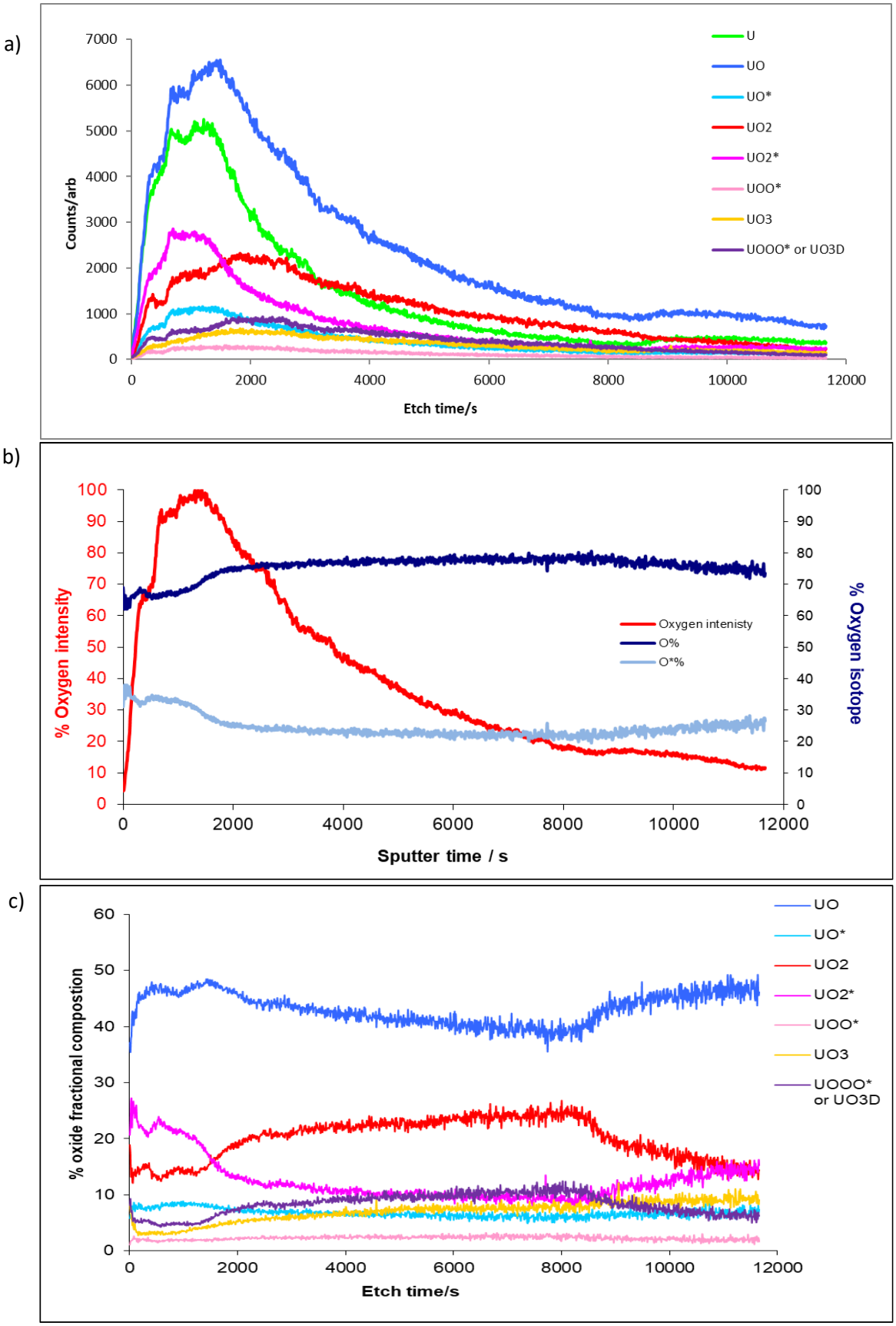

Figure 4.24 Uranium experiment at 21.98 °C 18.63 mbar experiment, a) positive depth profile, b) % fractional composition with respect to oxygen isotopes, c) % fractional composition with respect to molecular ions of interest.

a)

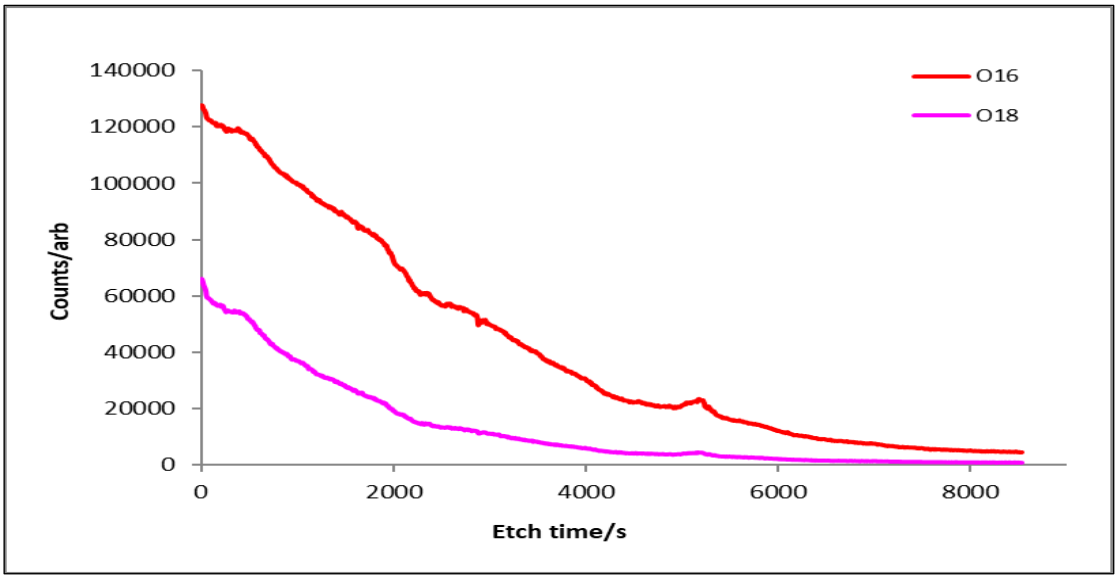

b)

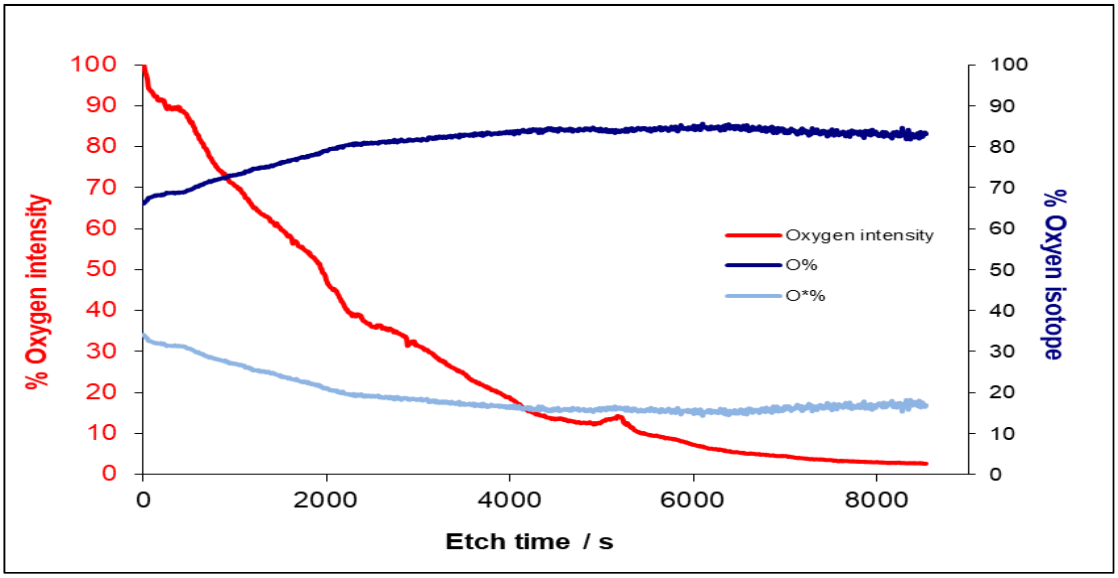

Figure 4.25 Uranium experiment at 30°C 30mbar experiment, a) negative depth profile, b) % fractional composition with respect to oxygen isotopes

From the oxide thicknesses calculated and using etch rates calculated using SRIM[68], see table 4.6, the majority of depth profiles remain within the oxide, meaning that the oxide-metal interface is never reached. Even for profiles where the oxide-metal interface should be detected (based on the thickness estimate) a clean interface is unlikely. The oxides are very thick and therefore SIMS analysis is challenging. As the surface is etched away eventually there will be interference from the walls of the etched region and the emitted secondary ions. The deeper you go the less clean the signal becomes with regards to the buried interfaces and the ion yield (to the detector) decreases because of ion collision with the trench walls (Figure 4.26).

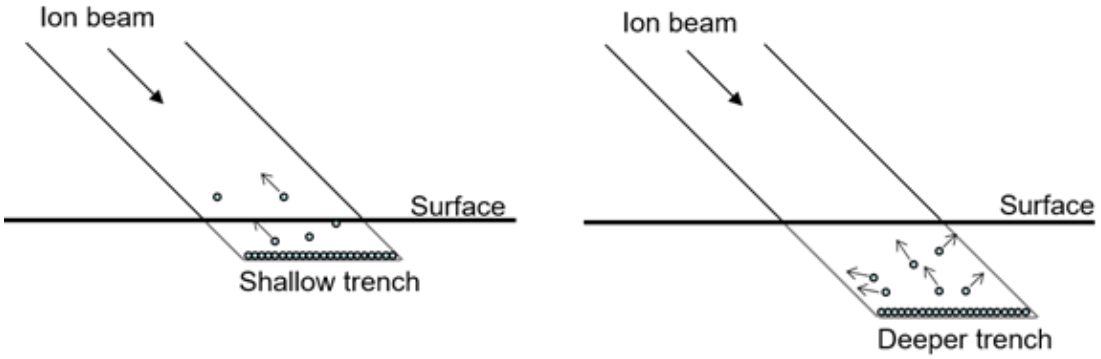

Figure 4.26 Schematic describing how deeper etching promotes surface collisions with the trench walls, thus effecting the ion yield.

The chance of detecting any hydride is limited as this is expected to be located near to the oxide metal interface. Typically, a beam current of 3nA is applied to the surface in order to etch through the thick oxide. This means that, if hydride was present, it would be virtually impossible to see using these SIMS parameters. In order to investigate hydride, a much smaller beam current would be required and therefore a much thinner oxide and thus shorter exposure times would be desirable.

The profiles show mixed oxides containing both O-16 and O-18 species. Therefore, deducing relevant mechanistic information is challenging. The exposures were administered sequentially and over long exposure lengths. Therefore, it is possible that there may be a mixture of oxide products and possibly dissociated oxygen ions on the surface that contribute to the SIMS depth profiles. The contribution of ^{16}O versus ^{18}O can be compared to the water vapour exposure times of $D_2{}^{16}O$ and $H_2{}^{18}O$ respectively (Table 4.7). It can be seen that in the 45.28 °C experiment where the exposure times are virtually equal, the SIMS depth profiles do not replicate this. Instead they show a greater proportion of ^{16}O within the system. The values for the 27.98 °C experiment are consistent with the exposure time percentages. A credible reason for the increased ^{16}O is residual air within the SIMS chamber as well as air exposure during transfer or storage in-between analyses. Due to reaction rates being faster, the experiments conducted at higher temperatures were stored for longer than the lower temperature experiments due to SIMS availability, therefore increasing the chance of ^{16}O contamination, while the experiment conducted at 27.98 °C was analysed straight away.

Table 4.7 Comparison of the % water vapour exposure time for the two waters studied (D_2O and $H_2{}^{18}O$) with the average % of each oxygen isotope (^{16}O and ^{18}O respectively) detected within the SIMS depth profiles.

Average Temperature (°C)	% water vapour exposure time		SIMS depth profile mode	Average % oxygen within SIMS depth profile	
	$D_2{}^{16}O$	$H_2{}^{18}O$		^{16}O	^{18}O
45.28	52	48	Positive	61	39
			Negative	79	21
27.98	83	17	Positive	81	19
			Negative	83	17

Oxygen-16 is the dominant species throughout the profiles in both negative and positive modes. In positive mode, variations in the oxide are more evident, with some clear changes in dominance of oxide stoichiometry and oxygen ions within the oxide. This was most clearly demonstrated in the 45 °C experiment, where the oxide is thickest. In this profile clear changes in oxygen ion intensity are seen and suggest a rise in oxygen-18 fraction as the oxide-metal interface is approached. This would be consistent with anionic diffusion which has previously been determined. The data indicate that new oxide forms at the oxide-metal interface via an oxygen containing species (OH^- and/or O^{2-}) diffusing inwards towards the metal (Figure 4.27).

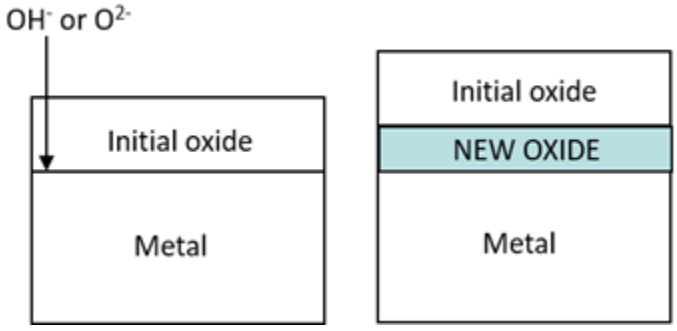

Figure 4.27 Schematic showing the location of new oxide at the oxide-metal interface for uranium

The experiments involving labelled species simultaneously in the water vapour plus oxygen experiments should show more clearly details on the mechanism, reacting species and any exchanges that occur.

4.3.2 Analysis after exposure to water vapour plus oxygen

There were two reaction schemes investigated –

$H_2{}^{18}O + {}^{16}O_2$

$D_2{}^{16}O + {}^{18}O_2$

The use of the labelled waters and oxygen will allow isotopic analysis of the SIMS depth profiles. Previous work has shown the oxide product (UO_{2+x}) to form from solely the water[2,3], solely the oxygen[22] or a combination of both water and oxygen[6].

Due to the difficulty in measuring accurate rates for the water vapour plus oxygen rates the kinetic data has not been used to provide an estimate of the oxide thickness for each of the samples. SRIM has been used in order to calculate sputter yields for uranium and oxygen in UO_2 (section 3.4.4). From this sputter yield a depth can be determined for each profile, as presented in Table 4.8.

Table 4.8 Etch depths calculated using SRIM.

Exposure	Mode of SIMS	Depth profile (seconds)	Gun current (nA)	Magnification	Etch Depth (µm)
$H_2{}^{18}O + {}^{16}O_2$	positive	5908	3.1	x3000	8.0
	negative	10394	3.1	x3000	14.0
$D_2{}^{16}O + {}^{18}O_2$	positive	14363	3.1	x3000	20
	negative	8597	3.1	x3000	12

Despite not being able to calculate the rates from the kinetic data, it is expected that the oxides will be significantly thinner than those produced from the water vapour only experiments because corrosion rates appeared markedly reduced.

4.3.2.1 $H_2{}^{18}O + {}^{16}O_2$ system

Figure 4.28a shows a depth profile in positive mode for the uranium experiment at 55.77 °C with $H_2{}^{18}O + {}^{16}O_2$, with figure 4.28b highlighting the oxide metal interface. Figure 4.28c presents the data from the SIMS in negative mode. In figure 4.28b at approximately 3500 second etch time (~4.9 µm depth) the oxide-metal interface can be seen. The metal peak is seen to be present throughout the profile (possibly fragmentation peak) but at low intensity. As the surface is etched away the metal peak starts to increase in intensity from a depth of ~2 µm onwards.

Figure 4.28c, the negative depth profile, does not show any changes in ion dominance, with O* and O*H having the highest intensity followed by O. These intensities decrease gradually over the full etch time of 10000 seconds.

The presence of hydroxyl ions (negative mode) and very low quantities of uranium hydroxide ions (positive mode) suggest that OH^- is involved in the corrosion mechanism. Uranium hydride was profiled in negative mode. However, the counts are extremely low compared to the oxygen ions and therefore very difficult to accurately confirm and identify.

In the positive SIMS oxide fraction composition profile with respect to oxygen isotopes (figure 4.29a), a change from O-18 to O-16 is seen after approximately 4500 seconds of etching; this correlates to a depth of 6 µm. The start of the change occurs after 3500 seconds which corresponds to the approach to the oxide-metal interface (figure 4.29a). In figure 4.29b, the positive oxide fraction composition with respect to molecular ions, the change in oxides can be seen clearly, with the intensity of UO_2* dropping and the intensities of both UO and UO_2 increasing. There is also an oxide containing both O-16 and O-18 detected – UOO* with a mass of 272. It is noted that this mass value could also be UO_2H_2 or UO_2D. However, the profile appears to mirror the one for UO_2 and not for UO_2H.

a)

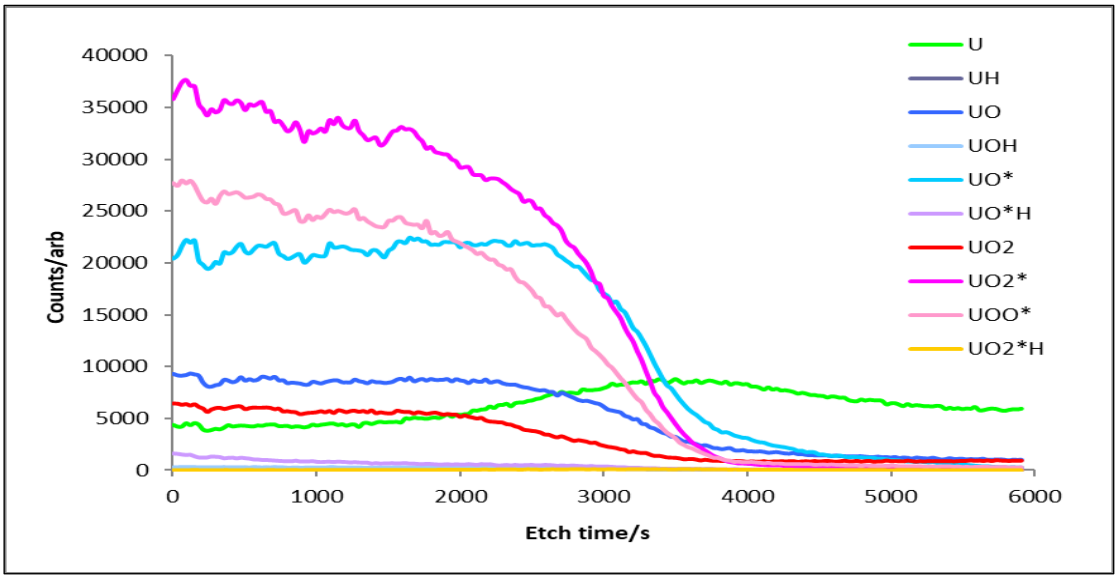

b)

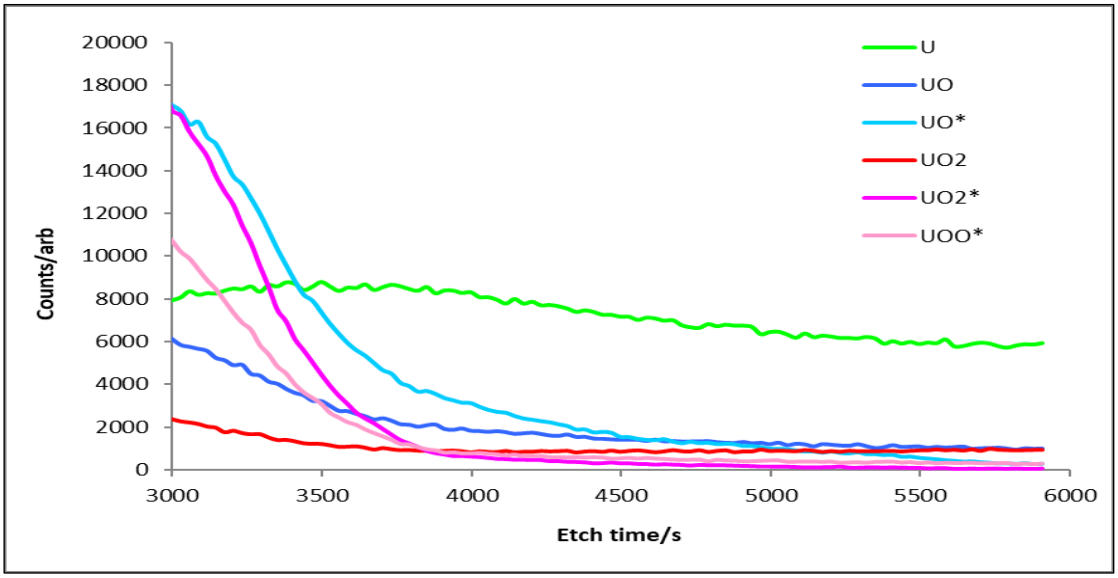

c)

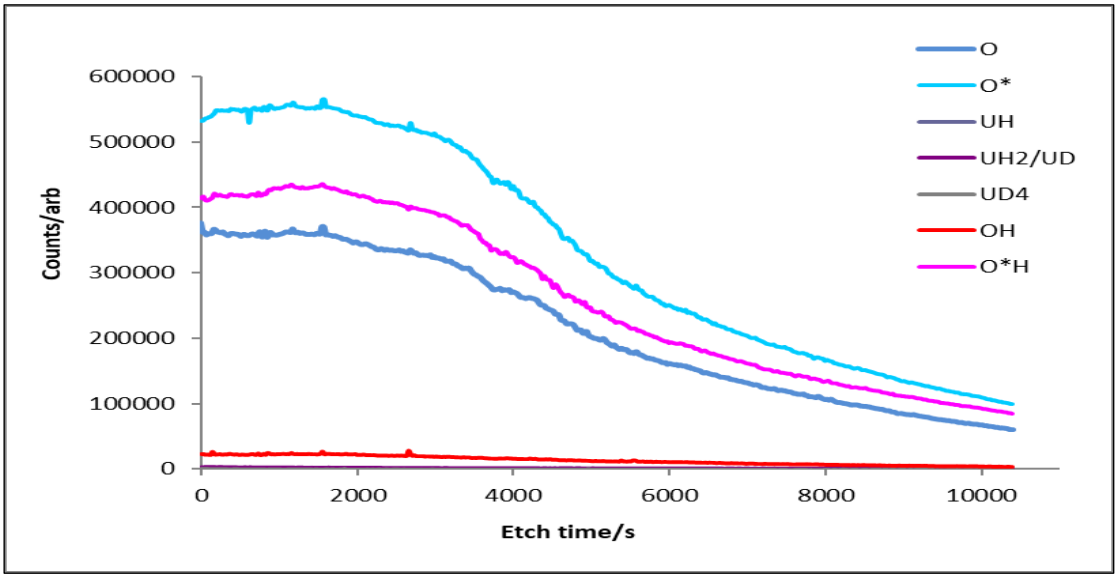

Figure 4.28 Depth profiles of the 55 °C $H_2{}^{18}O$ +$^{16}O_2$ experiment, a) positive mode, b) positive mode highlighting the oxide-metal interface 3000-6000 second etch time, c) negative mode.

a)

b)

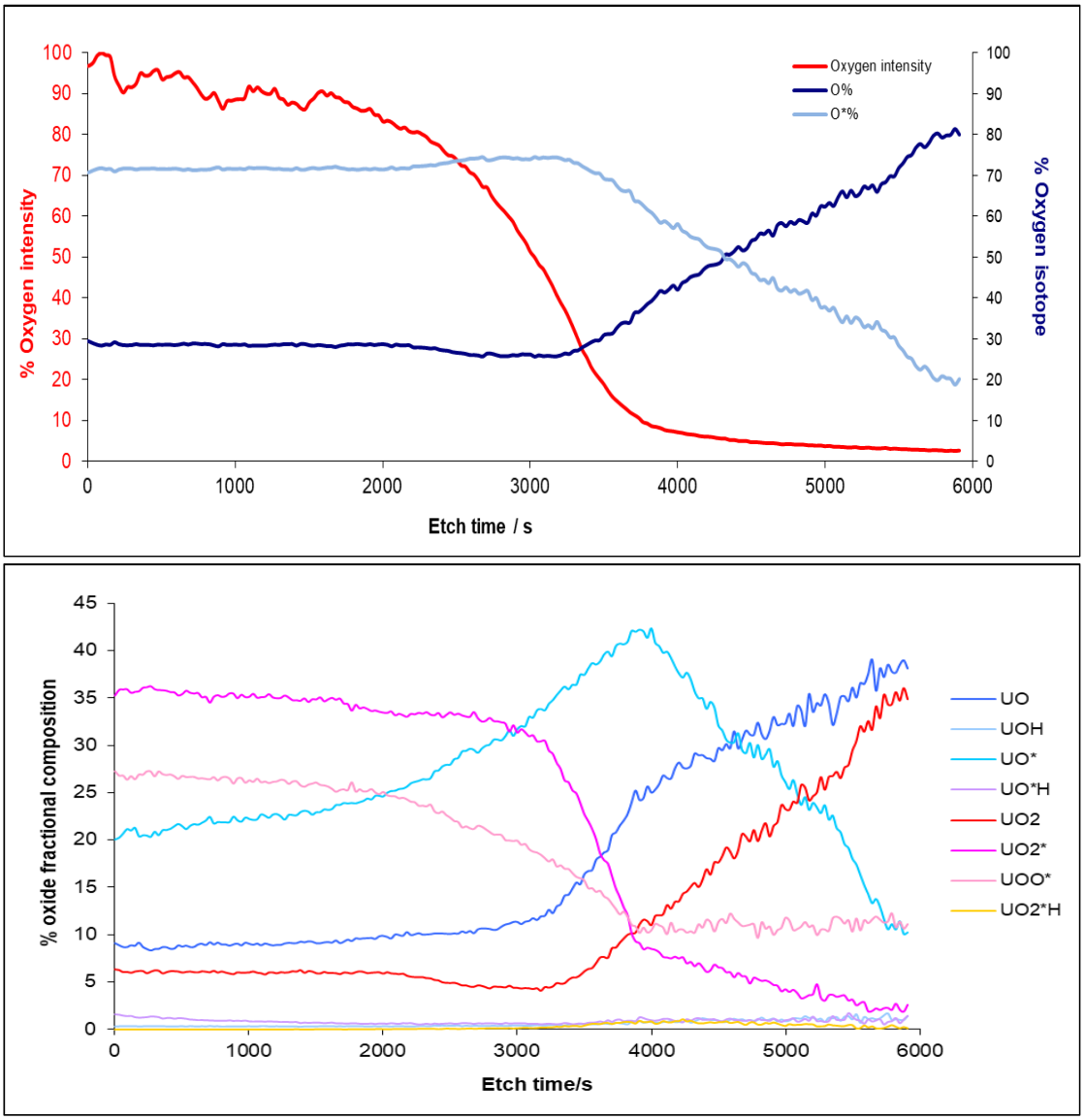

Figure 4.29 Positive profile for 55 °C $H_2{}^{18}O$ + $^{16}O_2$ experiment converted to % fractional composition for a) oxygen isotopes, b) oxide molecular ions of interest.

These changes in oxygen ion dominance suggest a number of things. The oxide species that dominate within the surface oxide all contain oxygen 18, suggesting that the oxygen (in this case oxygen-18) from the water is involved in the mechanism to form uranium oxide. As the oxide-metal interface is approached the O-16 oxides (both UO_2 and UO) increase in intensity.

The detection of this mixed oxide possibly suggests an exchange occurs during dissociation and possibly recombination of water and free oxygen. This recombination has been seen previously[2–5,74] and showed that in a mixed system (H_2O + O_2) the oxide formed from the

water with the residual head-space oxygen combining with the free hydrogen ions to form more water. Thus, water could then react with the uranium to form further oxide.

$U + H_2O + O_2 \longrightarrow UO_2 + H_2O$

The proportion of O_2 formed oxide increases with reaction time/depth which in turn leads to the isotopic identity of the reacting gas becoming lost and, therefore, the isotopic identity of the oxide.

a)

b)

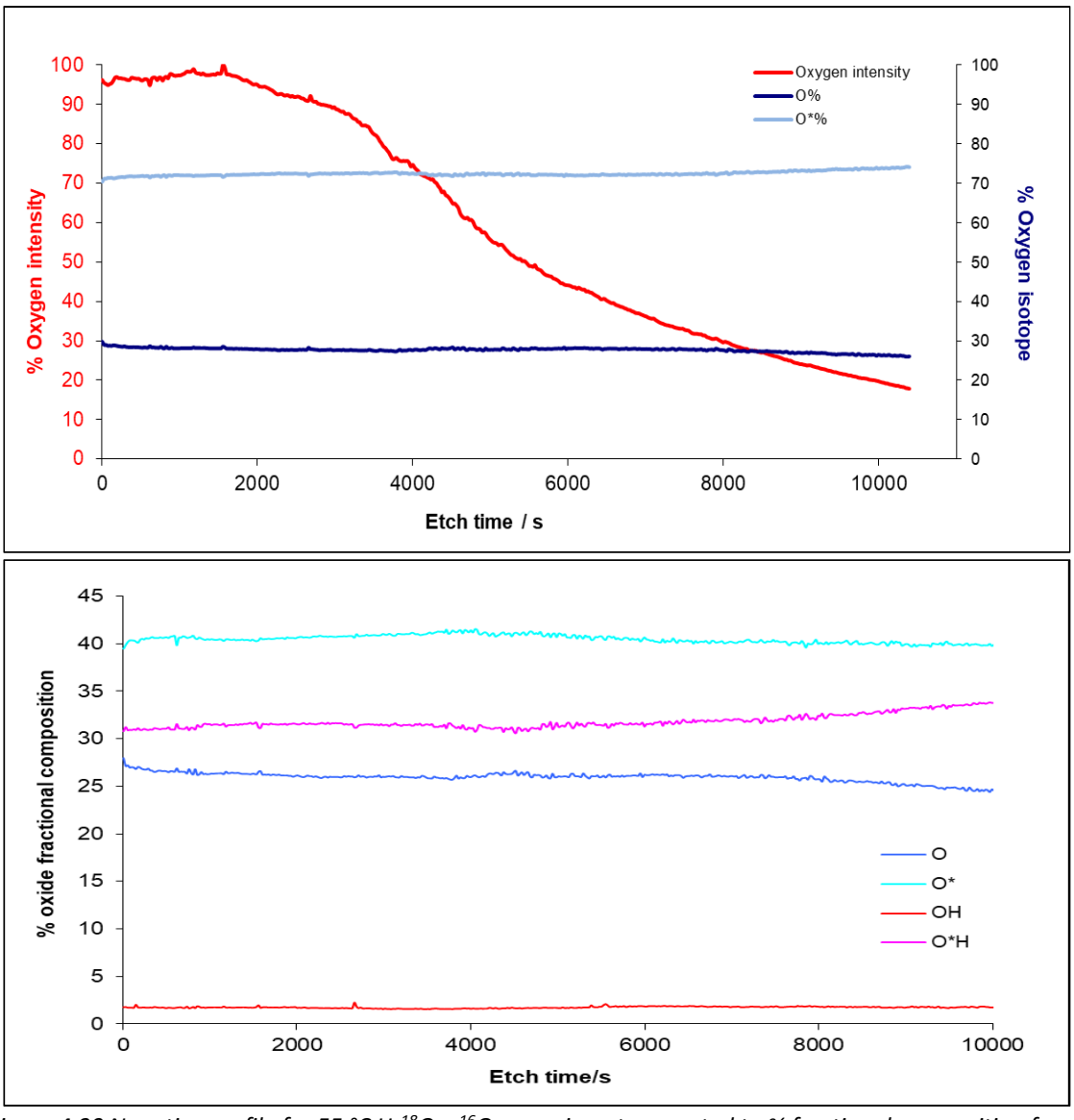

Figure 4.30 Negative profile for 55 °C $H_2{}^{18}O$ + $^{16}O_2$ experiment converted to % fractional composition for a) oxygen isotopes, b) oxide molecular ions of interest.

The negative SIMS oxygen (figure 4.30a) and oxide (figure 4.30b) fractional ion compositions show no such change. The O-18 ion remains dominant throughout the profile, again suggesting that the water is heavily involved in forming the reaction product. The O-16

content remains constant at ~30%, as O-16 is present in air and within the chamber it is not possible to confirm whether this is from the reaction/recombination discussed above or contamination. The reaction using labelled oxygen should help confirm this. The strong intensity of the hydroxyl ions from the water (containing O-18) helps suggest that OH^- is a key part of the mechanism.

4.3.2.2 $D_2{}^{16}O + {}^{18}O_2$ system

For the experiment with $D_2{}^{16}O + {}^{18}O_2$, a clear dominance in O-16 was seen in both negative and positive modes. Figure 4.32 shows the negative SIMS depth profile (figure 4.32a) and the % oxygen fractional composition (figure 4.32b). It can be seen from figure 4.32b, that approximately 95% of the oxide is formed from the O-16 ions, suggesting that the reaction is mainly via water. However, there is some O-18 present, which cannot be from the background air, meaning that oxygen may also be involved in the reaction. As discussed, H_2O recombination may occur which then leads on to oxidation of uranium with the $^{18}O_2$ oxygen.

Figure 4.33 shows a positive SIMS profile (figure 4.33a), the % oxygen fractional composition with respect to oxygen isotopes (figure 4.33b) and with respect to molecular oxide ions (figure 4.33c). As with the negative SIMS profile there is a clear dominance (90%) of O-16 ions. From figure 4.33c, it can be seen that the dominant oxide is UO_2. However, there is again a mixed oxide UOO* detected at the surface, alluding to the possibility of an exchange or some hyperstoichiometry at the outermost oxide surface, see figure 4.31.

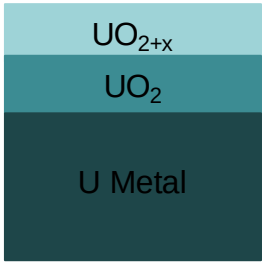

Figure 4.31 Schematic showing possibly hyperstoichiometric UO_{2+x} at the outermost oxide surface.

a)

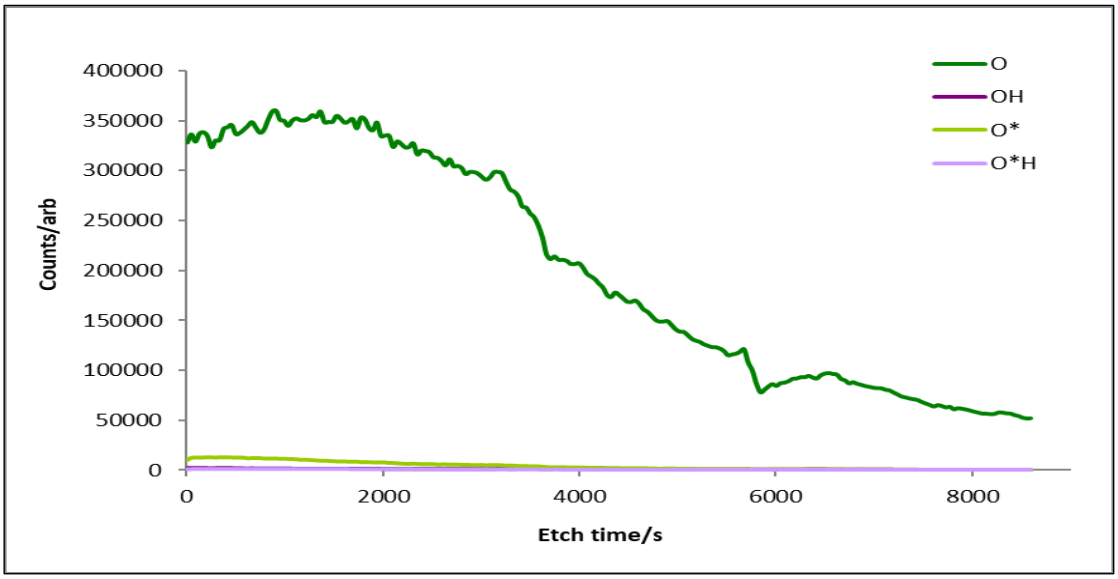

b)

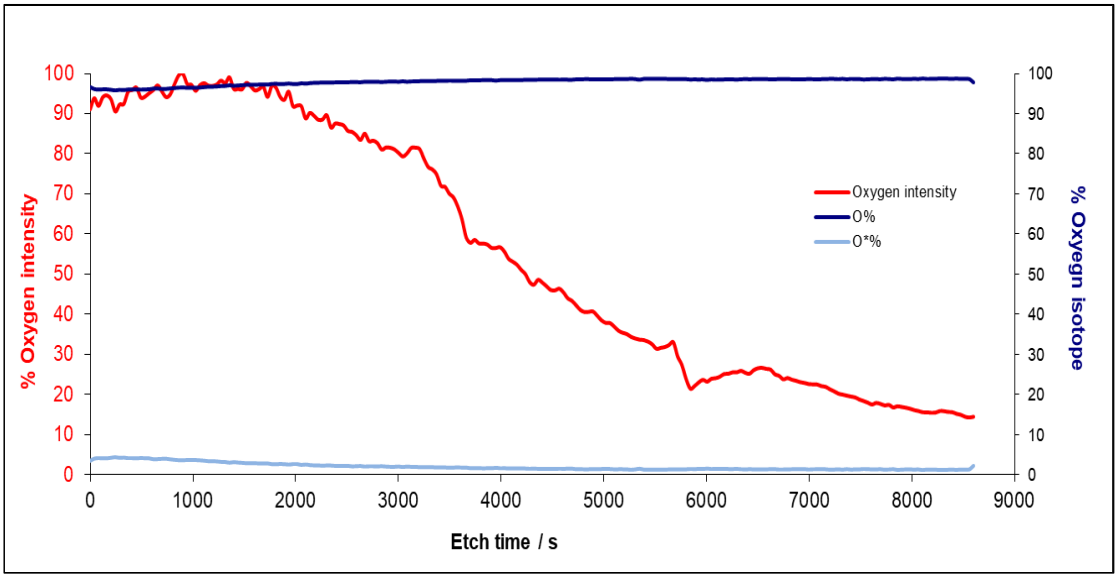

Figure 4.32 Uranium experiment at 55 °C 30 mbar $D_2{}^{16}O$ + 10 mbar $^{18}O_2$ experiment, a) negative depth profile, b) % fractional composition with respect to oxygen isotopes.

The mechanism for the water vapour plus oxygen reaction has been debated for a number of years. Isotopic studies[2,3,74] showed the oxygen in the reaction to be consumed via conversion to water (and not by formation of oxide). It was suggested that a strongly chemisorbed layer of oxygen makes the reaction rate independent of both oxygen and water vapour pressures. The water dissociates and the OH^- species diffuses to the oxide-metal interface to form oxide while the free oxygen is gradually transformed to water assisted by the catalytic nature of the oxide surface:

$$U + 2H_2{}^{18}O + {}^{16}O_2 \longrightarrow U^{18}O_2 + 2H_2{}^{16}O$$

a)

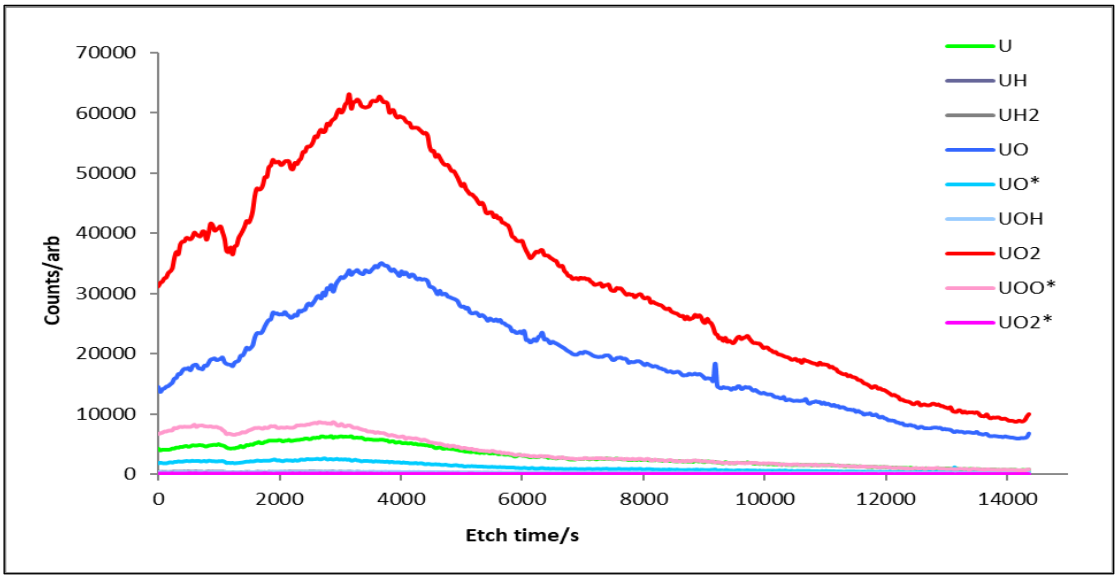

b)

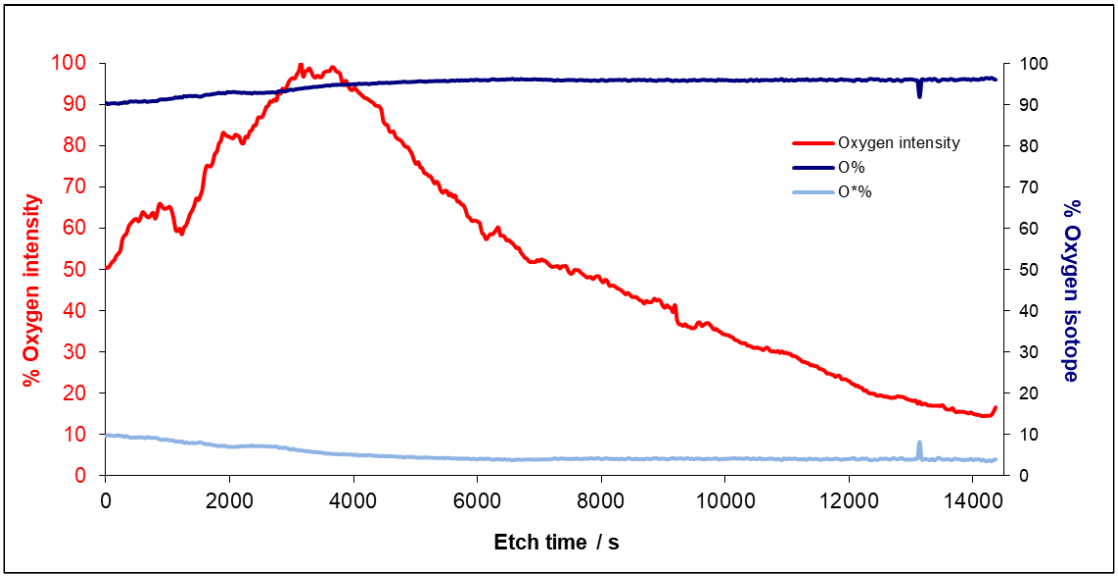

c)

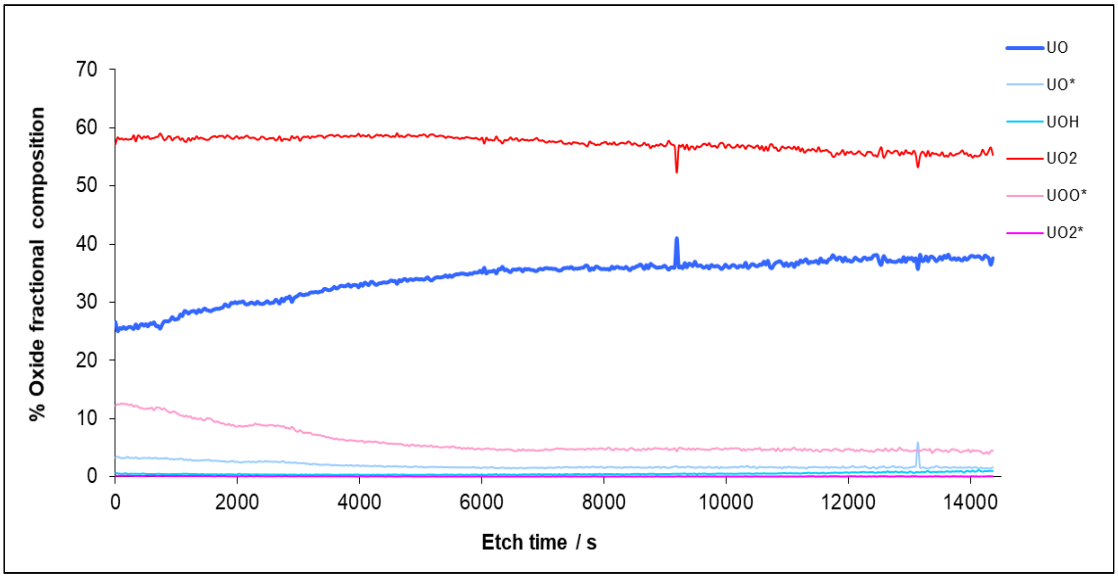

Figure 4.33 Uranium experiment at 55 °C 30 mbar $D_2{}^{16}O$ + 10 mbar $^{18}O_2$ experiment, a) positive depth profile, b) % fractional composition with respect to oxygen isotopes, c) % fractional composition with respect to molecular oxide ions.

McGillivray[6] showed using SIMS on mixed systems (on much shorter exposures) that both O-18 and O-16 were involved and suggested simultaneous diffusion of both OH^- and O^{2-} to the oxide metal interface. Similar to Baker[2,3] the inhibition in rate was due to preferential adsorption of oxygen on the surface.

The data from this study show both O-16 and O-18 oxide products suggesting that both water and oxygen are involved in some way. There are some hydroxyls and hydroxides seen, confirming that OH^- diffusion is part of the mechanism. An oxide containing both O-16 and O-18 is detected, suggesting that some form of exchange occurs between the oxygen species. The recombination of water from production hydrogen with the surface adsorbed oxygen would explain the presence of both oxygen species within the oxide.

4.3.3 Summary

Some of the SIMS depth profiles show clear definitive oxide structure while others show oxides intermixed with one another. The analyses did not provide conclusive mechanistic information due to the thickness of the oxides, in most cases, preventing the oxide-metal interface being reached during the profiles. The thickness of the oxide also limited the ability to look for hydride. If present it would be expected to be located at the oxide-metal interface. Analysis on thin oxides using a more sensitive technique such as atom probe tomography should provide more insight into the mechanism.

In the water vapour plus oxygen reaction, oxides containing both species were detected. This result aligns with the proposed mechanism by Baker[2,3] and Harker[74], of water recombination occurring, which leads to the depletion of oxygen while the concentration of water remains constant. The recombined water (containing oxygen from O_2) then reacts with uranium at the oxide-metal interface to produce new oxide.

4.4 APT analysis

APT utilises a needle-shaped specimen with a tip radius of between 20 nm and 100 nm. The technique exploits the effect of an intense electric field upon which is superimposed an ultrafast voltage or laser pulse, for the highly controlled field evaporation of individual ions from the surface of the specimen. Each detected ion can be directly correlated to the pulse which caused

its evaporation from the tip, enabling measurement of the time-of-flight and, hence, the chemical identification of the (molecular) ion. From the position at which each ion strikes the detector and the sequence of evaporation, a straightforward reverse-projection algorithm can be used to precisely reconstruct the original location in three-dimensions (3D) within the specimen. Ultimately, a 3D atom-by-atom reconstruction of the specimen incorporating tens-to-hundreds of millions of atoms is generated, enabling high resolution elemental mapping.

In this study APT was used to examine the initial oxidation of uranium after exposure to water vapour (in the form of air or $D_2{}^{16}O$). The corrosion is limited to provide thin oxides for analysis in an effort to identify hydride formation at the oxide-metal interface.

4.4.1 Uranium exposed to air

Figure 4.34a shows an example APT reconstruction for a uranium tip, featuring a surface-oxidised region of the material followed by the sub-surface (unreacted) bulk metal region. The morphology of the oxide-metal interface was uneven and undulated in all specimens studied.

In Figure 4.34b a 24 at.% UO_x isoconcentration surface is used to define the position of the oxide-metal interface. UO_x is defined as any complex ion containing both uranium and oxygen regardless of stoichiometry, whilst the 24% value was chosen as it gave the most defined interface shape. Figure 4.34b also indicates the presence of two distinct oxide features; the surface oxide marked as 1 and an incidental oxide feature marked as 2.

Oxide 1 was formed on the coupon during the planned exposure time prior to tip formation, whereas oxide 2 was formed during tip formation. When the liftout is conducted, the dualbeam is required to open in order to allow the pre-fabricated silicon tips to be loaded (see figure 3.7c and figure 3.7d). It is possible that during this step the liftout of material is exposed to the atmosphere and therefore some unintentional oxidation occurs along the surface and sides of the liftout. As the tip shown in figure 4.34 is from the edge of the liftout the location of the incidental oxide is concurrent with this incidental oxidation.

There is also the possibility of further atmospheric exposure during transportation from the dual beam in Bristol to the atom probe instrument in Oxford. However, this would be more uniform forming a thin layeraround the entire surface of the tip.

An apparent increase in uranium hydride content is observed at the oxide-metal interface, as highlighted by the light blue 0.5 at.% UH isosurface plotted in Figure 4.34(c).

The change in chemical composition across the surface metal-oxide interface labelled '1' in Figure 4.34b has been characterised using a proximity histogram (proxigram) analysis, shown in Figure 4.35. Having defined a 3D surface, in this case using the UO_x isoconcentration surface in Figure 4.34b, the proxigram measures the chemical composition as a function of the perpendicular distance from this 3D surface.

Due to the tendency for complex ions of oxides to vary in oxidation state depending on where they are observed on the tip, Figure 4.35 decomposes the proximity histogram into individual elemental contributions rather than complex ions. The decomposed profiles show a concentration of approximately 95 at.% U in the bulk metal, accompanied by small amounts of hydrogen and oxygen. Near the oxide-metal interface the oxygen content rises rapidly from virtually zero to around 50 at.% over a distance normal to the defined interface of approximately 3 nm. At around 5 nm above the interface the oxygen content plateaus at approximately 60 at.% oxygen, which is close to stoichiometric. This is consistent with the SIMS data from Baker[2,3], who report oxidation involving water vapour as producing oxides of lower stoichiometry than the hyperstoichiometric oxides (*i.e.* UO_{2+x}) formed in pure oxygen.

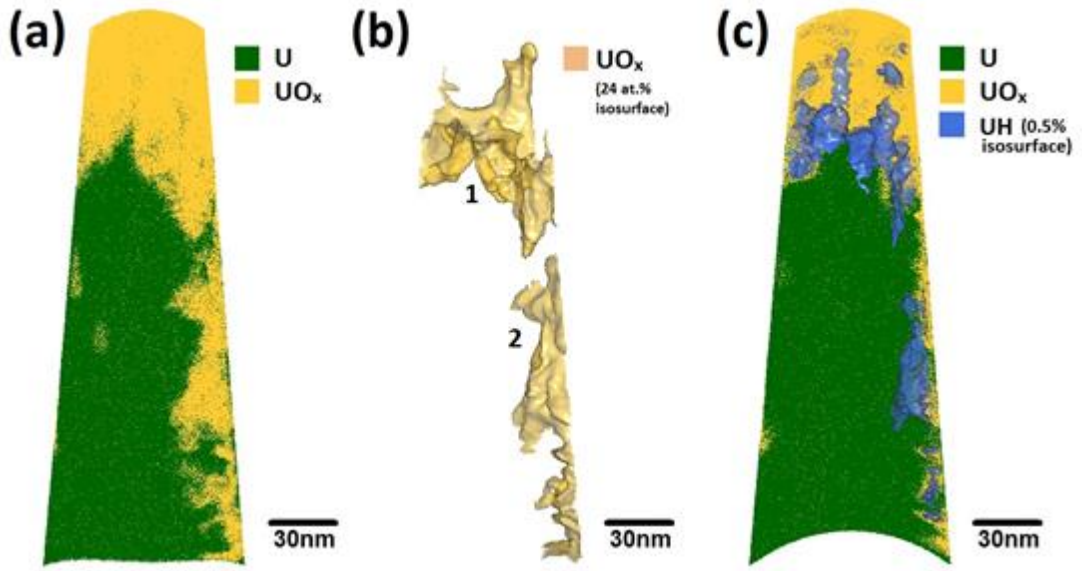

Figure 4.34 (a) An atom probe map of a tip extracted from a uranium sample exposed to air for approximately 1 hour, showing U and UO_x ions in green and orange, respectively. The original surface of the uranium is located at the top of the specimen, (b) a 24 at.% UO/UO_2 isosurface indicating two oxide regions on the specimen; (marked 1) at the original surface and (marked 2) generated on the side of the specimen during sample preparation, (c) the same atom map as in (a), but with an isoconcentration surface indicating 0.5 at.% UH in blue to reveal the locations where hydride ions are detected. For (c), the front face of the dataset is cropped away to show a cross-section

Most interestingly, the data demonstrates that there is a significant increase in the hydrogen content at the interface between the metal and oxide regions. This hydrogen signal is fully accounted for from hydrogen combined within the uranium hydride molecular ions observed at 119.5 Da (UH^{2+}) and 239 Da (UH^+). The initial assignment of UH^+ molecular ions as from uranium hydride, which has the formal stoichiometry of UH_3, is substantiated using previous time-of-flight secondary ion mass spectrometry (ToF-SIMS) and density functional theory (DFT) evidence[76]. The DFT suggests that molecular UH_x cations where $x > 1$ suffer from instability and are thus expected to decompose within the time-frame of ToF-SIMS measurements (which are comparable to APT measurement time-frames). The ToF-SIMS confirms that only UH^+ cations are evidenced, while heavier molecular ions are observed only as anions (*i.e.* UH_x^-, where $x \geq 2$). Anions of this type are not observed in APT because of the strongly positive electric field that is applied to the specimens.

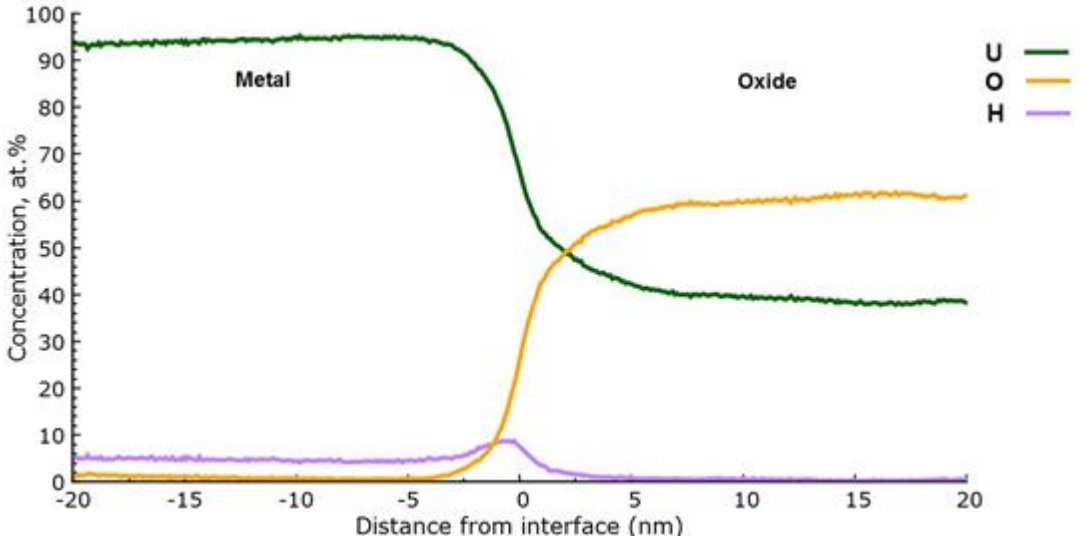

Figure 4.35 Proximity histogram of the surface oxide feature marked as 1 in Figure 4.34(b). All complex ions are decomposed into their constituent elements.

For the uranium samples analysed, the thickness of the hydride layer varied between 3 and 5 nm and the peak concentrations of UH molecular ions varied between 12 at.% and 20 at.%. There was no hydride signal present within the oxide layer. However, there was around 5 at.% H from UH ions within the bulk metal matrix. This is certainly an artefact due to hydrogen contamination occurring from the analysis chamber during the time-frame of the experimental measurement. This effect is most noticeable in the metal, rather than the oxide, due to the increased reactivity of the fresh metal surface as it is continuously exposed during successive APT tip profiling measurements, and the fact that after the H is adsorbed the UH ions are more readily evaporated than U. However, since APT does not suffer from the matrix effects which can limit the reliability of SIMS measurements at interfaces, one must conclude that the increase in the hydride molecular ion intensity at the oxide-metal interface is strongly indicative of the presence of a genuine discrete hydride layer, since its intensity is considerably higher than the 5 at.% background contamination evidenced within the bulk metal.

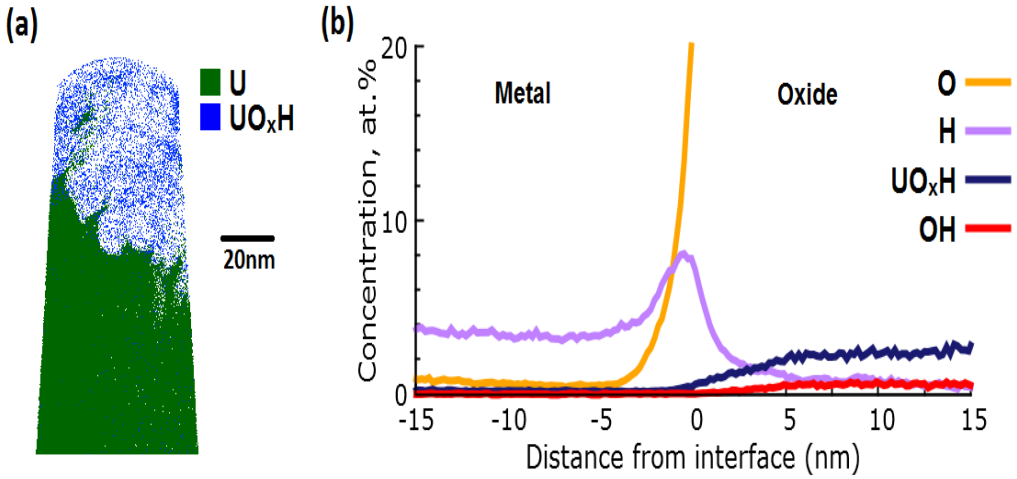

Figure 4.36 (a) Atom map showing the location of uranium hydroxide ions in the same dataset shown in Figure 4.34, (b) a magnification of the proxigram across the metal-oxide interface for the same specimen, showing the distribution of UO_xH and OH species within the oxide.

The evidence of a hydride layer forming at the oxide-metal interface clearly suggests the involvement of hydroxyl ions in the oxidation mechanism, but does not definitively prove it. Figure 4.36 shows an atom map which reveals the location of hydroxyl species, together with a proxigram similar to that in Figure 4.35, but with the OH-related complex ion species ranged as separate signals to clarify their position relative to the decomposed O and H signals. The proxigram data in Figure 4.36b indicates hydroxyl content within the corrosion layer; from evidence at 17 Da (OH^+), 127.5 Da (UOH^{2+}), 255 Da (UOH^+), 135.5 Da (UO_2H^{2+}) and 271 Da (UO_2H^+). This hydroxyl content is evenly distributed throughout the oxide, but is absent at the interface with the metal where the hydride signal is observed, suggesting that the hydroxyl species decompose at the hydride layer. This result agrees well with the basic mechanism proposed by Baker[2,3] in which both hydride and oxide are formed from hydroxyl species which diffuse through the oxide. This is also in line with the hydroxyl and hydroxide results found by SIMS (figures 4.28-4.30).

Even within the ultra-high vacuum (UHV) of the LEAP instrument (around $2x10^{-11}$ mbar), significant quantities of hydrogen, in the form of water, hydrocarbons and hydrogen molecules, exist on the analysis chamber walls, sample and in the gas phase. Therefore, there is the possibility that some of the hydride detected is due to a reaction whilst within the chamber and not from the reaction with air. As with the SIMS analysis the use of deuterated water was used to provide an unambiguous signal to locate where the hydrogen ultimately

resides in a material since it does not naturally occur in significant quantities and so any D-containing peaks in the mass spectrum can be positively attributed to the corrosion mechanism being tested[77].

4.4.2 Uranium exposed to D_2O

Figure 4.37 compares the mass spectra for the two exposures (air and D_2O), specifically the difference between the U^{2+} ion and its hydrides and deuterides. In the specimen exposed to air only, the ^{235}U and ^{238}U ions are observed at 117.5 Da and 119 Da, respectively, as well as the monohydride complex ions at 118.0 Da and 119.5 Da.

For the uranium exposed to D_2O vapour, a distinct peak is observed at 120.0 Da that is not present in the previous spectra, which we attribute to uranium deuteride. In addition, there is a small correlated feature at 118.5 Da that is associated with ^{235}UD. This is a clear indication that despite several weeks of storage under inert gas between the preparation and analysis of these specimens, some deuterium remains in the material. This finding necessitates that the deuterium is chemically bound, and therefore further supports our assignment of the feature to be UD_3 (the deuterated uranium hydride).

Figure 4.38 shows the atom map for a uranium specimen exposed to D_2O vapour. A corrugated oxide structure similar to that shown in Figure 4.34 is observed. As before, a 24 at.% isosurface of both UO and UO_2 complex ions has been created and shown in Figure 4.38(b), with each distinct region labelled. Again two distinct features are seen: the surface oxide marked as 1; and an incidental oxide (defined again as the oxidation occurring due to atmospheric exposure during transportation of the tip to the atom probe instrument) marked as 2.

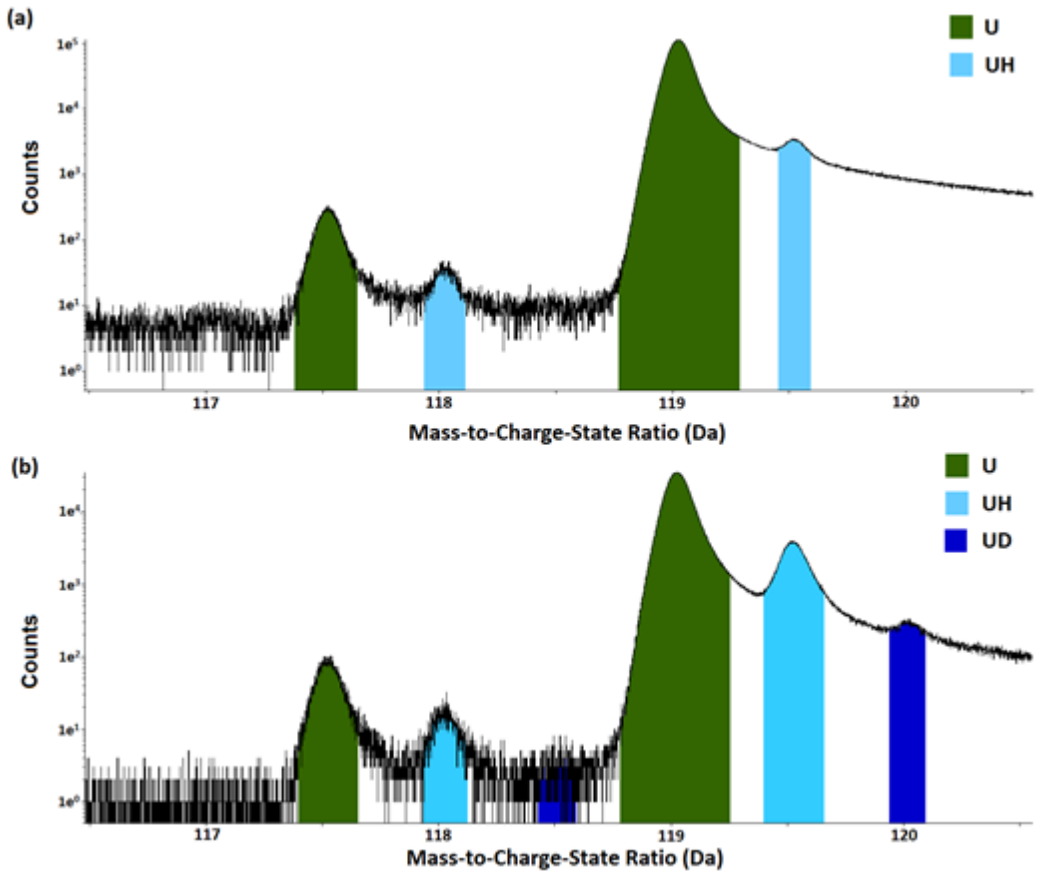

Figure 4.37 Comparison of the mass spectra (in log scale) magnified to concentrate on the U^{2+} ion and its respective hydrides and deuterides summed across the entire specimen for (a) the depleted uranium sample exposed to air under ambient conditions for one hour as shown in Figure 4.34 and (b) the uranium sample exposed to D_2O vapour as shown in Figure 4.38.

Figure 4.38(a) highlights the layer of uranium deuteride formed as part of the oxidation reaction with D_2O. The location of the deuteride is equivalent to that of the hydride revealed in figure 4.34. However, in these deuterium-labelled oxidation experiments, the deuteride at the oxide-metal interface can only have formed from the reaction with D_2O. This experiment therefore confirms the proposed hydroxyl driven mechanism by removing any possibility of an experimental artefact being responsible for the observed hydride layer.

Figure 4.39 shows the proxigram, in complex ion form, for the surface oxide-metal interface marked 1 in Figure 4.38b. As before, the overall morphology following water vapour oxidation is the same, an underlying pure U matrix, followed by an uneven metal-oxide interface decorated by a spike in hydride content, with a surface formed oxide layer increasing rapidly in oxygen content from 0 at.% ~2.5 nm below the interface up to approximately 60 at.% oxygen through the remainder of the oxide to the surface.

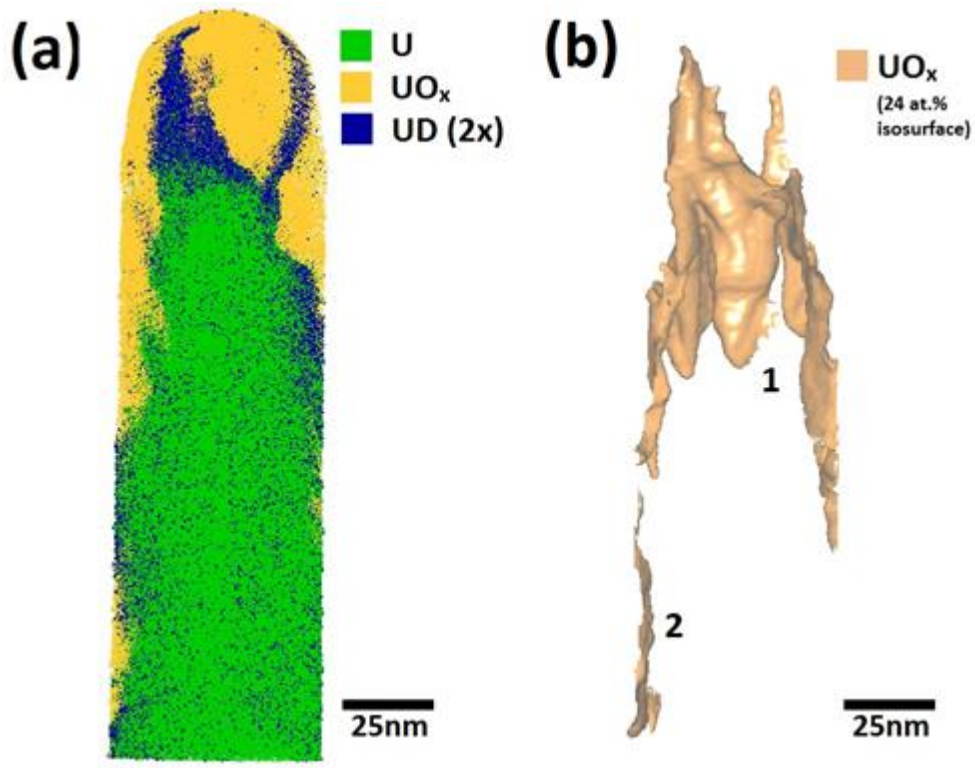

Figure 4.38 (a) Atom map for the uranium sample exposed to deuterated water for approximately 2 hours, highlighting the region of uranium deuteride. The original surface of the sample is located at the top of the specimen. The uranium deuteride molecular ions (in blue) are displayed at twice the size of the uranium and uranium oxide ions to clarify their position near to the oxide-metal interface, (b) 24 at.% UO/UO_2 isosurface used to calculate the proximity histograms in Figure 4.39.

The deuteride peak seen in Figure 4.39a is not observed in the proxigram shown in Figure 4.39c for the incidental oxide feature on the side of the tip, marked as '2' in Figure 4.38b and demonstrated by the deuterium ion intensity being indistinguishable from the background noise levels detected by the experiment. This evidence confirms our earlier hypothesis that this incidental oxide forms after the intentional oxidation exposure, lift-out and needle preparation, and probably occurs during the transport of the specimens to the atom probe instrument.

The measured UD intensity for the interfacial region reduces to background levels at around 5.5 nm below the interface, whilst the equivalent UH content continues into the metal matrix at a near-constant level of around 3 at.%. The strong localisation of the UD feature is further evidence that the constant, non-zero UH plateau in the metal is an artefact due to hydrogen contamination occurring during tip evaporation (*i.e.* during data collection). Moreover, the

localisation of the deuteride signal to the interfacial region supports the earlier hypothesis that the UH peaks observed in the ambient air oxidation experiments reveal a significant aspect of the corrosion mechanism occurring for uranium oxidation in the presence of water vapour.

The 120.0 Da and 240.0 Da peaks ascribed to UD match the location of the UH layer observed at the interface in the ambient air oxidation experiments extremely well. This result, confirmed by the comparison of proxigram data between figures 4.35 and 4.39, provides irrefutable evidence that the hydride layer at the metal-oxide interface is a real chemical feature, rather than an artefact of hydrogen contamination from the vacuum system.

The width of the UD layer was consistently 5 nm – 8 nm in thickness for all four of the specimens where the metal-oxide interface was successfully observed thus, slightly wider than the peak observed in the air exposed samples. However, it is unclear from the data presented here whether this apparent increase in the hydride layer thickness when deuterated species are present is significant, since the conditions employed (i.e. air compared to D_2O) cannot be considered as completely equivalent. However, it can be stated that the thickness of this hydride layer cannot increase indefinitely as a function of oxidation, since the SIMS investigations (section 4.3) and previous literature[6] have failed to reveal the presence of hydride even when examining heavily oxidised samples.

The interfacial deuteride feature observed in Figure 4.39 is accompanied by a corresponding hydride feature. Although this could be due to hydrogen contamination from the vacuum chamber, the relative concentrations of deuteride to hydride suggest several alternative explanations. This could be simple contamination of the D_2O source used in the deuterated water vapour experiments, since its purity was not specifically confirmed. However, it could also be a result of subsequent reaction with air, during transport between sample preparation and analysis. This could suggest that the hydride is being both consumed and regenerated as the reaction proceeds, and the observation of both deuteride and hydride within the same interfacial layer could reveal evidence of this continual regeneration process for the hydride layer.

The rate of uranium corrosion in water vapour environments is notably faster than that observed in dry oxygen or dry air, and the stoichiometry of the H_2O-formed oxide shows less divergence from that of pure UO_2. The hydride layer resides at the oxide-metal interface and likely imparts a physical separation of the oxide from the underlying bulk metal. Thus, for oxidation of uranium in water vapour environments the presence of the hydride layer must perform a fundamental function within the reaction mechanism, and hence accelerate the reaction kinetics compared to oxygen driven corrosion where no hydride layer is possible. The presence of hydroxyl content within the oxide, and the near stoichiometric oxide formed (without excess oxygen at interstitial lattice sites), strongly suggests that the hydroxyl ions are the oxygen source for the formation of additional uranium oxide.

If hydroxyl ions provide the oxygen source, atomic hydrogen will also be present as a free radical, which would readily establish a layer of hydride through reaction with the metal. As subsequent hydroxyl ions diffuse across the steadily expanding oxide layer, oxidation of the hydride must occur to generate new oxide at the hydride-oxide interface. This oxidation process would consume the hydride interfacial layer, and as the results here suggest a near constant, albeit thin, hydride layer, this layer must undergo continual regeneration from the highly reactive atomic hydrogen produced during the decomposition of OH species at the oxide-hydride interface. The mechanism for the regeneration of the hydride layer is not clear from this APT study. However, the factors controlling the thickness of the hydride will be dependent on this regeneration mechanism, and are probably determined by the competitive rates for the reaction of hydrogen free radicals to either (i) form molecular hydrogen or (ii) regenerate the hydride.

A further consequence of a near constant thickness hydride layer being maintained at the oxide-metal interface is that, as the oxidation reaction proceeds, excess hydrogen must be created at the oxide-hydride interface, as evidenced from gas phase data in pure water vapour reaction studies. The influence of this hydrogen continually flowing through the oxide, from the hydride-oxide interface to the surface, would be expected to maintain a reduced (*i.e.* certainly not hyperstoichiometric) oxide during the water-driven oxidation of uranium,

which is consistent with both the stoichiometry of the APT oxide layer and the observations of Baker[2,3].

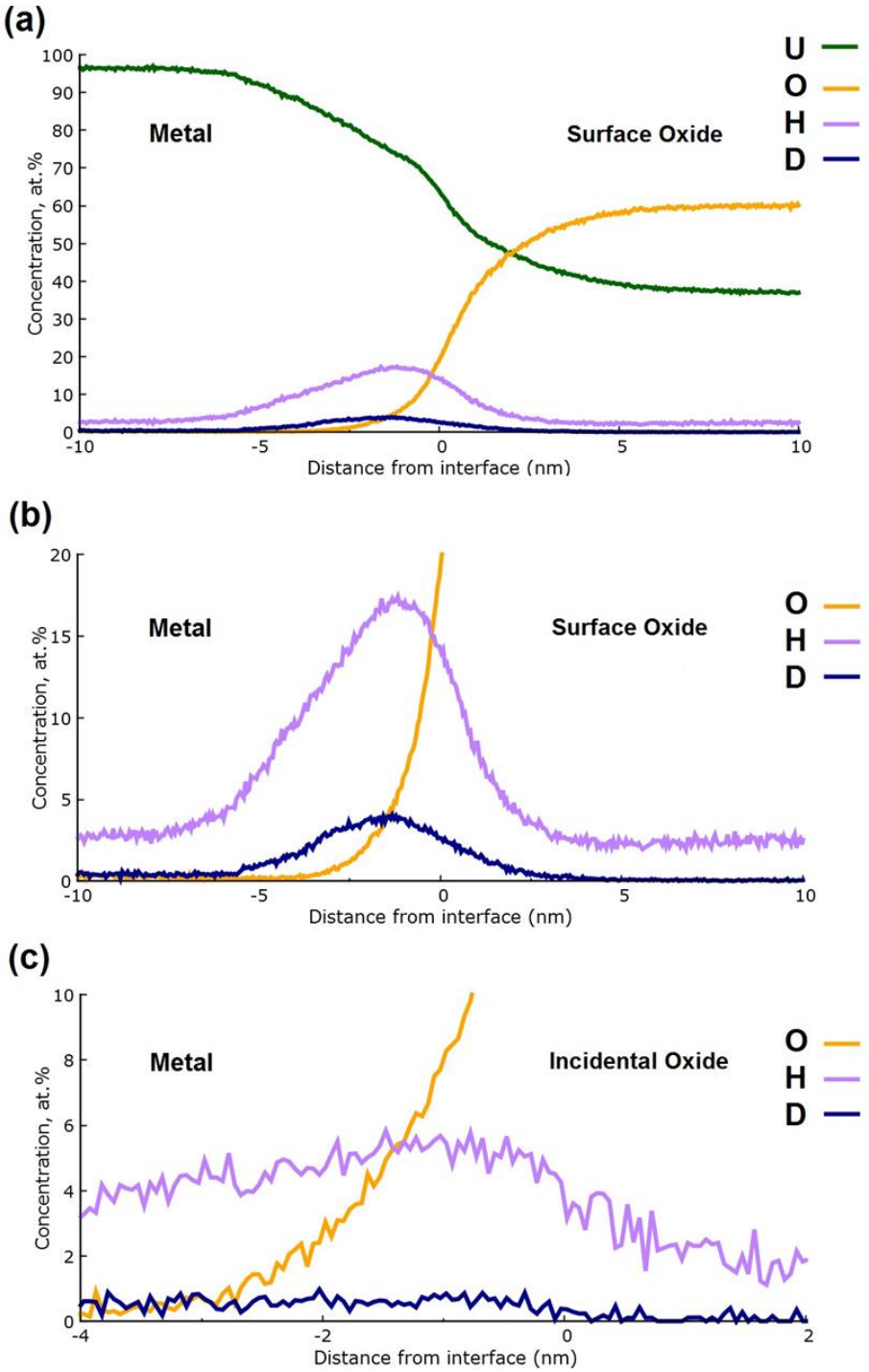

Figure 4.39 a) Proxigram of the interface at the top of the sample (marked as '1' in Figure 4.38). (b) Close-up of the interfacial region (marked as '1' in Figure 4.38) where a clear deuterium signal mirrors the location of the hydride peak observed in Figure 4.35, (c) Proxigram for the incidental oxide from the same dataset (identified as '2' In Figure 4.38), showing negligible deuterium content.

4.4.3 Summary

The atom probe experiments demonstrate clear evidence that the formation of hydride occurs during the corrosion of uranium in the presence of water vapour, forming as a near-constant layer at the oxide-metal interface. Within the oxide hydroxyl species were present (detected as OH and UO_xH molecular ions), which suggests that they play a significant role in the oxidation mechanism. The results suggest that excess hydrogen must be generated at the hydride-oxide interface which would be expected to diffuse through the oxide to escape at the oxide surface. This provides possible mechanistic insight into the reason for the oxide not increasing in oxidation state and becoming hyperstoichiometric UO_{2+x}, since the diffusion of (reducing) hydrogen species through the oxide would maintain the oxide at a reduced oxidation state, or reduced stoichiometry.

4.5 Chapter conclusions

The aim of the uranium experiments was to determine mechanistic information on the uranium water vapour reaction with and without oxygen present. Long-term corrosion experiments were conducted in order to obtain kinetic data in the form of corrosion rates that could be used for comparison with previous work and with the corrosion of the uranium niobium alloys studied later.

The corroded uranium material was then analysed using SIMS to produce isotopic depth profiles in an attempt to determine the diffusing species and also to investigate hydride formation. APT was also used to investigate hydride formation on much thinner uranium oxides.

From the kinetic experiments a good correlation was seen. However, the rates and activation energies deduced were not as expected. The rates recorded were slower than those previously reported by Glascott[73], Ritchie[19] and Baker[2,3],and the activation energy derived were considerably higher than Ritchie[19] and Colmeanres[21] but similar to a value previously reported by Baker[2,3]. It is proposed that the slower corrosion rates seen here could be due to the purity of the uranium metal used. The low carbon material used in this study has been shown to exhibit slower corrosion rates than high carbon material[74]. There is also the possibility that ingress of oxygen (accidentally) into the reaction cell led to a reduction in

corrosion rate. When oxygen was intentionally added to the water vapour reaction, the rate was seen to reduce significantly as previously reported[4].

From the SIMS analysis of the water vapour system, the depth profiles were shown to vary dramatically. Some of the samples showed clear changeovers from oxides containing O-16 from $D_2{}^{16}O$ and O-18 from $H_2{}^{18}O$, helping to reaffirm anionic diffusion as a mechanism for corrosion. The main issue with SIMS analysis is that the oxide was too thick for depth profiles to reach the oxide-metal interface. This meant that no hydride, if present, could be detected. The majority of oxides had undergone spallation, meaning that obtaining consistent depth analysis was challenging.

When the samples exposed to isotopically-labelled water and oxygen ($D_2{}^{16}O$ + $^{18}O_2$ or $H_2{}^{18}O$ + $^{16}O_2$) were analysed, it was seen that both O-16 and O-18 ions were present in the profiles. However, the oxide product was shown to be predominantly formed from the oxygen originating from the water.

From the atom probe analysis, a clear hydride layer was detected as a result of uranium corrosion in air. This was reaffirmed to be from the water vapour reaction when D_2O was used in place of air. The hydride was located between the oxide and the bulk metal. The detection of hydroxides within the oxide helps confirm the mechanism of Baker[2,3] where OH^- diffuses to the oxide-metal interface, both hydride and oxide are formed. The hydride undergoes oxidation to form new oxide as well as undergoing continual regeneration from the highly reactive atomic hydrogen.

Further work using APT to investigate this hydride layer would be of great interest and would allow confirmation that the hydride layer in turn reacts to form oxide. The use of labelled waters and oxygens could possibly be used in order to study this further. As well as a study with increased exposure times, in an attempt to detect the hydride layer as it grows and then oxidises.

5 Chapter five – results of niobium water vapour reaction

For niobium, there is limited literature on the water vapour reaction under the experiment conditions relevant to this study (<70 °C). The literature suggests a clear breakaway region at 750 °C possibly associated with the nucleation and growth of Nb_2O_5. Previous analysis on the oxidised material reveals the oxidation to be via anionic diffusion with oxide forming at the oxide metal interface, therefore the same mechanism as uranium. The actual oxide structure remains debated, with only some researches detecting the suboxides (NbO and NbO_2). The manner in which niobium oxidises is very important for the alloy system, therefore a clear understanding of the oxidation mechanism of the base metal is key.

The reaction of niobium metal with $D_2{}^{16}O$ vapour followed by $H_2{}^{18}O$ vapour has been studied. In addition to studying the kinetic data of the $D_2{}^{16}O$ reaction, the samples have been analysed using SIMS and APT to provide information on the mechanism. For the kinetic analyses both pressure and temperature were investigated. Pressure dependence was seen and an Arrhenius relationship was found. The SIMS analysis showed a range of oxidation states and oxide products, providing some insight into the mechanism. ATP was carried out on niobium metal samples exposed to air and these showed large regions of niobium hydride.

5.1 Material characterisation using EDX

EDX was carried out pre and post water vapour exposure. An SEM image of the surface was taken to show the topography of the niobium.

5.1.1 EDX of freshly polished niobium surface

Figure 5.1 shows the SEM image of the polished niobium coupon before exposure to any water vapour. The coupon was polished manually using silicon carbide (SiC) paper with grits 320-1200. From the image it can be seen that there are no distinct features such as inclusions, only polishing marks and scratches.

Figure 5.2 shows the spectrum of the sample showing the main elements present are niobium and oxygen as expected. The elemental maps are shown in Figure 5.3, with yellow and green

representing niobium and oxygen respectively. From Figure 5.3, it can be seen that the majority of the surface is niobium with small spots of oxygen distributed throughout.

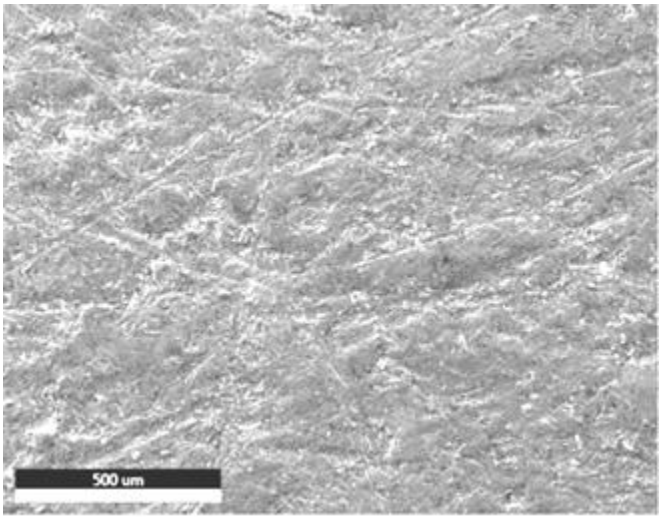

Figure 5.1 SEM image of the surface of a polished niobium coupon (polished using SiC paper 320-1200 grit).

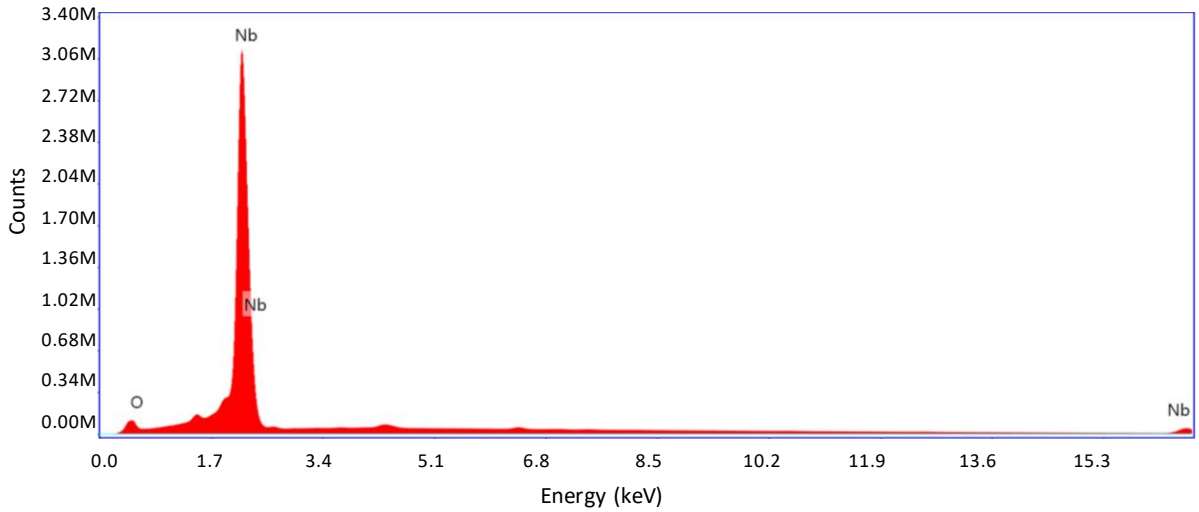

Figure 5.2 Spectrum of polished niobium coupon.

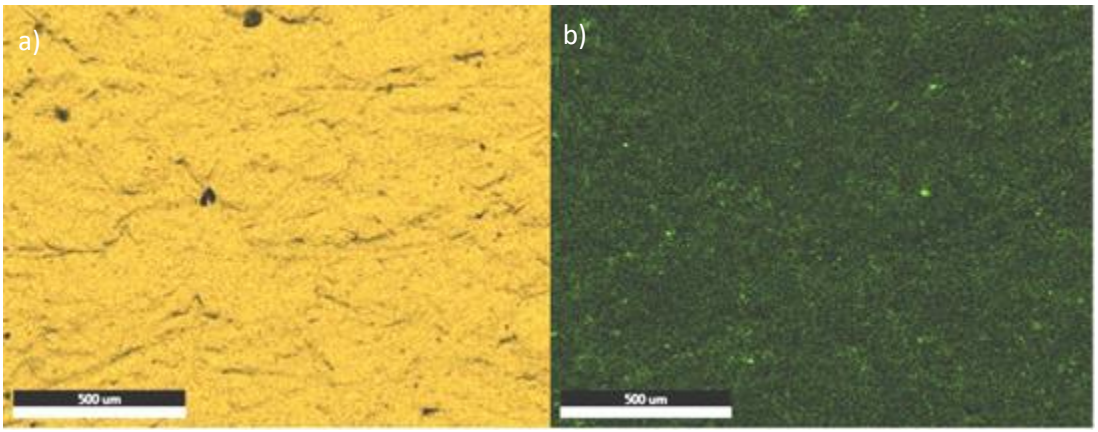

Figure 5.3 EDX elemental analysis of niobium coupon, a) yellow showing niobium, b) green representing oxygen.

5.1.2 EDX of niobium surface after water vapour exposure

An SEM image of the sample corroded at 69.50 °C and 307.67 mbar (Figure 5.4) shows a much rougher surface than that seen in figure 5.1, highlighting that oxidation has occurred.

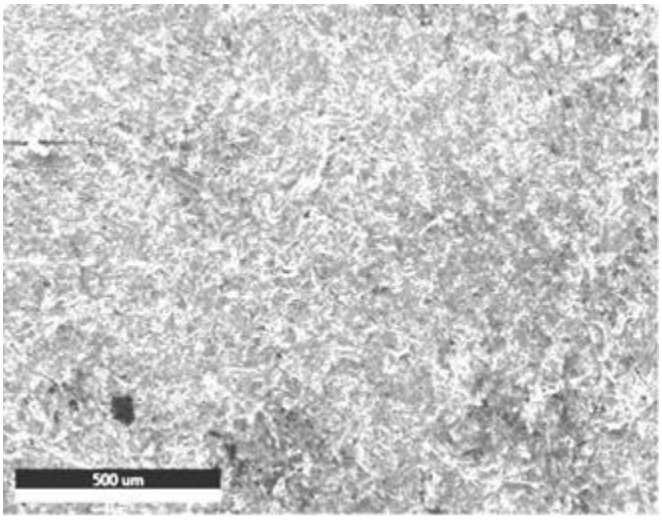

Figure 5.4 SEM image of the surface of niobium coupon corroded at 69.50 °C and 307.67 mbar.

Figure 5.5 shows the EDX analysis of the corroded niobium surface and Figure 5.6 the elemental maps of the surface for niobium and oxygen. It can be seen that the O peak in the EDX spectrum (figure 5.5) is little different to that of the clean surface (figure 5.2). This implies that the extent of oxidation is small compared to the EDX interaction volume, which is typically around 1 μm^3.

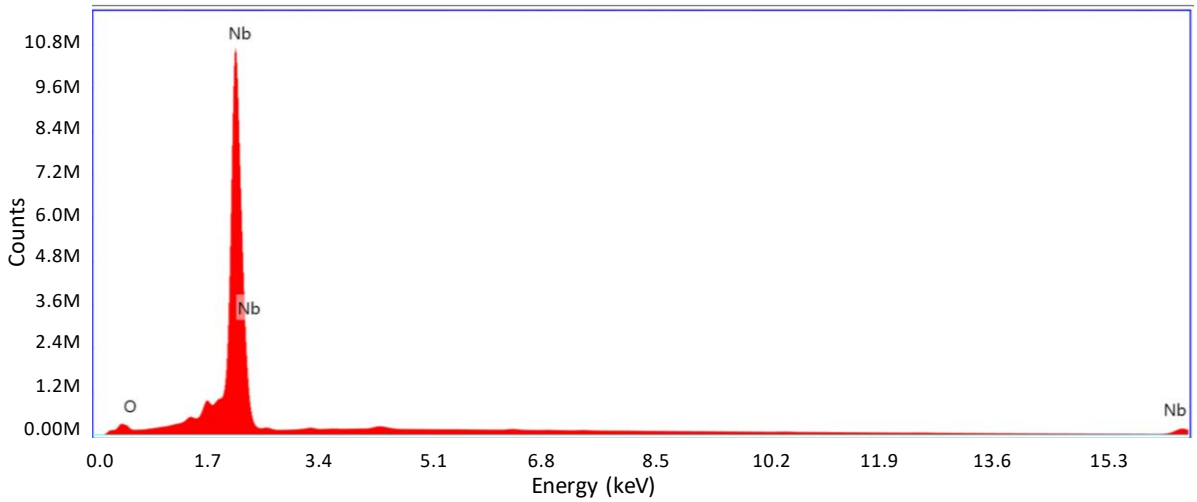

Figure 5.5 Spectrum of corroded niobium coupon.

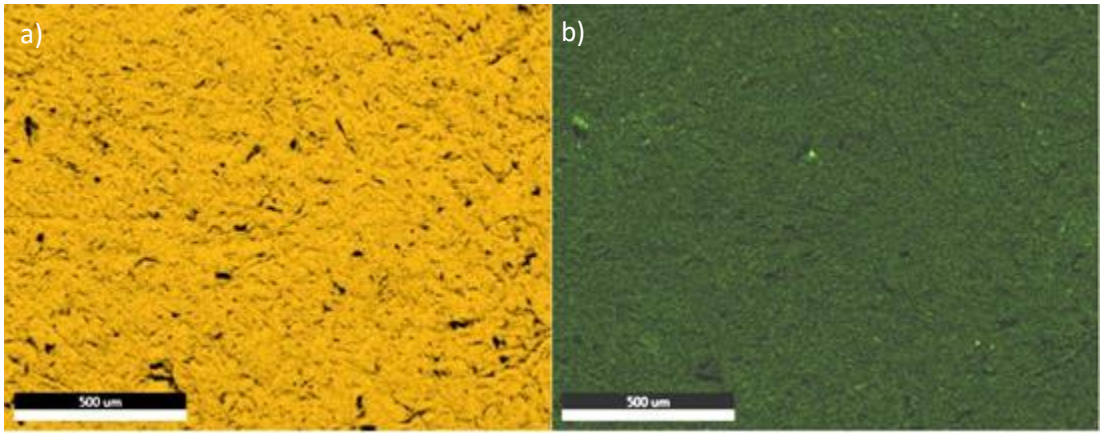

Figure 5.6 EDX elemental analysis of corroded niobium coupon, a) yellow showing niobium, b) green representing oxygen.

5.1.3 Summary

- Polished coupon surface detected no distinct features such as inclusions
- Corroded sample shows a much rougher surface, showing clear oxidation

5.2 Corrosion kinetics

For niobium, the effects of water vapour pressure and temperature have been investigated. The kinetic data are presented from both the $D_2{}^{16}O$ reaction and the subsequent $H_2{}^{18}O$ reaction. For $H_2{}^{18}O$ the kinetics will be within the bulk reaction and should therefore remain consistent with the final $D_2{}^{16}O$ rate.

The effect of pressure was investigated at 70 °C (mean temperatures of experiments ranged from 69.34-69.96); with four different water vapour pressures – 307.67 mbar, 263.63 mbar, 69.19 mbar and 31.58 mbar. These values are the actual starting pressures and vary slightly from the desired/proposed pressures mentioned in section 3. The desired values are only theoretical values calculated from an equation by Greenspan[67]. Therefore, changes in temperature and impurities within the water will impact the actual pressure.

The temperature dependence was investigated at four temperatures between 20-70 °C with a desired starting pressure of 30 mbar. The desired temperatures were 70 °C, 55 °C, 45 °C and 30 °C. The actual temperatures varied slightly due to changes in the room temperature. For the 30 °C experiment, the reaction cells were placed in the laboratory rather than within an oven. This meant that the temperature varied quite significantly throughout seasonal

changes. It also meant that the temperature was lower than desired, with the temperature average being ~24 °C. The lower temperature therefore affects the starting pressure of the experiment. For this temperature the predicted starting pressure is 21.75 mbar which is reasonably close to the actual starting pressure of 20.35 mbar.

Errors associated with the thermocouples (Type K) and the transducers should be noted. For the thermocouples the accuracy is ±2.2 °C or ±0.75%, whichever is greater. For the transducers there a few factors addressed in their performance rating:

- Long term drift ±0.1% span/annum
- Accuracy ±0.25%
- Thermal error 1% (0 °C to 70 °C), 2% for 40 to 250 mbar ranges (0 °C to 50 °C)

The actual average temperatures and starting pressures of the niobium $D_2{}^{16}O$ experiments were:

- 69.50 ±2.2 °C experiment starting pressure of 307.67 mbar ±4.20 %
- 69.62 ±2.2 °C experiment starting pressure of 263.63 mbar ±3.41 %
- 69.48 ±2.2 °C experiment starting pressure of 66.86 mbar ±0.91 %
- 69.35 ±2.2 °C experiment starting pressure of 39.71 mbar ±0.57 %
- 58.33 ±2.2 °C experiment starting pressure of 24.30 mbar ±0.56 %
- 44.73 ±2.2 °C experiment starting pressure of 29.28 mbar ±0.71 %
- 23.54 ±2.2 °C experiment starting pressure of 20.35 mbar ±0.49 %

The actual average temperatures and starting pressures of the niobium $H_2{}^{18}O$ experiments were:

- 64.36 ±2.2 °C experiment starting pressure of 412.90 mbar ±4.07%
- 64.33 ±2.2 °C experiment starting pressure of 257.10 mbar ±3.45%
- 69.74 ±2.2 °C experiment starting pressure of 57.97 mbar ±0.87%
- 71.49 ±2.2 °C experiment starting pressure of 35.76 mbar ±0.57%
- 58.36 ±2.2 °C experiment starting pressure of 21.48 mbar ±0.53%
- 44.58 ±2.2 °C experiment starting pressure of 2.90 mbar ±0.60%
- 26.63 ±2.2 °C experiment starting pressure of 19.33 mbar ±0.47%

There was an issue of a leak within the cell for the 45 °C $H_2{}^{18}O$ experiment and therefore the kinetic data are not presented.

For the reaction with water vapour plus oxygen, previous work has suggested that this addition may lead to an increase in rate as compared to the pure oxygen reaction[31]. For uranium it has been seen to have the opposite effect, see chapter 4 and previous literature[4,21]. The experiments with water vapour plus oxygen were carried out at a desired temperature of 55 °C and with the desired starting pressures of 40 mbar (30 mbar water vapour and 10 mbar oxygen). Both isotope regimes were investigated – $D_2{}^{16}O$ + $^{18}O_2$ and $H_2{}^{18}O$ + $^{16}O_2$. However, there was an issue with the data logger for the $D_2{}^{16}O$ + $^{18}O_2$ experiment and therefore the kinetic data are not presented. The niobium still underwent the exposure and therefore the coupon was available for SIMS analysis. For the $H_2{}^{18}O$ + $^{16}O_2$, the actual temperature was 57.83 °C and pressure of 63.57 mbar (48 mbar water + 15 mbar oxygen). The reason for the increased starting pressure is most likely due to salt impurities and temperature fluctuations within the laboratory.

The assumed reaction of niobium with water vapour is –

$Nb + H_2O \longrightarrow NbO + H_2$ (initial oxide formed).

The NbO then reacts with further H_2O to form NbO_2.

$NbO + H_2O \longrightarrow NbO_2 + H_2$ (further oxidation occurs)

The NbO_2 then eacts with further H_2O to form Nb_2O_5.

$2NbO_2 + H_2O \longrightarrow Nb_2O_5 + H_2$ (after long exposure, pentoxide formed)

As the experiments conducted in this study are all long term (months – years), it is expected that the pentoxide will be formed. Therefore this is the equation that has been carried forward in order to calculate rates.

5.2.1 Reaction with sequential water vapour exposure

5.2.1.1 Pressure dependence

5.2.1.1.1 Niobium + $D_2{}^{16}O$ at 69.50 °C and 307.67 mbar experiment

Figure 5.7 shows the temperature and pressure data from the experiment conducted at 69.50 °C and 307 mbar. From the figure there are a few key points to note. Firstly, there is a region

(highlighted by the circle) where there were no data collected. This is due to the data scan system that logs and records the pressure and temperature data being accidentally switched off. For the temperature it can be seen to fluctuate a few degrees throughout but at 400000 min a much larger change is seen. The fluctuations are due to changes in temperature within the laboratory. There is no form of regulation such as air conditioning. Therefore, the temperature of the laboratory varies throughout the year and the changes can be seen as seasonal effects.

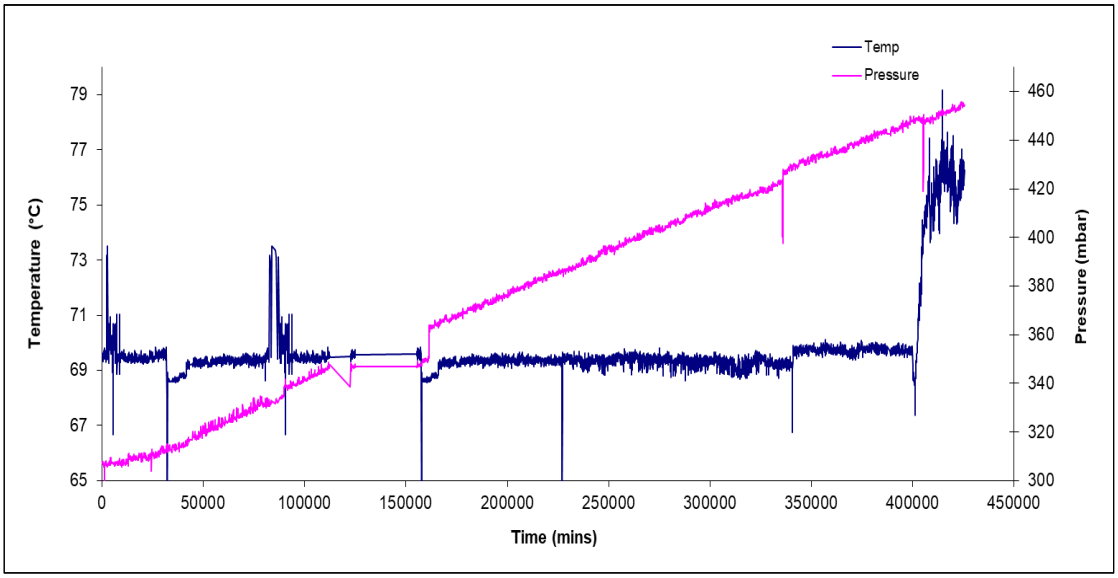

Figure 5.7 Pressure and temperature graph for the niobium at 69.50 °C and 307.67 mbar $D_2{}^{16}O$ experiment

When the pressure data are converted into the amount of hydrogen evolved (see section 3.1.3 for details), it can be seen that the overall rate is relatively linear see Figure 5.8.

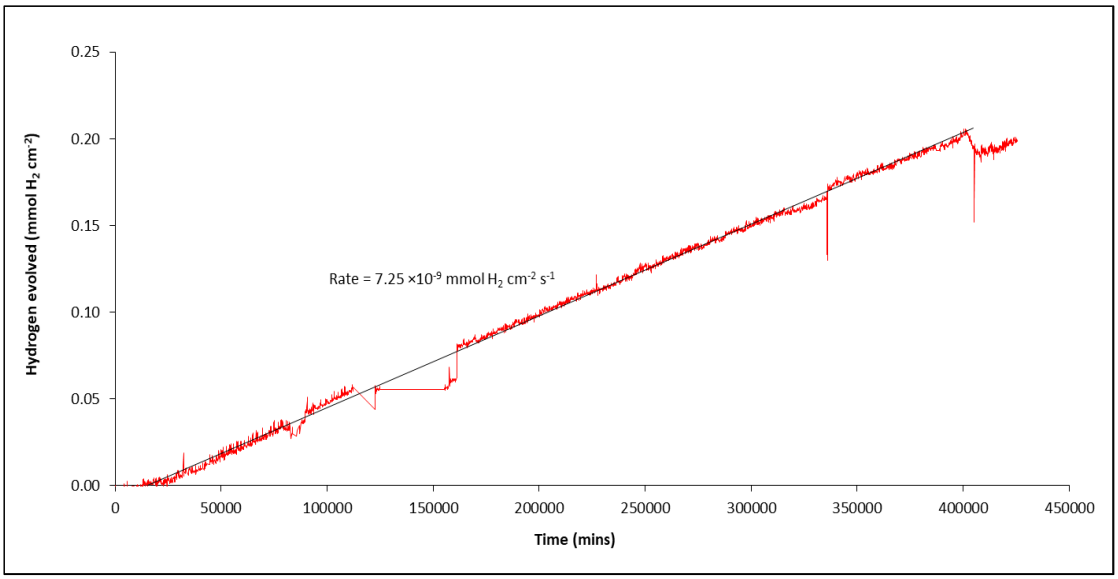

Figure 5.8 Graph showing the amount of hydrogen evolved in mmol cm^{-2} for the Niobium at 69.50 °C and 307 mbar $D_2{}^{16}O$ experiment.

5.2.1.1.2 Niobium + $D_2{}^{16}O$ at 69.62 °C and 263.63 mbar experiment

Figure 5.9 shows the pressure and temperature data for the experiment conducted at 69.62 °C and 263.63 mbar. It can be seen that again there is the same down period when the data scan unit was not logging. The temperature remains relatively constant varying only by 1 °C throughout. Therefore, the effect on the pressure is expected to be a lot less. When the rate is calculated (Figure 5.10) again a couple of regions are seen. There is no clear reason for the change.

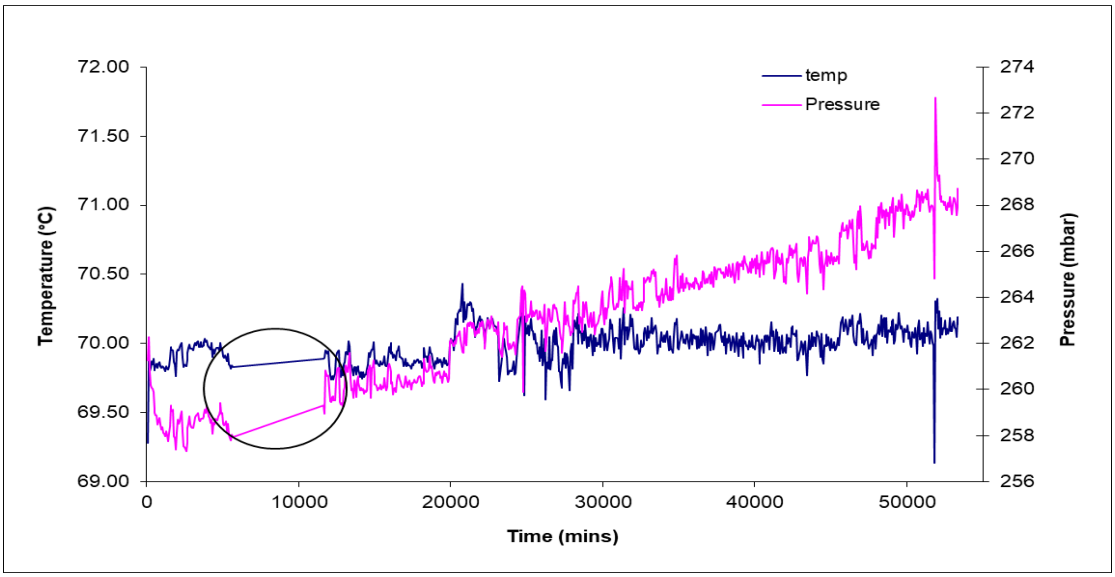

Figure 5.9 Pressure and temperature graph for the niobium at 69.62°C and 263.63 mbar $D_2{}^{16}O$ experiment.

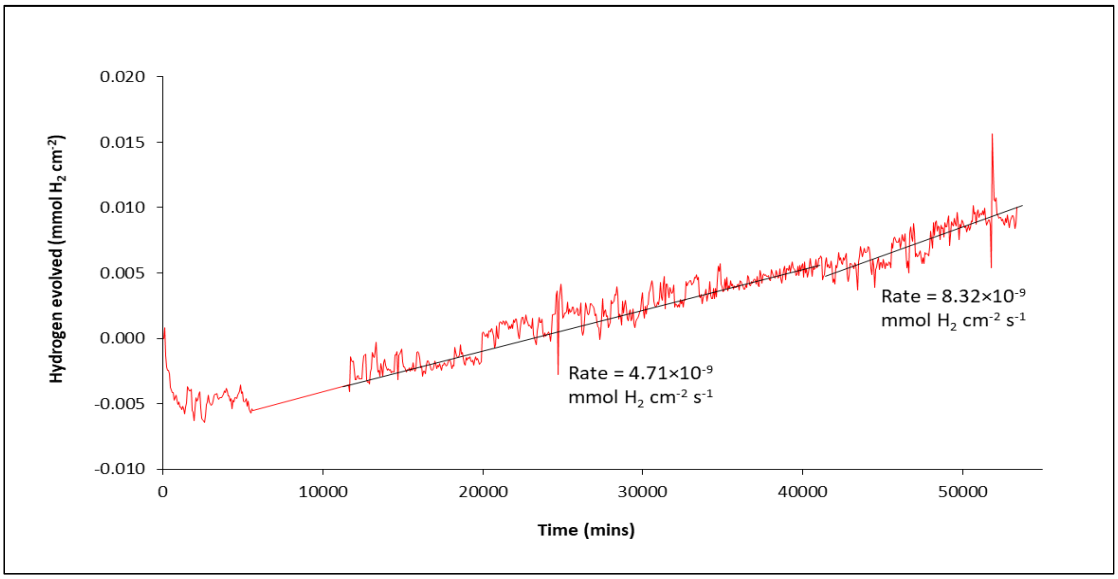

Figure 5.10 Hydrogen evolved (mmol cm^{-2}) for the niobium at 69.62 °C and 263.63 mbar $D_2{}^{16}O$ experiment.

5.2.1.1.3 Niobium + $D_2{}^{16}O$ at 69.48 °C and 66.88 mbar experiment

For the experiment conducted at 69.48 °C and 66.88 mbar there was an accident with the initial experiment where the crucible containing the water was knocked over and therefore had spilt within the cell. The use of chloride salt lead to corrosion of the pot itself which then affected the pressure and thus rate data. Therefore, the experiment needed to be stopped and restarted using a different cell and a fresh salt solution. The coupon was not re-polished so the reaction should just be a continuation of the previous run. Figure 5.11a presents the pressure and temperature of the initial run before the water spilt and figure 5.11b presents the data from the restart.

a)

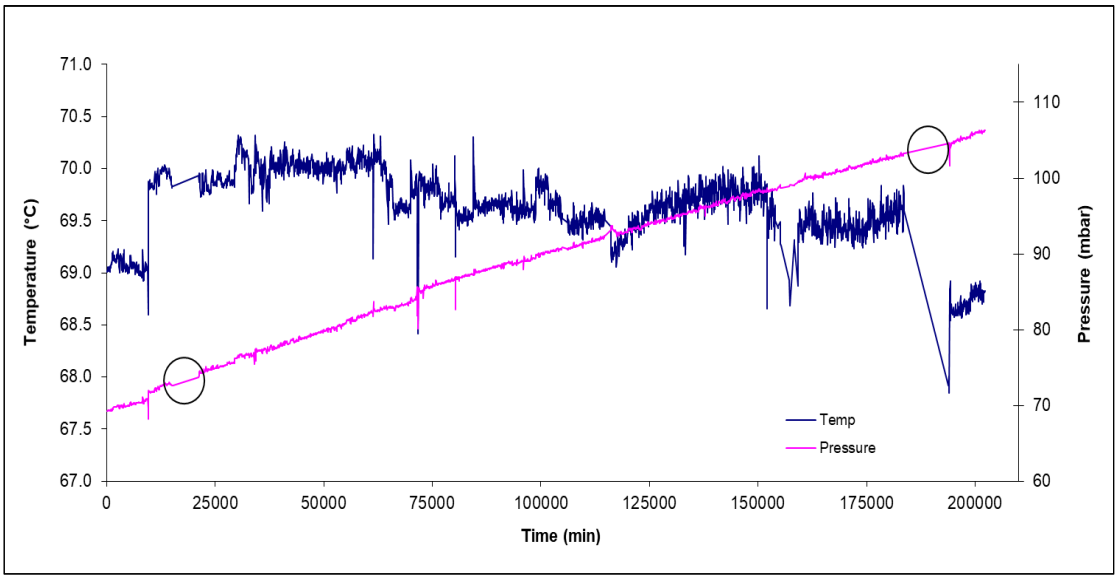

b)

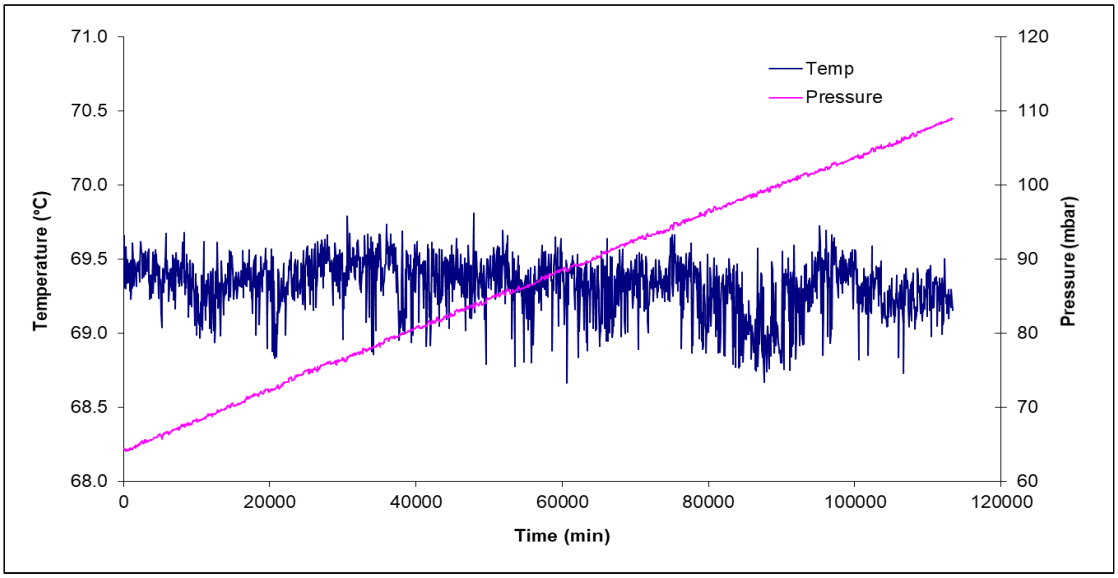

Figure 5.11 Pressure and temperature graphs for the niobium at 69.48 °C and 66.88 mbar $D_2{}^{16}O$ experiment, a) first run, b) after a restart due to the pot being tipped over within the oven.

In figure 5.11a there are a couple of down periods where the data scan unit was off but in general the pressure increased linearly with time. The temperature fluctuated by a few degrees. In the restart the pressure and temperature can be seen to be very stable throughout. When the data are converted to a rate, there are two clear regions in the initial run (figure 5.12a). However, the rates are reasonably similar. For the restart there was only one rate region. However, the rate derived of 9.86 $\times 10^{-9}$ is significantly higher than the rates obtained from the initial run. One possible cause for an increase in rate is that during the freeze pump thaw process, a water droplet managed to get onto the surface of the coupon and therefore changed the reaction. One other possible cause could be the presence of oxygen within the system as this has been suggested to increase the rate[31].

a)

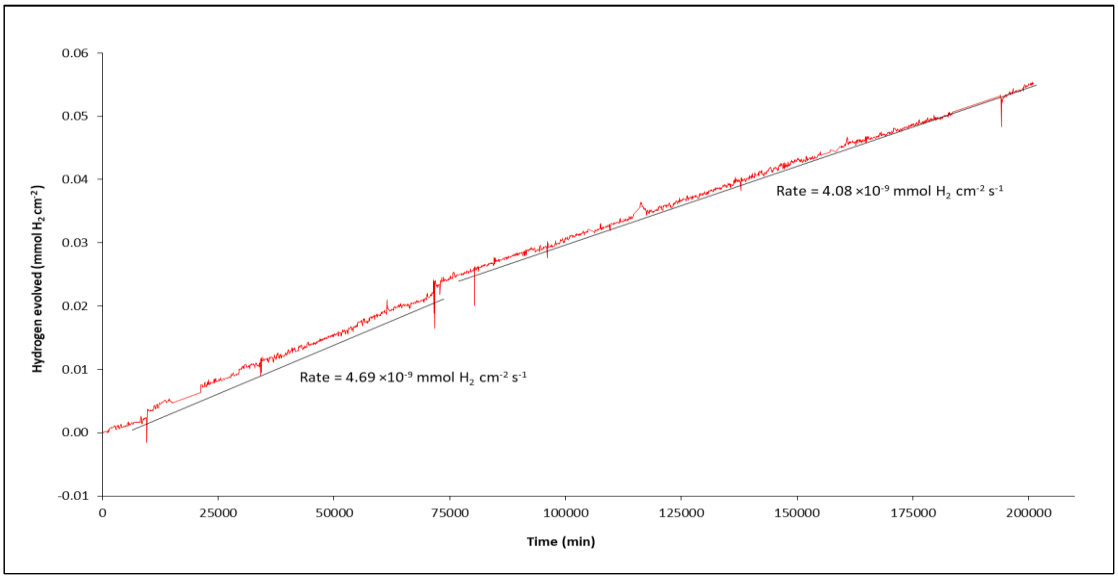

b)

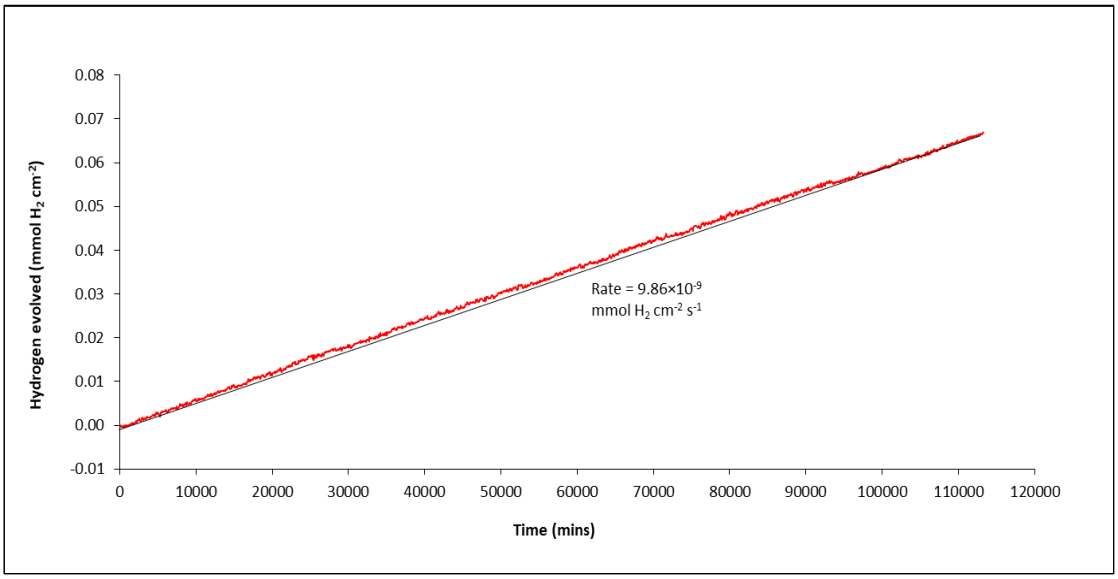

Figure 5.12 Hydrogen evolved for the niobium at 69.48 °C and 66.88 mbar $D_2{}^{16}O$ experiment, a) first run, b) after a restart. Rates are shown in mmol H_2 cm^{-2} s^{-1}.

5.2.1.1.4 Niobium + $D_2{}^{16}O$ at 69.35 °C and 39.71 mbar experiment

For the reaction at 69.35 °C and 39.71 mbar there were a few issues which resulted in the experiment needing to be restarted twice. For these restarts the cell did not require opening. The system was just frozen, evacuated and then allowed to thaw before being placed back in the oven and the logger system restarted. Again there is the possible risk that during evacuation, the water was not fully frozen allowing a water droplet to reach the coupons surface and thus changing the reaction.

Figure 5.13a presents the initial data which are very noisy and show the pressure and temperature to jump around a lot. However, it is the early stages of the reaction and as previously seen data can vary while the reaction moves to a stable linear regime.

Following the first restart (figure 5.13b) the data are a lot more stable although a clear change can be seen around 120000 minutes with the temperature dropping by a few degrees and the pressure increasing by a few mbar. This suggests that the temperature is having an effect on the pressure of the system, However, for the rate calculation this effect is taken into account. There is also a period of down time but the pressure remains constant afterwards.

Following the second restart the pressure and temperature are more stable than both the initial and the first restart. The pressure increases linearly with time and the temperatures fluctuates only slightly by 1 °C.

Figure 5.14 shows the rate plots for each of the experimental runs. Obviously for the initial run there is not a clear linear region and therefore the rate taken is only an approximation. The first restart showed two regions. However when the rate is calculated both regions have a similar rate suggesting that once the temperature influence is taken into account the data are fairly consistent. For the second restart the rate derived (6.37 $\times 10^{-9}$ mmol H_2 cm^{-2} s^{-1}) is similar to that obtained from the initial run (6.41 $\times 10^{-9}$ mmol H_2 cm^{-2} s^{-1}). However, these both differ to the lower rate of the first restart (5.10 $\times 10^{-9}$ mmol H_2 cm^{-2} s^{-1}).

a)

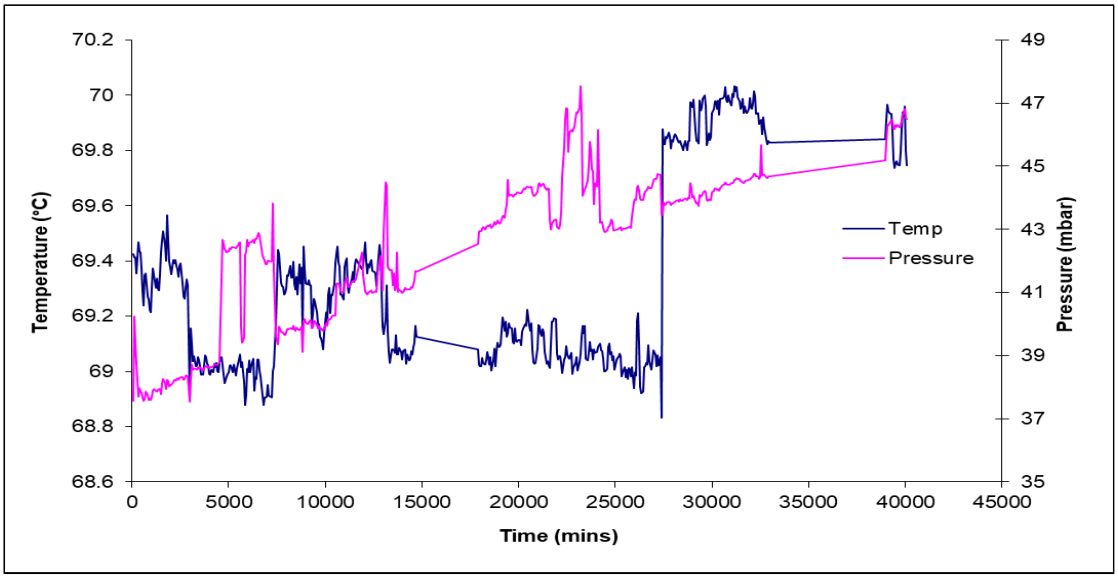

b)

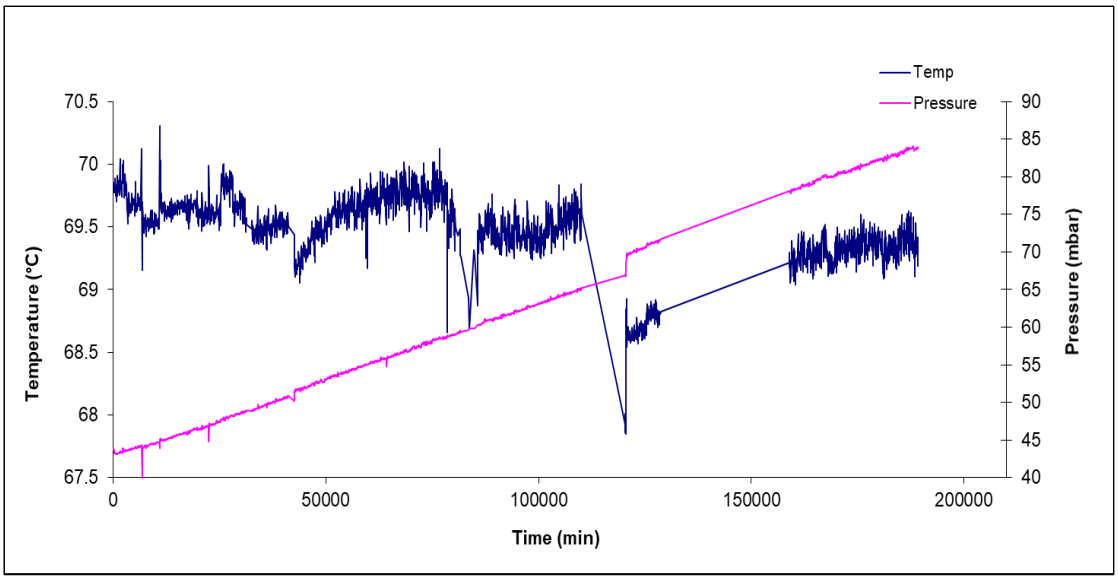

c)

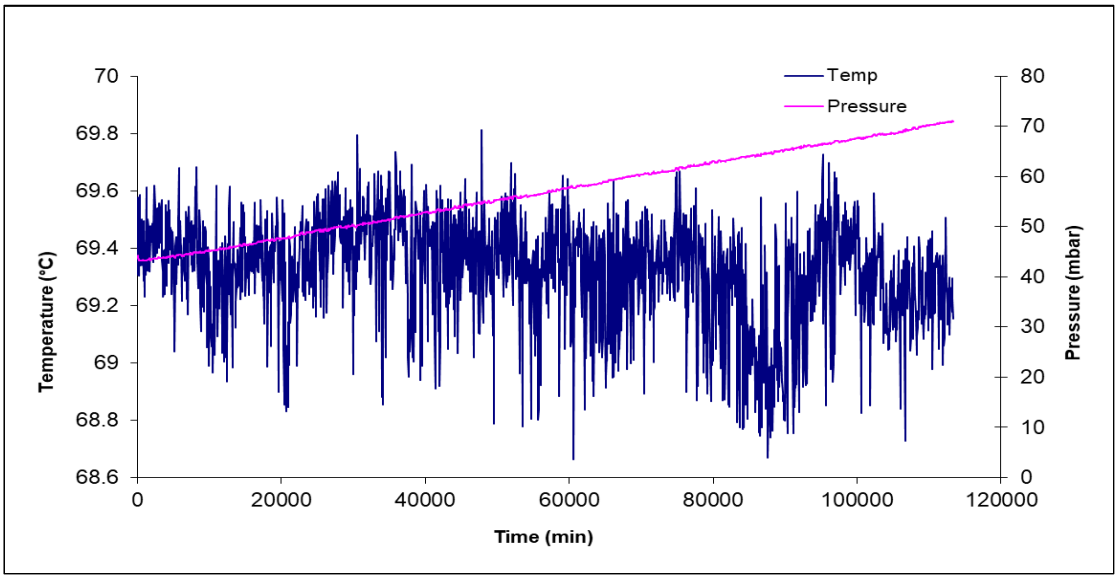

Figure 5.13 Pressure and temperature graphs for the niobium at 69.35 °C and 39.71 mbar $D_2{}^{16}O$ experiment, a) initial run, b) after a restart, c) after a second restart.

a)

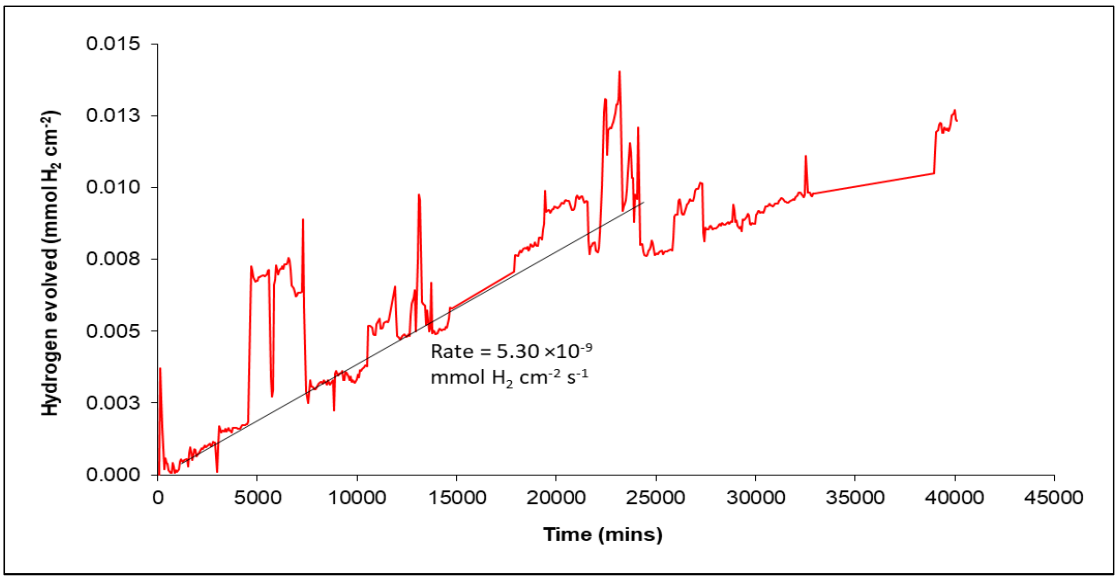

b)

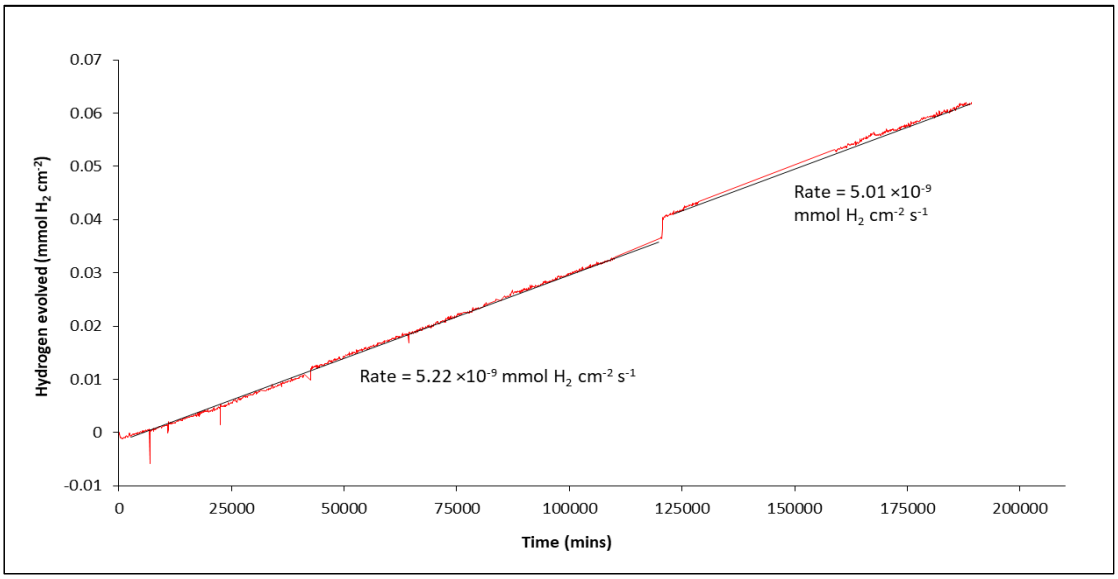

c)

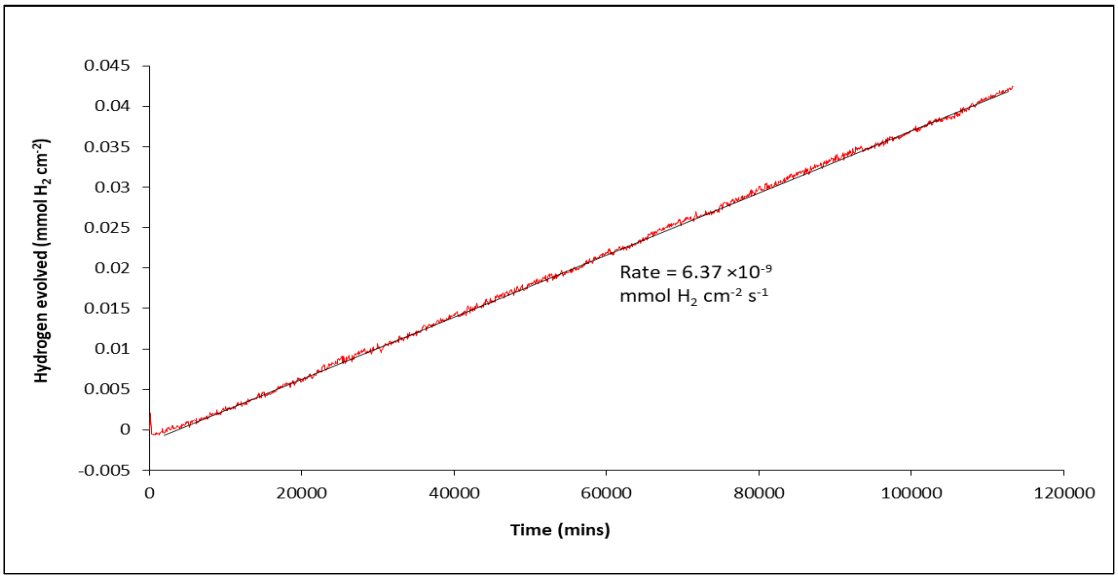

Figure 5.14 Hydrogen evolved graphs for the niobium at 69.35 °C and 39.71 mbar $D_2{}^{16}O$ experiment, a) initial run, b) after restart, c) after second restart.

5.2.1.1.5 Comparison of pressure experiments

Table 5.1 contains the rate data for each of the four experiments and Figure 5.15 is a plot of rate (mmol H_2 cm^{-2} s^{-1}) against pressure (mbar). It can be seen that there is a slight offset for corrosion rate at zero water vapour pressure; when there is no water vapour present the corrosion rate should obviously be zero. This artefact is almost certainly due to noise in the data points, which cannot be avoided when using pressure measurements to obtain the corrosion rate.

Table 5.1 Data for niobium experiments at 70 °C and four different pressures – 307 mbar, 263.63 mbar, 67.51 mbar and 42.25 mbar

Starting pressure (mbar)		Temperature		1000/T (K^{-1})	Rate (mmolH_2 $cm^{-2}s^{-1}$)	Average rate (mmolH_2 cm^{-2} s^{-1})
Desired	**Actual**	**(°C)**	**(K)**			
301	307.67	69.48	342.63	2.919	4.94E-09	7.25E-09
		69.30	342.45	2.920	1.04E-08	
		69.72	342.87	2.917	6.42E-09	
226	263.63	69.94	343.09	2.915	4.71E-09	6.52E-09
		69.86	343.01	2.915	8.32E-09	
65.3	69.03	69.06	342.21	2.922	4.69E-09	6.18E-09
		69.96	343.11	2.915	4.08E-09	
	64.72	69.32	342.47	2.920	9.86E-09	
32.3	37.57	69.16	342.31	2.921	5.30E-09	5.47E-09
	43.86	69.58	342.73	2.918	5.22E-09	
		69.33	342.48	2.920	5.01E-09	
	43.69	69.32	342.47	2.920	6.37E-09	

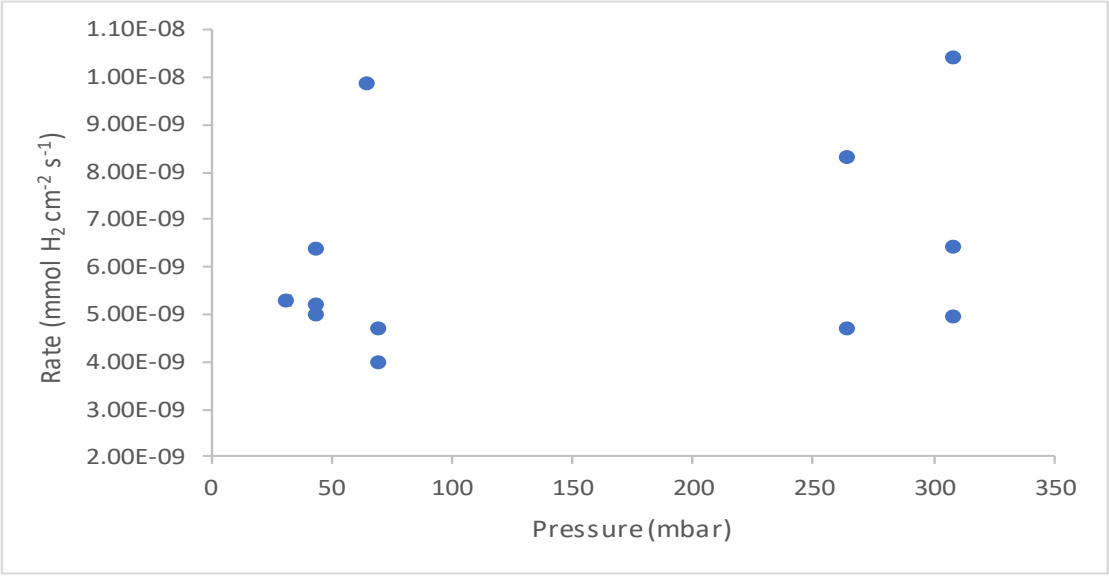

Figure 5.15 Plot of rate (mmol H_2 cm^{-2} s^{-1}) vs pressure (mbar) for the niobium experiments conducted at approximately 70 °C.

A significant amount of scatter can be seen in Figure 5.15 making it difficult to determine a trend and therefore any pressure dependence. When the average rate for each of the four pressures studied is plotted (Figure 5.16) there is limited correlation and appears to show no pressure dependency for niobium.

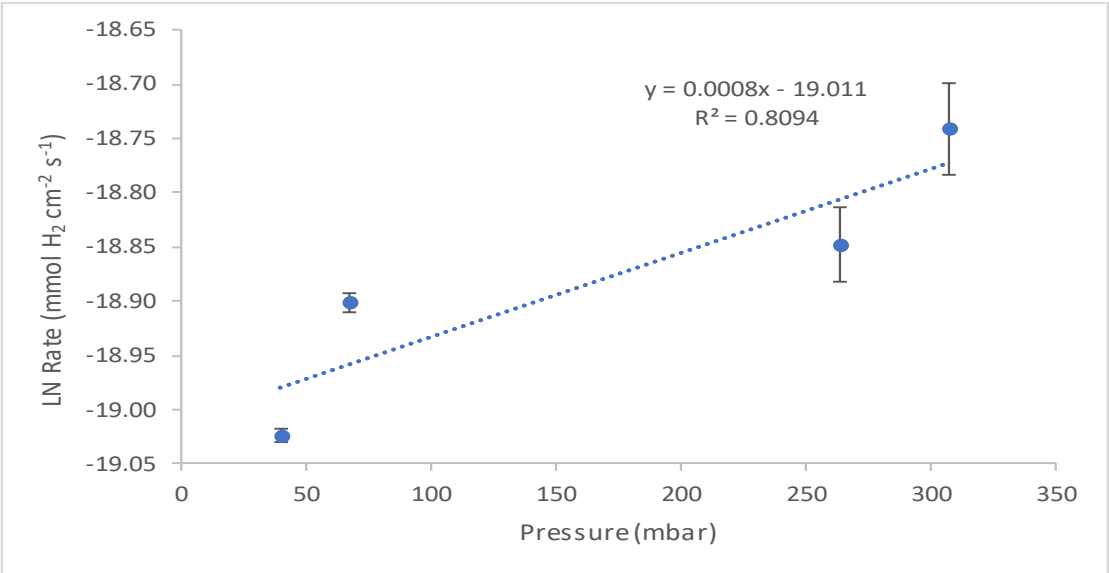

Figure 5.16 Plot of average rate (mmol H_2 cm^{-2} s^{-1}) at each averaged pressure for the 70 °C niobium experiments. The error bars are calculated from the transducer %accuracy and are not an indication of confidence in the data.

Previous work[26] has shown the reaction with oxygen to be independent of pressure at temperatures 250-300 °C. The kinetics have been found to be parabolic and logarithmic with

oxygen at temperatures below 300 °C. At higher temperatures a pressure dependence of $P^{½}$ has been detected and is attributed to the linear kinetics associated with the formation (and continual cracking and healing) of Nb_2O_5. With water vapour Blackburn[28] reported parabolic kinetics with slopes of 0.33 for experiments conducted between 200-700 °C on mechanically polished samples and 0.5 when samples were prepared by abrasion with a blast of alumina powder.

For uranium and UNb alloys a pressure dependence of $P^{½}$ was also determined for the water vapour reaction[21,73]. Both these assume the oxidation reaction to occur the diffusion of hydroxyl ions through the oxide, where they subsequently react to form new oxide at the oxide-metal interface. Then, for every molecule of vapour two equally charged, hydroxyl ions should be formed through interaction with a lattice bound oxygen ion at the gas-oxide interface (surface). If two moles of hydroxyl ions are generated for every mole of gas phase water vapour which dissociates at the surface, a $P^{½}$ relationship should be anticipated.

5.2.1.2 Temperature dependence

Four temperatures were investigated (70 °C, 55 °C, 45 °C and 30 °C) while the pressure was kept to 30 mbar. Figure 5.17 shows the temperature and pressure data for the experiment conducted at 55 °C. There were technical issues with the data scan unit and it was not logging for long periods of time. Therefore, the data are presented over three separate plots in Figure 5.17 and Figure 5.18.

a)

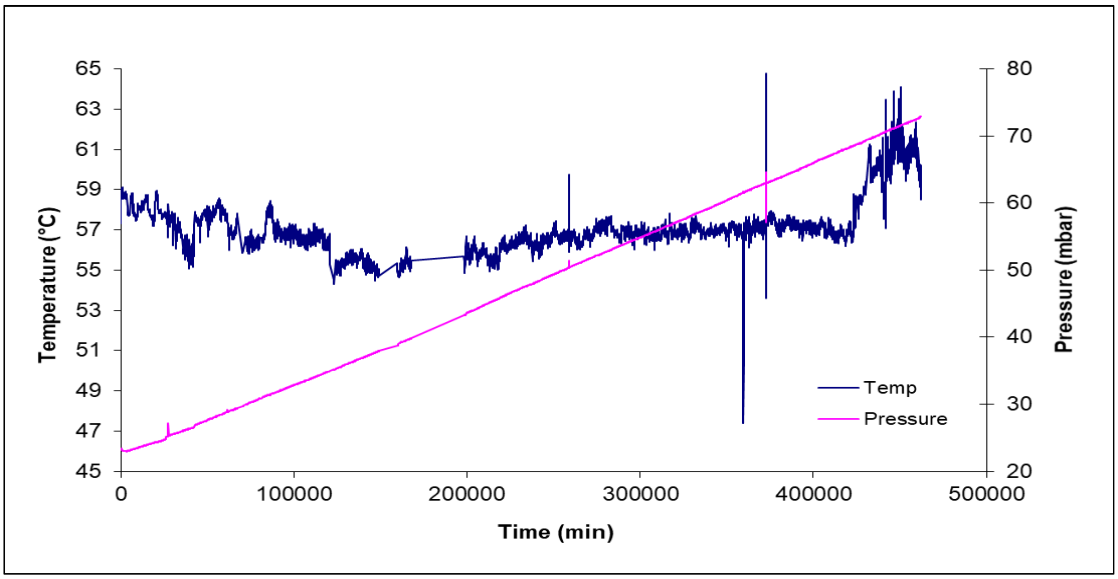

b)

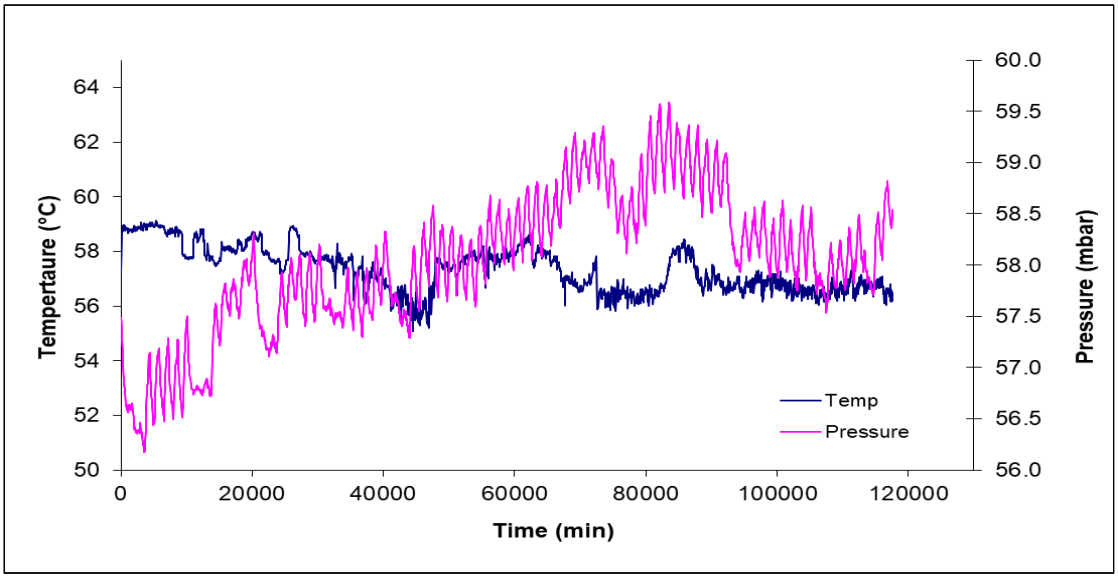

c)

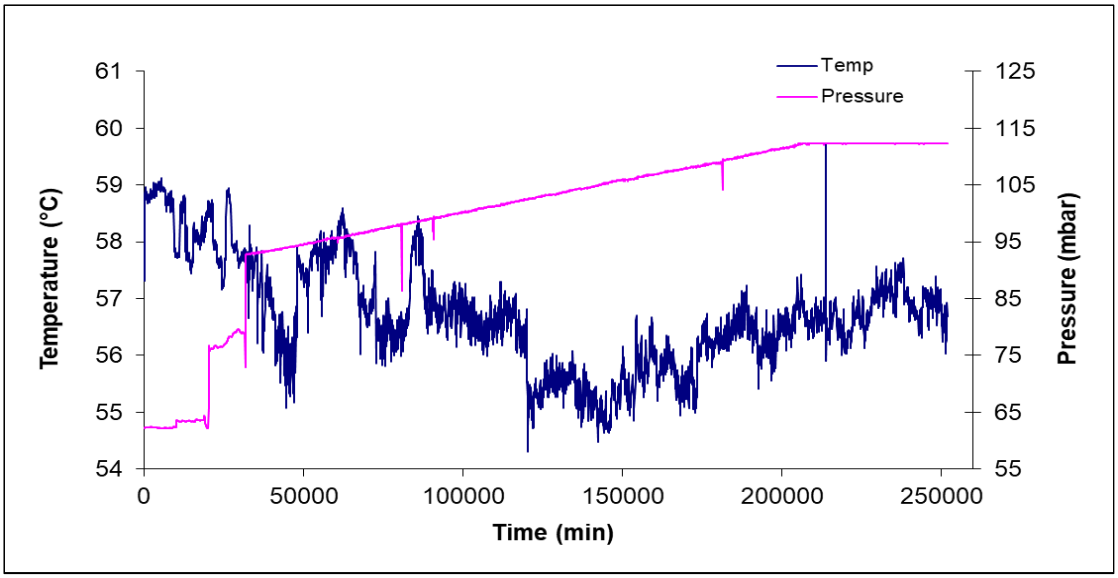

Figure 5.17 Temperature and pressure data for the niobium at 58.33 °C and 24.30 mbar $D_2{}^{16}O$ experiment, a) initial run, b) after down period, c) after second down period.

a)

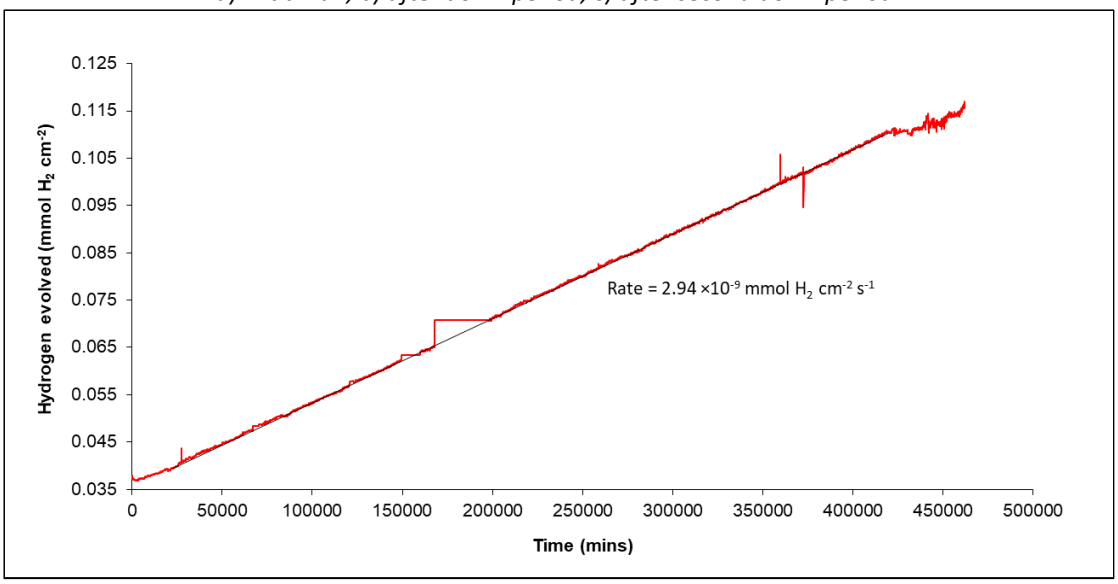

b)

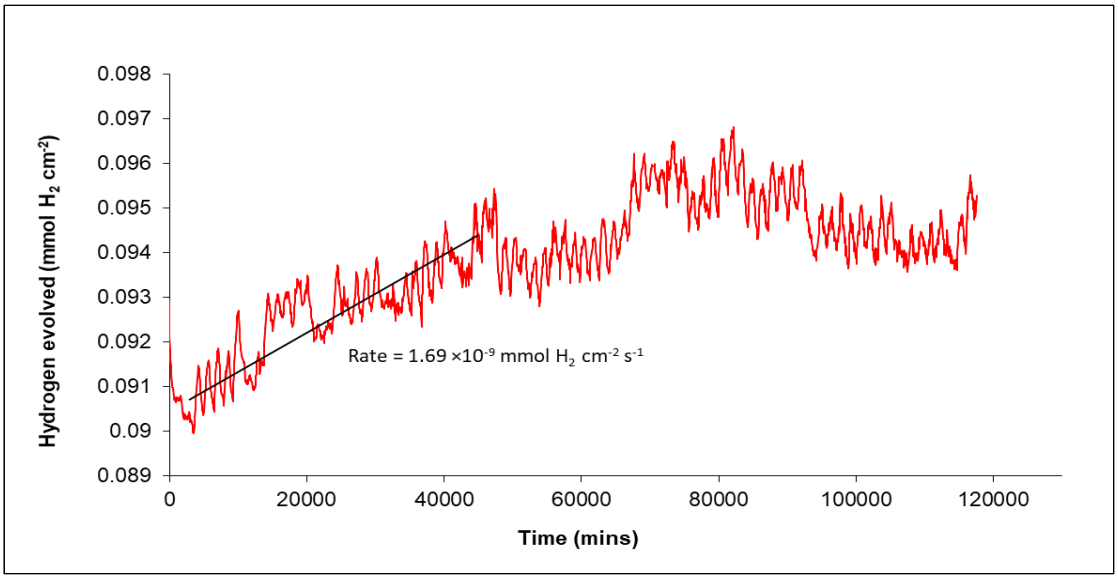

c)

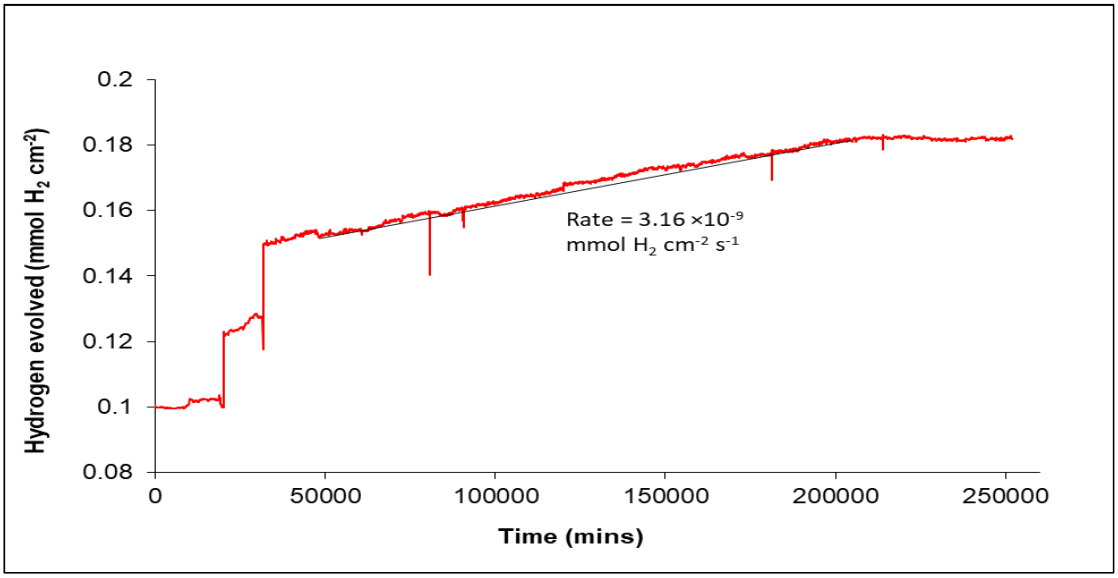

Figure 5.18 Hydrogen evolved graph for the niobium at 58.33 °C and 24.30 mbar $D_2{}^{16}O$ experiment, a) initial run, b) after down period, c) after second down period. Rates are shown in mmol H_2 cm^{-2} s^{-1}.

The experiments at 45 °C and 30 °C were started at the same time as the 55 °C experiment Therefore the issues with the data scan unit affected them all in the same way, with data from each experiment presented as separate plots and with each of them showing a very noisy second run (Figure 5.19 and 5.20). As previously discussed this noisy run is most likely due to issues with the data scan unit and transducers after a long period of down time and therefore not logging correctly. Due to the noise it is difficult to obtain an accurate rate for this segment of the reaction.

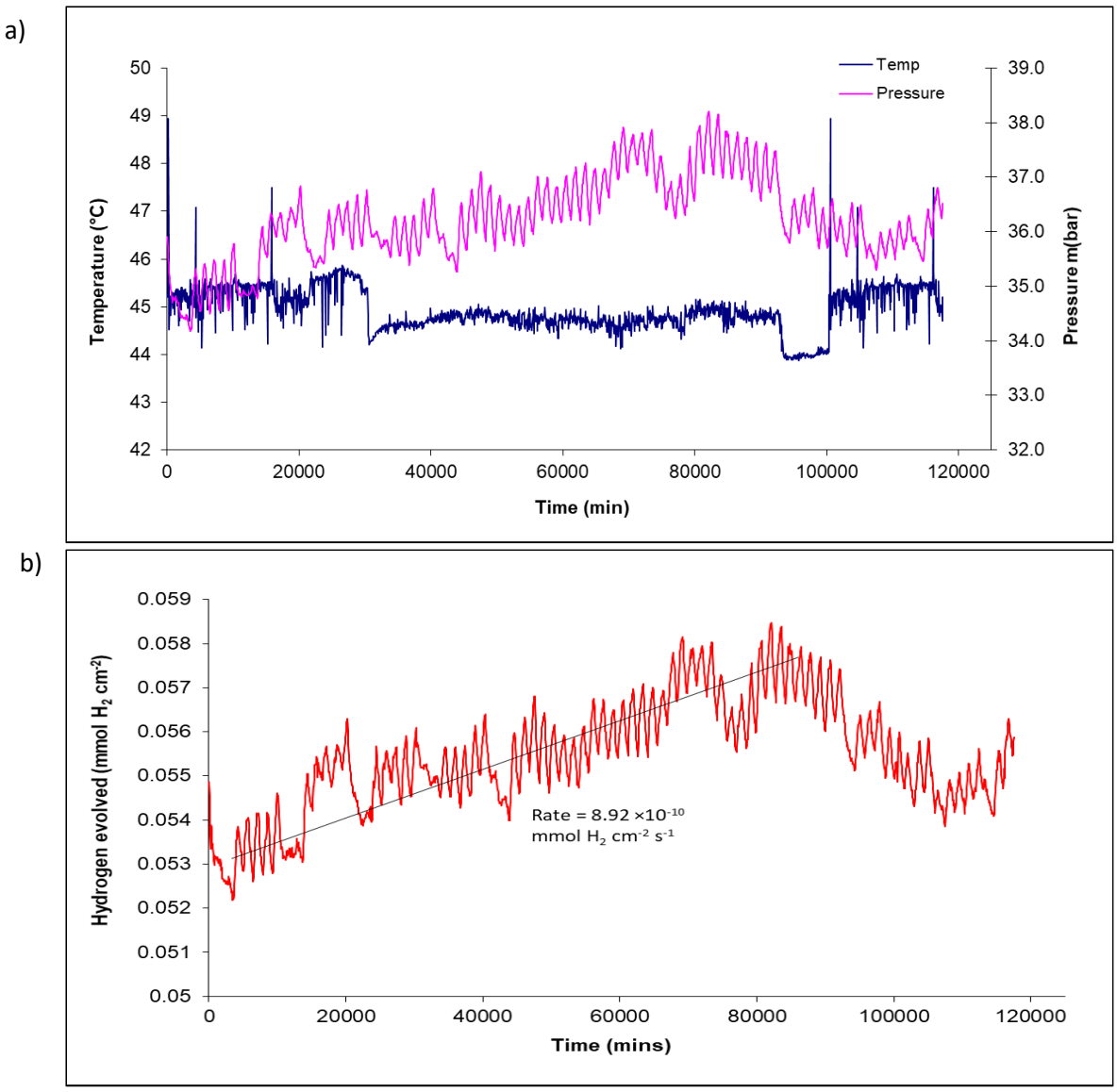

Figure 5.19 Data for the second period of the niobium 44.73 °C and 29.28 mbar experiment, a) pressure and temperature data, b) hydrogen evolved versus time. Rates are shown in mmol H_2 cm^{-2} s^{-1}.

a)

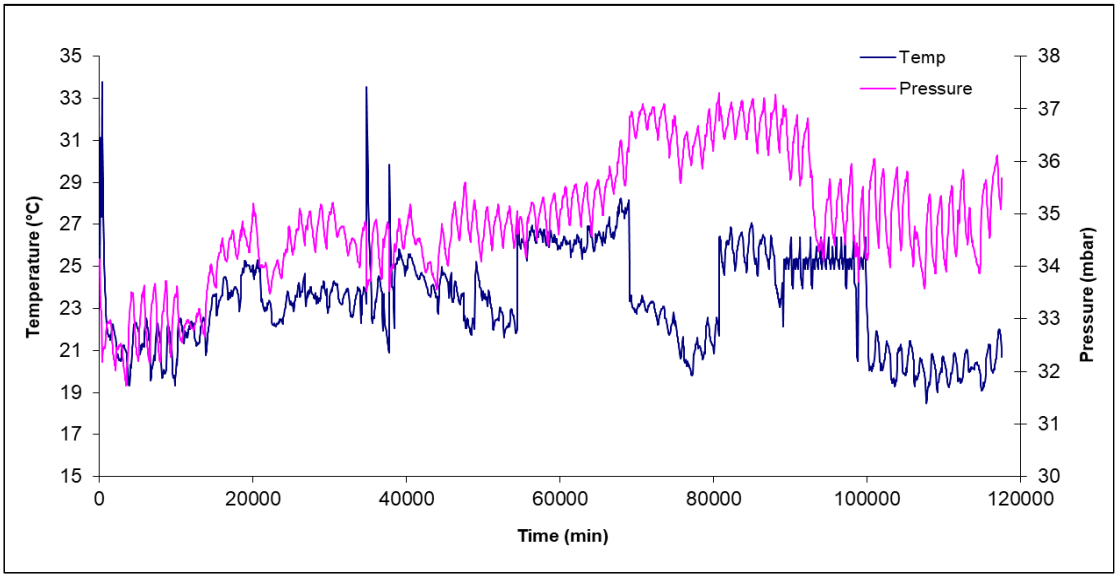

b)

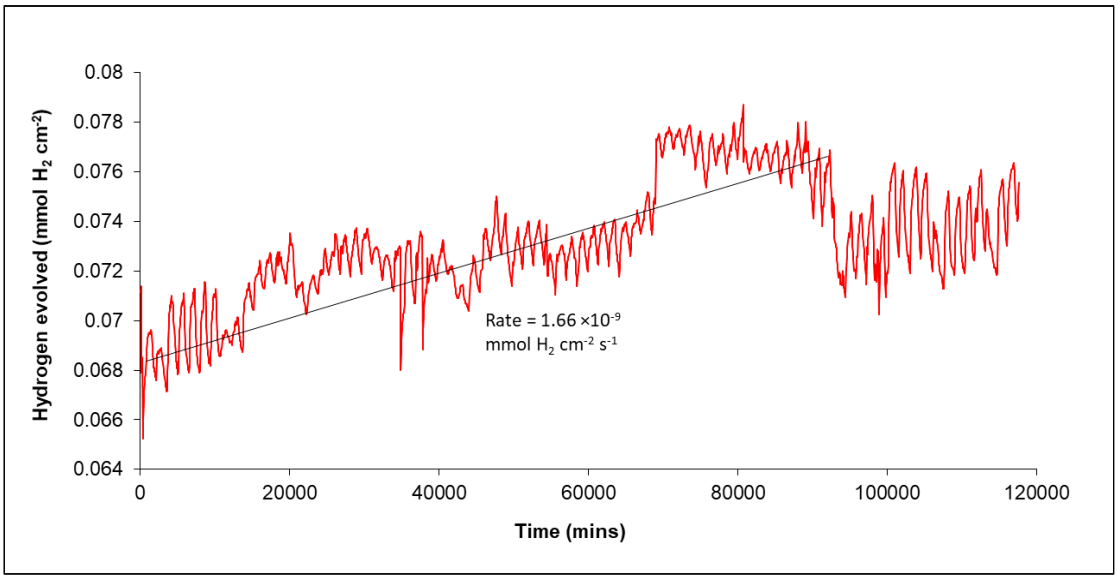

Figure 5.200 Data for the second period of the niobium 23.54 °C and 20.35 mbar experiment, a) pressure and temperature data, b) hydrogen evolved versus time. Rates are shown in mmol H_2 cm^{-2} s^{-1}.

Figure 5.21 and Figure 5.22 present Arrhenius plots for all of the niobium data, with the latter presenting the average rate date for each temperature. Table 5.2 contains all of the rate data for each temperature and pressure. There are multiple rates calculated for each set of conditions due to the number of restarts required after issues with the data scan unit.

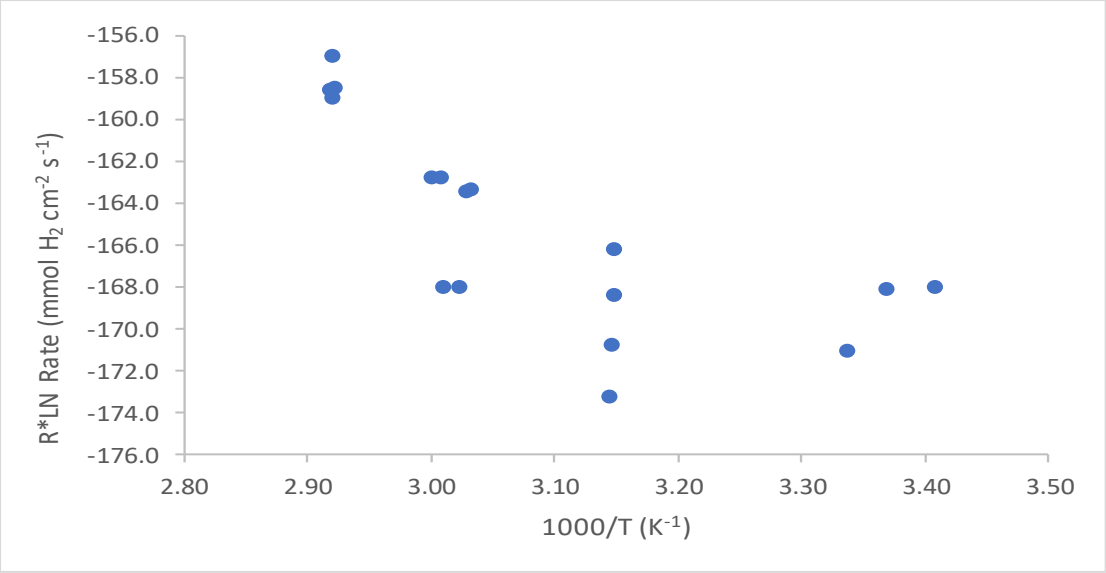

Figure 5.21 Arrhenius plot for the water vapour corrosion rate of niobium.

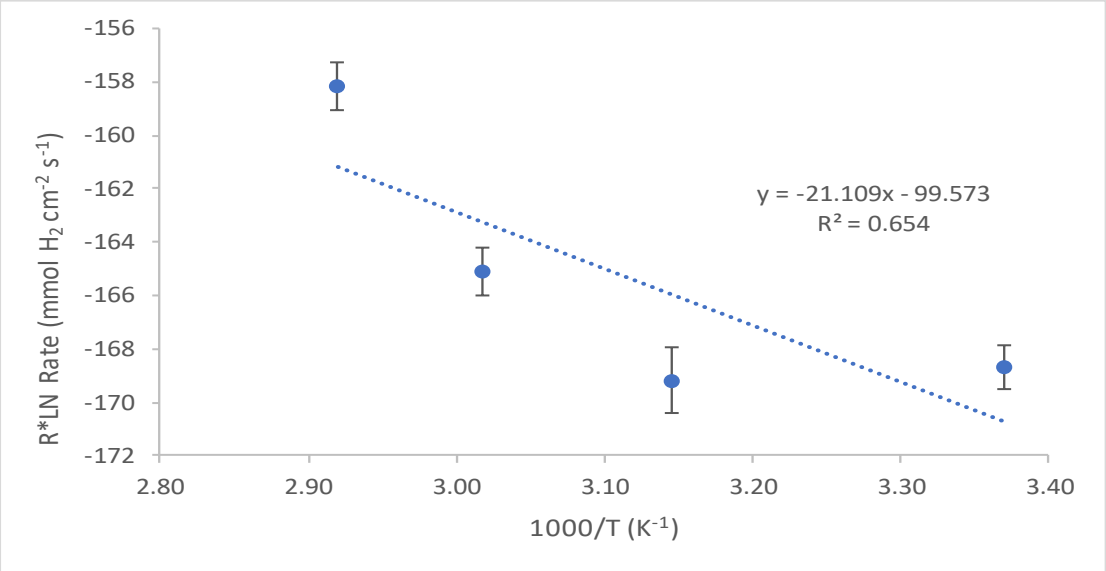

Figure 5.22 Arrhenius plot for the water vapour corrosion average rates of niobium. The error bars are calculated from the transducer %accuracy and are not an indication of confidence in the data.

The derived activation energy is 21.109 kJ mol^{-1}. Previous work has found Ea between 32 and 93 kJ mol^{-1} for the temperature range 800-1000 °C[35]. This temperature range is said to be in the breakaway region and therefore represents a different mechanism to the reaction conditions studied here.

When the rate data from the $D_2{}^{16}O$ reactions are compared to the $H_2{}^{18}O$ counterparts it can be seen that the rates are not too dissimilar (Table 5.3 and Figure 5.23). There is also a small difference in activation energy for the two regimes. For uranium, a significant difference in

the $D_2{}^{16}O$ and $H_2{}^{18}O$ rates was seen, with $H_2{}^{18}O$ being faster. There was also a large discrepancy in activation energy for uranium. It was suggested that there may be some form of contaminant/impurity present within the D_2O system such as oxygen, and for uranium this has been found to inhibit the rate. For niobium, however, oxygen has been said to possibly accelerate the rate, meaning the presence does not have the same inhibitory effect.

Table 5.2 Rate data for niobium at 30 mbar and four different temperatures - 70 °C, 55 °C, 45 °C and 30 °C.

Temperature			1000/T (K^{-1})	Starting pressure (mbar)		Rate (mmol H_2 cm^{-2} s^{-1})	Average rate (mmol H_2 cm^{-2} s^{-1})
Desired (°C)	Actual (°C)	Actual (K)		Desired	Actual		
70	69.16	342.31	2.92	32.30	31.57	5.30E-09	5.47E-09
	69.58	342.73	2.92		43.86	5.22E-09	
	69.33	342.48	2.92			5.01E-09	
	69.32	342.47	2.92		43.69	6.37E-09	
55	57.11	330.26	3.03	31.30	23.41	2.91E-09	2.38E-09
	56.59	329.74	3.03			2.96E-09	
	57.66	330.81	3.02			1.69E-09	
	60.12	333.27	3.00			3.16E-09	
	59.21	332.36	3.01		22.42	1.68E-09	
	59.26	332.41	3.01		27.07	1.85E-09	
45	44.75	317.90	3.15	28.90	29.28	1.21E-09	1.45E-09
	44.60	317.75	3.15			1.60E-09	
	44.98	318.13	3.14			8.92E-10	
	44.58	317.73	3.15			2.09E-09	
30	20.35	293.50	3.41	31.40	20.35	1.68E-09	1.50E-09
	23.66	296.81	3.37			1.66E-09	
	26.61	299.76	3.34			1.17E-09	

Table 5.3 Rate data for all niobium $H_2{}^{18}O$ experiments.

Temperature		**1000/T(K)**	**Starting Pressure (mbar)**	**Rate (mmol H_2 cm^{-2} s^{-1})**
°C	**K**			
64.36	337.51	2.96	412.9	1.38E-09
64.33	337.48	2.96	257.1	1.52E-09
69.74	342.89	2.92	57.97	1.51E-08
71.49	344.64	2.90	35.76	6.16E-09
58.36	330.00	3.03	21.48	2.13E-09
44.58	318.71	3.14	25.90	2.36E-09
26.63	299.71	3.34	19.33	2.33E-09

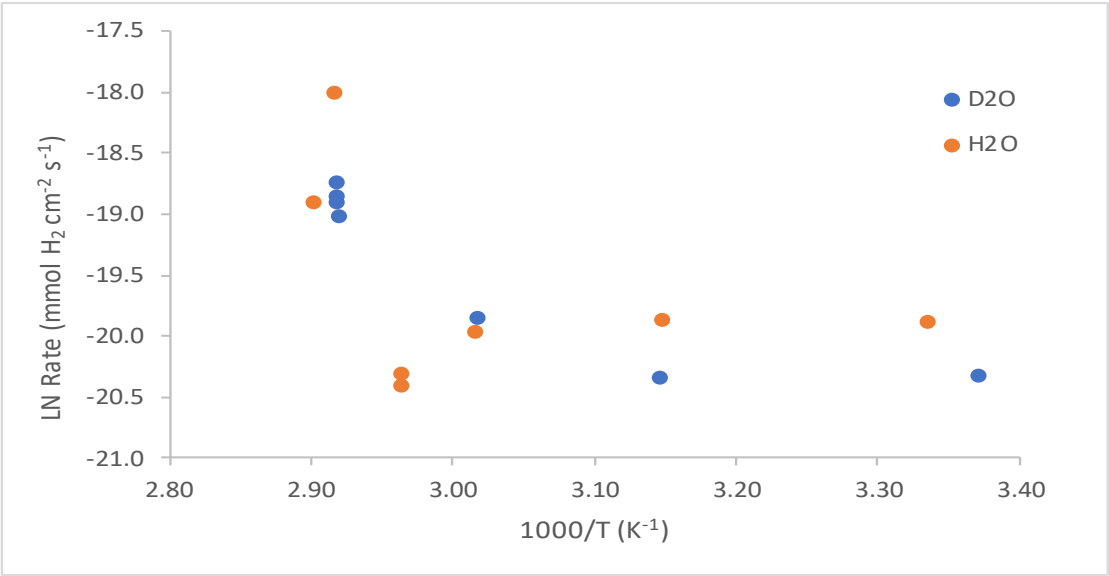

Figure 5.23 Graph comparing the niobium data for the $D_2{}^{16}O$ with the $H_2{}^{18}O$ experiments.

This focus of this work is on the corrosion of uranium niobium alloys. Both metals have been analysed to provide a base line for the alloy study. It is only right to compare the kinetic data for the two bulk metals, uranium and niobium. Figure 5.24 presents the rate data for the $D_2{}^{16}O$ and $H_2{}^{18}O$ experiments conducted in the temperature range of 20-70°C with the desired pressure of 30 mbar. As can be seen for the higher temperatures 70-45 °C uranium has a faster rate of reaction.

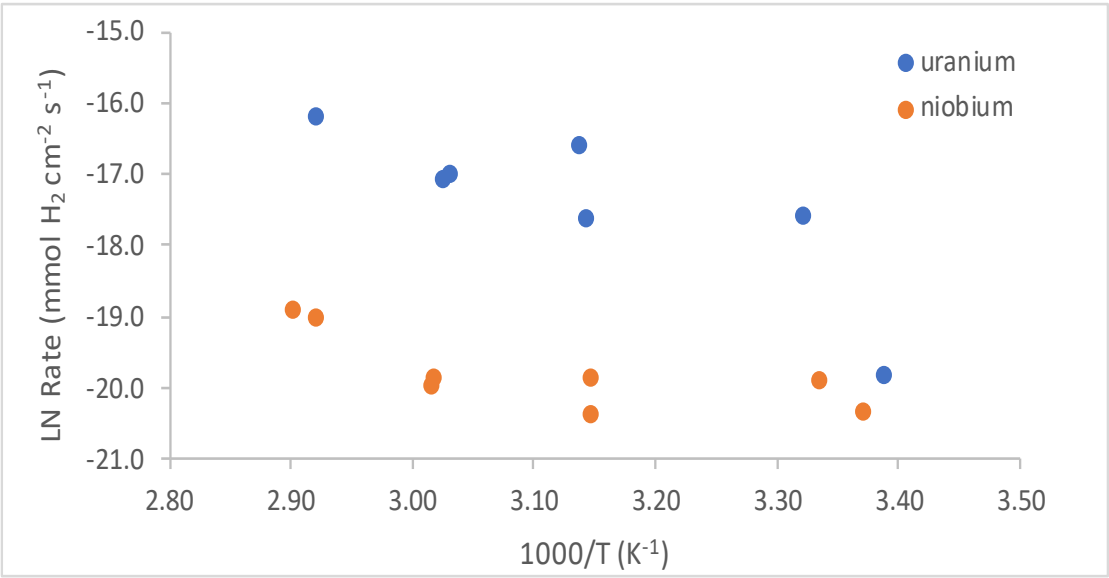

Figure 5.24 Graph comparing the niobium and uranium kinetic data for all water vapours ($D_2{}^{16}O$ and $H_2{}^{18}O$).

5.2.2 Reaction with water vapour plus oxygen

For niobium, previous literature has shown the addition of oxygen to the water vapour reaction to increase the rate. In the experiment conducted here, the $H_2O/^{16}O$ mix produced marginally faster reaction rates than the water vapour with no oxygen. Figure 5.25 and Figure 5.26 show the data from experiment with $H_2{}^{18}O$ + $^{16}O_2$ at 57.83 °C and a total pressure of 63.57 mbar (48 mbar of H_2O and 15 mbar of O_2). Figure 5.25 shows the pressure and temperature data while figure 5.26 shows the volume of gas within the reaction cell and the calculated rate data for the experiment. Table 5.4 contains the rate data for the two water vapour + oxygen experiments and the water vapour experiment for comparison.

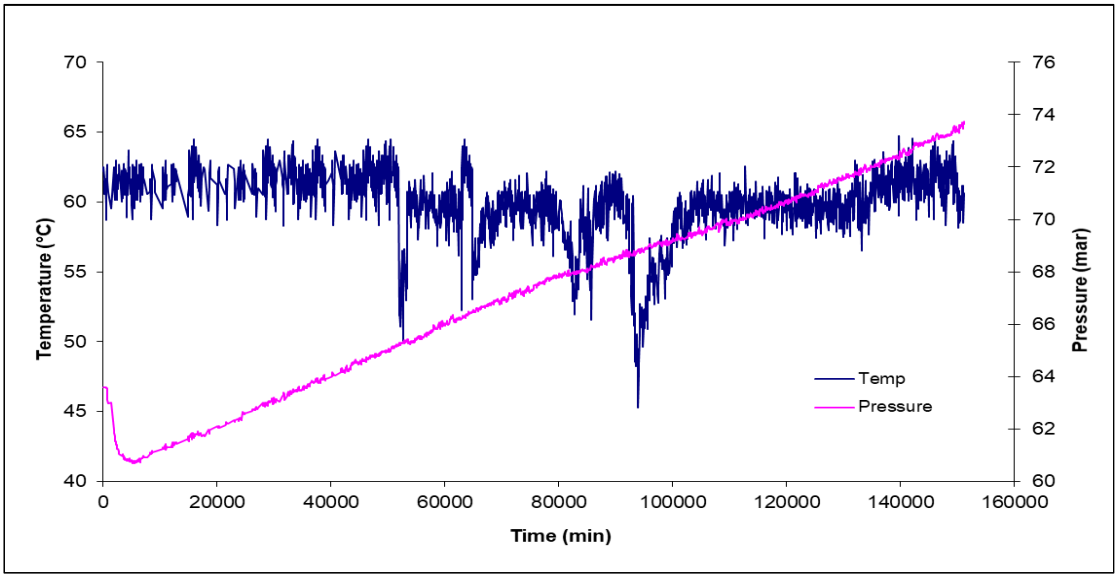

Figure 5.25 Pressure and temperature data for the niobium with $H_2{}^{18}O$ + $^{16}O_2$ at 59.75 °C and 63.57 mbar.

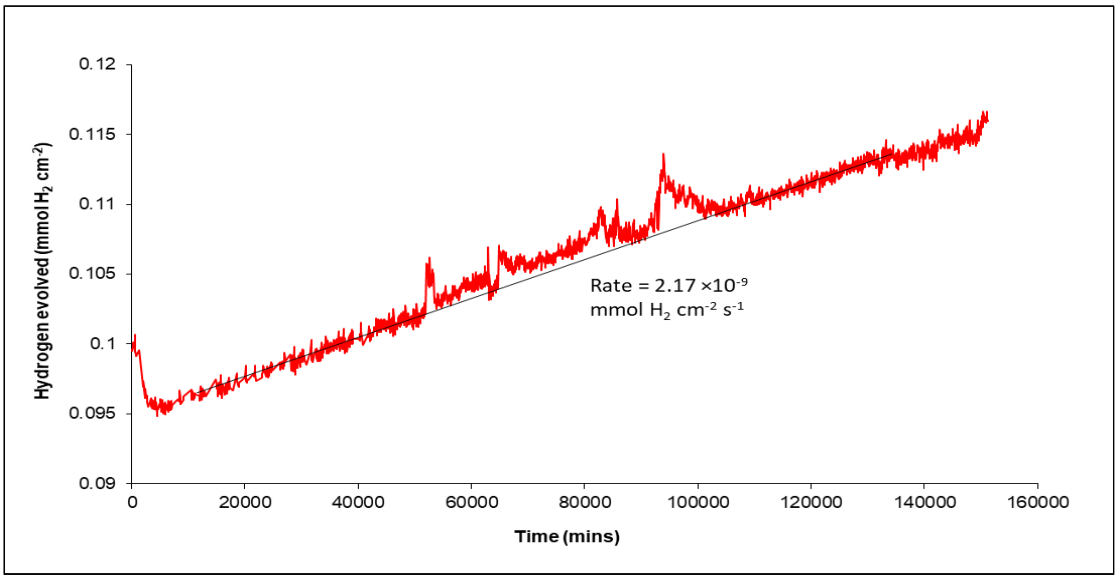

Figure 5.26 Volume of gas and rate against time for the niobium with $H_2{}^{18}O$ + $^{16}O_2$ at 59.75 °C and 63.57 mbar.

Table 5.4 Rate data for niobium at 55 °C in water vapour and water vapour plus oxygen mixture

Exposure mixture		Temperature		1000/T(K^{-1})	Starting Pressure (mbar)	Rate (mmol H_2 cm^{-2} s^{-1})
Water	Oxygen	(°C)	(K)			
$D_2{}^{16}O$	None	58.33	331.48	3.02	24.30	2.38E-09
$H_2{}^{18}O$	None	58.36	331.51	3.02	21.48	2.13E-09
$H_2{}^{18}O$	$^{16}O_2$	59.75	332.90	3.00	63.57	2.17E-09

Comparing the data in table 5.4 it can be seen that the rate for the water vapour plus oxygen reaction is similar to that of the pure water vapour reaction. Literature has shown the rate in water vapour to be slow compared to that with oxygen[31]. A much higher temperature is required with water vapour than oxygen to reach the breakaway phase which is related to the formation of Nb_2O_5 oxide[28]. The addition of a small partial pressure of oxygen to the water vapour has been shown previously to result in accelerated oxidation according to the normal kinetics for oxidation in oxygen. In this case it was found that the oxygen reacted preferentially with the niobium, and the protective oxide film was reformed when all the oxygen had been consumed[31].

5.2.3 Summary

- No pressure dependence seen for niobium; previous work by Blackburn showed a cubic dependence
- Arrhenius relationship seen with an E_a of 21.9 $kJmol^{-1}$; previous work showed a range of 39-93 $kJmol^{-1}$ for temperatures 800-1000 °C
- Rates appear similar with $H_2{}^{18}O$ than $D_2{}^{16}O$ – while uranium showed faster rates with $H_2{}^{18}O$
- The addition of oxygen to the reaction did not have a marked effect on the kinetics.
- Rates for niobium water vapour reaction are slower compared to uranium

5.3 SIMS analysis of corroded samples

Following exposure to $D_2{}^{16}O$ and $H_2{}^{18}O$ the reacted niobium samples were analysed using SIMS. The use of isotopically-labelled water (O or H) allowed some mechanistic information to be deduced from SIMS depth profiling of the oxide surface. Any change in the oxygen ions in the profile provides fundamental information on the diffusing species and the overall

reaction. For the water vapour experiments initially $D_2{}^{16}O$ was used followed by a switch to $H_2{}^{18}O$. Therefore, changes from ^{16}O and ^{18}O containing ions are key. The use of deuterated water allows investigation into any hydride formation that has previously been seen[46,47].

Blackburn[28] proposed that the reaction at low temperatures involves solution of oxygen in the metal and formation of NbO and NbO_2 on the surface. At higher temperatures the initially protective film of Nb_2O_5 is supplanted by a scale which offers no barrier to rapid oxidation; this is deemed breakaway oxidation. The mechanism for this is the nucleation and growth of Nb_2O_5 on NbO_2. For water vapour it has been found that this growth is much slower than for oxygen, meaning that the protective phase of oxidation lasts for a longer time.

For niobium, information on the analysis of the oxidised surface by SIMS is very limited, especially at low temperatures. Therefore, an additional experiment using $D_2{}^{16}O$ only was conducted at 58.15 °C and 27.07 mbar starting pressure. This allowed the spectra and depth profiles from the SIMS analysis to provide a baseline for the sequential D_2O/H_2O experiments.

5.3.1 Analysis after $D_2{}^{16}O$ only

Figure 5.27 presents positive spectra from the D_2O experiment, with figure 5.27b focussing on the niobium metal and hydride peaks. Table 5.5 presents the masses for the peaks of interest. There are a number of peaks associated with hydrogen; these are due to the small amount of hydrogen present within the D_2O solution, hydrogen in the air and residual hydrogen within the SIMS chamber.

From figure 5.27a it can be seen that the dominant oxide is NbO at 108.7 daltons. There is also a clear hydride peak seen at 96.8 daltons which is associated with either NbH_4 or NbD_2. A mass spectrum was run between 260-280 daltons in order to look for the Nb_2O_5 peak; however, any peaks were masked in the background.

Figure 5.28 presents the negative spectra from the D_2O experiment, focussing on the oxygen ions as these are dominant in negative mode. Table 5.5 presents the masses for the peaks of interest. Again, there are peaks linked with hydrogen; these are due to the small amount of hydrogen present within the D_2O solution, hydrogen in the air and residual hydrogen within

the SIMS chamber. It can be seen that the intensity of the low mass oxygen peaks (16-19 daltons) is significantly greater than that for the higher mass ions containing niobium (100-150 daltons). This means that if both niobium and oxygen ions are profiled together then the niobium ions would produce very low counts and tend to be lost within the profile. Due to this, depth profiles were separated to focus on the oxygen ions and then on the niobium-containing ions. For the D_2O only experiment the oxygen ion profiles are less important. However, for the experiments involving sequential water exposures ($D_2{}^{16}O$ then $H_2{}^{18}O$) the oxygen profiles may show important mechanistic information.

a)

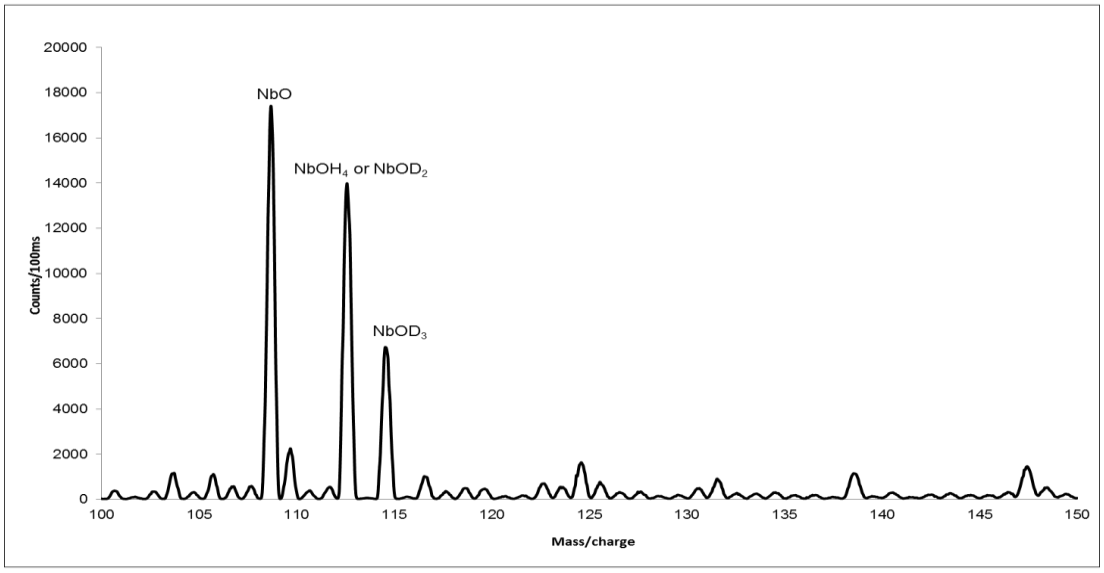

b)

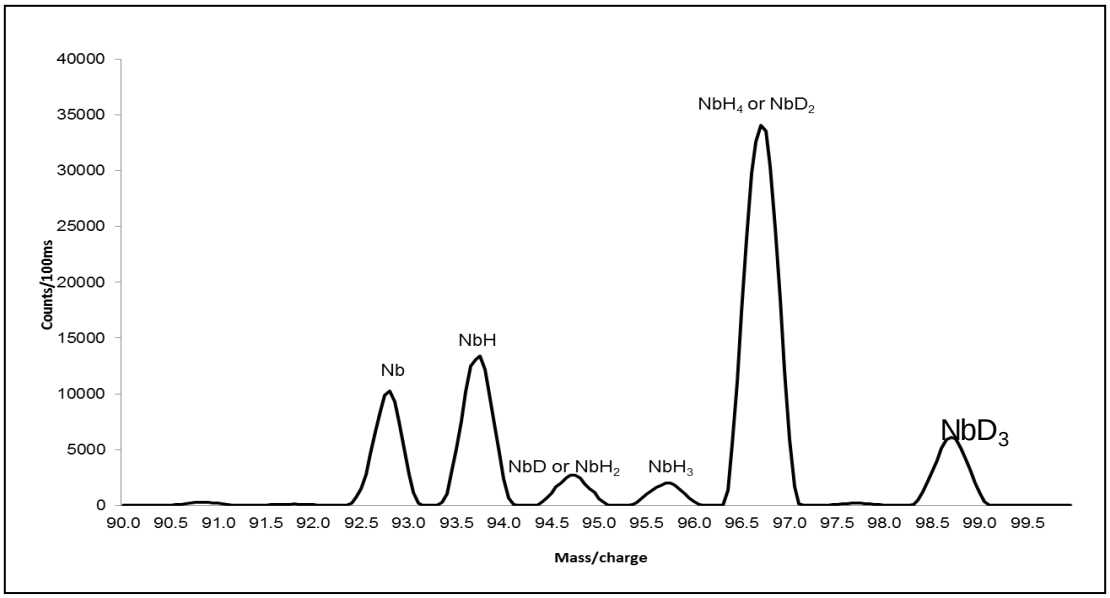

Figure 5.27 Spectra of the positive ions for the niobium exposed to D_2O only experiment, a) 100-200 mass range, b) focussing on the niobium metal and hydride ions (90-100 mass range).

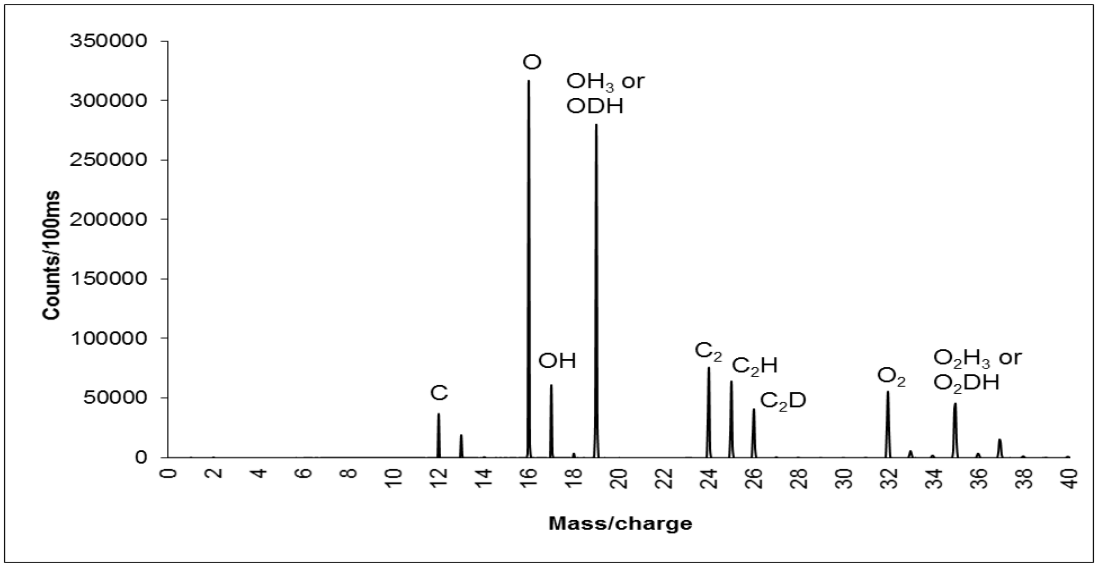

Figure 5.28 Spectrum of the negative ions for the niobium exposed to D_2O only experiment 0-100 mass range, showing the oxygen ions.

Figure 5.29 presents the positive depth profiles from the D_2O experiment. The beam current and magnification were altered due to the oxide being relatively thin. Previously a beam current of 3 nA had been used. However, this was found to be etching through the niobium oxide too quickly so the beam current was lowered to 1 nA. The magnification and beam current alter both the etch area and the sputter rate, values for both are included in the figure captions (Figure 5.29 and 5.30).

Table 5.5 Associated masses of the positive and negative ions for the niobium exposed to D_2O only experiment.

Positive mode		Negative mode	
Mass	**Possible ion**	**Mass**	**Possible ion**
93	Nb	16	O
94	NbH	17	OH
95	NbH_2 or NbD	18	OH_2 or OD
96	NbH_3or NbHD	19	OH_3
97	NbH_4 or NbD_2	93	Nb
99	NbD_3	94	NbH
109	NbO	95	NbD
110	NbOH	109	NbO
111	$NbOH_2$ or NbOD	110	NbOH
112	$NbOH_3$	111	$NbOH_2$ or NbOD
113	$NbOH_4$ or $NbOD_2$	112	$NbOH_3$ or $NbOH_2D$
115	$NbOD_3$	117	$NbOD_4$
117	$NbOD_4$	125	NbO_2
125	NbO_2	126	NbO_2H
127	NbO_2H_2 or NbO_2D	127	NbO_2H_2 or NbO_2D
128	NbO_2H_3	128	NbO_2H_3

Figure 5.29a shows the main ions as niobium oxide (NbO), niobium hydride (NbH_4 or NbD_2) and niobium metal. The profiles for the metal and oxide appear parallel with one another. The hydride peak decreases in intensity gradually with etch depth. There are also some hydroxides present. These suggest that OH^- (or OD^-) from the water vapour is involved in the mechanism. The presence of hydride also helps to reaffirm that OH^- is the diffusing species. Figure 5.29b is a profile using a lower beam current. Therefore, the oxide and metal peaks are the focal point of the profile. Again, hydride and hydroxides are present but their intensities are relatively low. The oxide and metal peaks are again aligned with one another. In figure 5.29c a higher magnification is used (x1000 compared to x300 for figures 5.30a and 5.30b). Therefore, the peaks of oxide and metal are not seen and there is just the gradual decline in intensity with depth before the metal ion dominates.

Figure 5.30 presents the negative depth profiles from the D_2O experiment. The beam current and magnification were altered due to the oxide being relatively thin. Previously a beam current of 3 nA had been used. However, this was found to be etching through the oxide too quickly. Therefore, the beam current was lowered to 1 nA.

Figure 5.30a shows the main ions as niobium oxide (NbO and NbO_2) and niobium metal (Nb). There is no spike/peak seen; the intensities simply decrease gradually with depth. This profile was taken using a 3 nA beam current. Therefore, if the oxide is relatively thin, the surface may have been etched too quickly. Figure 5.30b shows a profile where the beam current was reduced to 1 nA, and this profile shows a clear spike in intensities for the oxides (NbO and NbO_2), in addition to one for niobium metal (Nb) and a possible niobium hydroxide (NbO_2H_3). Figure 5.30c presents the depth profile for the oxygen ions. From this figure it can be seen that the oxygen ion is dominant but that there is also a clear peak for a hydroxyl at a lower intensity.

a)

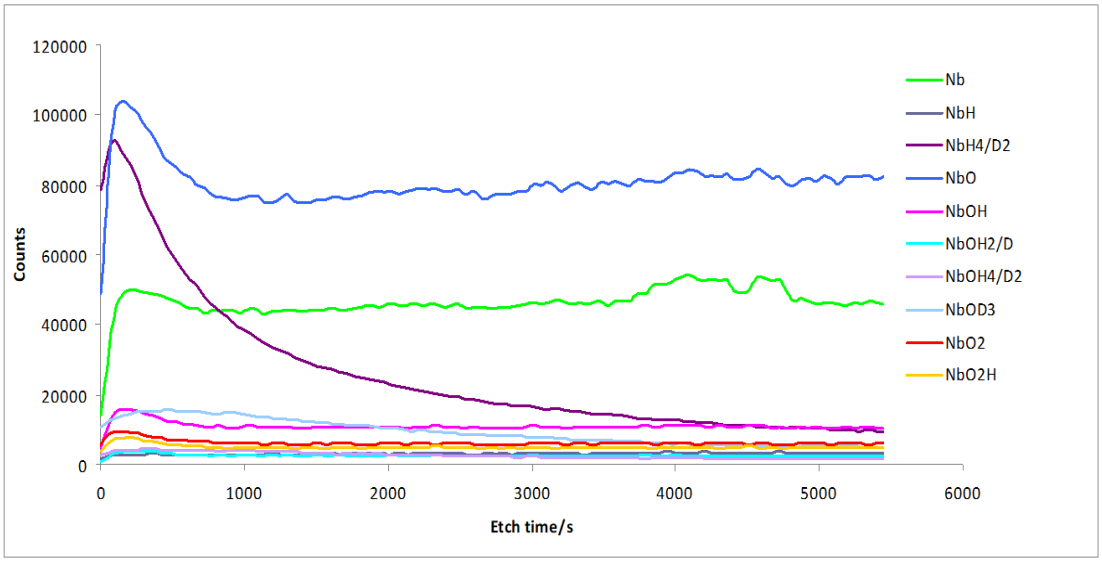

b)

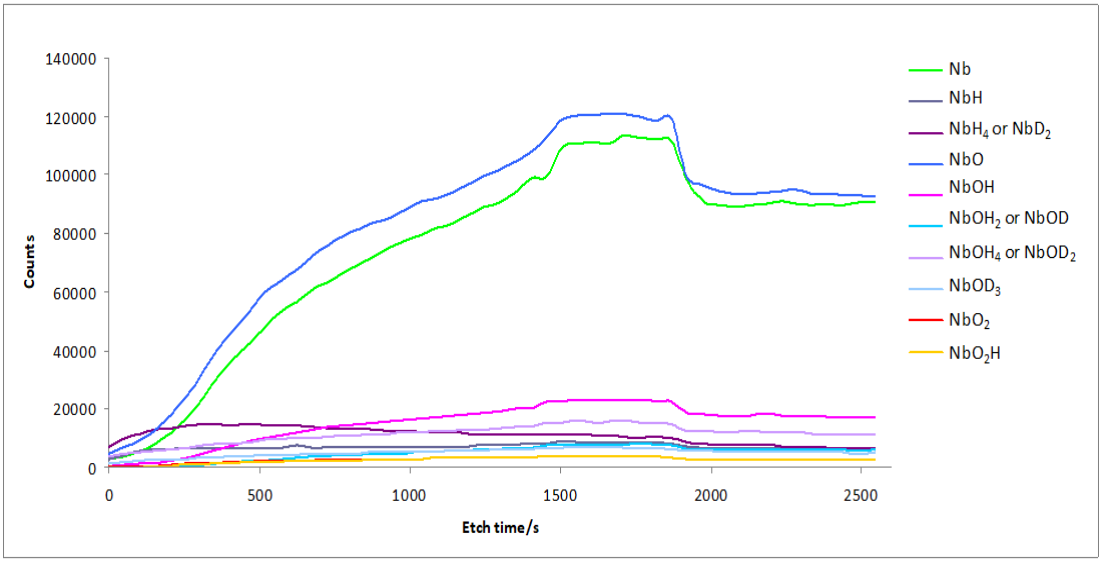

c)

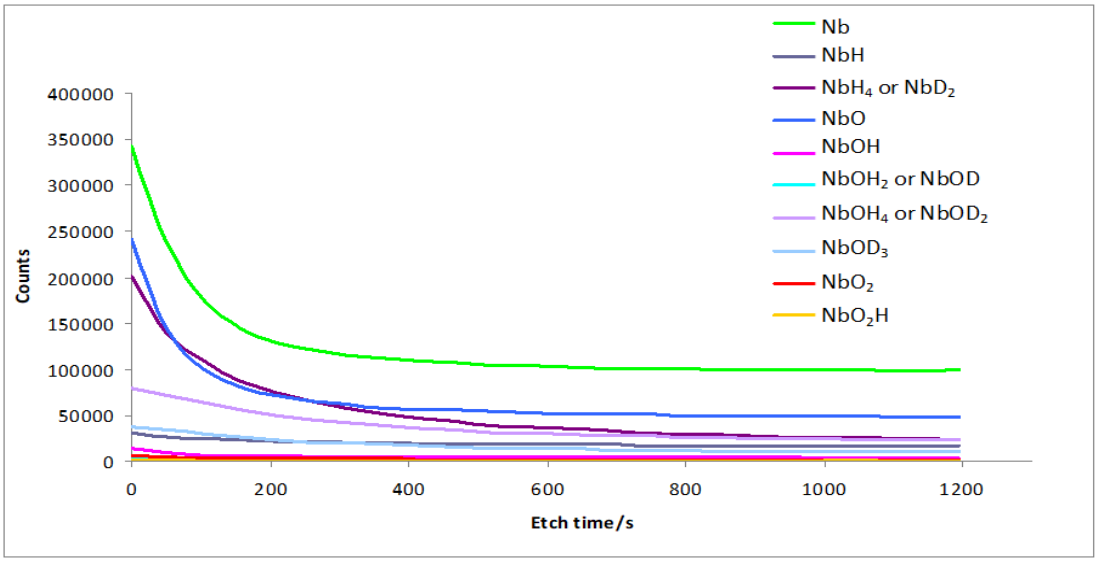

Figure 5.29 Positive depth profiles of niobium exposed to $D_2{}^{16}O$ only, a) magnification of x300, beam current 3 nA, etch area of 234999 µm², sputter rate 0.0068 nm/s b) magnification of x300, beam current 1 nA, etch area of 234999 µm², sputter rate 0.0023 nm/s c), magnification of x1000, beam current 1nA, etch area of 21950 µm², sputter rate 0.0253 nm/s.

a)

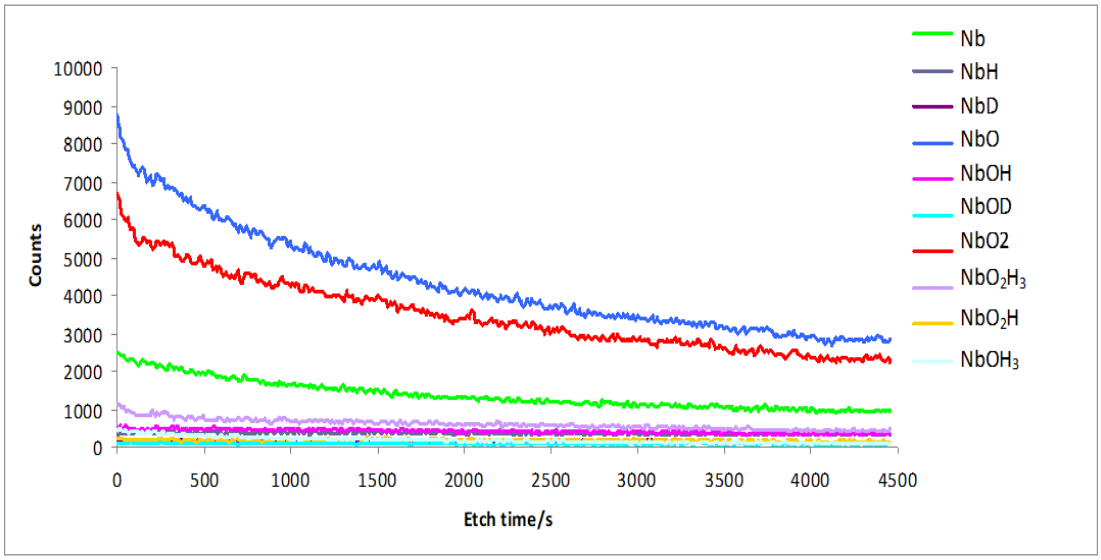

b)

Figure 5.30 Negative depth profiles of niobium exposed to $D_2{}^{16}O$ only, a) magnification of x300, beam current 3 nA, etch area of 234999 µm², sputter rate 0.0068 nm/s, b) magnification of x300,beam current 1 nA, etch area of 234999 µm²,sputter rate 0.0023 nm/s, c) profile of the oxygen ions at a magnification of x300, beam current 1 nA, etch area of 234999 µm², sputter rate 0.0253 nm/s.

5.3.2 Analysis after exposure to sequential water vapour

The kinetic data have been used to provide an estimate of the oxide thickness for each of the samples. Table 5.6 shows the oxide thickness from each of the water vapour exposures. SRIM has been used in order to calculate sputter yields for niobium and oxygen in Nb_2O_5, as this is the most thermodynamically stable oxide (section 3.4.4). From this sputter yield a depth can be determined for each profile, presented later in Table 5.7. Therefore, from the estimated thickness from the kinetic data and the etch depth calculated from SRIM it is possible to determine whether the oxide metal interface has been reached during the profiles. For the majority of the samples the depth profiles should be through the oxide and have reached the oxide-metal interface. For the experiments conducted at 66.93 °C and 307.76 mbar and 70.42 °C and 39.71 mbar only positive mode depth profiles are presented as there was an issue with the collection in negative mode.

Table 5.6 Calculated oxide thickness values for all of the niobium experiments. The total time includes the exposure to both $D_2{}^{16}O$ and $H_2{}^{18}O$. This value can then be compared to the etch depths of SIMS analysis.

Temperature (°C)	Pressure (mbar)	Water	Exposure time (hours)	Time to grow 1µm Nb_2O_5 (hours)	Thickness of Nb_2O_5 (µm)
66.93	307.67	$D_2{}^{16}O$	10058.0	1401.4	7.2
		$H_2{}^{18}O$	6493	1401.4	4.6
		Total			**11.8**
69.98	263.63	$D_2{}^{16}O$	3745.0	892.4	4.2
		$H_2{}^{18}O$	5182	892.4	5.8

		Total			**10.0**
69.61	66.88	$D_2{}^{16}O$	6494.0	919.4	7.1
		$H_2{}^{18}O$	1489	919.4	1.6
		Total			**8.7**
70.42	39.71	$D_2{}^{16}O$	5269.0	1044.1	5.0
		$H_2{}^{18}O$	10561	1044.1	10.1
		Total			**15.2**
58.34	24.30	$D_2{}^{16}O$	13863.0	2425.9	5.7
		$H_2{}^{18}O$	2829	2425.9	1.2
		Total			**6.9**
44.65	29.28	$D_2{}^{16}O$	15759.0	3981.8	4.0
		$H_2{}^{18}O$	0	3981.8	0.0
		Total			**4.0**
25.09	20.35	$D_2{}^{16}O$	12655.0	3749.1	3.4
		$H_2{}^{18}O$	4123	3749.1	1.1
		Total			**4.5**

Table 5.7 Etch depths calculated using SRIM, a sputter yield of 2.17 nm/s was used.

Temperature (°C)	**Pressure (mbar)**	**Mode of SIMS**	**Depth profile (seconds)**	**Gun current (nA)**	**Magnification**	**Etch depth (µm)**
66.93	307.67	positive	13872.0	3.0	x5000	24.7
		negative	NO PROFILE			
66.98	263.63	positive	18040	3.0	x5000	32.1
		negative	17492.0	3.0	x3000	11.3
69.61	66.88	positive	5969	3.0	x5000	10.6
		negative	6829	3.0	x5000	12.2
70.42	39.71	positive	10806	3.0	x5000	19.2
		negative	NO PROFILE			
58.34	24.30	positive	11107	3.0	x5000	19.8
		negative	3921.0	3.0	x5000	7.0
44.65	29.28	positive	18099	3.0	x5000	32.2
		negative	16617	3.0	x3000	10.8
25.09	20.35	positive	5405	1.0	x100	0.012
		negative	5371	1.0	x100	0.012

Figure 5.31 shows depth profiles for the niobium water vapour experiment at 69.50 °C and 307.67 mbar. Figure 5.31a is the depth profile presented in terms of counts vs etch time. The prevailing species were Nb and Nb_2. However, if the profile is zoomed in to the first 1000 s and a maximum of 3000 counts, a change from $Nb^{16}O$ to $Nb_2{}^{18}O_5$ at approximately 700 s can be seen.

The change in oxide can be seen more clearly in figure 5.31b where the oxygen-containing species are collated. Figure 5.31b uses the data from the depth profile in figure 5.31a to construct profiles showing the % oxide fractional composition as a function of oxygen isotopes and oxygen containing molecular ions respectively. For more details on this refer to section 3.4.3.

As can be seen in figure 5.31b there is a crossover in oxygen isotopes. As the oxygen-18 appears after the oxygen-16, the profile suggests that the new oxide is formed at the metal-oxide interface and that therefore anionic diffusion is occurring with the oxygen-containing species diffusing inwards to the metal-oxide interface. Figure 5.31c shows a clear change from NbO to Nb_2O_5 as the profile gets deeper into the sample.

a)

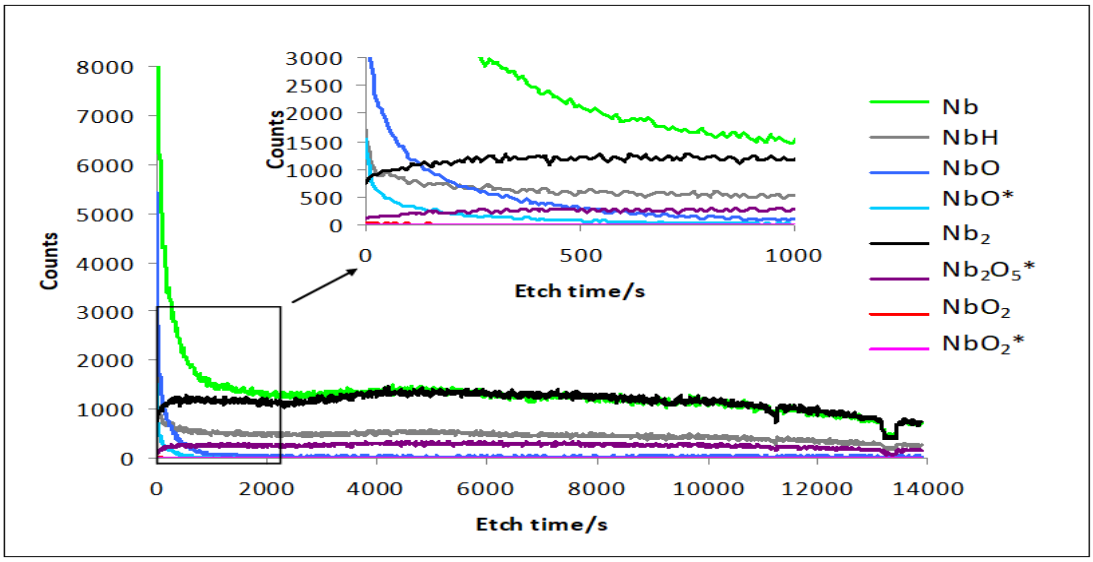

b)

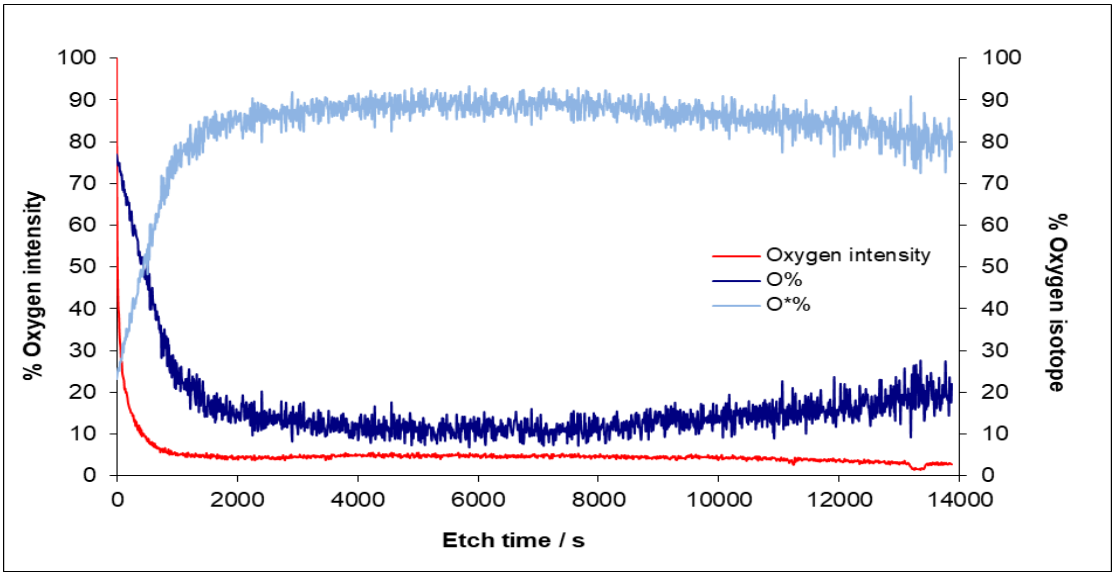

c)

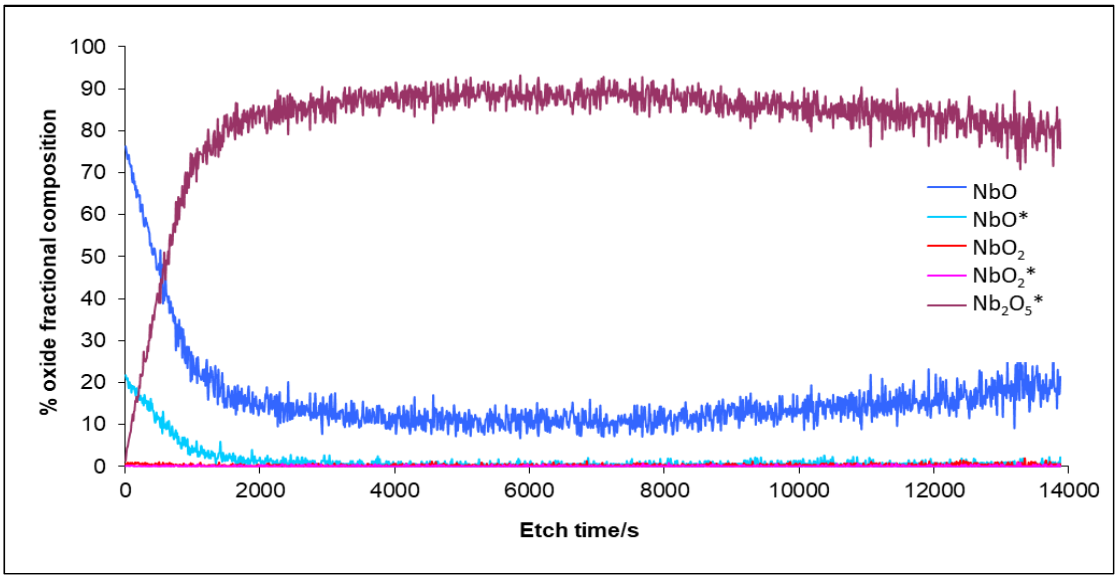

Figure 5.31 SIMS depth profile data from the experiment at 66.93 °C and 307.67 mbar, a) positive depth profile, b) profile showing % fractional composition with respect to oxygen isotopes, c) profile showing % fractional composition with respect to molecular ions of interest.

Figure 5.32 shows depth profiles for the niobium water vapour experiment at 69.48 °C and 67.57 mbar in negative modes and the % oxygen fractional composition for this profile. From the depth profile (figure 5.32a) it can be seen that after the oxygen ion peaks, there are peaks for niobium hydride (NbH, NbH_2/D and NbD_2). Niobium hydride has been detected previously using various techniques[46,48,78]. The region of hydride trails off at 2500 s and is replaced by the oxygen ions once more. In figure 5.32b, the % oxygen fractions show that the principal ion is O-16.

a)

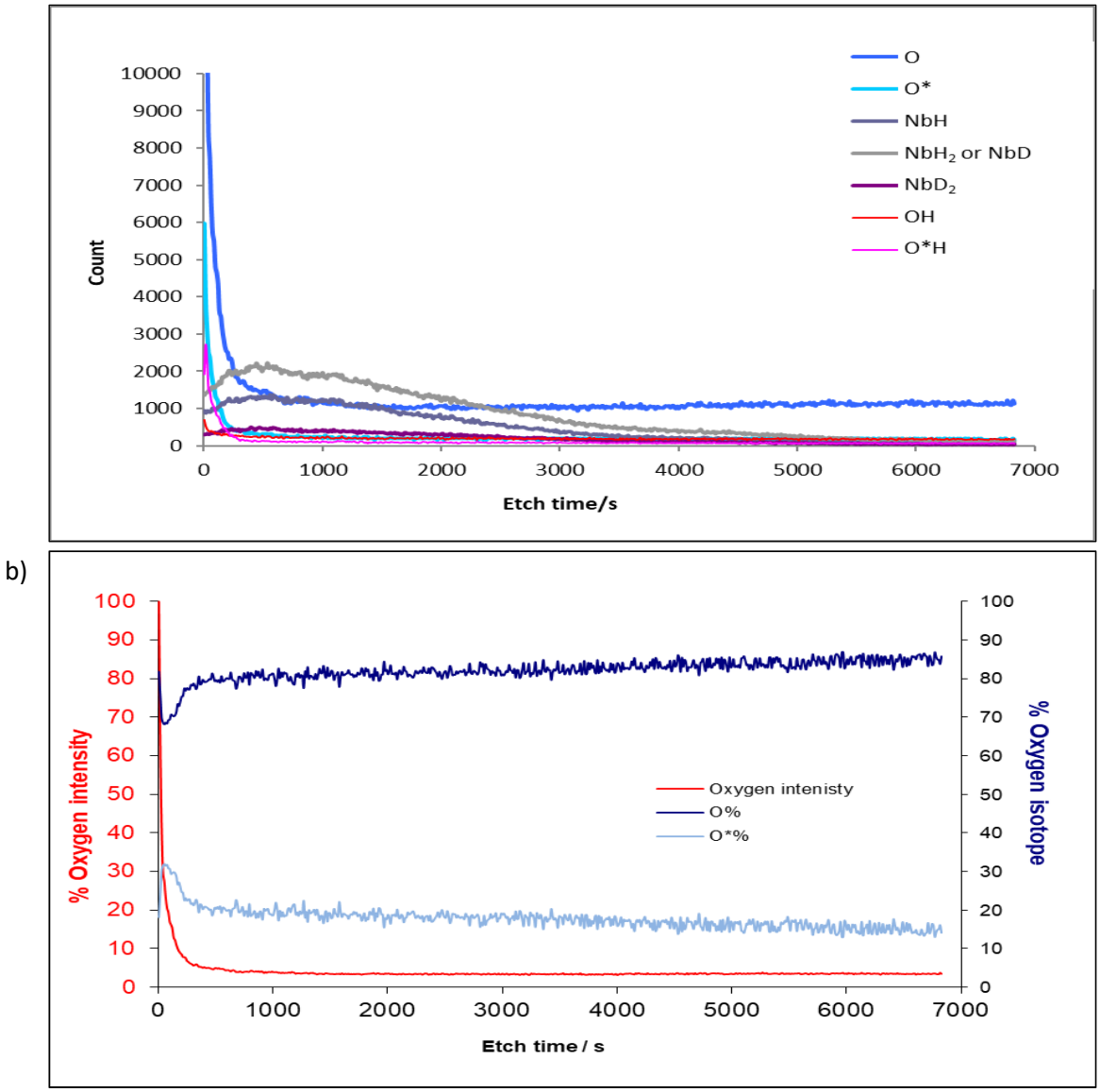

Figure 5.32 Data from the experiment conducted at 69.48 °C and 67.57 mbar, a) negative depth profile, b) % oxygen fractional composition, with respect to oxygen isotopes.

a)

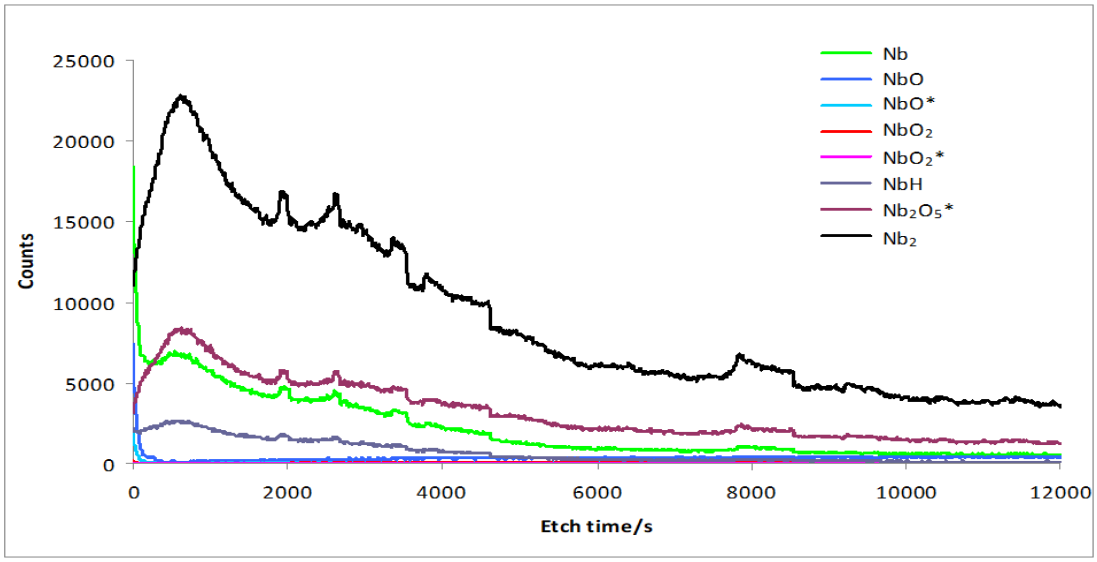

b)

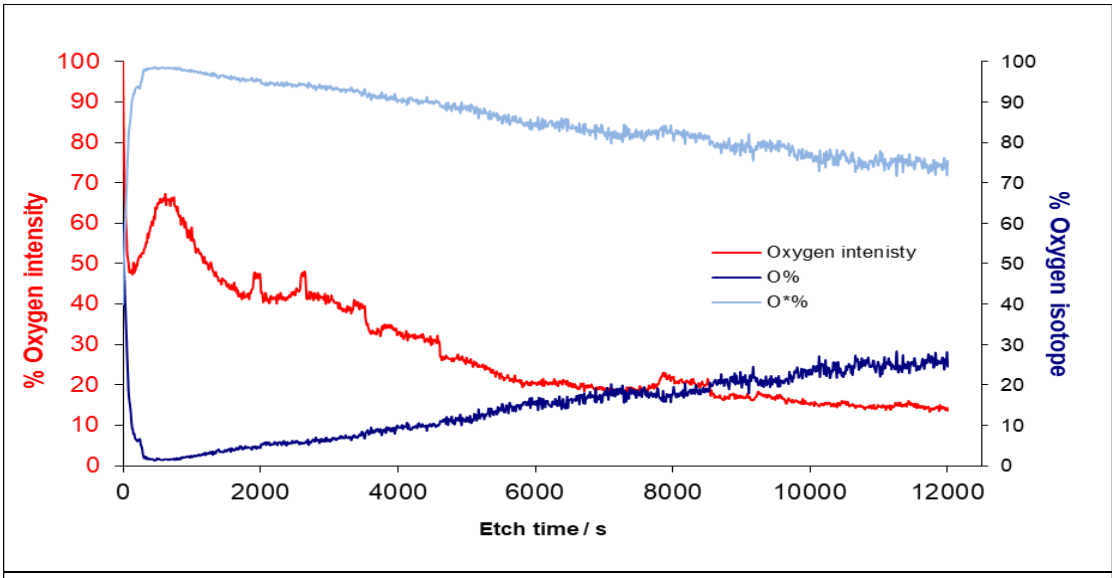

c)

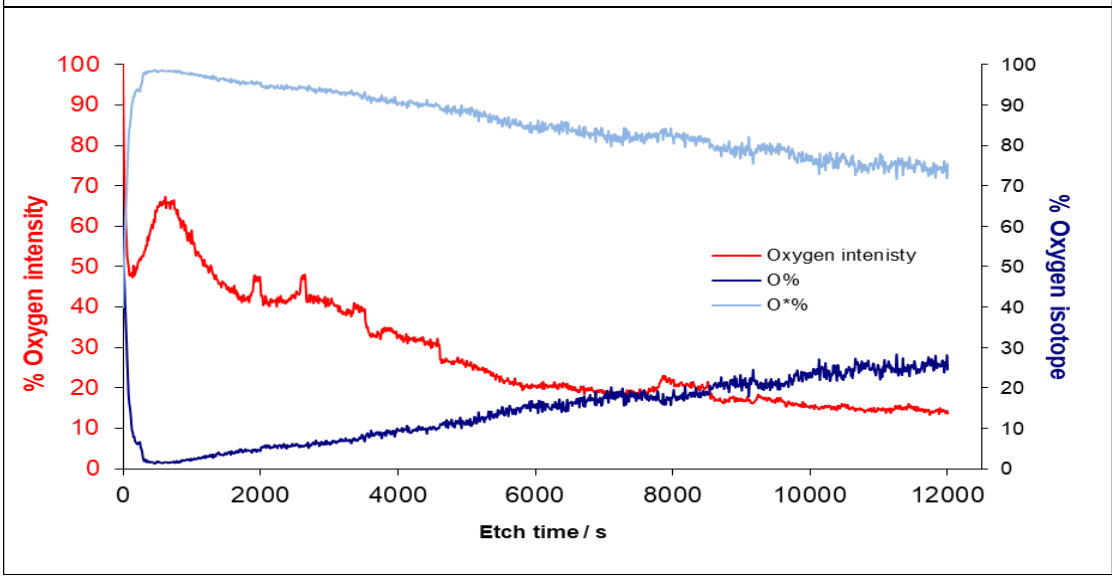

Figure 5.33 SIMS data from the experiment conducted at 69.34 °C and 37.57 mbar, a) positive depth profile, b) % fractional composition with respect to oxygen isotopes, c) % fractional composition with respect to molecular ions of interest.

Figure 5.33 shows depth profile for the niobium water vapour experiment at 69.34 °C and 37.57 mbar in positive mode. The profiles are presented in terms of counts vs etch time. The prevailing species were Nb and Nb_2 followed by $Nb_2{}^{18}O_5$. The positive profile is very similar to those seen for the 69.50 °C 307.67 mbar experiment (Figure 5.31). When the % oxygen isotope is calculated for each of the profiles, the results again are similar to the experiment conducted at 69.50 °C and 307.67 mbar. For the positive profile, the dominant oxygen isotope is O-18, with the dominant oxide species being Nb_2O_5*. The percentage of O-18 (and Nb_2O_5*) is decreasing throughout the profile, with the O-16 concentration therefore increasing.

Figure 5.34 shows depth profiles for the niobium water vapour experiment at 44.73 °C and 29.28 mbar in positive and negative modes. For the positive depth profile (figure 5.34a) it can be seen that the species with the highest counts are Nb and NbO. Following these species there a number of species around the 10000-20000 counts. The most dominant species is NbO_2. This is then overtaken by NbH at 2500 s and Nb_2 at 7500 s. In the negative depth profile, the O-16 ion prevails followed by NbD and Nb. The labelled oxides are not in high abundance in this experiment; this is seen clearly in Figure 5.36 where the % oxygen fractions are plotted for each of the positive and negative depth profiles. The oxide Nb_2O_5* was detected in the mass spectra. However, within the profile the intensity is minimal, this is in contrast to the profiles for the experiments conducted at ~ 70 °C.

a)

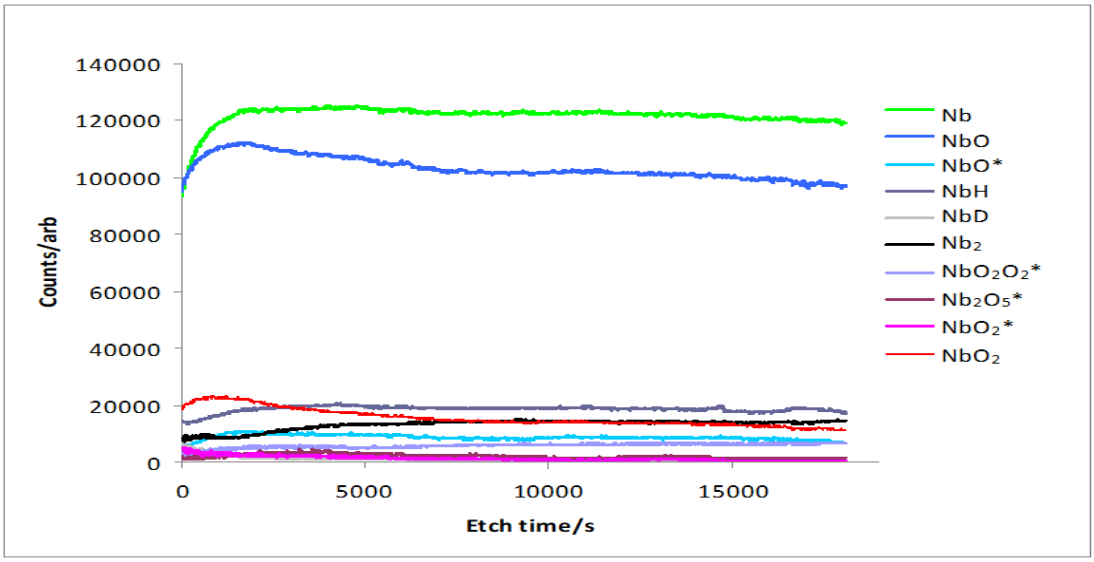

b)

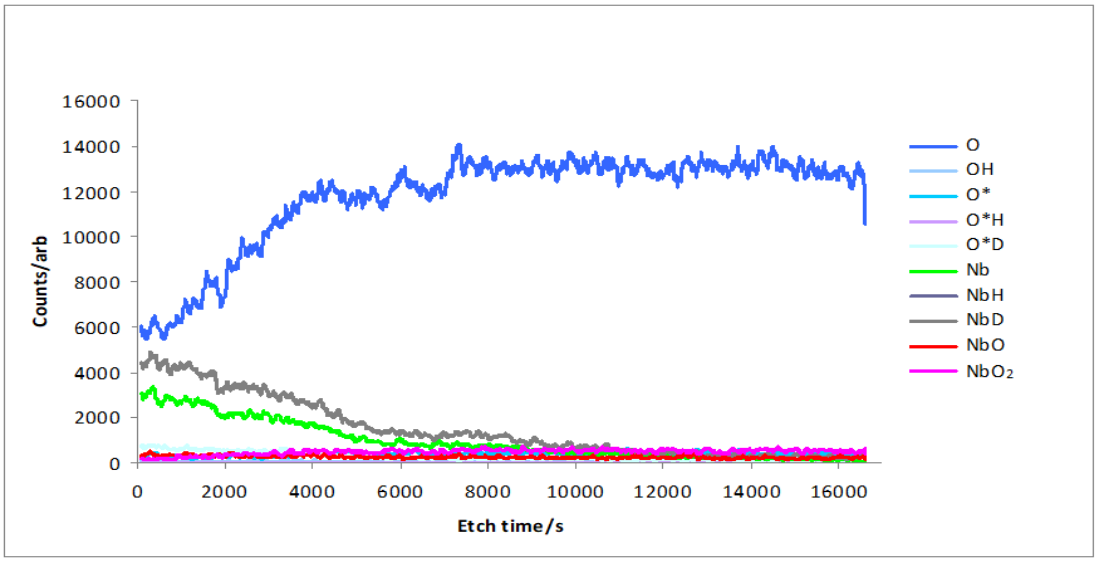

Figure 5.34 Depth profiles from niobium experiment at 44.73 °C 29.28 mbar in the form of counts/arb vs etch time/s, a) positive depth profile, b) negative depth profile.

a)

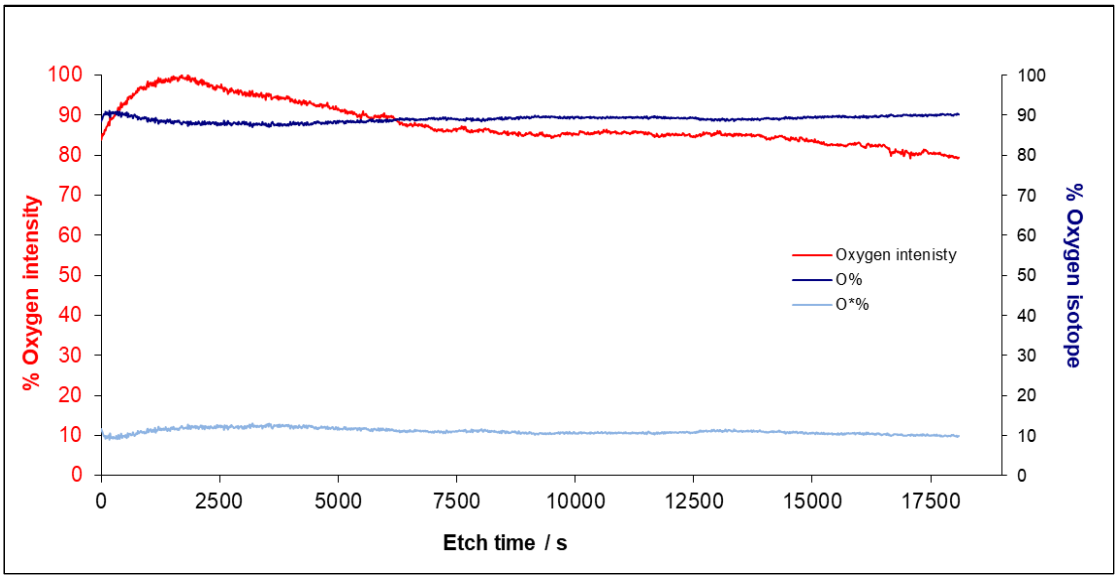

b)

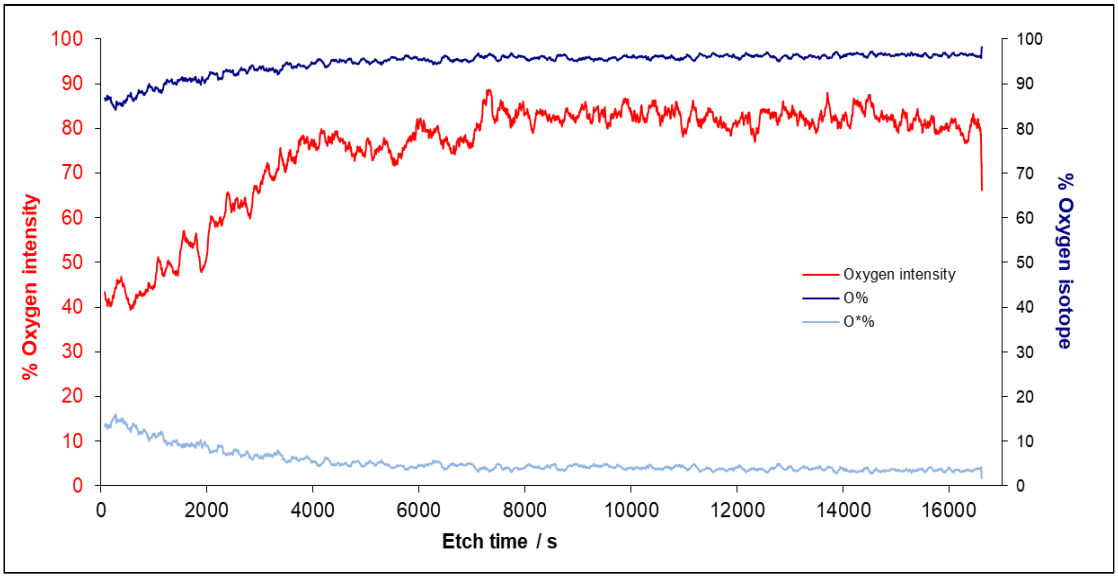

Figure 5.35 % oxygen fractional composition data from the experiment conducted at 44.73 °C and 29.28 mbar, a) positive profile, b) negative profile.

Figure 5.36 shows depth profiles for the niobium water vapour experiment at 30 °C and 30 mbar in positive and negative modes. The profiles are very similar to the 45 °C experiment, with Nb and NbO dominating in positive mode and O in negative. Again, the labelled oxides are not in high abundance in this experiment. This is seen clearly in Figure 5.37 where the % oxygen fractions are plotted for each of the positive and negative depth profiles.

a)

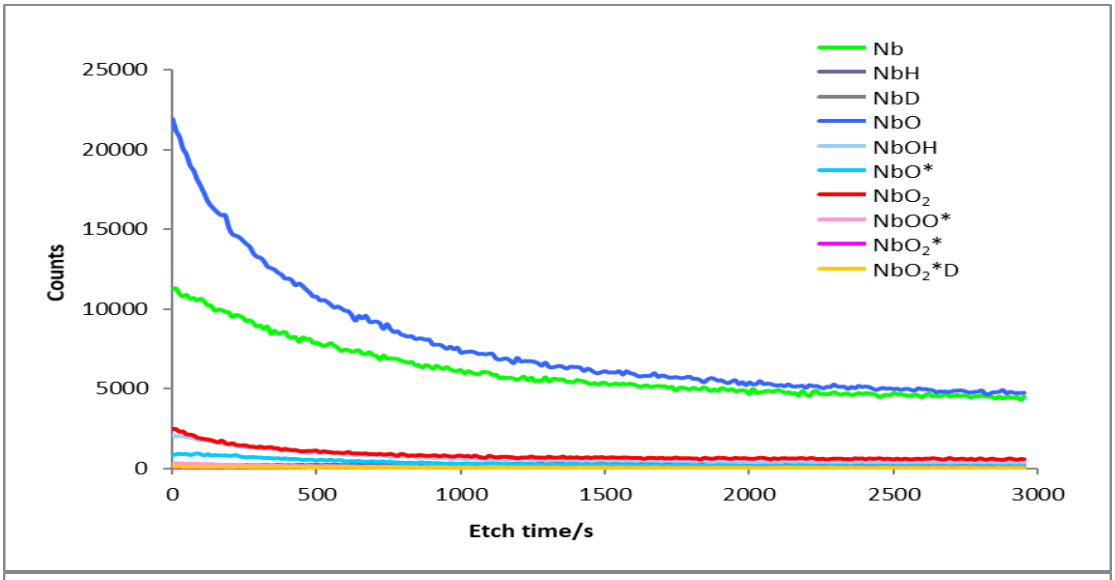

b)

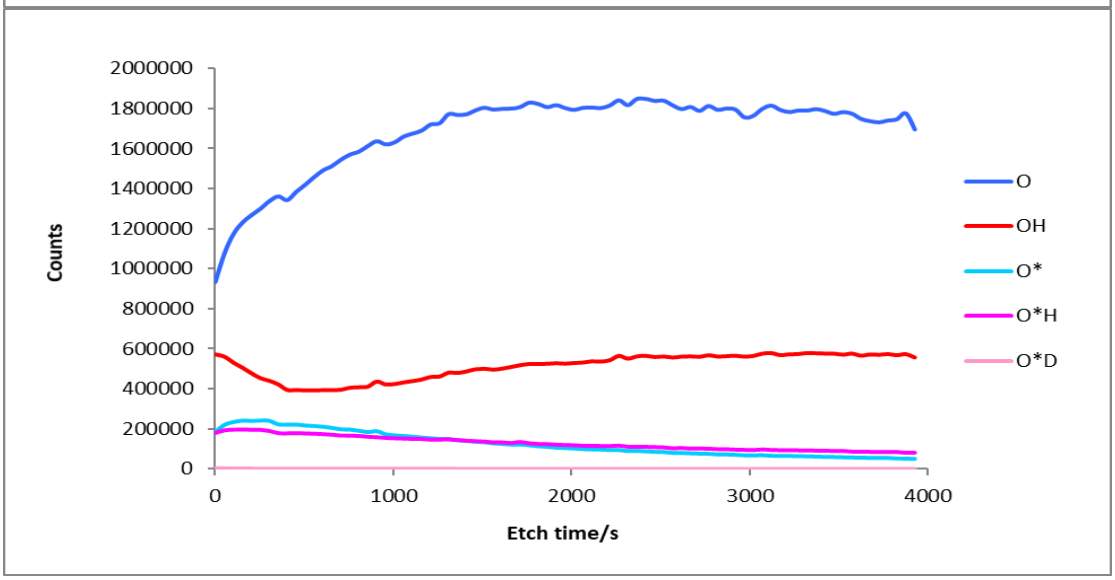

Figure 5.36 Depth profiles from niobium experiment at 23.54 °C and 20.35 mbar in the form of counts vs etch time, a) positive depth profile, b) negative depth profile.

a)

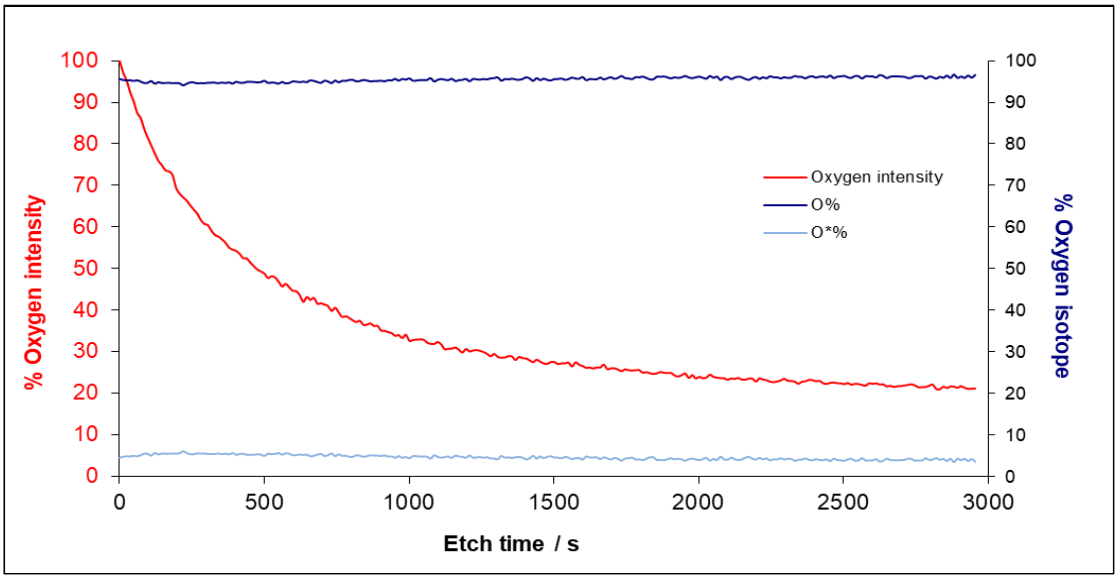

b)

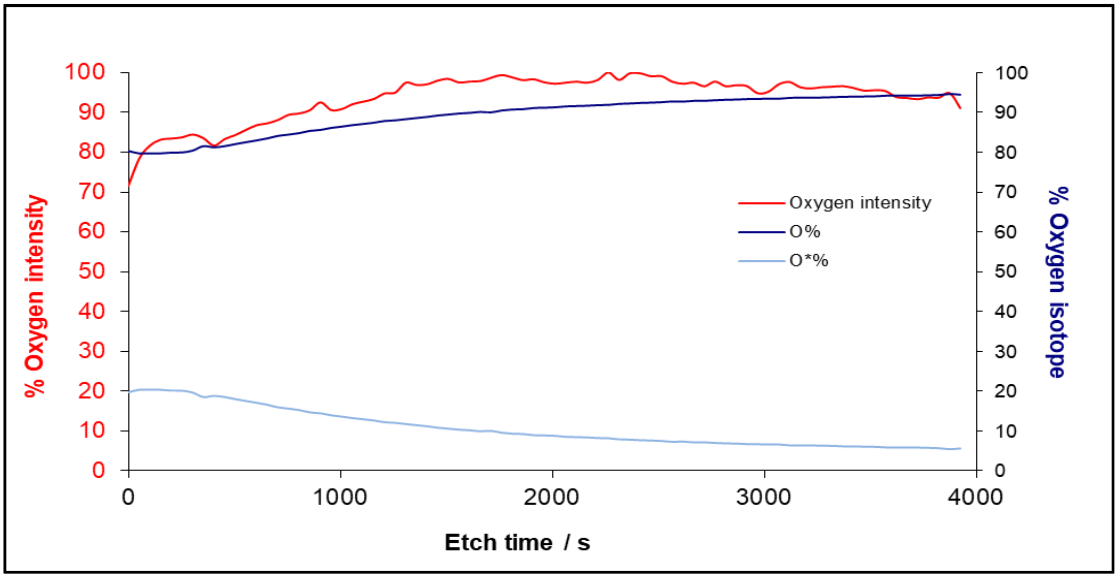

Figure 5.37 % oxygen fractional composition data from the experiment conducted at 23.54 °C and 20.35 mbar, a) positive profile, b) negative profile.

For the majority of the profiles it has been found that the oxygen-16 ion dominates. The exceptions to this are in the positive depth profiles of the 70 °C and 307 mbar experiment, the 70 °C and 43 mbar experiment and the 70°C 263 mbar experiment (data not shown). In these profiles the dominant oxygen isotope is O-18, with the dominant species Nb_2O_5*. In the experiments conducted at lower temperatures the Nb_2O_5* ion was either not detected or was detected with a very low intensity. It is important to note that it is the oxygen-18 pentoxide detected, as $H_2{}^{18}O$ is the second oxide exposure. It suggests that the formation could possibly be related to length of exposure.

The profiles show mixed oxides containing both O-16 and O-18 species. Therefore, deducing relevant mechanistic information is challenging. The exposures were administered sequentially and over long exposure times. Therefore, it is possible that there may be a mixture of oxide products and possibly dissociated oxygen ions on the surface that contribute to the SIMS depth profiles. The contribution of ^{16}O versus ^{18}O can be compared to the water vapour exposure times of $D_2{}^{16}O$ and $H_2{}^{18}O$ respectively, see Table 5.8.

It can be seen that the oxygen percentages within the SIMS depth profiles often do not reflect the % exposure times. It is often the case that there is significantly more O-16 present. A possible reason for the increased O-16 is residual air within the SIMS chamber as well as air exposure during transfer or storage in-between analyses. There are a few experiments where the O-18 % from the SIMS profiles is significantly greater than expected. For these instances it is possible that there are isotope ions with the same mass and therefore could be either an O-16 or an O-18 species, therefore effecting the calculated values.

Table 5.8 Comparison of the % water vapour exposure time for the two waters studied (D_2O and $H_2{}^{18}O$) with the average % of each oxygen isotope (O-16 and O-18 respectively) detected within the SIMS depth profiles.

Temperature (°C)	Pressure (mbar)	% water vapour exposure time		SIMS operating mode	Average % oxygen within SIMS depth profiles	
		$D_2{}^{16}O$	$H_2{}^{18}O$		^{16}O	^{18}O
66.93	307.67	61	39	positive	18	82
66.98	263.63	42	58	positive	26	74
				negative	85	15
69.61	67.57	81	19	positive	84	16
				negative	84	16
70.42	37.57	33	67	positive	10	90
58.34	23.41	83	17	positive	92	8
				negative	15	85
25.09	20.35	75	25	positive	92	8
				negative	93	7

Looking at the profiles compared to the data seen for uranium (section 4.3.1), it can be seen that the oxide is considerably thinner which allows a slightly more detailed analysis, with the detection of the oxide-metal interface in some of the profiles. It also allows SIMS to detect

the relatively low quantities of hydride present within the niobium system. For the uranium analysis the oxide was too thick to permit the technique of depth profiling to detect any thin layers of hydride.

5.3.3 Analysis after exposure to water vapour plus oxygen

The water vapour plus oxygen experiments were carried out in two ways –

1) $H_2{}^{18}O$ and $^{16}O_2$ together within the reaction cell
2) $D_2{}^{16}O$ and $^{18}O_2$ together within the reaction cell

5.3.3.1 $H_2{}^{18}O + {}^{16}O_2$ system

Figure 5.38a presents the positive depth profile; initially NbH is present followed quickly by Nb. In the first negative profile (figure 5.38b) species containing niobium are profiled. The signal for higher masses is much less in negative mode and therefore these ions become swamped when O/O* are profiled. There is a clear peak in NbO and NbO_2 at 250 seconds. There is a species with mass 128 present, this could either be a mixed oxygen hydroxide (NbOO*H) or a mixed hydrogen hydroxide (NbO_2HD) suggesting that some form of exchange has occurred, possibly a mechanism of H_2O recombination similar to that seen for uranium[2,3,74] could be occurring (section 4.3). The second negative depth profile (figure 5.38c) presents the oxygen ions. In this profile O and O*H are the main species present. They peak at approximately 250 and 500 seconds respectively before slowly decreasing, exchanging overall dominance a couple of times on the way.

Figure 5.39 presents the % oxygen fractions for both the positive and negative profiles from figure 5.38. In the positive profile O-16 is clearly the leading ion. This is also the case for the negative profile for the niobium ions (figure 5.39b). However, in the negative profile the isotopes are a lot closer in percentage with them being approximately equal for a period of 500 seconds. This corresponds to the period in the depth profile (figure 5.39b) where O*H overtakes O as being the main ion.

a)

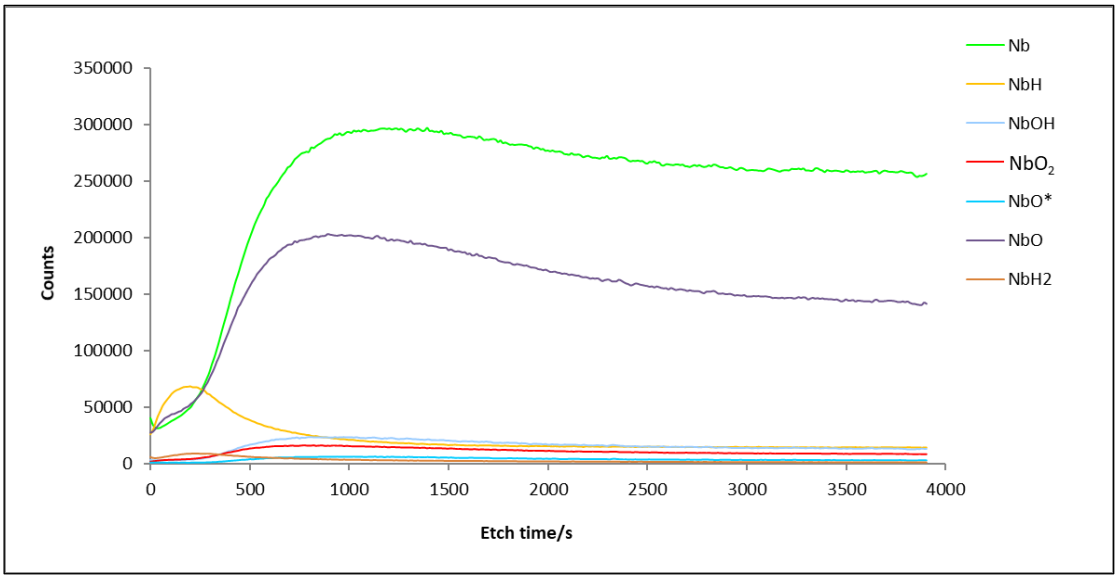

b)

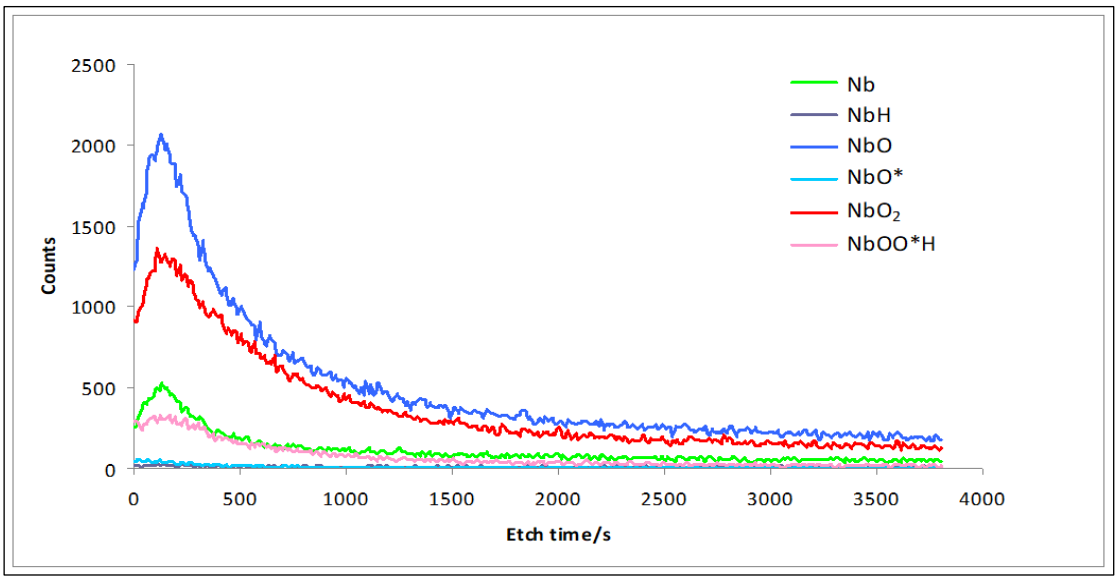

c)

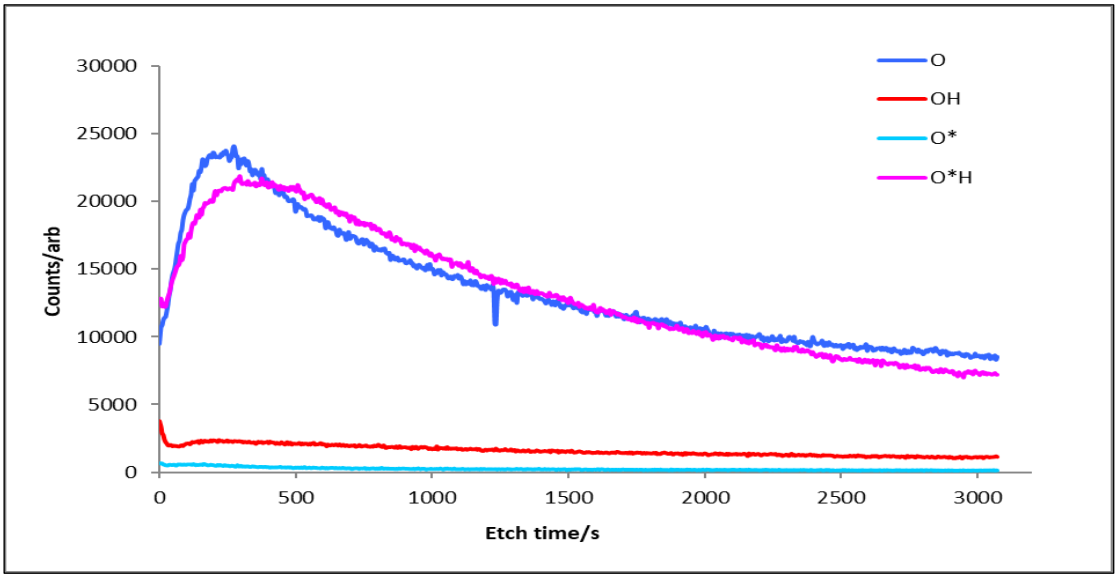

Figure 5.38 Depth profiles of niobium experiment $H_2{}^{18}O$ + $^{16}O_2$ at 59.75 °C and 63.57 mbar, a) positive profile, b) negative profile showing Nb ions, c) negative profile showing O ions.

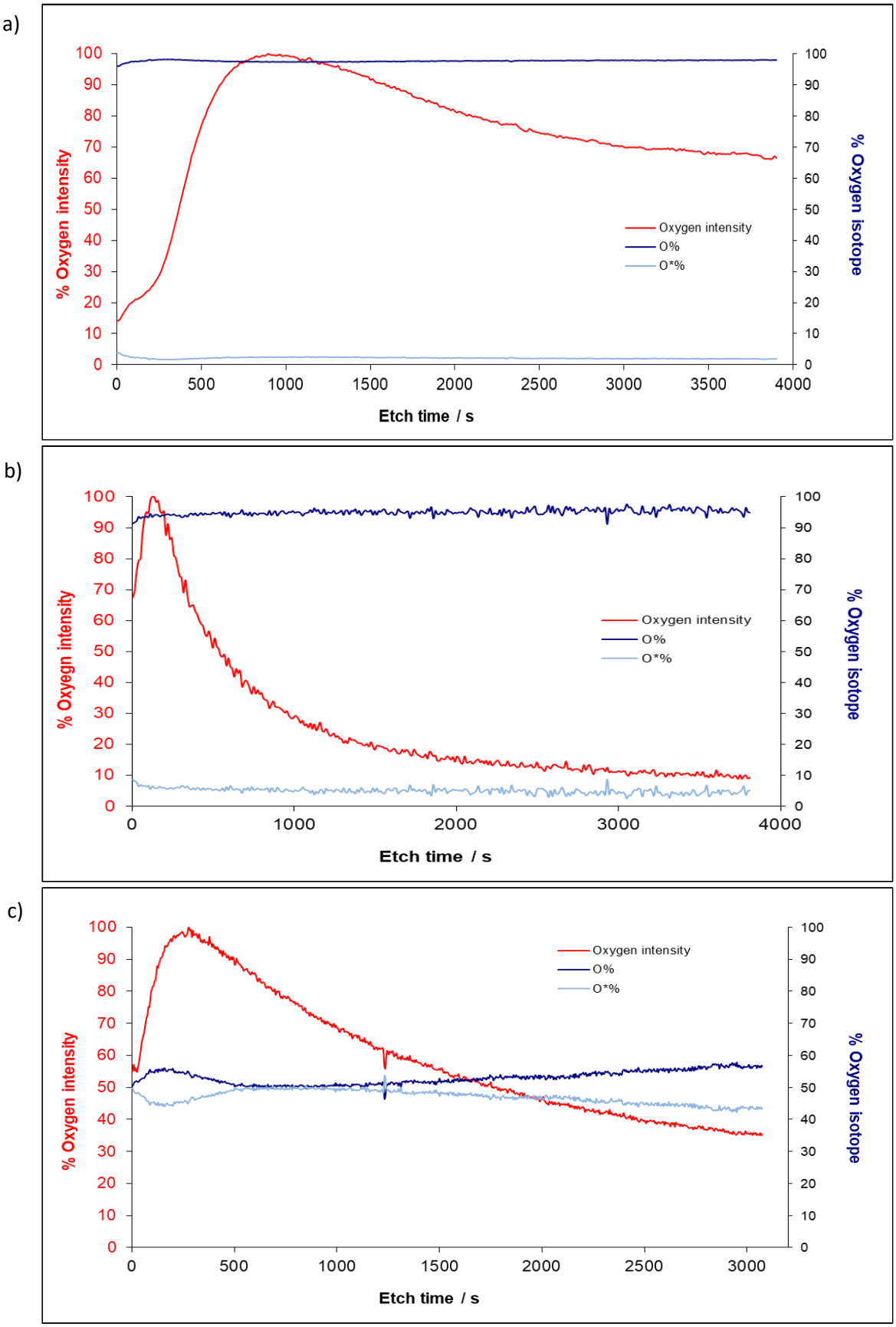

Figure 5.39 % oxygen fractional composition data from the experiment conducted with $H_2{}^{18}O$ + $^{16}O_2$ at 59.75 °C and 63.57 mbar, a) from the positive depth profile, b) from the negative niobium profile, c) from the oxygen negative depth profile.

This dominance of O-16 possibly suggests that the reaction is occurring with the oxygen species from the oxygen rather than the water. This has previously been suggested for uranium[22]. However, the SIMS results presented in section 4.3 did not support this theory. For niobium the reaction with oxygen is faster than the reaction with water vapour[35]. This is opposite to that seen for uranium[4]. The kinetics of the water vapour plus oxygen reaction showed no change compared to the water vapour only reaction, suggesting that there is no significant change in mechanism.

Passier[35] suggested that for the water reaction OH transport is not involved and that H_2O is rapidly and completely decomposed in to NbO_2, followed by very slow oxygen incorporation into the oxide lattice. A dramatic decrease of the reaction rate was seen when hydrogen was added, indicating that the dissociative adsorption of H_2O is an equilibrated step. It was suggested therefore that the limiting step is surface reaction of oxygen incorporation into the oxide scale. Therefore, a dominance of the O ions from the oxygen is not unexpected. The presence of mixed oxides suggests that some form of exchange reaction occurs within the system, possibly similar to that seen for uranium. Hydrogen is present from the decomposition of water; it is available to react with the metal to form hydride (as previously seen) or it is possible that it may combine with free oxygen ions at the surface to form water.

5.3.3.2 $D_2{}^{16}O + {}^{18}O_2$ system

Figure 5.40a presents the positive depth profile; initially NbD_2 is dominant followed quickly by a hydroxide (NbO*D or $NbOD_2$). The number of variants in this system makes it difficult to accurately determine the species present. The presence of the hydroxides suggests that an exchange has occurred as the oxygen-18 species arises from the oxygen and not from the water.

In the first negative profile (figure 5.40b) oxygen ion species are profiled. In this profile O*H or OHD are the main species present, with the O* and O ions next. The mass of 19 daltons can be associated with either O*H or OHD, both of which would involve some form of exchange to occur. The presence of minimal oxygen-16 oxides (NbO and NbO_2) suggest that water is not involved in the formation of oxide and its involvement is simply decomposing to

release hydrogen and oxygen, that can undergo further reaction to form hydride and oxide respectively.

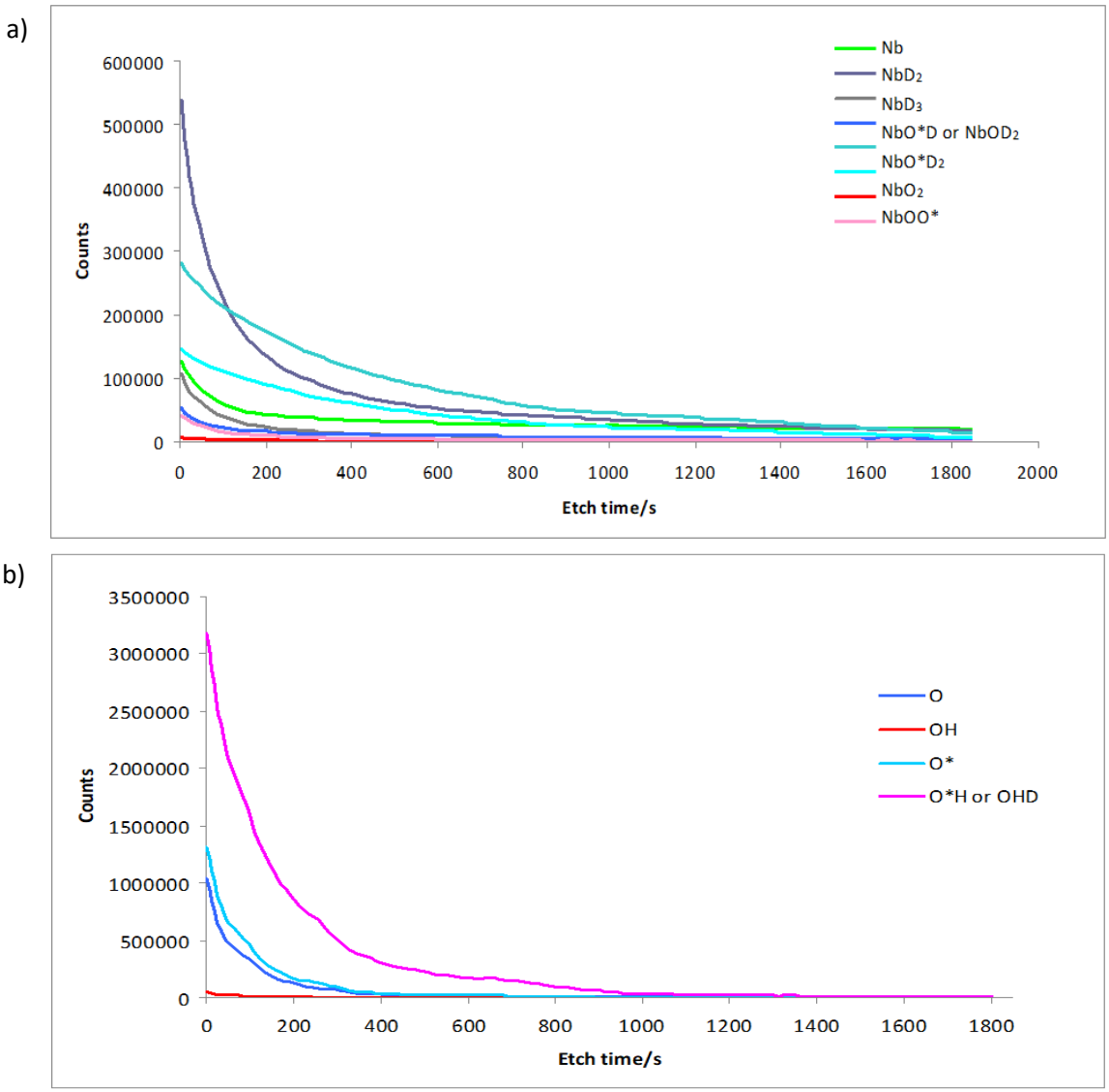

Figure 5.40 Depth profiles of niobium experiment with $D_2{}^{16}O + {}^{18}O_2$, a) positive profile, b) negative profile showing O ions.

5.3.4 Summary

The variety in the data does not allow a full mechanism to be determined. If the O-18 oxide was seen to peak after the O-16 then anionic diffusion could be confirmed, with the oxygen species diffusing inwards and the fresh oxide forming at the oxide-metal interface. If the O-16 peaked after the O-18 then the opposite would be true.

However, the SIMS depth profiles do not show these consistent changes. One reason for this may be the length of the experiments. The majority of the experiments have been oxidising for a couple of years meaning there is likely to be significant quantities of dissociated oxygen and water (O^{2-} or OH^-) species present on the surface and diffused within in the oxide itself. Also the SIMS profiles are etched to a significant depth, as discussed in the uranium section, (section 4.3). It is likely that there will be interference from the walls of the etched region and the emitted secondary ions. The deeper you go the less clean the signal becomes with regards to the buried interfaces and the ion yield (to the detector) decreases because of ion collision with the trench walls (figure 5.24). This means that a clean interface may not be seen. To fully understand the water corrosion of niobium, shorter sequential oxidation (using $D_2{}^{16}O$ then $H_2{}^{18}O$) water vapour experiments are required.

In the experiments with water vapour and oxygen, the SIMS analysis suggests that the reaction is via the oxygen and not the water. This is the opposite to what was seen for uranium, where the dominating oxide contained oxygen from the water vapour. However, Passier[35] found the reaction with water vapour to be with O^{2-} as opposed to OH^- and as there was no clear change in kinetics for the mixed system it could be surmised that the mechanism is the same, with O^{2-} reacting to form oxide and the water decomposing, providing hydrogen for hydride formation and oxygen for further oxidation of the metal. This could in turn lead to mixed oxides and hydrides being detected.

The differences between uranium and niobium in proposed diffusing species and the effect oxygen has on the water vapour reaction will provide interesting effects on the alloy system.

5.4 APT analysis

APT of pure niobium and surface interfaces has been reported[46–48,79,80]. The niobium oxide formed on electropolished niobium wire was reported to have a thickness of approximately 10-15 nm with a stoichiometry indicative of an Nb_2O_5 structure[79,80]. Significant quantities of H and NbH have also been observed in the material below the oxide layer, due to the high solubility of H in Nb[48].

In previous work by Yoon-Jun Kim[48], NbO, NbO_2 and Nb_2O_5 were found 0-10 nm in depth, then a niobium metal layer ~ 5 nm was seen followed by a relatively thick ~40 nm NbH layer before returning to niobium metal. He then provided more detailed analysis of the oxide using electron energy-loss spectroscopy (EELS) which showed NbO_2 top 2 nm, Nb_2O_5 with other oxides from the next 2 nm, approaching Nb interface 1nm NbO layer detected which then extends into Nb grain for 2-3 nm. It was also shown that the residual H_2 gas inside the UHV chamber did not play a significant role in the chemical analyses.

Due to niobium's use in superconducting radio frequency (SRF) cavities there has been much work investigating niobium hydride as this is believed to be a contributor to the degradation of the cavities[46,47]. Niobium easily absorbs hydrogen if its protective oxide is compromised and it can then reduce its stability in corrosive media either via local charge transfer or via elastic strain. It was found that absorption into lattice vacancies is preferred over interstitial sites and that each vacancy can accommodate six hydrogen atoms. These vacancies can serve as a nucleation for hydride phase formation. When both oxygen and hydrogen are present, oxygen absorption is more favourable and oxygen atoms can migrate to the vacancies preventing hydrogen atoms accumulating there and, thus, reducing the ability to form precipitated hydride phases.

5.4.1 Niobium exposed to air

Figure 5.41 shows an atom map of the niobium after exposure to air for an hour. Figure 5.42 shows a concentration profile through the z-axis of the specimen. The vast majority of the sample was Nb, with an increase in hydrogen content in the first 60 nm of the tip, tailing off from around 30 at.% NbH at the surface to less than 5 at.% at 150 nm depth. Oxidation of the Nb was very limited, and oxygen content limited to only 0.37 at% (0.11 wt%). Due to the lack of an oxide layer it is not possible to determine whether the NbH profile on this tip is due to a distinct hydride layer as seen previously[48] or due to diffusion of H atoms into niobium.

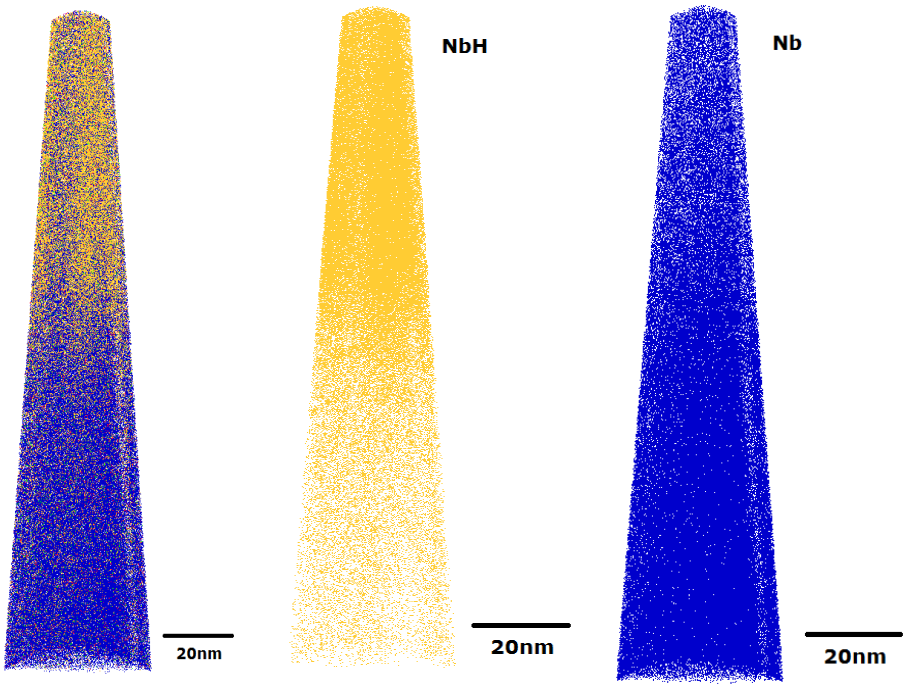

Figure 5.41 Atom map of niobium exposed to air for 1 hour.

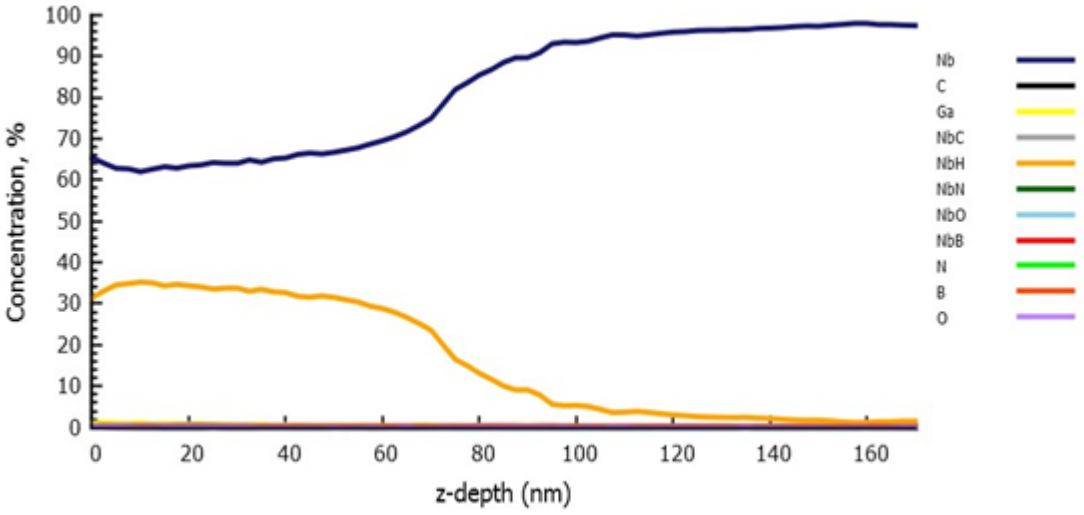

Figure 5.42 Concentration profile for niobium specimen after exposure to air for 1 hour.

Previous work, figure 5.43, has shown an oxide layer between 5-10 nm thick[48,79]. However, no oxide was detected in this study.

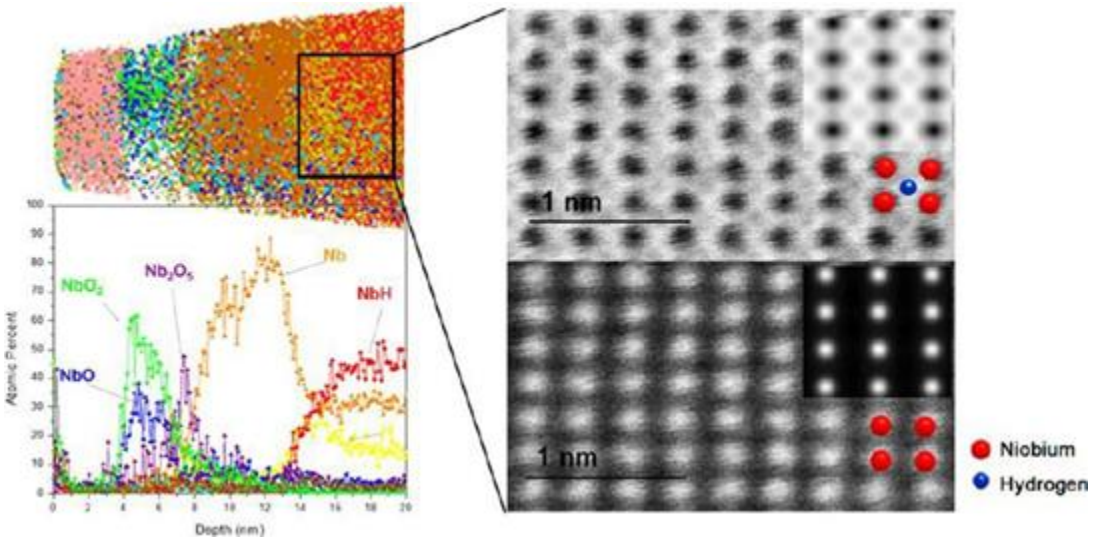

Figure 5.43 Atom probe data from reference[48] clearly demonstrating niobium oxide presence at the surface followed by a niobium hydride layer.

For uranium it was found that due to the large size of the specimen atoms compared to the Ga^+ ions, the damage from the ion beam was minimal; however, the presence of a protective layer of platinum had a detrimental effect on atom probe yield, as fracture could occur at the interface between the platinum and uranium. It was therefore decided to carry out in-situ lift out and thus annular milling on a strip with no protective cap. The same sample preparation was conducted for niobium and the alloys. Niobium, however, is not as dense as uranium; therefore, it is likely to have undergone some radiation damage from the gallium ions in the FIB during tip preparation. From the kinetic analysis, it can be assumed that the oxide would be relatively thin. Therefore, it is likely to have been removed during the preparation of the atom probe tips.

5.4.2 Summary

The atom probe tomography data presented here are limited and due to not using platinum during tip preparation the small amount of oxide present was probably removed. However, from the data in figure 5.42 it can be confirmed that niobium hydride is formed and this supports the SIMS data (section 5.3), and data previously reported on niobium and hydride formation[46,47].

5.5 Chapter conclusions

For niobium the kinetics were investigated, showing no pressure dependency for the temperatures 20-70 °C. An activation energy of 21 kJ mol^{-1} was derived. When oxygen is added to the water vapour reaction, no marked effect is seen with the rates remaining similar. When the kinetic data are compared to pure uranium, it is seen that niobium reacts at a significantly slower rate. It was also seen for uranium that the addition of oxygen to the reaction inhibited the rate substantially. This will have a significant impact on how the alloy reacts with water vapour and water vapour plus oxygen.

For the SIMS analysis, multiple depth profiles were carried out on each coupon for each experimental condition. The profiles varied quite significantly, with a variety of species as the dominant one and with various changeovers occurring throughout each profile. Some of the profiles did show a change from O-16 to O-18, suggesting anionic diffusion was occurring. Of interest was the presence of niobium hydride around the oxide-metal interface. This presence was supported by albeit limited atom probe data presented here. The atom probe data showed a distinct niobium hydride region before returning to bulk metal. If this atom probe analysis were to be repeated using a platinum layer as protection against radiation damage from the FIB, it is hoped that the surface oxide region would be detected.

6 Chapter six – results of uranium niobium alloy water vapour reaction

In the current chapter the reaction of UNb alloy with $D_2{}^{16}O$ vapour followed by $H_2{}^{18}O$ vapour has been studied. Niobium is added to uranium to enhance the corrosion resistance of uranium. Therefore, initially the corrosion kinetics of the reaction were investigated to see how the corrosion rates differ to the metal constituents and how the corrosion rate changes as a function of niobium content. It has previously been shown that as the niobium content increases the corrosion rate reduces, thus providing enhanced resistance[8]. The effect of oxygen on the water vapour reaction has also been studied as this has opposing effects on the two metal counterparts, inhibiting the reaction for uranium[3,21], while accelerating the corrosion rate for niobium[31].

In addition to following the kinetics of each reaction the samples were characterised and analysed pre and post exposure to determine any structural and/or compositional changes occurring on the sample surfaces. To this end a combination of SIMS, APT and EDX techniques has been applied to elucidate the mechanism of enhanced corrosion resistance, specifically investigating the role niobium plays and the structure of the oxide produced.

6.1 Material characterisation using EDX

EDX was used to provide elemental information on the material pre and post water vapour exposure, allowing the extent of oxidation and, most importantly, the niobium distribution to be visually recorded. The quantitative analysis by EDX also provides an estimate of the niobium content. For the quantitative analysis, oxygen was detected however die to the difficulty of accurately quantifying for oxygen by EDX it has not been included within the data. Therefore only the wt% values for niobium and uranium are provided.

6.1.1 EDX of freshly polished alloy surface

6.1.1.1 UNb3

Figure 6.1**Error! Reference source not found.** shows the SEM image of a polished UNb3 c oupon directly after preparation. The coupon was polished manually using silicon carbide

(SiC) paper with grits 320 – 1200 with ethanol as the lubricant. From the image it can be seen that there are defined polishing marks and scratches visible at low magnification.

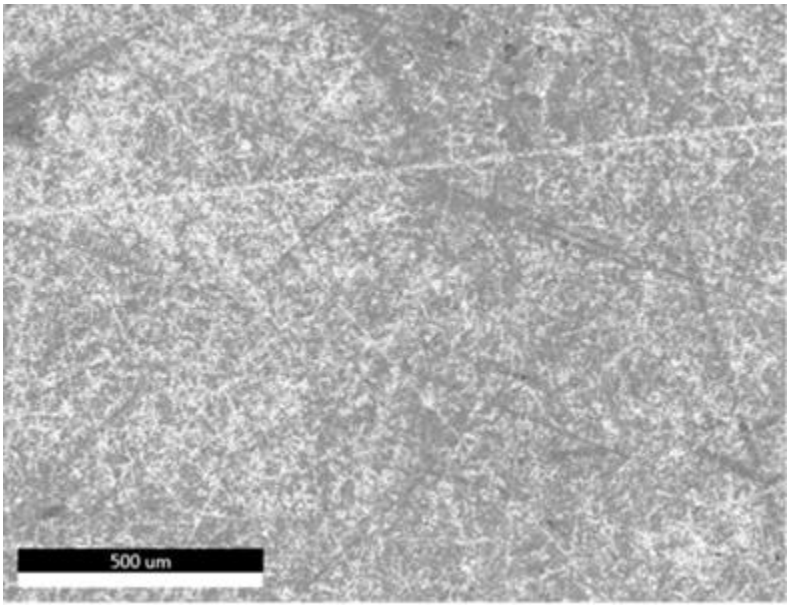

Figure 6.1 SEM image of a polished UNb3 coupon.

The spectra obtained for each of the phases present are shown in Figure 6.2. From the spectra it can be seen that the blue phase appears enriched in niobium. It must be noted that carbon presence is a possibility but it can sometimes be difficult to differentiate the peak due to its close proximity to oxygen and the constraints of EDX to accurately measure low masses.

The elemental maps are shown in Figure 6.3, with green, brown and yellow representing oxygen, niobium and uranium respectively. From figure 6.3, it can be seen that the majority of the surface is bulk alloy with oxygen uniformly distributed throughout. However, there are a few regions enriched in niobium, see figure 6.3c.

Table 6.1 contains the elemental analysis for both of the phases identified in figure 6.2. For the dominant phase (ascribed to the alloy), table 6.1a, appears to show 2.00 wt% of niobium present which is slightly lower than expected. However, it is within the margin for error. From the niobium rich phase, it can be seen that there is a significant increase in weight percent to 44.08% suggesting that this is a niobium rich phase (table 6.1b).

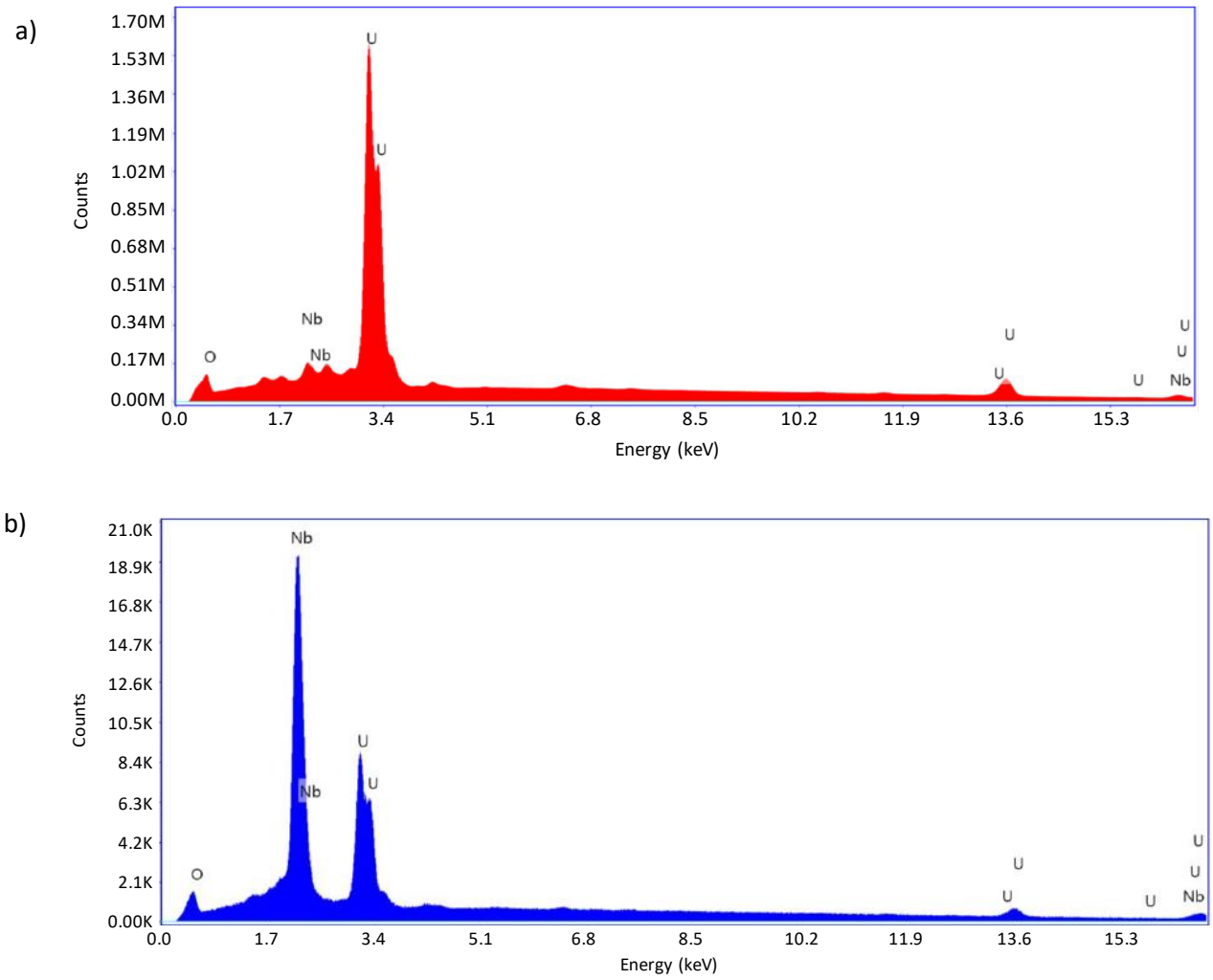

Figure 6.2Spectra from EDX analysis on polished UNb3 surface, a) for the phase U M/Nb L/O K, b) for the phase Nb L/U M.

The quantitative measurements conducted here by EDX are very crude and therefore will not be used as a basis to derive oxide stoichiometries. As seen by the elemental maps, oxygen is detected and is assumed to be surface oxide therefore not reported within the quantitative analysis. The quantitative analysis presented in Table 6.1 is therefore used to display the ratio of U:Nb to highlight deviations from that of the expected niobium concentration.

As previously stated there is the possibility of some carbon presence and therefore these weight/atomic percentages may not be a true representation of everything on the surface. It is possible that carbides are present on the surface which would lead to a reduction in the

metal constituent of the carbide within the bulk. This could be a possible reason why the niobium content in the bulk is lower than expected as this has been seen previously[81].

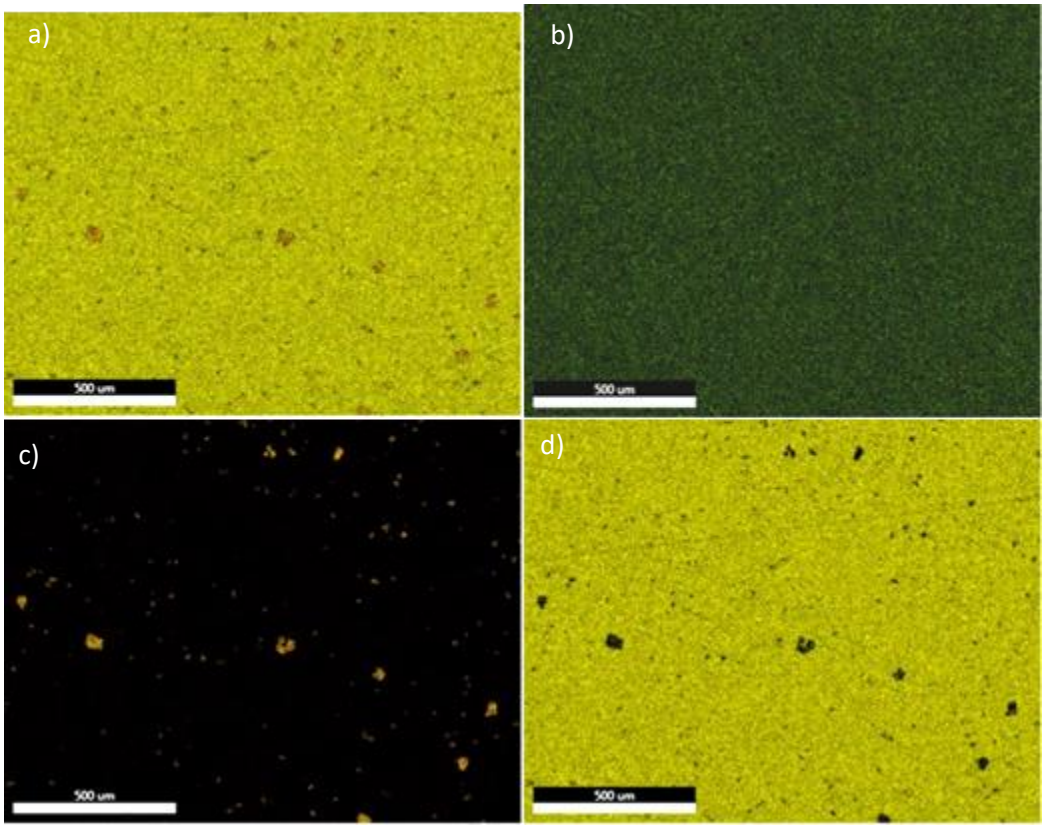

Figure 6.3 EDX elemental analysis of the polished UNb3 surface, a) elemental map showing all elements, b) map highlighting oxygen in green, c) map highlighting niobium in brown, d) map highlighting uranium in yellow.

Table 6.1 Elemental EDX analysis of the polished UNb3 surface, showing both weight and atomic percent of each element, the net intensity of each element (peak intensity minus background) and the % error of the intensity value, a) dominant U M/ Nb L / O K phase, b) minor niobium rich phase Nb L / U M.

a)

Element	Weight %	Net Int.	Error %
Nb L	2.00	801.8	4.15
U M	81.52	28936.4	1.48

b)

Element	Weight %	Net Int.	Error %
NbL	44.08	20913	2.62
U M	37.70	10711.1	3.08

6.1.1.2 UNb6

Figure 6.4 shows the SEM image of the polished UNb6 coupon pre exposure to any water vapour. The coupon was polished manually using silicon carbide (SiC) paper with grits

320 – 1200, again using ethanol as a lubricant. From the image it can be seen that there are clear polishing marks and scratches.

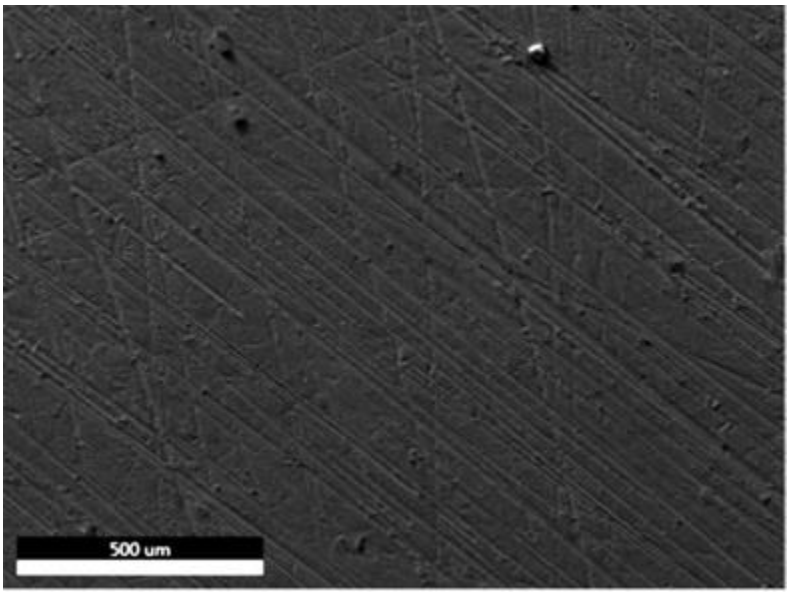

Figure 6.4 SEM image of a polished UNb6 coupon.

Figure 6.5 shows the EDX spectra of the polished UNb6 coupon for the two phases present. The main elements present are uranium, niobium and oxygen, as expected. Again, carbon is difficult to differentiate from the oxygen peak. In this instance there is a much smaller increase in intensity for the niobium peaks (figure 6.5b) compared to that seen for UNb3 (figure 6.2b).

The elemental maps are shown in Figure 6.6, with green, brown and yellow representing oxygen, niobium and uranium respectively. It can be seen that the majority of the surface is uranium with small spots of oxygen distributed throughout. There are fewer niobium-rich regions present than were seen for UNb3, see figure 6.6c and figure 6.3c respectively.

Table 6.2 contains the elemental analysis for both of the phases identified in Figure 6.5. For the dominant phase, table 6.2a appears to show 2.98 wt% of niobium present which is again lower than that expected, but the error is relatively large and therefore the value is within the accepted range. From the second phase, there is slight enrichment in niobium, with a content of 8.60 wt%. As with UNb3, oxygen was detected but is not reported in Table 6.2.

a)

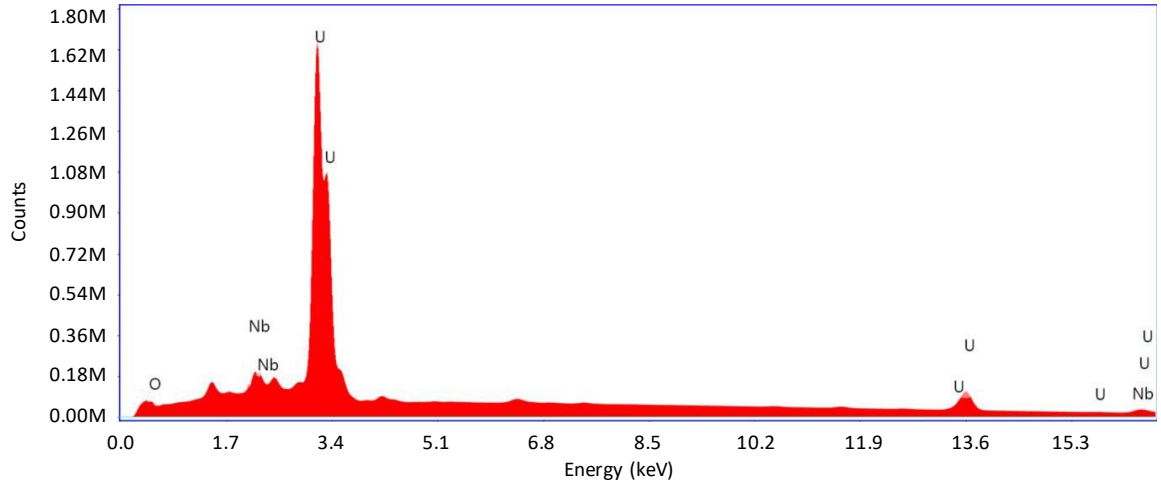

b)

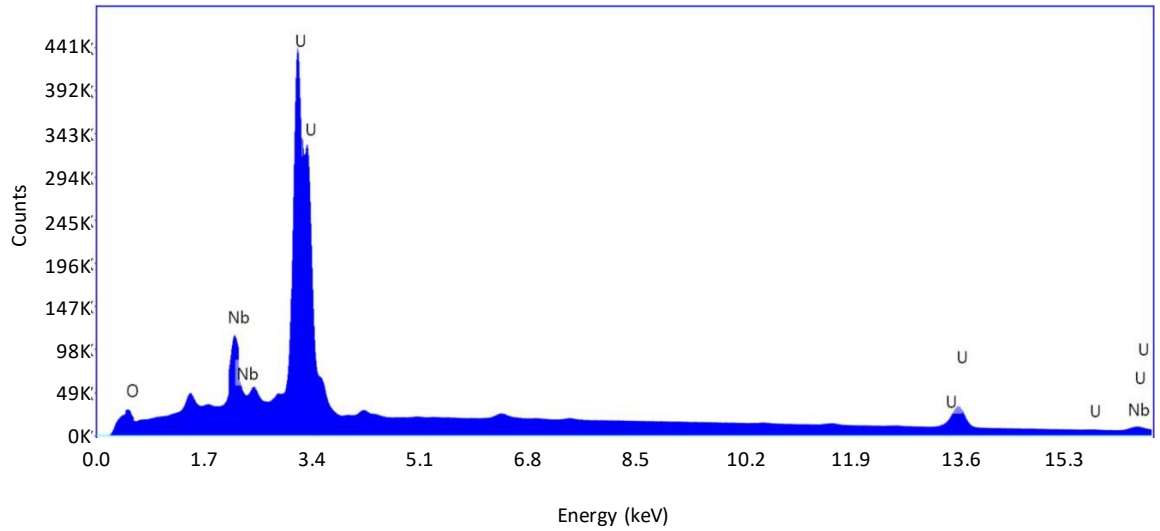

Figure 6.5 Spectra from EDX analysis on polished UNb6 surface, a) dominant U M/ Nb L phase, b) minor niobium rich *U M / Nb L phase.*

Table 6.2 Elemental EDX analysis of the polished UNb6 surface, a) dominant U M/Nb L phase, b) minor niobium rich U M/Nb L phase.

a)

Element	Weight %	Net Int.	Error %
NbL	2.98	1097.1	4.27
U M	85.20	27704.6	1.23

b)

Element	Weight %	Net Int.	Error %
NbL	8.60	3358.1	3.94
U M	76.11	24761.1	1.10

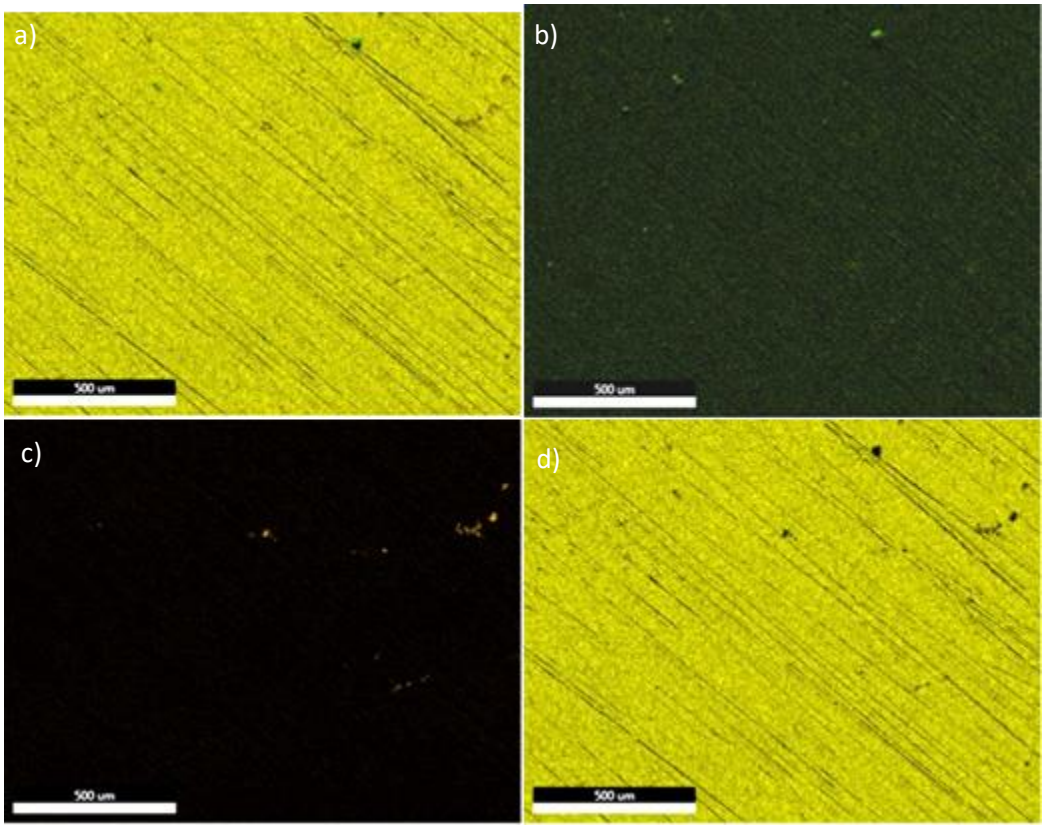

Figure 6.6 EDX elemental analysis of the polished UNb6 surface, a) elemental map showing all elements, b) map highlighting oxygen in green, c) map highlighting niobium in brown, d) map highlighting uranium in yellow.

6.1.2 EDX of alloy surface after water vapour exposure

6.1.2.1 UNb3

Figure 6.7 shows an SEM image and a photograph of a UNb3 coupon after exposure to water vapour at 55 °C for 1502 hours. From the SEM image (figure 6.7a) it can be seen that the polishing marks and scratches are still evident and the topography of the surface does not appear to have changed significantly compared to the freshly polished surface in figure 6.1a. From the photograph (figure 6.7b), however, it can be seen that the material has changed in colour from a shiny mirror-finish (after polishing) to a tarnished dull appearance.

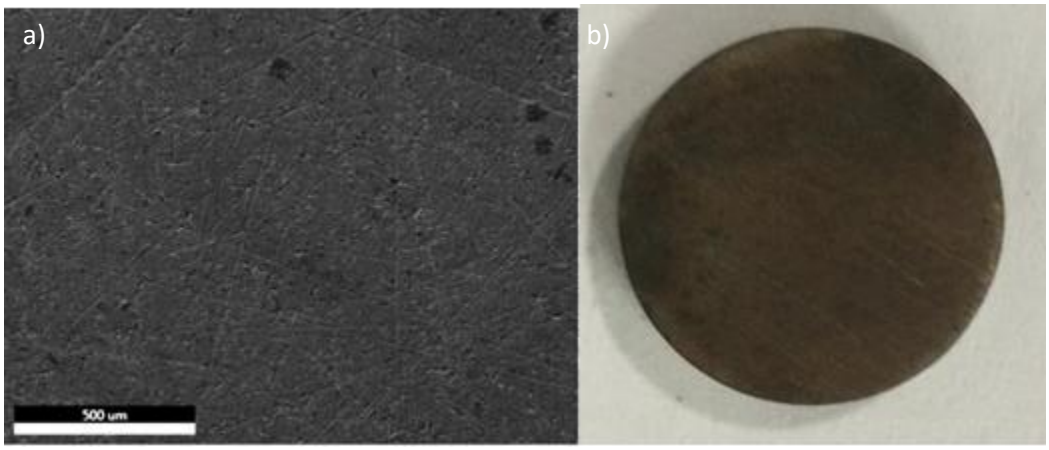

Figure 6.7 Corroded UNb3 coupon from the experiment conducted at 55 °C with a water vapour pressure of 30 mbar, a) SEM image of the surface, b) photograph of the oxidised surface showing some decolourisation.

The spectra obtained for each of the phases present are shown in Figure 6.8. From the spectra it can be seen that the blue phase appears enriched in niobium. The spectra also appeared to show a peak for carbon. This is not profiled in the elemental maps or in the quantitative analysis. Therefore, these values will be treated as a guide only and no definitive conclusions on oxide stoichiometry drawn from them.

The elemental maps are shown in Figure 6.9, with green, brown and yellow representing oxygen, niobium and uranium respectively. From Figure 6.9, it can be seen that the majority of the surface is uranium (figure 6.9d) with small spots of oxygen (figure 6.9b) distributed throughout. However, there are a few regions enriched in niobium (figure 6.9c), as seen for the polished surface in Figure 6.3. It is also possible that these niobium-rich regions are carbides as it has previously been found that niobium carbides are formed in the alloy[81].

Table 6.3 contains the elemental analysis for the three phases identified in figure 6.8. For the U M/Nb L phase (red), table 6.3a appears to show a very low niobium content of 0.88 wt%. For the other prevailing phase of U M/Nb L/O K (yellow), where all elements (U, Nb and O) are present, table 6.3b shows a higher niobium content of 3.56 wt%, which is very close to the expected value.

For the niobium-rich phase, Nb L/U M (table 6.3c) it can be seen that there is a significant increase in weight percent to 50.29% suggesting a niobium-rich region is present.

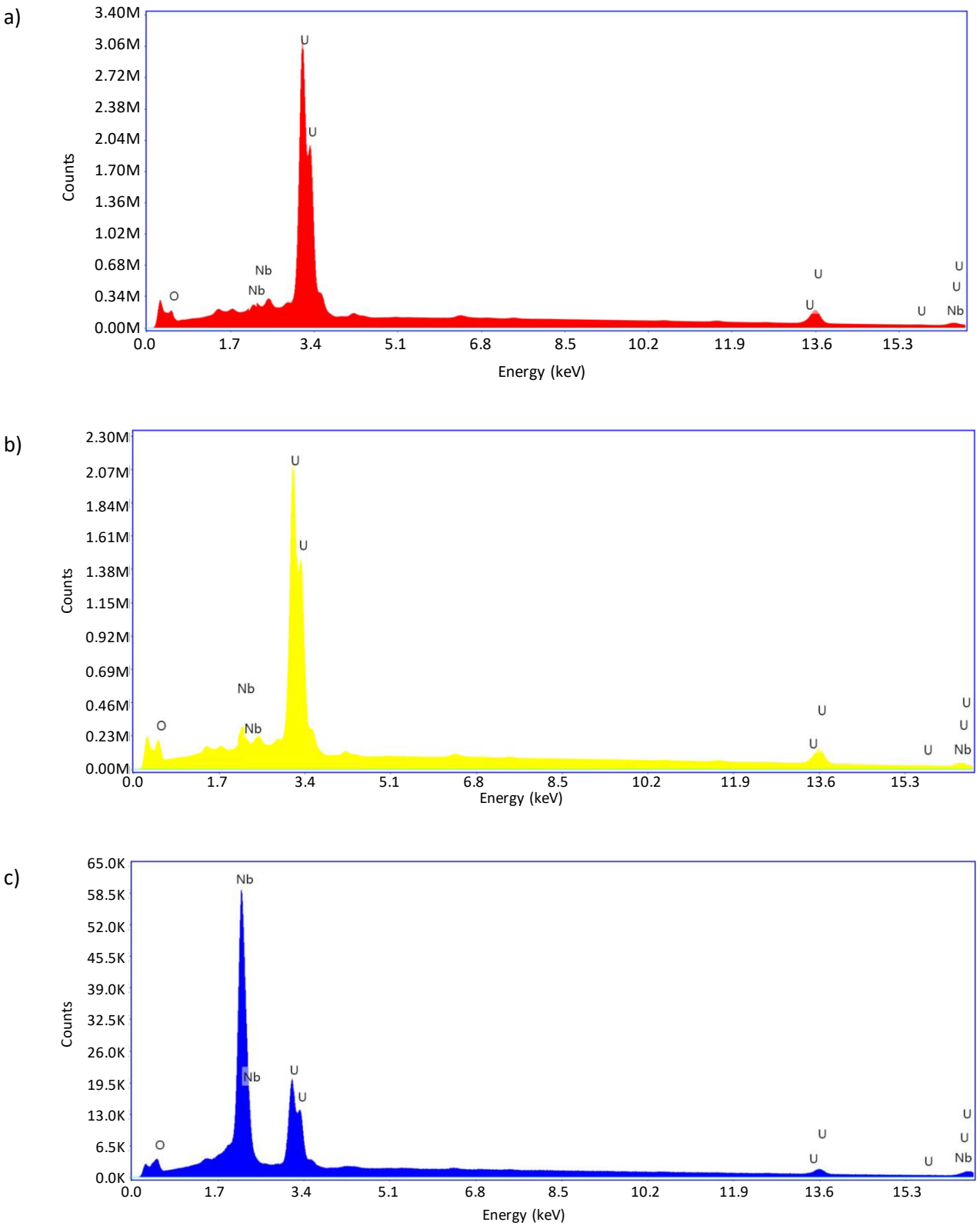

Figure 6.8 Spectra from EDX analysis on corrode UNb3 surface, a) for the phase U M/Nb L, b) for the phase U M/Nb L/O K, c) for the phase Nb L/U M.

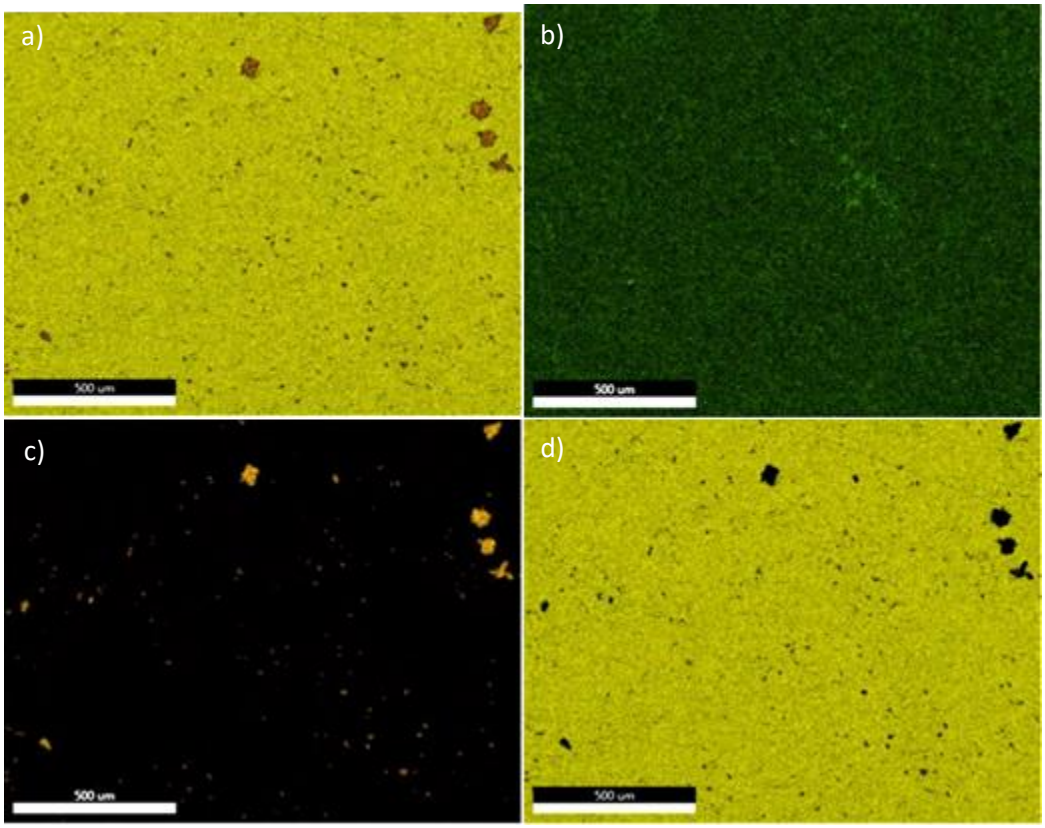

Figure 6.9 EDX elemental analysis of the corroded UNb3 surface, a) elemental map showing all elements, b) map highlighting oxygen in green, c) map highlighting niobium in brown, d) map highlighting uranium in yellow.

Table 6.3 Elemental EDX analysis of the corroded UNb3 surface, a) U M/Nb L phase, b) U M/Nb L/O K phase, c) minor Nb L/U M phase.

a)

Element	Weight %	Net Int.	Error %
NbL	0.88	242	4.26
U M	85.32	21006	1.43

b)

Element	Weight %	Net Int.	Error %
NbL	3.56	1025.1	3.94
U M	78.47	19631.7	1.46

c)

Element	Weight %	Net Int.	Error %
NbL	50.29	18012.3	2.29
U M	33.12	6747	2.68

6.1.2.2 UNb6

Figure 6.10 shows an SEM image of the UNb6 uranium coupon after exposure to water vapour at 55 °C for 14,835 hours. From the SEM image it can be seen that the topography of the sample is a lot rougher that that seen in figure 6.4 for the freshly polished surface. This is different to what was seen for UNb3 where the surface showed no marked change on oxidation. It must be noted that the water vapour exposure for UNb3 (1502 hours) was significantly shorter than that for UNb6 (14,835 hours) and therefore it is not unexpected for there to be large differences in the oxidation.

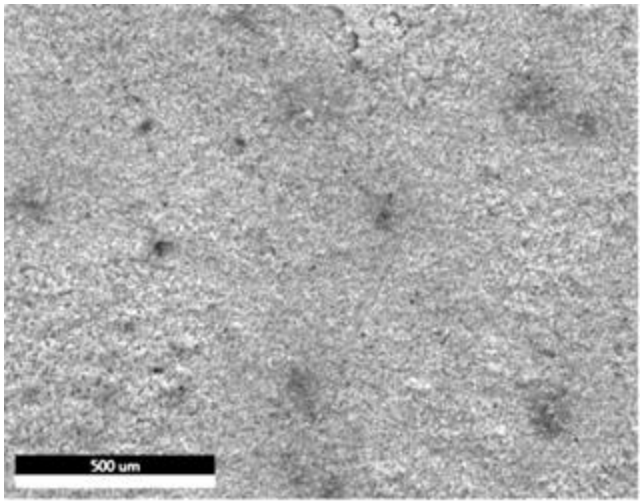

Figure 6.10 SEM image of corroded UNb6 coupon from the experiment conducted at 55 °C with a water vapour pressure of 30 mbar.

The spectra obtained for each of the phases present are shown in Figure 6.11. For the niobium-rich blue phase, as was seen for the polished coupons, there is a much smaller increase in intensity for the niobium peaks for UNb6 (figure 6.11b) compared to that seen for UNb3 (figure 6.8c). The minor phase (yellow) shows increased oxygen intensity suggesting an increase in an oxide phase.

The elemental maps are shown in Figure 6.12, with green, brown and yellow representing oxygen, niobium and uranium respectively. From Figure 6.12, it can be seen that the majority of the surface is uranium (figure 6.12d) with small spots of oxygen (figure 6.12b) distributed throughout. However, there are a few regions enriched in niobium (figure 6.12c), though much less than that seen for UNb3 (figure 6.9c).

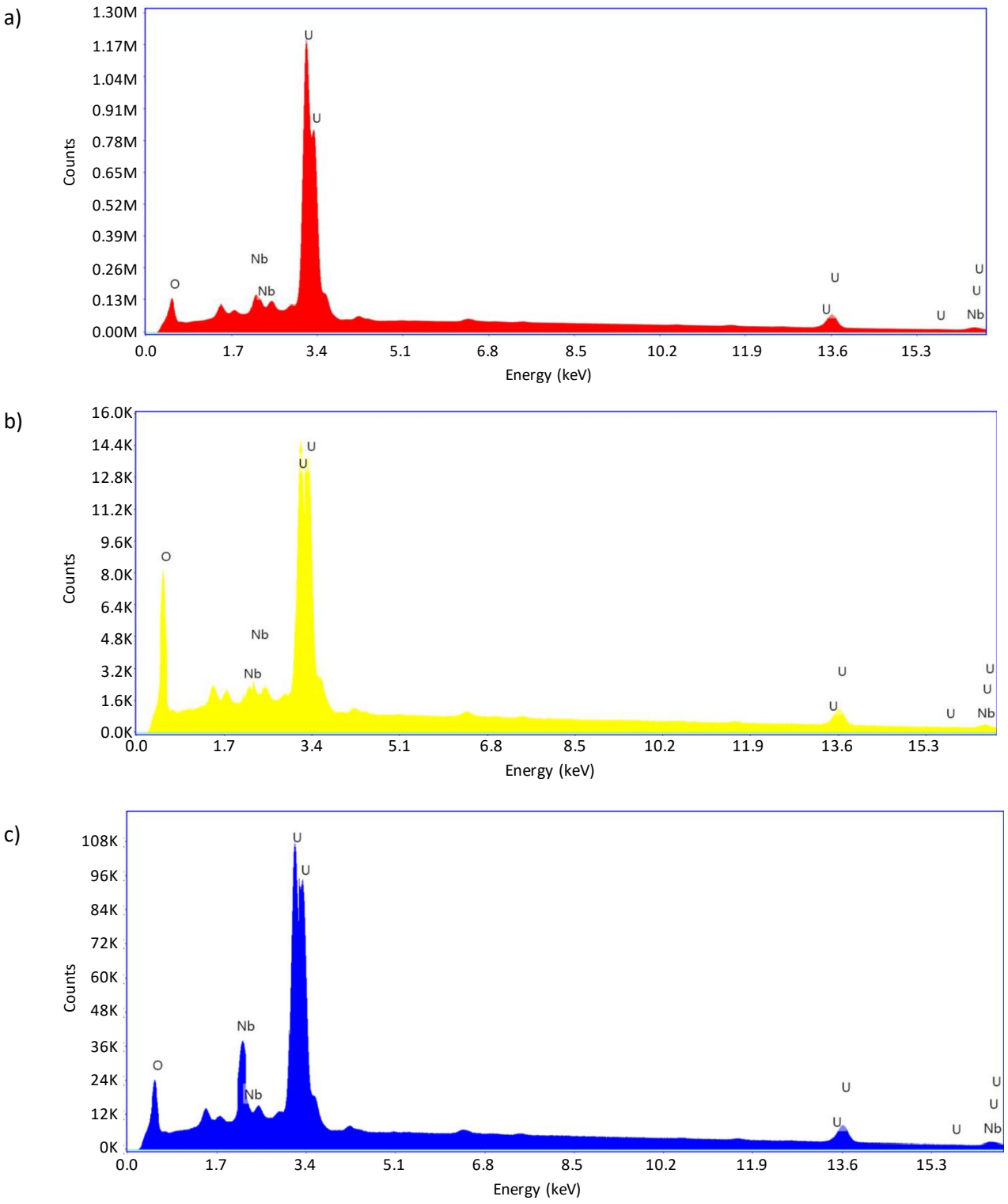

Figure 6.11 Spectra from EDX analysis on corroded UNb6 surface, a) for the phase U M/Nb L/O K, b) for the phase U M/Nb L/O K, c) for the phase U M/O K/Nb L.

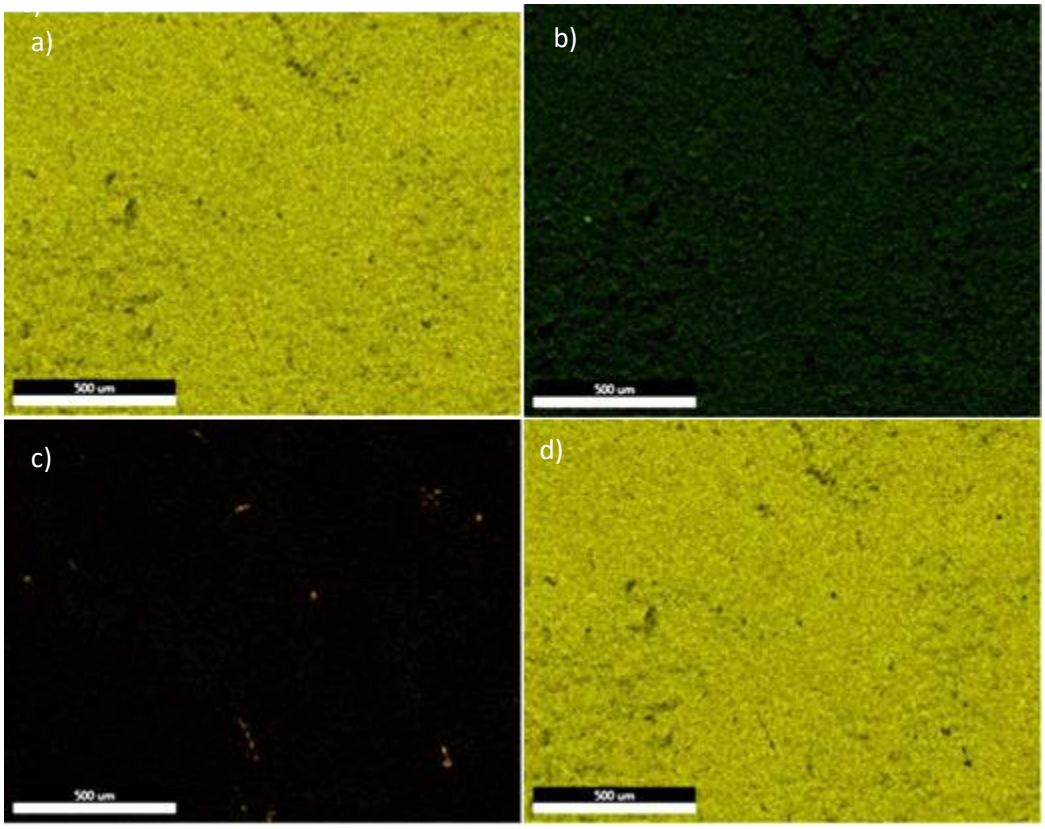

Figure 6.12 EDX elemental analysis of the corroded UNb6 surface, a) elemental map showing all elements, b) map highlighting oxygen in green, c) map highlighting niobium in brown, d) map highlighting uranium in yellow.

Table 6.4 contains the elemental analysis for the three phases identified in figure 6.11. For the U M/Nb L/O K phase (red), table 6.4a shows a niobium content of 2.71 wt%, which is lower than the expected 6 wt% value; however, the U M/Nb L/O K phase (blue) shows an increased niobium content of 8.11 wt%. For the U M/O K/Nb L phase (yellow) the niobium content is considerably diminished with only 0.79 wt% present. These elemental quantifications possibly suggest that there are regions enriched in uranium relative to niobium in the surface oxide.

All three phases show significant oxygen content compared to both the UNb6 polished surface and the UNb3 surface. Again, it must be noted the UNb6 coupon has been exposed to water vapour for a substantial amount of time, while the UNb3 has had a much shorter exposure time. Therefore, this increased oxygen is not necessarily all that surprising.

Table 6.4 Elemental analysis of the corroded UNb6 surface a) for the phase U M/Nb L/O K, b) for the phase U M/Nb L/O K, c) for the phase U M/O K/Nb L.

a)

Element	Weight %	Net Int.	Error %
NbL	2.71	1014	3.86
U M	75.29	24468.3	1.67

b)

Element	Weight %	Net Int.	Error %
NbL	8.11	2894.8	3.62
U M	60.78	17600.3	1.79

c)

Element	Weight %	Net Int.	Error %
NbL	0.79	311.1	16.93
U M	51.75	17178.2	3.26

6.1.3 EDX of TEM section of the alloy after water vapour exposure

6.1.3.1 UNb3

Figure 6.13 shows an SEM image of a TEM section taken from the UNb3 coupon after exposure to water vapour at 45 °C. The region highlighted is where the EDX analysis was conducted. Figure 6.14 presents the phase analysis of this region, showing there to be only one phase present, U M/Nb L.

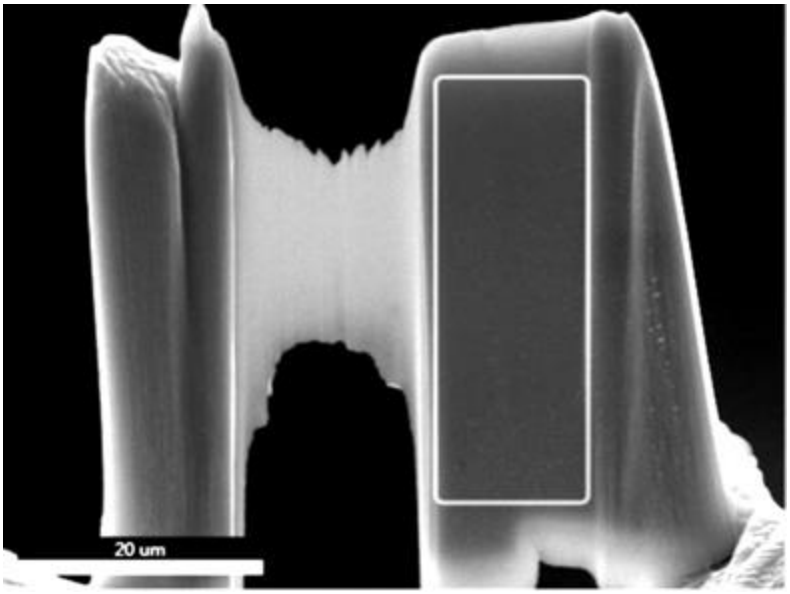

Figure 6.13 SEM image of a TEM section lifted from a UNb3 coupon after exposure to water vapour at 45 °C.

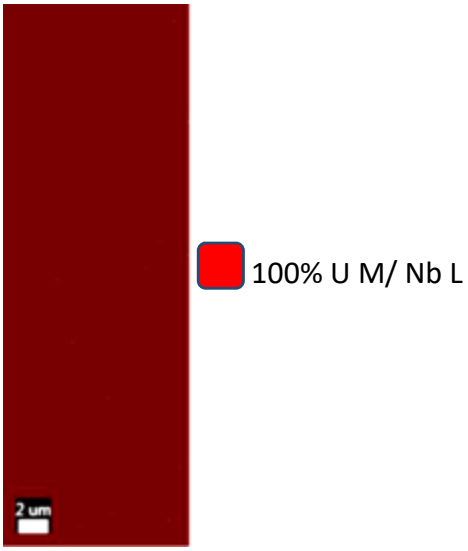

Figure 6.14 Phase maps of polished UNb6 surface.

Figure 6.15 presents the spectral analysis of the surface with elemental maps for uranium, niobium and oxygen shown in Figure 6.16. It can be seen that uranium is the dominant species in both the spectrum and the elemental maps with small peaks seen for both oxygen and niobium. There are no distinct niobium-enriched regions as seen for the surface analysis both pre and post water vapour exposures.

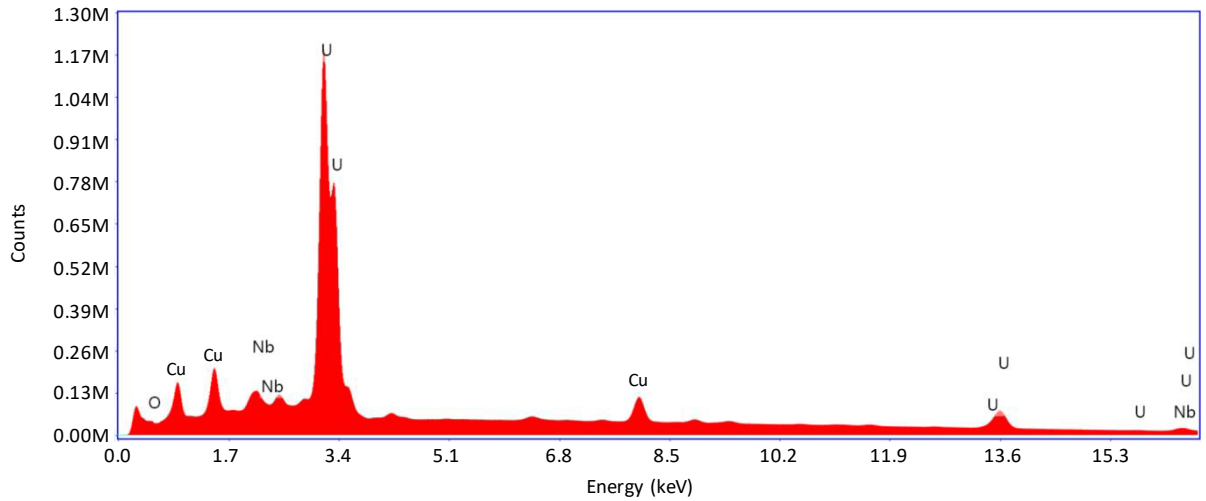

Figure 6.15 Spectrum of EDX analysis of UNb3 TEM section.

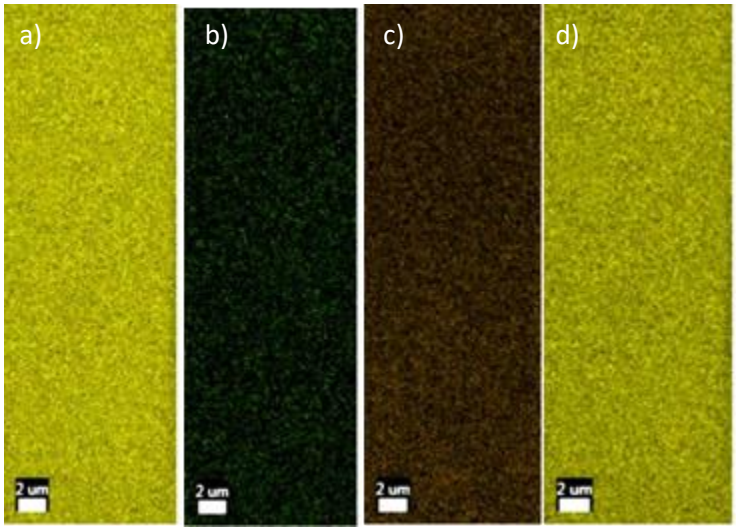

Figure 6.16 EDX elemental analysis of the UNb3 TEM section, a) elemental map showing all elements, b) map highlighting oxygen in green, c) map highlighting niobium in brown, d) map highlighting uranium in yellow.

Table 6.5 contains the elemental analysis for the single phase identified in figure 6.14. The niobium content appears consistent to that expected, 3.81 wt% versus 3 wt% suggesting a homogenous bulk.

Table 6.5 Elemental analysis of the corroded uranium surface.

Element	Weight %	Net Int.	Error %
Nb L	3.81	979.6	4.27
U M	84.54	19068.7	1.19

6.1.3.2 UNb6

Figure 6.17 shows an SEM image of a TEM section taken from the UNb6 coupon after exposure to water vapour at 45 °C. The region highlighted is where the EDX analysis was conducted. From the SEM image it can be seen that there are clear layers/regions present. Figure 6.18 presents the phase analysis of this region, showing there to be two phases present, U M/Nb L (red) and Nb L/U M/O K (blue). The clear layer seen in the SEM image is depicted as a distinct phase in the EDX analysis.

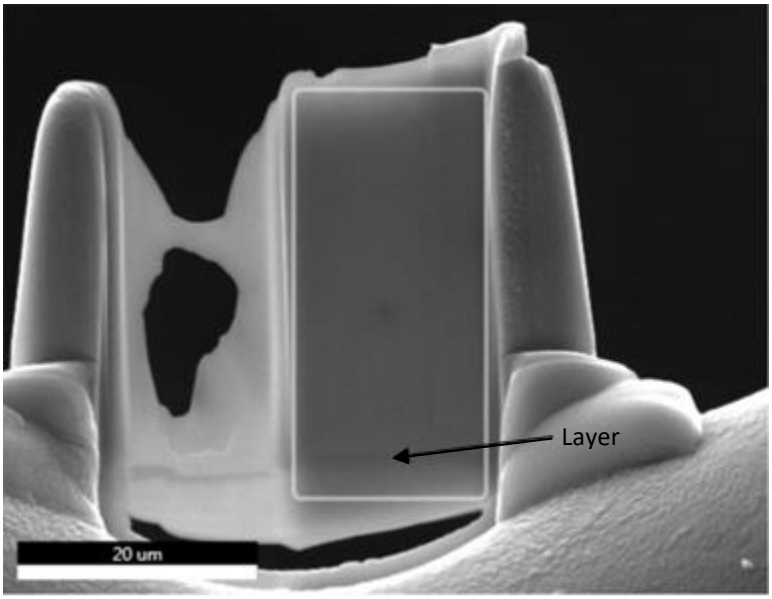

Figure 6.17 SEM image of a TEM section lifted from a UNb6 coupon after exposure to water vapour at 45 °C.

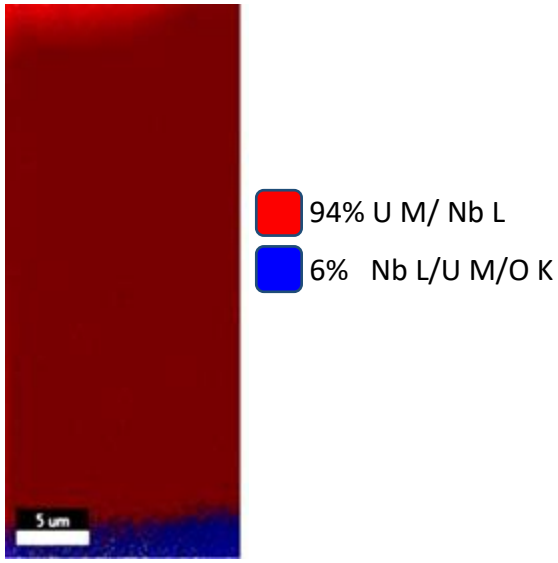

Figure 6.18 Phase maps of the TEM section from UNb6 coupon showing two distinct phases present.

Figure 6.19 presents the spectral analysis of each of the two phases. For the dominant phase (figure 6.19a), uranium, niobium and oxygen are all present with the uranium being the highest in intensity. For the minor phase (figure 6.19b) niobium is seen to increase in intensity. There are also clear peaks assigned to copper from the TEM grid as well as possible gallium and platinum from the sample preparation.

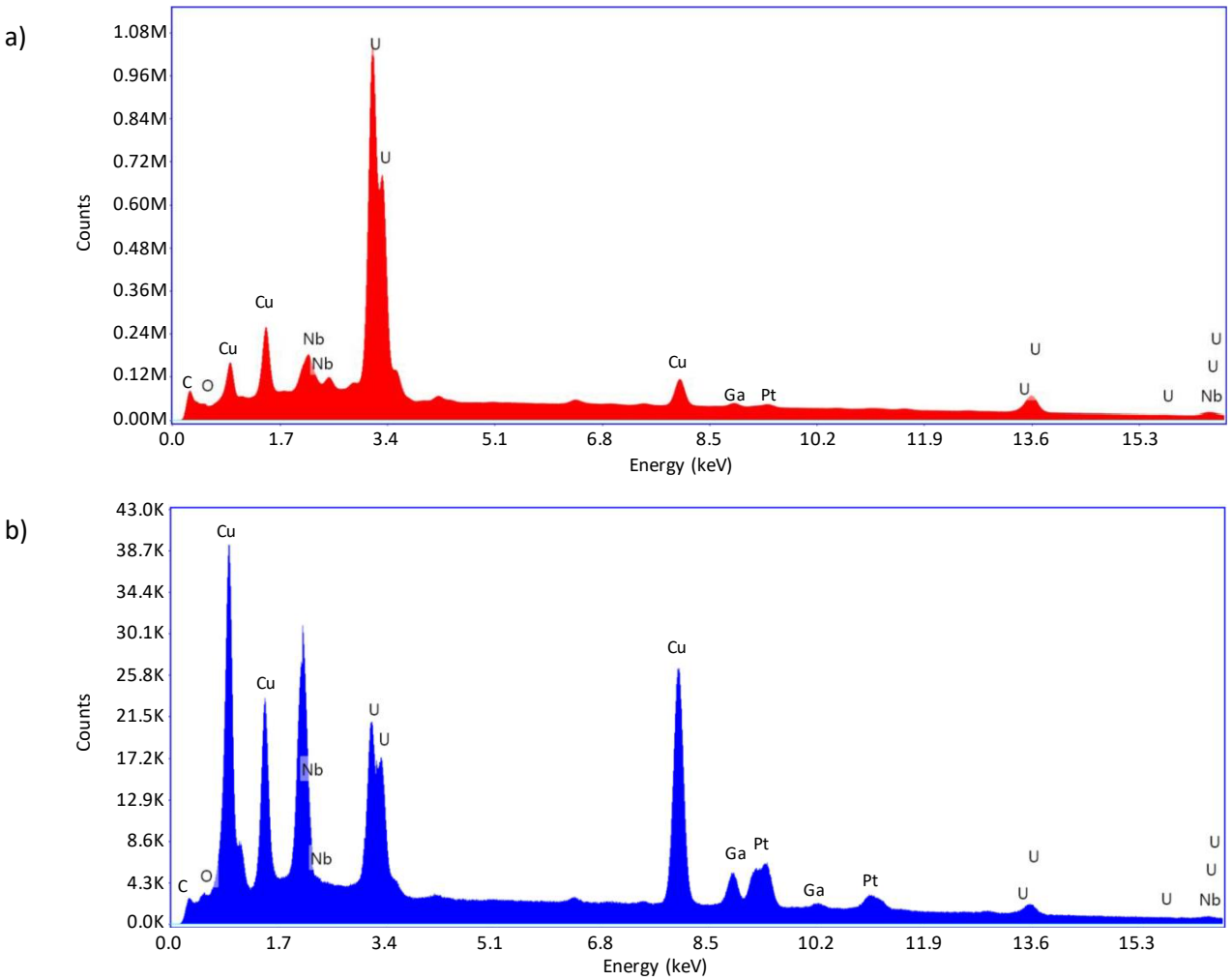

Figure 6.19 Spectra of EDX analysis of UNb6 TEM section, a) for phase U M/Nb L, b) for phase Nb L/U M/OK.

Figure 6.20 presents the elemental maps for the region analysed, highlighting the uranium, niobium and oxygen distributions. It can be seen that the majority of the surface is uranium, with oxygen and niobium distributed throughout. The area near the bottom that has been assigned to a different phase shows a clear increase in niobium, suggesting that this region (and thus phase) is niobium-rich. This was seen for the polished and corroded alloy samples but not for the UNb3 TEM section, suggesting that there may be a difference in the bulk material.

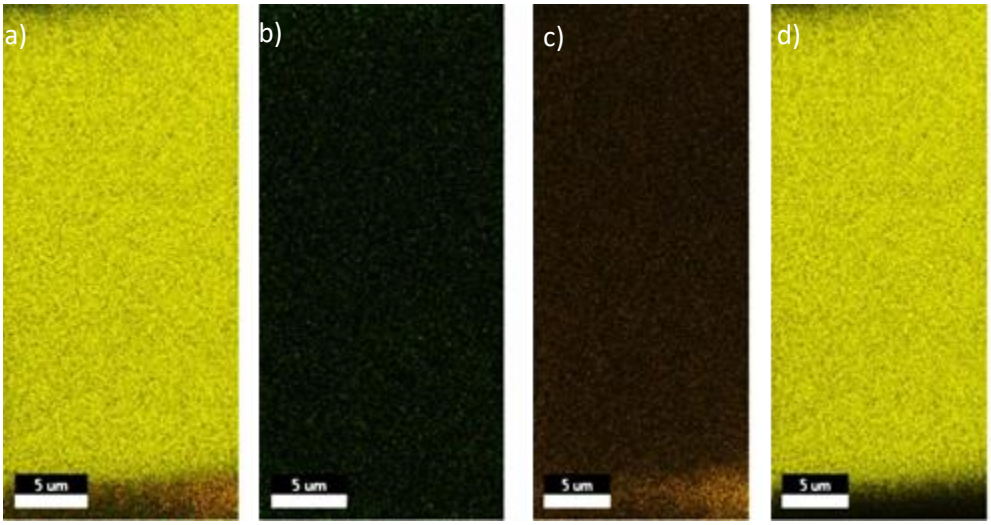

Figure 6.20 EDX elemental analysis of the UNb6 TEM section, a) elemental map showing all elements, b) map highlighting oxygen in green, c) map highlighting niobium in brown, d) map highlighting uranium in yellow.

Table 6.6 contains the elemental analysis for the two phases identified in figure 6.18. The niobium content of the dominant phase is not too dissimilar to that expected suggesting that the depletion seen for the surface analysis pre and post water vapour exposure (tables 6.2 and 6.4 respectively) is not seen within the bulk. Possibly related to the uranium dioxide being found at the outermost surface.

However, the presence of this additional niobium-rich phase near the bottom of the lift-out suggests that there may be clear bands/regions within the bulk that are niobium-rich. It has previously been stipulated that aging of the UNb6 alloy can lead to spinodal decomposition[1]. If this is the case, then this segregation of the niobium and uranium will impact both the kinetic and mechanistic aspects of the water vapour reaction.

Table 6.6 Elemental analysis of UNb6 TEM section, a) for phase U M/Nb L, b) for phase Nb L/U M/OK.

a)

Element	Weight %	Net Int.	Error %
NbL	7.26	1920.6	4.05
U M	79.87	17921.6	1.06

b)

Element	Weight %	Net Int.	Error %
NbL	32.60	6831.5	2.74
U M	38.69	5260.5	1.77

6.1.4 Summary

For UNb3 it has been clearly identified that regions of the surface are enriched in niobium relative to the bulk background composition. This was seen pre and post water vapour exposure. For UNb6 the niobium is more evenly dispersed by comparison. On oxidation the UNb3 surface was seen to change colour. However, the EDX elemental analysis did not show a significant change in oxygen content while the UNb6 appears heavily oxidised showing clear changes in oxygen content and topography of the surface. However, the UNb6 exposure was for a far greater duration (14,835 hours) than the UNb3 (1502 hours) and therefore this apparent enhanced oxidation cannot be fairly compared.

From the TEM data there are clear differences for the two alloys. The UNb3 section showed no distinct niobium rich phases and is considered to be a reliable bulk sample. In comparison the UNb6 section showed a clear band, rich in niobium, at the bottom of the lift-out. This band found within the UNb6 bulk suggests possible decomposition due to aging could have occurred which will impact the kinetics of the water vapour reaction. If there are areas depleted in niobium then these regions could possibly react at a similar rate to pure uranium, thus counteracting the corrosion resistance provided by niobium's slower oxidation rates.

For future work, it would greatly aid in the characterisation of the alloy for EDX to be repeated with an aim to investigate the carbon presence in more detail. Further analysis on any carbide inclusions and their composition (niobium or uranium) would vastly improve this data set and would allow the quantitative analysis to be more accurately utilised.

6.2 Corrosion kinetics

Experiments on UNb6 and UNb3 were conducted at three different temperatures. The pressure dependence has previously been shown to be $P_{(H_2O)}^{½}$ for the range of temperatures investigated in this study[12]. Therefore, only one pressure was used throughout. The pressure of approximately 30 mbar was chosen as salts were readily available to provide the required pressure at each of the temperatures.

The kinetic data are presented from both the $D_2{}^{16}O$ reaction and the subsequent $H_2{}^{18}O$ reaction. For the $H_2{}^{18}O$ the kinetics will be within the bulk reaction and should therefore remain consistent with the final $D_2{}^{16}O$ rate. For UNb3 only the experiment conducted at 45°C used both $D_2{}^{16}O$ and $H_2{}^{18}O$, the experiments at 55 °C and 30 °C were conducted with $D_2{}^{16}O$ only.

Errors associated with the thermocouples (Type K) and the transducers should be noted at this point. For the transducers the reported accuracy by the manufacturer is ±2.2 mbar or ±0.75%, whichever is greater. For the transducers there are several reported factors addressed in its documented performance rating:

- Long term drift ±0.1% span/annum
- Accuracy ±0.25%
- Thermal error 1% (0 °C to 70°C), 2% for 40 to 250 mbar ranges (0 °C to 50 °C)

When experimental data referring to temperature or pressure are presented and discussed they will highlight the associated error.

The desired temperatures were 55 °C, 45 °C and 30 °C, the actual temperatures varied slightly due to changes in the room temperature. For the 30 °C experiment, the reaction cells were placed in the laboratory rather than within an oven. This meant that the temperature varied quite significantly throughout due to seasonal changes. It also meant that the temperature was lower than desired, with the mean temperature being ~22 °C and ~23 °C for UNb3 and UNb6 respectively. The lower temperatures therefore affect the starting pressure of the experiment. The pressure values are only theoretical/predicted values calculated from an equation by Greenspan[67]. Therefore, changes in temperature and impurities within the water will impact the actual pressures achieved in the experiments.

The actual average temperatures and starting pressures of the UNb3 $D_2{}^{16}O$ experiments were:

- 52.94 ±2.2 °C experiment starting pressure of 44.54 mbar ±0.61%
- 44.41 ±2.2 °C experiment starting pressure of 27.37 mbar ±0.60%
- 21.93 ±2.2 °C experiment starting pressure of 23.71 mbar ±0.37%

The actual average temperatures and starting pressures of the UNb6 $D_2{}^{16}O$ experiments were:

- 57.08 ±2.2 °C experiment starting pressure of 25.70 mbar ±1.01%
- 44.57 ±2.2 °C experiment starting pressure of 24.83 mbar ±0.73%
- 22.80 ±2.2 °C experiment starting pressure of 15.30 mbar ±0.54%

The actual average temperatures and starting pressures of the UNb6 $H_2{}^{18}O$ experiments were:

- 57.33 ±2.2 °C experiment starting pressure of 23.00 mbar ±0.59%
- 44.87 ±2.2 °C experiment starting pressure of 23.30 mbar ±0.57%
- 26.64 ±2.2 °C experiment starting pressure of 19.81 mbar ±0.35%

The actual average temperatures and starting pressures of the UNb3 $H_2{}^{18}O$ experiments were:

- 44.80 ±2.2 °C experiment starting pressure of 28.87 mbar ±1.02%

For the reaction with water vapour plus oxygen, previous work has shown the oxygen to inhibit the evolution of hydrogen and reduce the reaction rate[12]. The experiments with water vapour plus oxygen were carried out at a desired temperature of 55 °C and with the desired starting pressures of 40 mbar (30 mbar water vapour and 10 mbar oxygen). Both isotope regimes were investigated, $D_2{}^{16}O + {}^{18}O_2$ and $H_2{}^{18}O + {}^{16}O_2$. There were issues with the data not logging correctly for the start of both $H_2{}^{18}O + {}^{16}O_2$ experiments and for the UNb3 $D_2{}^{16}O + {}^{18}O_2$ experiment. Therefore, the recorded data are midway through the reaction and the recorded starting pressure is significantly higher than the desired 40 mbar:

1) $D_2{}^{16}O + {}^{18}O_2$, actual temperatures are pressures:

UNb3 – 59.00 ±2.2 °C experiment starting pressure of 85.13 mbar ±1.92%

UNb6 – 57.43 ±2.2 °C experiment starting pressure of 90.17 mbar ±2.05%

2) $H_2{}^{18}O + {}^{16}O_2$, actual temperature and pressures:

UNb3 – 59.58 ±2.2 °C experiment starting pressure of 90.89 mbar ±2.05 %

UNb6 – 59.13 ±2.2 °C experiment starting pressure of 55.37 mbar ±1.27 %

Isotopically-labelled water and oxygen are used in order to allow SIMS analysis of the corroded sample. The identity of isotopes within the corrosion products will provide key mechanistic information.

The main assumption made is that any increase in pressure was due to the evolution of hydrogen through the reaction:

$U_{(s)} + 2H_2O_{(g)} \longrightarrow UO_{2(s)} + 2H_{2(g)}$

This reaction also implies a secondary assumption that uranium is the only metal of significance during the corrosion reactions. As the niobium content is only a few atomic percent, the chemical reactions of the niobium atoms are not considered significant when compared to the more thermodynamically reactive and numerous uranium atoms. Importantly this assumption does not imply that the niobium is insignificant within the underlying mechanism of corrosion resistance for these alloys.

The quality of corrosion rate obtained is influenced by:

1) Time required to achieve a linear reaction rate
2) Time required to ensure the unintentional influence of any other gas phase species has been removed (i.e. any initial free oxygen has been consumed by oxidation)
3) Accuracy of the measurement itself when some experiments are so much slower than others

The corrosion reaction with alloys has been found to be significantly slower compared to pure uranium. The majority of the experiments conducted in this study have been corroding for a substantial amount of time (> 1 year). However, there is still the possibility that the experiments have not been corroding for long enough to provide a constant linear rate (often revealed by time dependent rates higher in value than expected) or they are still being influenced, albeit typically by only a small amount, by other gas phase impurities within the cell, e.g. oxygen following loading of the cell (often revealed by very low or negative rates). With these assumptions and quality factors it is noted that the error bars for the alloy experiments are considerable. Despite this, the exposed samples still offer an opportunity to study the mechanism through the applied characterisation techniques.

The data are presented in two formats, firstly a plot showing the pressure (mbar) and temperature (°C) data for the exposure and secondly the amount of hydrogen evolved (mmol H_2 cm^{-2}) and the corresponding rate (mmol H_2 cm^{-2} s^{-1}) for that reaction.

6.2.1 Reaction with sequential water vapour exposure

6.2.1.1 UNb3

Figure 6.21 a, b and c present the pressure and temperature data for the UNb3 experiments at 52.92 °C, 46.41 °C and 21.74 °C respectively. In figure 6.21a, there is a significant period where the data scan unit was not recording (highlighted region). However, the pressure remained steady when the logger was back up and running. A change in temperature was seen after this period of down time. This could be due to temperature fluctuations within the room as there is no form of regulation. In figure 6.21b there is again a clear change in temperature. However, it is not seen to affect the pressure data and therefore could possibly be an issue with the thermocouple as the data appears much noisier. In figure 6.21c, the temperature can be seen to fluctuate throughout; this is due to the reaction cell being placed within the open laboratory without any temperature regulation. Due to the constant fluctuations the pressure data is nosier than the data for the other temperatures. However, there is still an increase seen.

Figure 6.22 compares the hydrogen evolved (mmol H_2 cm^{-2}) for the UNb3 experiments. The corresponding linear rate for each temperature is plotted to show the temperature dependence for UNb3 (Figure 6.23 and Table 6.7). There is a reasonable correlation seen for the temperature dependence in figure 6.23, with an R^2 value of 0.84. It must be noted that two of the UNb3 experiments are relatively short and are only with one water vapour exposure instead of the intended sequential oxidation; therefore, it is possible that the shorter exposure experiments may still be influenced by residual gases.

a)

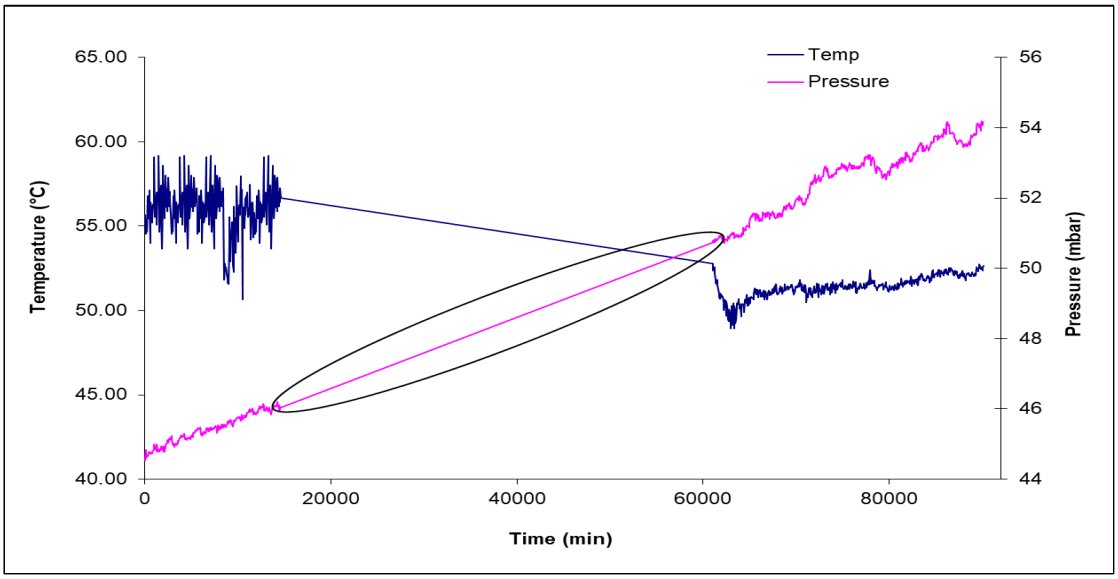

b)

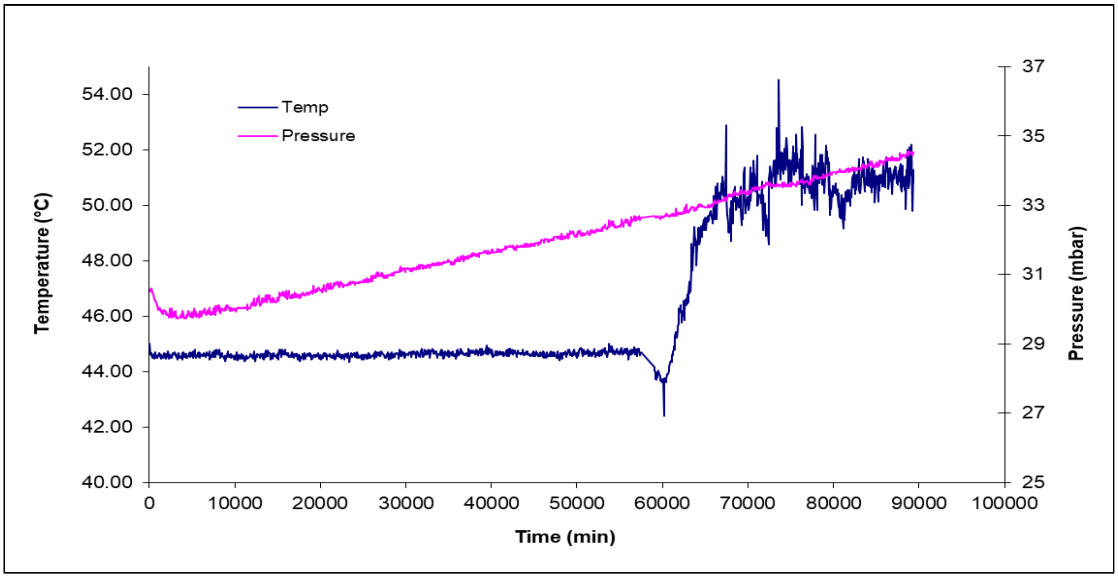

c)

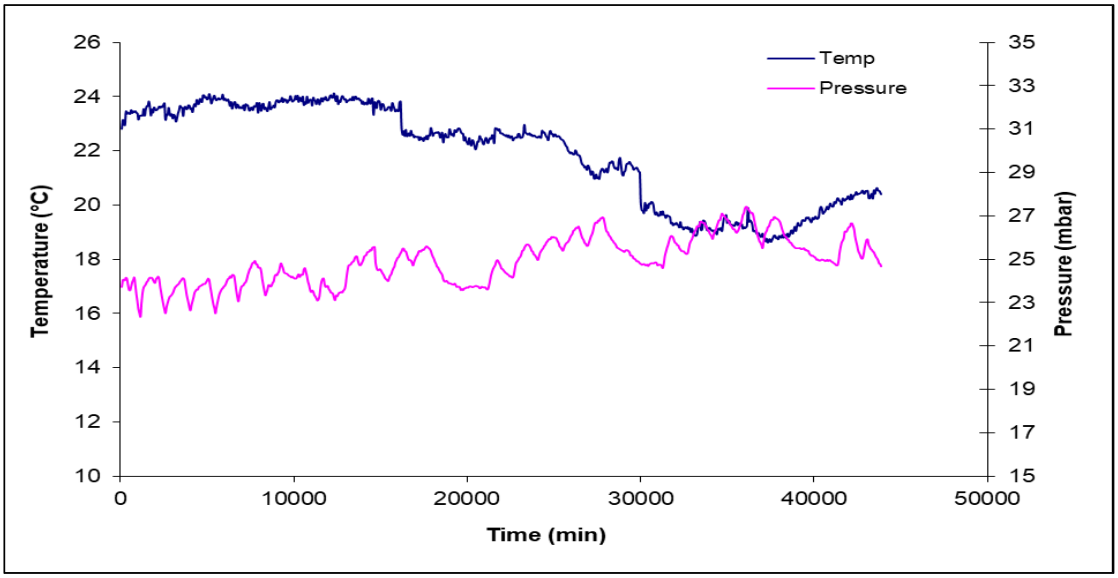

Figure 6.21 Pressure and temperature data for the UNb3 experiments, a) conducted at 52.94 °C and 44.54 mbar, b) conducted at 46.41 °C and 27.37 mbar, c) conducted at 21.93 °C and 23.71 mbar.

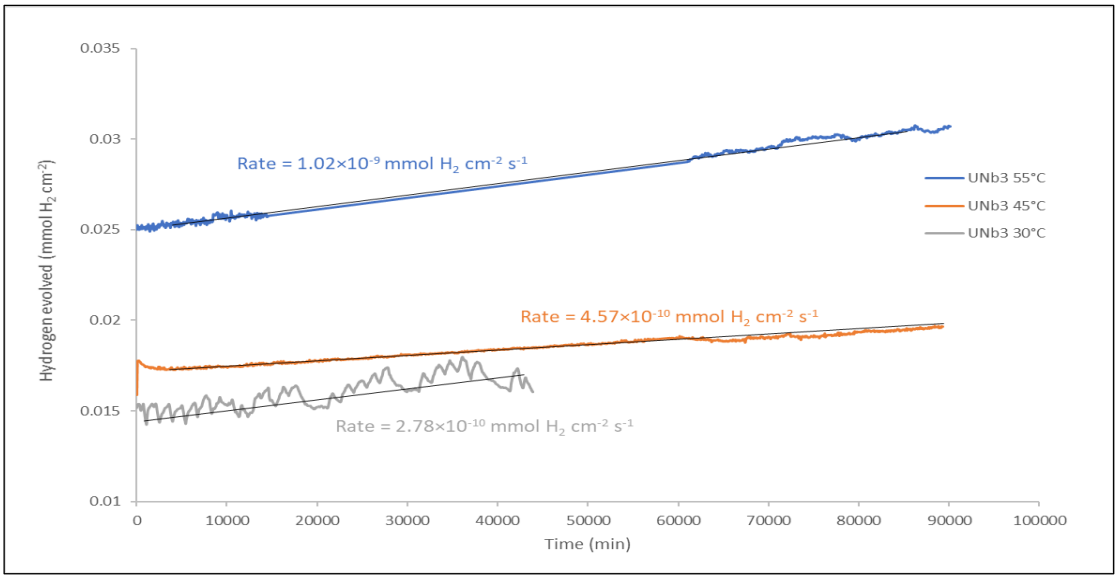

Figure 6.22 Amount of hydrogen evolved (mmol H_2 cm^{-2}) for the UNb3 experiments, displaying the calculated rate for each temperature. Rates are in mmol H_2 cm^{-2} s^{-1}.

Table 6.7 ***Rate data for the UNb3 experiments.***

Temperature			1000/ T(K^{-1})	Starting pressure (mbar)		Rate (mmol H_2 cm^{-2} s^{-1})	Rate (mmol H_2 cm^{-2} s^{-1} $mbar^{-0.5}$)
Desired (°C)	Actual (°C)	Actual (K)		Desired	Actual		
55	52.94	326.09	3.07	31.30	44.54	1.02E-09	1.51E-10
45	46.41	319.56	3.13	28.90	27.37	4.57E-10	8.27E-11
30	21.93	295.08	3.39	31.40	23.71	2.78E-10	5.71E-11

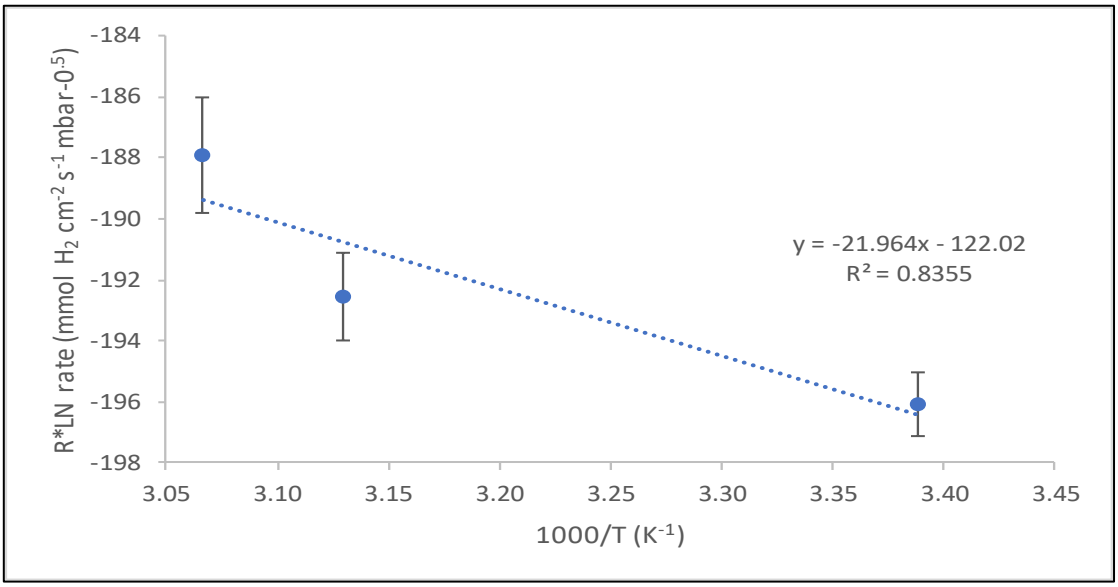

Figure 6.23Temperature dependence of UNb3. The error bars are calculated from the transducer % accuracy and are not an indication of confidence in the data.

6.2.1.2 UNb6

Figure 6.24a, b and c present the pressure and temperature data for the UNb6 experiments at 57.08 °C, 44.57 °C and 22.80 °C respectively. In figures 6.24a and 6.24b, there is a region where the logger was not recording and a separate region with an apparent increase in temperature near the end of the experiment. The pressure remains consistent with that expected so it is thought that these features are artefacts. In figure 6.24c, the temperature can be seen to fluctuate throughout; this is due to the reaction cell being placed within the open laboratory and the lack of temperature regulation within the laboratory. Due to the constant fluctuations the pressure data are nosier than the data for the other temperatures; however, there is still an increase seen.

Figure 6.25 presents the hydrogen evolved (mmol H_2 cm^{-2}) for the UNb6 experiments, with the corresponding pressure-corrected rates being presented in Figure 6.26 and Table 6.8. A very reasonable correlation with an R^2 value of 0.9908 was obtained.

a)

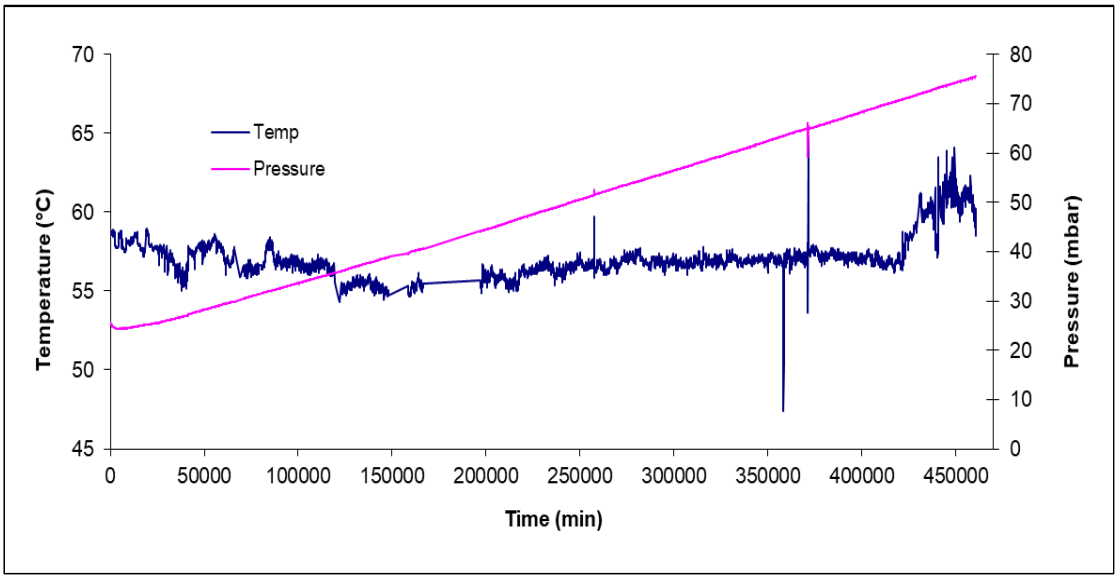

b)

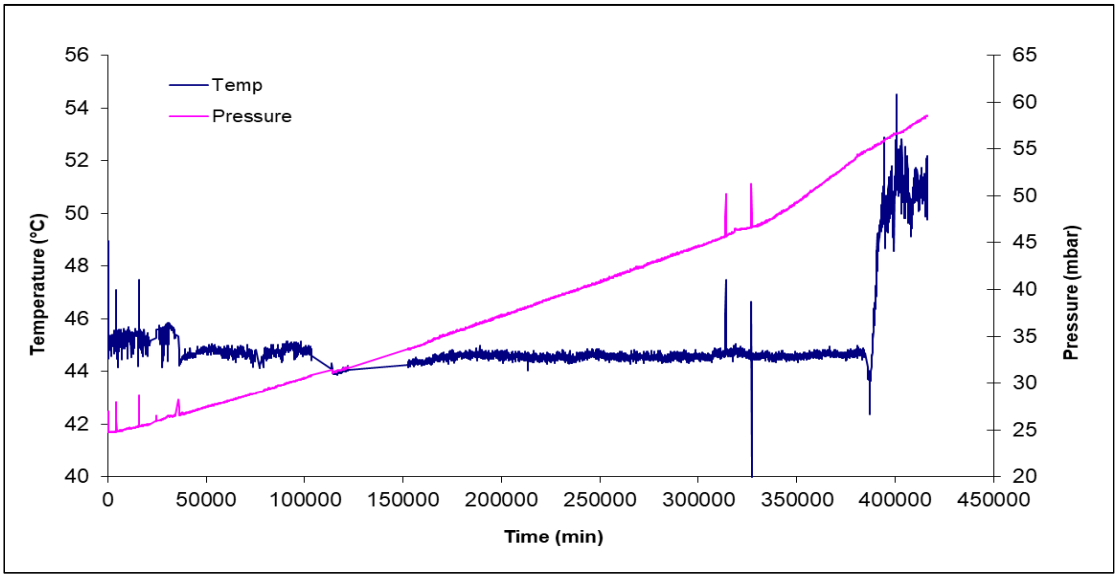

c)

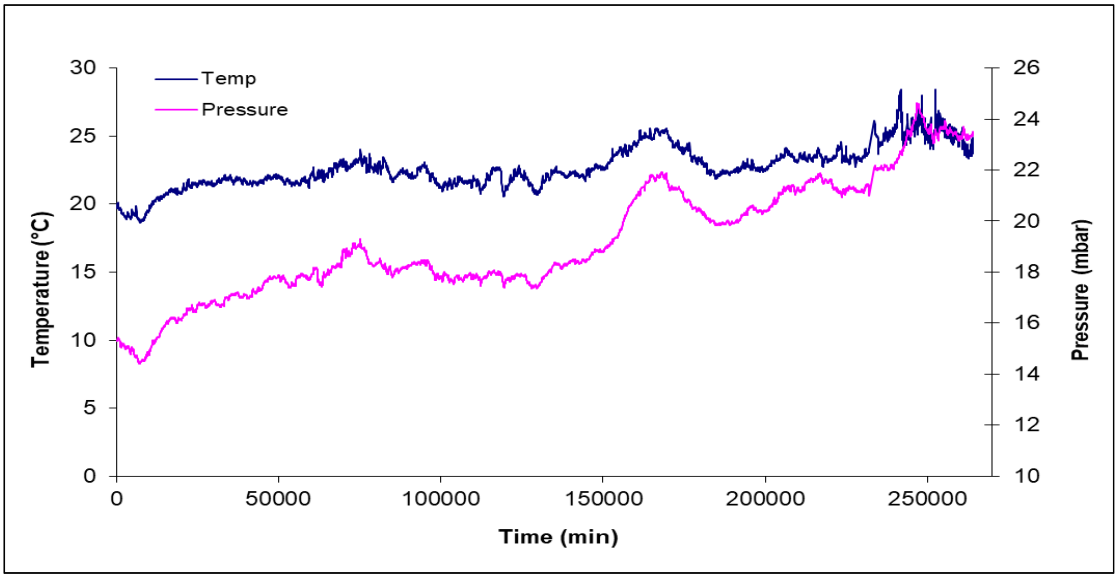

Figure 6.24 Pressure and temperature data for the UNb6 experiments, a) conducted at 57.08 °C and 25.70 mbar, b) conducted at 44.57 °C and 24.83 mbar, c) conducted at 22.80 °C and 15.30 mbar.

a)

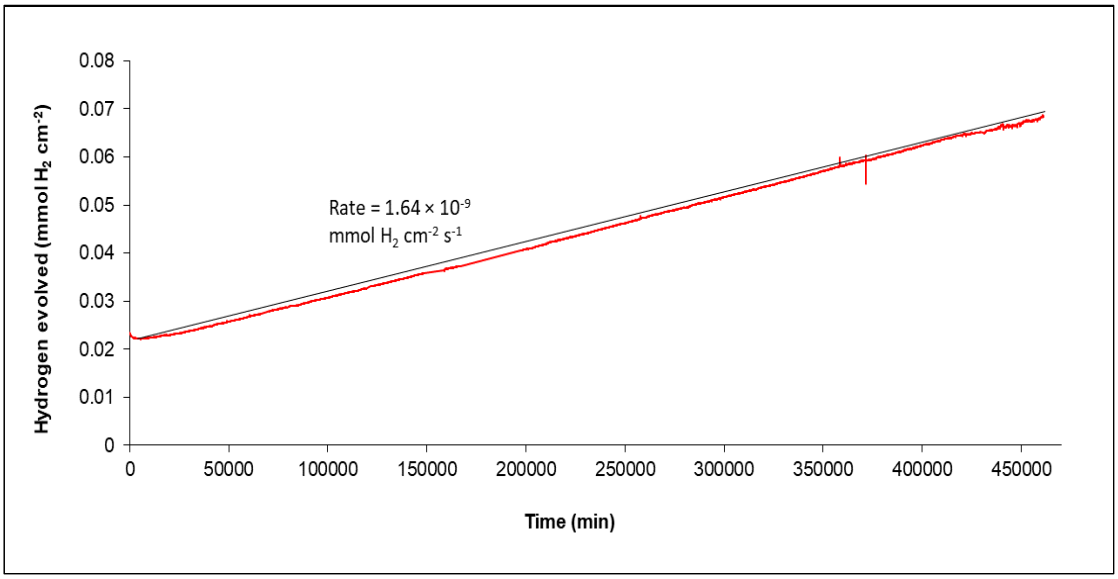

b)

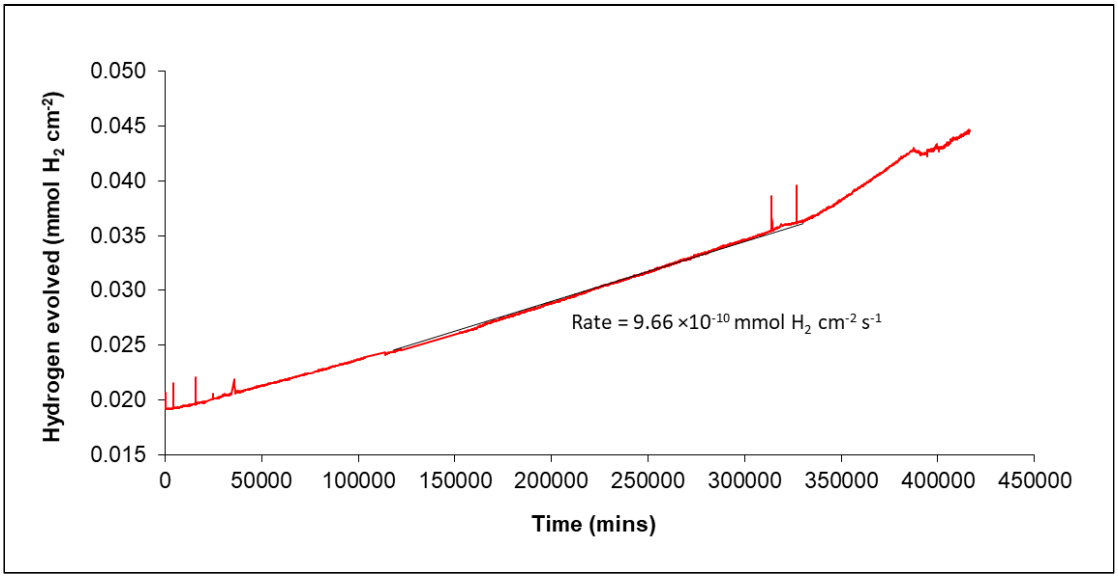

c)

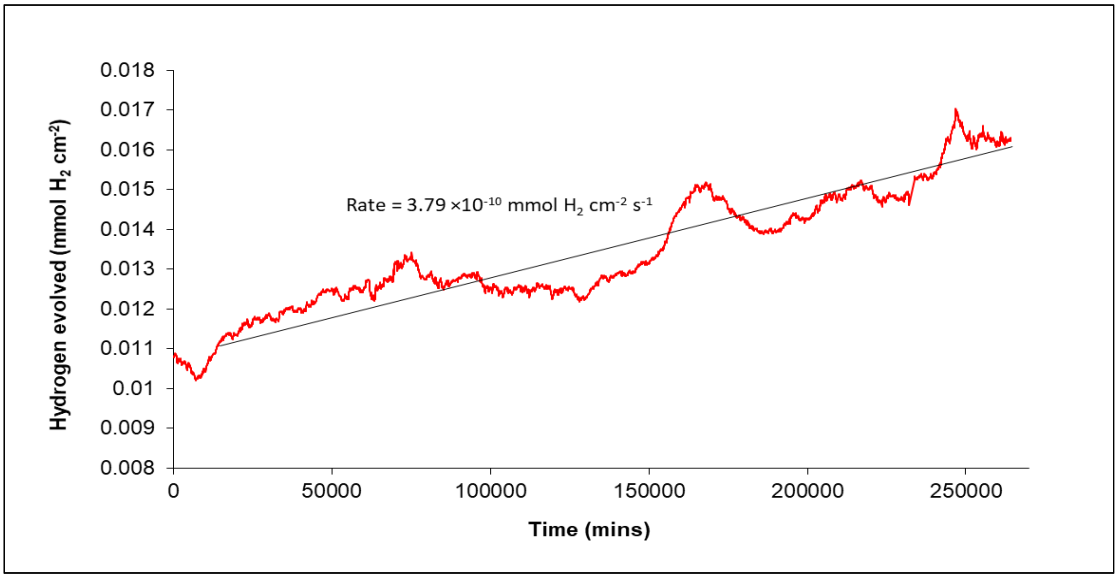

Figure 6.25 Amount of hydrogen evolved (mmol H_2 cm^{-2}) for the UNb6 experiments, a) conducted at 57.08 °C and 25.70 mbar, b) conducted at 44.57 °C and 24.83 mbar, c) conducted at 22.80 °C and 15.30 mbar.

Table 6.8 Rate data for the UNb6 $D_2{}^{16}O$ experiments.

Temperature			1000/T(K^{-1})	Starting pressure (mbar)		Rate (mmol H_2 cm^{-2} s^{-1})	Rate (mmol H_2 cm^{-2} s^{-1} $mbar^{-0.5}$)
Desired (°C)	Actual (°C)	Actual (K)		Desired	Actual		
55	57.08	330.23	3.03	31.30	25.70	1.64E-09	3.24E-10
45	44.57	317.72	3.15	28.90	24.83	9.66E-10	1.94E-10
30	22.80	295.95	3.38	31.40	15.30	3.79E-10	9.69E-11

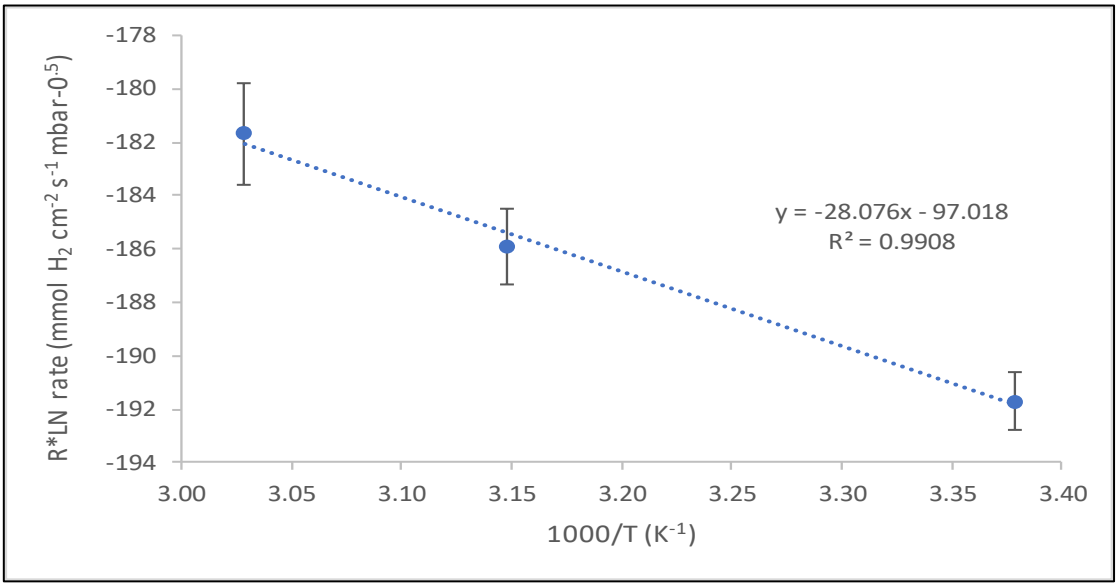

Figure 6.26 Temperature dependence of UNb6. The error bars are calculated from the transducer %accuracy and are not an indication of confidence in the data.

Table 6.9 contains the rate data for the $H_2{}^{18}O$ exposures with figure 6.27 comparing the data for the two waters. It can be seen that the rate values are similar, within error, suggesting that for UNb6 there was no contamination/residual gas within the reaction cells as was seen for uranium, where the reaction with $H_2{}^{18}O$ was found to be significantly quicker, see section 4.2.

Table 6.9 Rate data for the UNb6 $H_2{}^{18}O$ experiments.

Temperature			1000/T(K^{-1})	Starting pressure (mbar)		Rate (mmol H_2 cm^{-2} s^{-1})	Rate (mmol H_2 cm^{-2} s^{-1} $mbar^{-0.5}$)
Desired (°C)	Actual (°C)	Actual (K)		Desired	Actual		
55	57.33	330.23	3.03	31.30	23.00	1.66E-09	3.46E-10
45	44.87	318.02	3.14	28.90	23.30	1.33E-09	2.76E-10
30	26.64	299.79	3.34	31.40	19.81	2.20E-10	4.94E-11

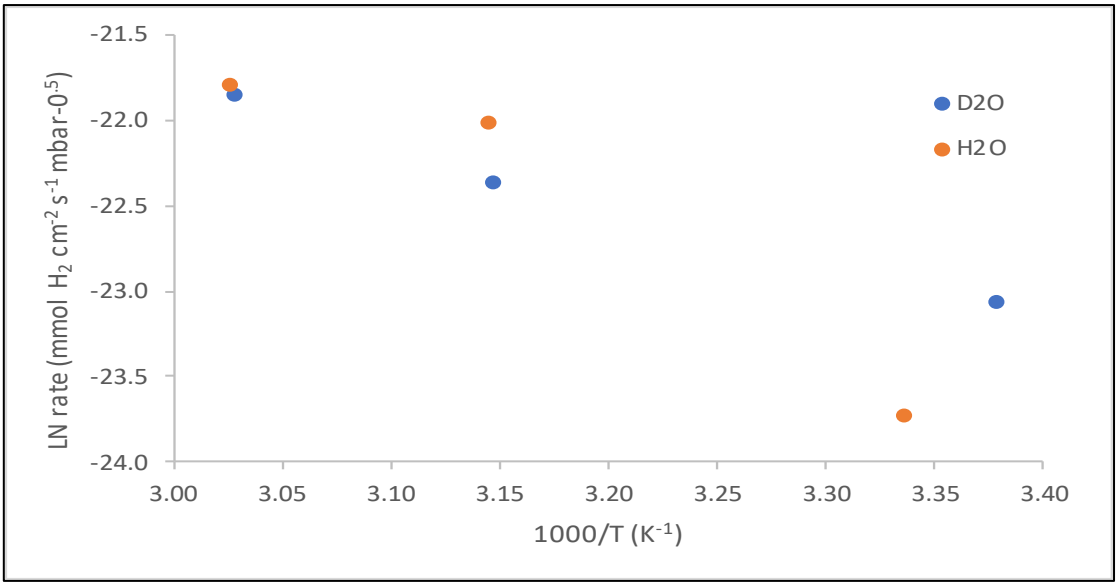

Figure 6.27 Comparison of rate data for the $D_2{}^{16}O$ and $H_2{}^{18}O$ experiments on UNb6.

6.2.1.3 Comparison of the two alloys

Figure 6.28 compares the rate data for the two alloys, UNb3 and UNb6. It can be seen that UNb6 appears to react faster with water vapour than UNb3. This is unexpected as previous work[8,11] has shown the increase in niobium content to significantly reduce the reaction rate. It must be noted that there is significant difference in exposure duration for a couple of the temperatures (55 °C and 30 °C) (Table 6.10), with UNb6 undergoing a significantly longer exposure to water vapour than UNb3. This is likely to have an impact on the corrosion rates derived, with UNb3 still in the early stages of reaction. However, it can be seen, for the 45 °C experiment, where both alloys experienced a similar duration of water vapour exposure, that figure 6.28 still shows the UNb6 to display a considerably faster corrosion rate than UNb3, suggesting that there may be another factor that is influencing the unexpected corrosion rates of the UNb6 alloy.

Table 6.10 Exposure durations (hours) for UNb3 and UNb6 water vapour experiments.

	Exposure time (hours)	
Temperature (°C)	**UNb3**	**UNb6**
55	1502	10671
45	13426	16198
30	2107	13344

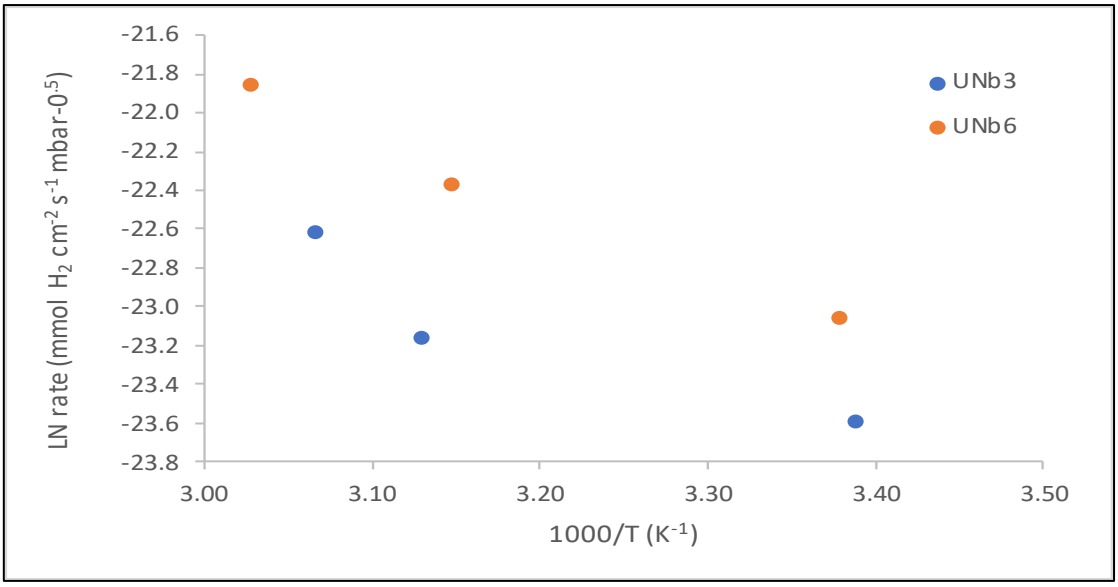

Figure 6.28 Data comparison of UNb3 and UNb6 for $D_2{}^{16}O$ exposure.

One possible reason for the apparent enhanced corrosion rate of UNb6 is possible phase segregation due to ageing. Both alloys, UNb3 and UNb6 are of a considerable age with the estimate being 6 and 30 years respectively. It has previously been seen that ageing can impact the physical properties of the alloys, often leading to an increase in strength but a loss of ductility and corrosion resistance. The UNb6 may have undergone some form of ageing due to storage within a moist atmosphere. From the EDX data in section 6.1, the UNb6 TEM section showed a clear niobium-rich band, suggesting that some form of segregation had occurred, possibly spinodal decomposition as has been suggested previously[1]. If this has occurred then it is not surprising for the UNb6 to react at a rate faster than expected as there will be regions depleted in niobium and therefore the material would corrode at a rate more consistent with pure uranium, i.e. much faster. Atom probe analysis may provide a clearer picture on whether any segregation has occurred in the alloys.

6.2.1.4 Comparison of all materials studied

Figure 6.29 presents an Arrhenius plot for all of the materials studied (U, Nb, UNb3 and UNb6). The activation energies for UNb3 and UNb6 of 21.97 kJ mol^{-1} and 28.08 kJ mol^{-1} respectively are similar to the value obtained for niobium (21.81 kJ mol^{-1}). As previously shown the rates for the alloys are slower than those for uranium. However, they are also slower than for pure niobium. Previous work has shown niobium to have slower kinetics than UNb6 alloy[8].

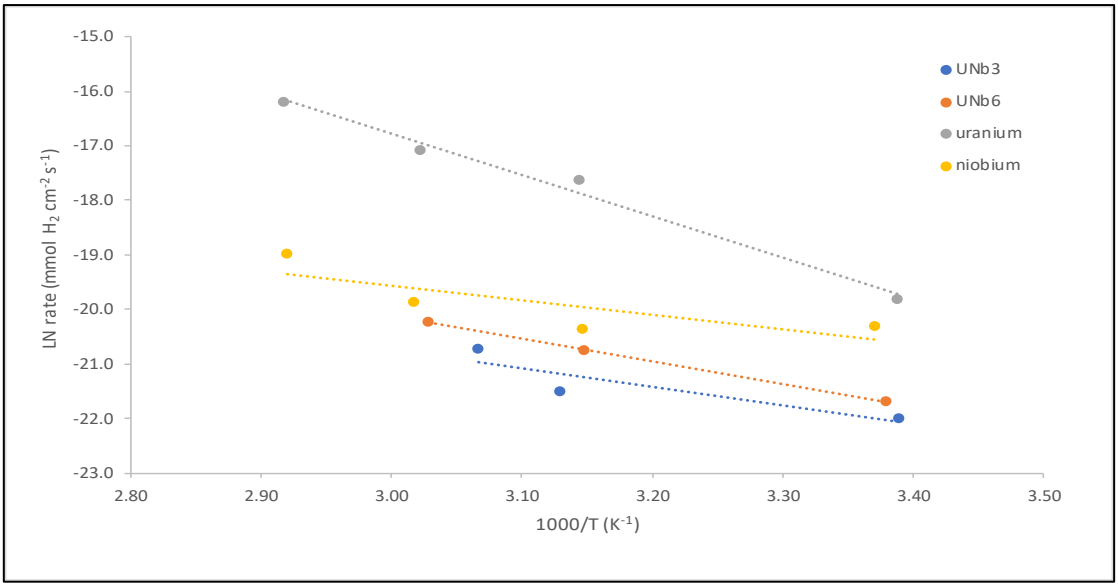

Figure 6.29 Data comparison of all materials for $D_2{}^{16}O$ exposure (U, Nb, UNb3 and UNb6).

Morrall[12] previously found there to be an empirical fit of corrosion rates of four different composition UNb alloys, with the E_a almost identical (uranium being 36.7 k $Jmol^{-1}$, UNb2 being 37.2 kJ mol^{-1} and UNb4 being 37.3 kJ mol^{-1}). This suggested that whatever the overall mechanistic processes might be, they appear consistent across the range of alloys investigated. In the present study the activation energies derived are similar for the alloys and niobium, albeit slightly lower than those reported by Morrall, but could possibly be suggesting that the corrosion mechanism for the alloy is similar to that of pure niobium.

6.2.2 Reaction with water vapour plus oxygen

6.2.2.1 $D_2{}^{16}O + {}^{18}O_2$ system

For uranium it was seen that the addition of oxygen to the water vapour reaction significantly reduced the rate of oxidation, while for niobium there was no observable change in the oxidation rate. For the alloys it was uncertain as to which effect would take precedence or whether there would be a combination of the two.

Figure 6.30 presents the data from the $D_2{}^{16}O + {}^{18}O_2$ experiments for UNb3 and UNb6. As previously mentioned there was an issue with the logging of the data and, therefore. The start of the experiments was not recorded. This means that the starting pressure, taken as the first pressure reading recorded (which should have been ~40 mbar), is higher than it should be. It

is also not possible to know if the reaction is still within the mixed gas oxidation stage, which for uranium inhibits the oxidation rate. In both data sets the pressure can be seen to increase with time and the temperature fluctuates by 4-6 °C. Interestingly for the UNb6 data, there is an initial non-linear period of pressure increase. This could possibly suggest that a change to a water-only oxidation mechanism has occurred, i.e. O_2 depletion has occurred and it is no longer a mixed system therefore the rate returns to that of the water vapour system. This has been reported previously for uranium[3,21].

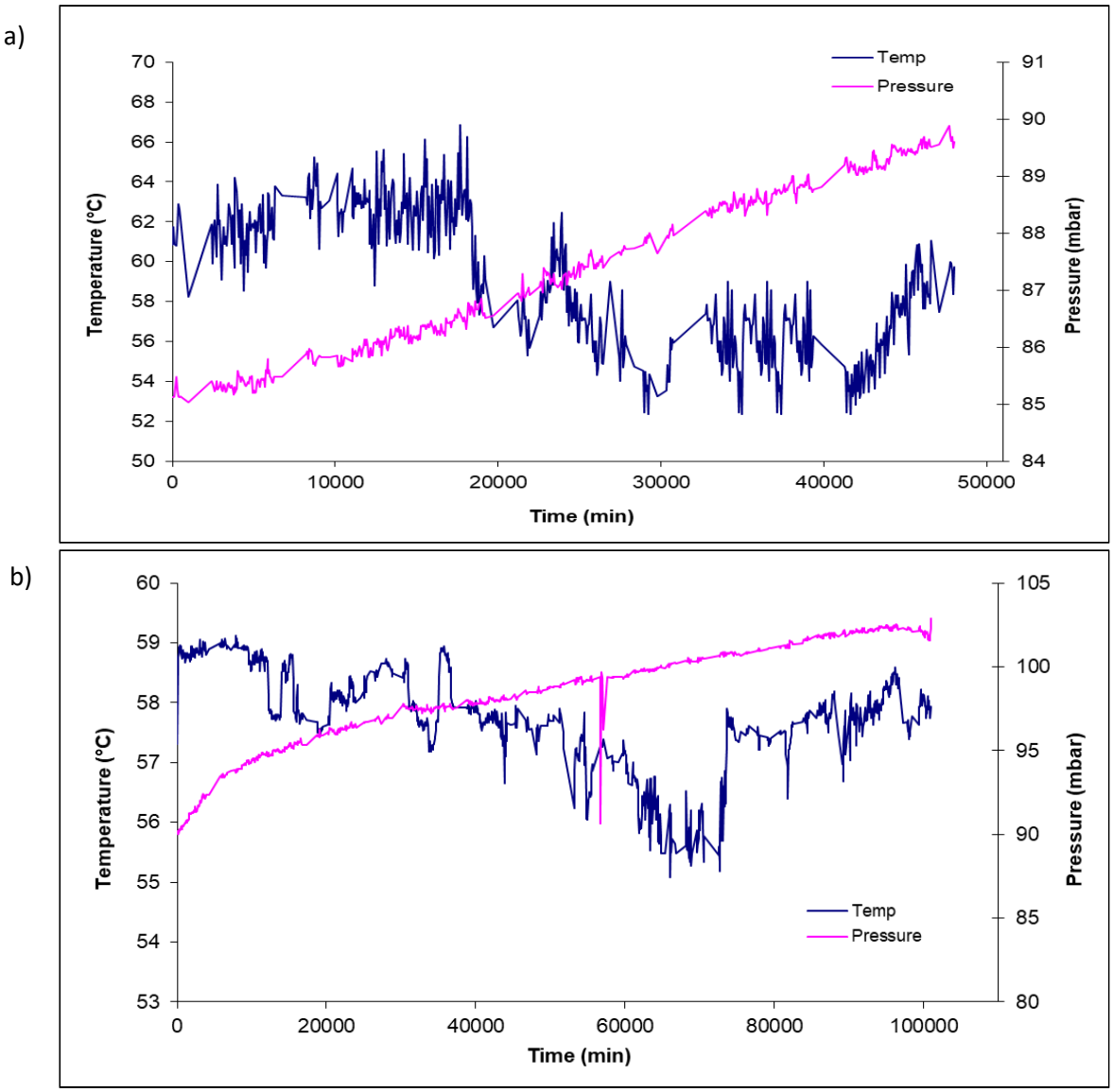

Figure 6.30 Pressure and temperature data for the $D_2{}^{16}O$ + $^{18}O_2$ exposures, a) UNb3 alloy at 59.00 °C and 85.13 mbar, b) UNb6 alloy at 57.43 °C and 90.17 mbar.

6.2.2.2 $H_2{}^{18}O + {}^{16}O_2$ system

Figure 6.31 presents the data from the $H_2{}^{18}O + {}^{16}O_2$ experiments for each of the alloys. As previously mentioned there was an issue with the logging of the data and therefore the start of the UNb3 experiment was not recorded. This means that the starting pressure (first pressure reading recorded) is higher than it should be. For UNb6 there was not such an issue and therefore the start of the experiment was captured, with a starting pressure of 55.37 mbar.

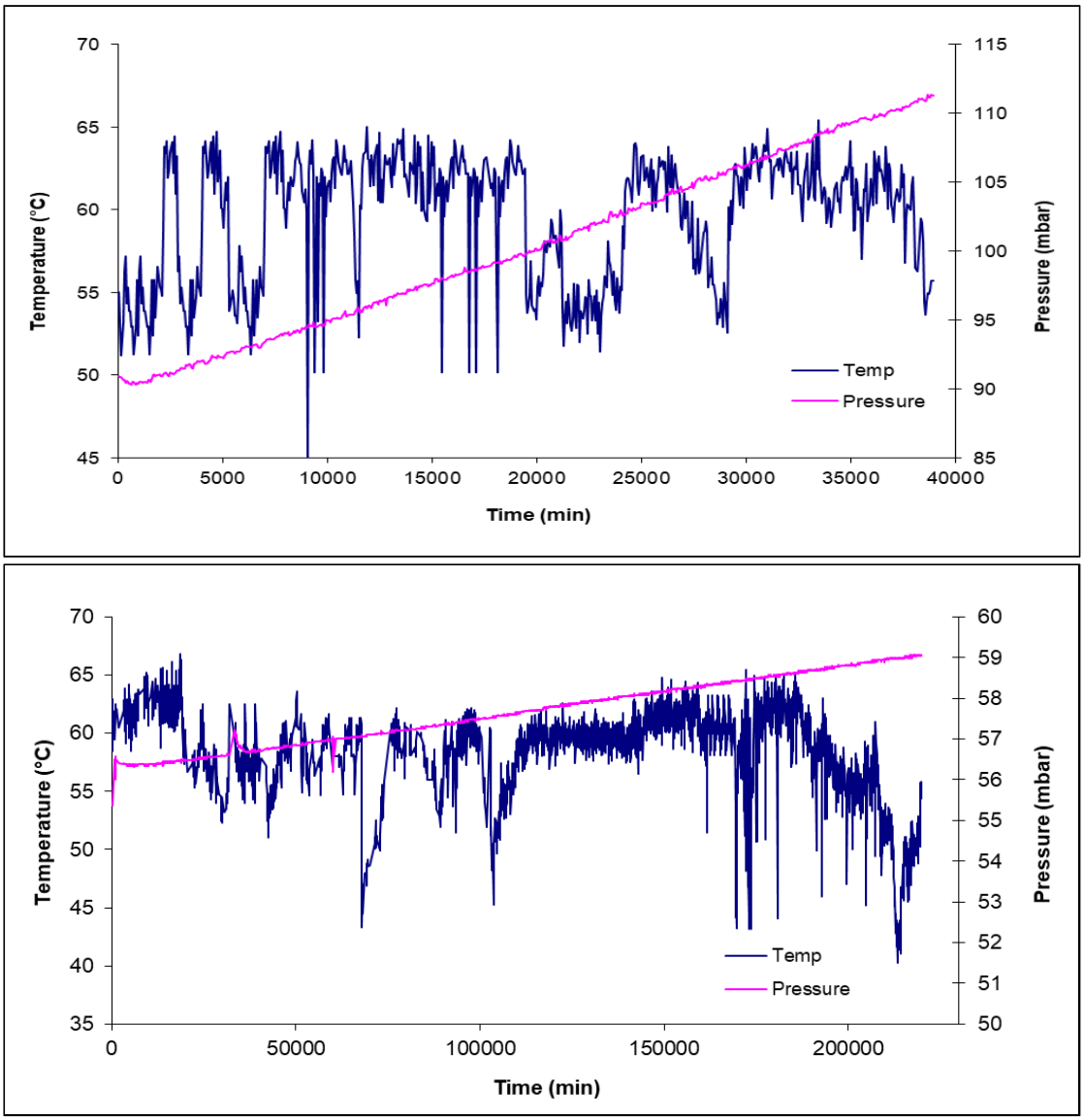

Figure 6.31 Pressure and temperature data for the $H_2{}^{18}O + {}^{16}O_2$ exposures, a) UNb3 alloy at 59.58 °C and 90.89 mbar, b) UNb6 alloy at 59.13 °C and 55.37 mbar.

6.2.2.3 Comparison of alloy data

Table 6.11 present the rate data for the water vapour and water vapour plus oxygen reactions conducted at ~55 °C. For UNb3 the rate for the $H_2{}^{18}O$+ $^{16}O_2$ reaction is actually faster than for the $D_2{}^{16}O$ only reaction. It must be noted that there is not a corresponding $H_2{}^{18}O$ reaction rate to allow absolute comparison. For UNb6 there was no difference in reaction rates for the two water reactions ($D_2{}^{16}O$ and $H_2{}^{18}O$). However, for both uranium and niobium the $H_2{}^{18}O$ reaction was significantly quicker, possibly due to some form of contaminant. Conversely for UNb6, the $H_2{}^{18}O$ + $^{16}O_2$ experiment shows the most divergence, with a much slower rate than both pure water reactions. Orman[82] showed that for lean UNb alloys (4.5 wt%), similar results were seen in the presence and absence of oxygen, while for alloys with a higher niobium content (6 and 8.5 wt%), the difference was more marked, consistent with the results presented here. It should be noted that as the initial parts of the water vapour plus oxygen reactions were not logged, it is likely that the O_2 will have been consumed in the early stages and therefore the data presented represents a water only oxidation rate.

Table 6.11 Reaction rates for water vapour and water vapour plus oxygen mixtures for UNb3 and UNb6 alloy, experiments conducted at ~55 °C.

Material	Exposure	Temperature (°C)	1000/T (K)	Pressure (mbar)	Rate (mmol H_2 cm^{-2} s^{-1})	Rate (mmol H_2 cm^{-2} s^{-1} $mbar^{-0.5}$)
UNb3	$D_2{}^{16}O$	52.94	3.07	44.54	1.02E-09	1.51E-10
	$D_2{}^{16}O$ + $^{18}O_2$	59.00	3.01	85.13	8.73E-10	9.46E-11
	$H_2{}^{18}O$ + $^{16}O_2$	59.58	3.01	90.89	4.82E-09	5.06E-10
UNb6	$D_2{}^{16}O$	57.08	3.03	25.70	1.64E-09	3.24E-10
	$H_2{}^{18}O$	57.33	3.03	23.00	1.66E-09	3.46E-10
	$D_2{}^{16}O$ + $^{18}O_2$	57.43	3.03	90.17	1.49E-09	1.57E-10
	$H_2{}^{18}O$ + $^{16}O_2$	59.13	3.01	55.37	5.65E-10	7.59E-11

6.2.2.4 Comparison of all materials

Figure 6.32 compares the data for water and the water vapour plus oxygen reaction for all materials. (For uranium and UNb6 average are taken (D_2O and H_2O rates), while for UNb3 only D_2O values are used and for niobium only H_2O values are used). The largest effect can be seen for uranium, where the addition of oxygen to the D_2O results in a much slower reaction, agreeing with previous literature. For the alloys only a slight decrease in rate is seen and niobium shows no measurable change. This result suggests that the oxidation/corrosion behaviour of the alloys is an amalgamation of the two differing mechanisms. For niobium it has been suggested that the reaction with water is via O^{2-} diffusion. Therefore, the addition

of oxygen to the reaction enhances the rate by providing more O^{2-} ions for diffusion. For uranium, it has been suggested that O_2 is either preferentially chemisorbed on the surface, preventing OH^- diffusion or the O_2 recombines with free hydrogen to form water, with the latter proven by Harker[74].

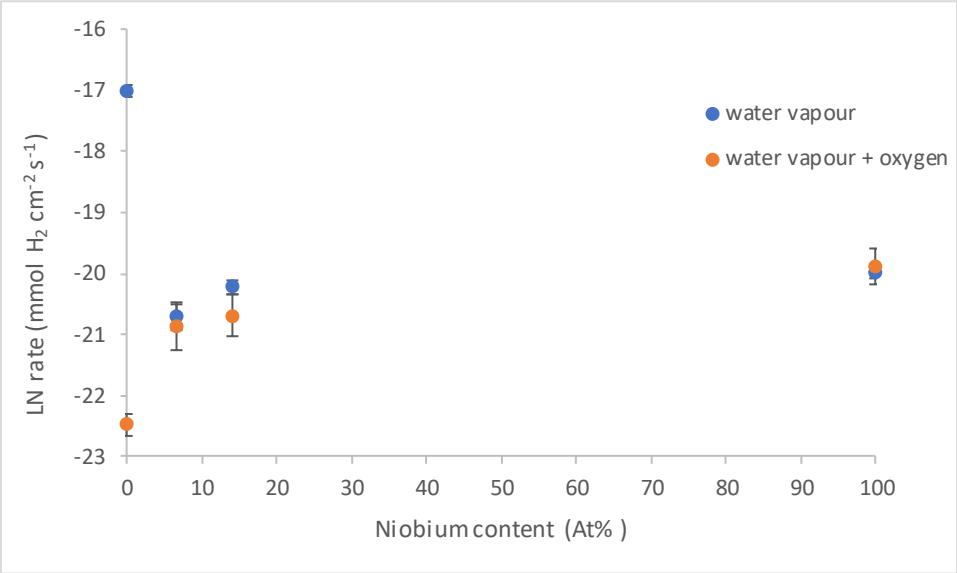

Figure 6.32 Graph comparing water vapour and water vapour plus oxygen reaction rates for all materials. The error bars are calculated from the transducer %accuracy and are not an indication of confidence in the data.

6.2.3 Summary

For water vapour oxidation, both alloys showed slower corrosion rates than either pure uranium or niobium. However, UNb6 appeared to react at a faster rate than UNb3 which was unexpected. It was postulated that ageing had led to this phenomenon, cause by phase segregation of the UNb6 thereby affecting its corrosion resistance. If phase separation of some form has occurred then there will be regions of niobium depletion where the material would then react as pure uranium, so much faster. Atom probe tomography of the alloys should provide more definitive information on any phase separation that has occurred.

For UNb6 oxidation there was no clear difference between the two water systems ($D_2{}^{16}O$ and $H_2{}^{18}O$) as there had been for both uranium and niobium. This suggests that no contamination/residual gas was within the system, as suggested for the pure metal systems.

When oxygen was added alongside water vapour to the system, there was a change in oxidation behaviour seen for UNb6, with the recorded rates for the oxygen plus water vapour reaction being slower than for water only. This is similar to what was seen for uranium in this and other studies[2,21]. For UNb3, the reaction with oxygen and $D_2{}^{16}O$ was seen to be slower than the pure $D_2{}^{16}O$ reaction. However, the reaction with $H_2{}^{18}O$ plus oxygen appears to react at a faster rate. Unfortunately, there was no $H_2{}^{18}O$ only reaction carried out on UNb3 and therefore a true comparison cannot be conducted. It should be noted that the data were only captured midway through the reaction due to issues with the data scan system. It has previously been shown that the rate is inhibited while oxygen is present. However, once depleted the reaction returns close to that of the pure water vapour system. Therefore, it is considered that the O_2 was already depleted and the rate measured was that of a pure water system; hence the rates recorded were very similar.

6.3 SIMS analysis of corroded samples

After the samples had been exposed to both of the water vapours, and sufficient rate data collected, the reacted coupons were analysed by SIMS. The use of the isotopic oxygen and hydrogen ions in the waters allowed some mechanistic information to be deduced from SIMS depth profiling of the oxide surface.

The key mechanistic information required concerns the presence/location of niobium within the profile (i.e. regions rich or depleted in niobium) and the oxides formed, e.g. are only uranium dioxide observed or are niobium oxides also present within the system. There is also the question of hydride formation as for uranium this was seen in the APT data and for niobium it was seen in both the SIMS and APT data.

In the profiles oxygen-18 is represented by a “*” in the depth profiles.

6.3.1 Analysis after exposure to sequential water vapour

6.3.1.1 UNb3

The kinetic data have been used to provide an estimate of the oxide thickness for each of the samples. Table 6.12 shows the calculated oxide thickness from each of the water vapour

exposures. An assumption is made that the main reaction product remains as stoichiometric UO_2, and therefore the oxide thickness calculations are based on mg U cm^{-2}. As the niobium content is only a few atomic percent, the chemical reactions of the niobium atoms are not considered significant when compared to the more thermodynamically-reactive and numerous uranium atoms. Importantly this assumption does not imply that the niobium is insignificant within the underlying mechanism of corrosion resistance for these alloys.

Stopping Range of Ions in Matter (SRIM) has been used in order to calculate a sputter yield to determine the etch depth for each profile. The etch depths calculated are presented in Table 6.13. From the estimated thickness and the etch depth, it is possible to determine whether the oxide-metal interface has been reached during the profiles.

Table 6.12 Calculated oxide thickness values for all of the uranium experiments. The total time includes the exposure to both $D_2{}^{16}O$ and $H_2{}^{18}O$. This value can then be compared to the etch depths of SIMS analysis.

Temperature (°C)	Water	Exposure time (hours)	Time to grow 1 µm UO_2 (hours)	Calculated thickness of UO_2 (µm)
52.94	$D_2{}^{16}O$	1502	14940.9	0.10
	Total			**0.10**
45.61	$D_2{}^{16}O$	13426	24232.8	0.55
	$H_2{}^{18}O$	4369	24232.8	0.18
	Total			**0.73**
21.93	$D_2{}^{16}O$	2107	36984.8	0.06
	Total			**0.06**

From the data in Table 6.12 and 6.13 it can be seen that for some of the profiles the oxide-metal interface should be evident. Figure 6.33 presents the depth profiles from the UNb3 52.94 °C experiment. In this experiment the exposure was only $D_2{}^{16}O$ and therefore no oxygen-18 will be present, and information on the diffusion (anionic/cationic) is therefore limited. However, the oxide can be seen to be thin with a clear transition to the metal seen (figure 6.33a). This profile is very different to the base metal reactions at the same temperature, showing that the addition of niobium to uranium does have a marked effect on the formation of oxide. Figure 6.33a contains the depth profile for the uranium containing ions while figure 6.33b contains the data from the niobium containing species; both were

obtained in positive SIMS operating mode. Figure 6.33c presents the negative profile, showing both oxygen-16 dominance as expected with some hydroxyl ions present in the form of OH and OH_3. The presence of these ions suggests that OH^- could be the diffusing species. There is further evidence for this, in the presence of hydroxide species in the positive profiles for uranium and niobium. The oxygen ion can be seen to increase with etch time; this is due to recombination of oxygen ions in the SIMS chamber.

Table 6.13 Etch depths calculated using SRIM, a sputter yield of 4.65 was used.

Temperature (°C)	Pressure (mbar)	Mode of SIMS	Depth profie (seconds)	Gun current (nA)	Magnification	Etch Depth (µm)
52.94	44.54	positive - U ions	6470	3.0	x1000	1.04
		positive - Nb ions	7757	3.0	x100	0.11
		positive - Nb ions	2361	3.0	x300	0.03
		negative	3207	3.0	x200	0.05
45.61	27.37	positive	3925	3.0	x100	0.06
		negative	6883	1.0	x300	0.03
21.93	23.71	positive – U	6470	3.0	x1000	1.04
		positive – Nb	7757	3.0	x100	0.11

In the niobium profile there is a clear deuteride peak present at the surface. This was also detected in the niobium SIMS and APT in sections 5.3 and 5.4 respectively. The profiles for uranium, niobium and oxygen are taken in different regions of the surface so it is difficult to build up an accurate structure of the oxide. However, the oxygen ion appears to follow a similar profile to the niobium and niobium oxide, in that they increase in intensity with depth, while the uranium oxide decreased rapidly in the first 1000 s before being replaced by the metal ion. From this it could be surmised that the outer-most layer is formed of UO_2, followed by the uranium metal, and there are then regions of niobium and niobium oxide within the uranium metal. This agrees with previous literature by Younes[50]. It should be noted that there is a clear difference in the counts (and thus intensity) between the uranium and niobium ions, with uranium showing much higher count values. Negative mode is more sensitive to lower masses, therefore, only oxygen ions were profiled.

a)

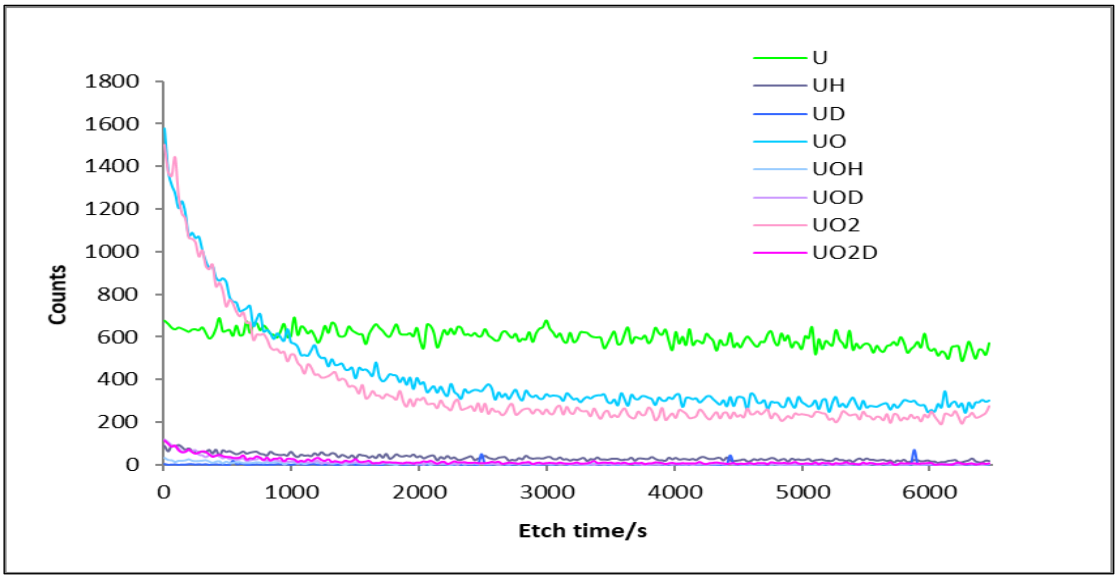

b)

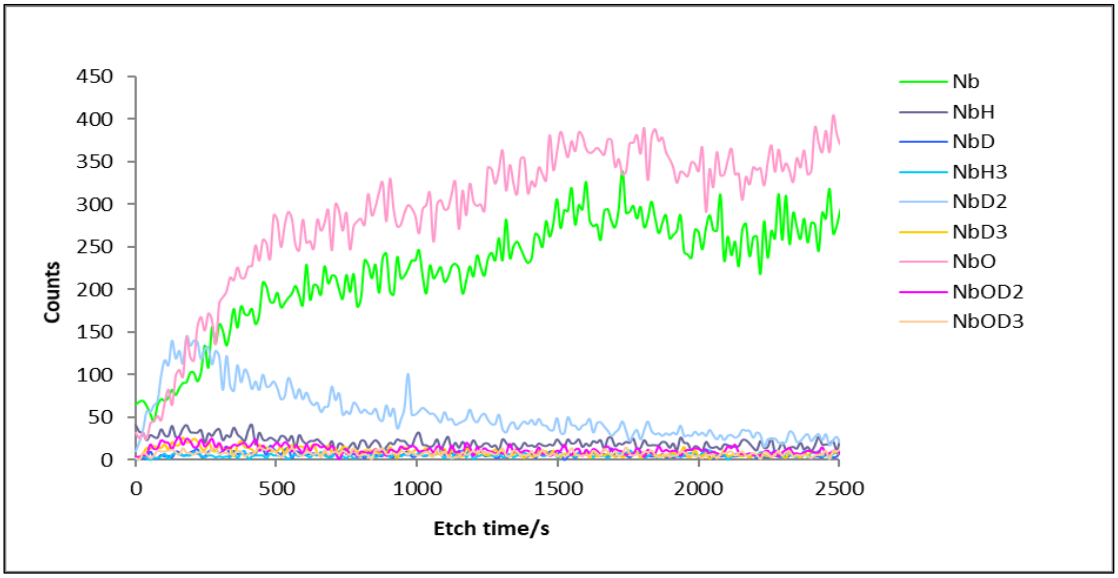

c)

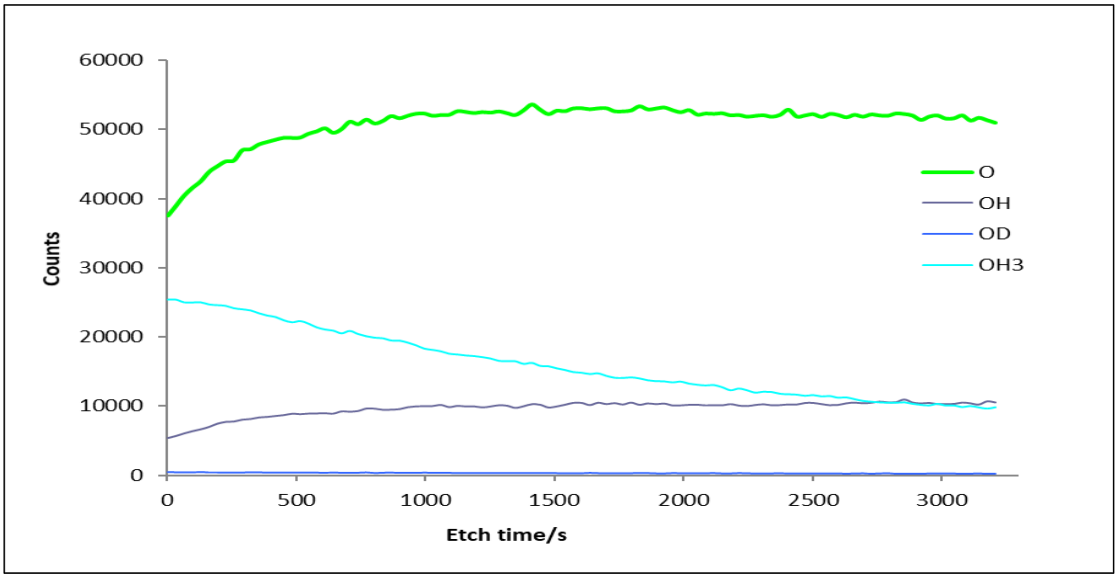

Figure 6.33 Depth profiles of UNb3 at 55°C 30 mbar, a) positive mode profile of uranium species, b) positive mode profile of niobium species, c) negative mode profile of oxygen species.

Figure 6.34 presents the data for the 45 °C experiment where UNb3 was sequentially exposed to $D_2{}^{16}O$ then $H_2{}^{18}O$. No clear changes in oxygen were seen, with O-16 dominating throughout. This can be seen clearly in figure 6.35, where the % oxide fractions are plotted. As no change is seen it is not possible to determine the mechanistic information. This is attributed to the alloy's corrosion resistance. The protective diffusion barrier will already have been formed by the time the second exposure ($H_2{}^{18}O$) takes place and therefore further oxidation is minimal and oxides containing O-18 are limited.

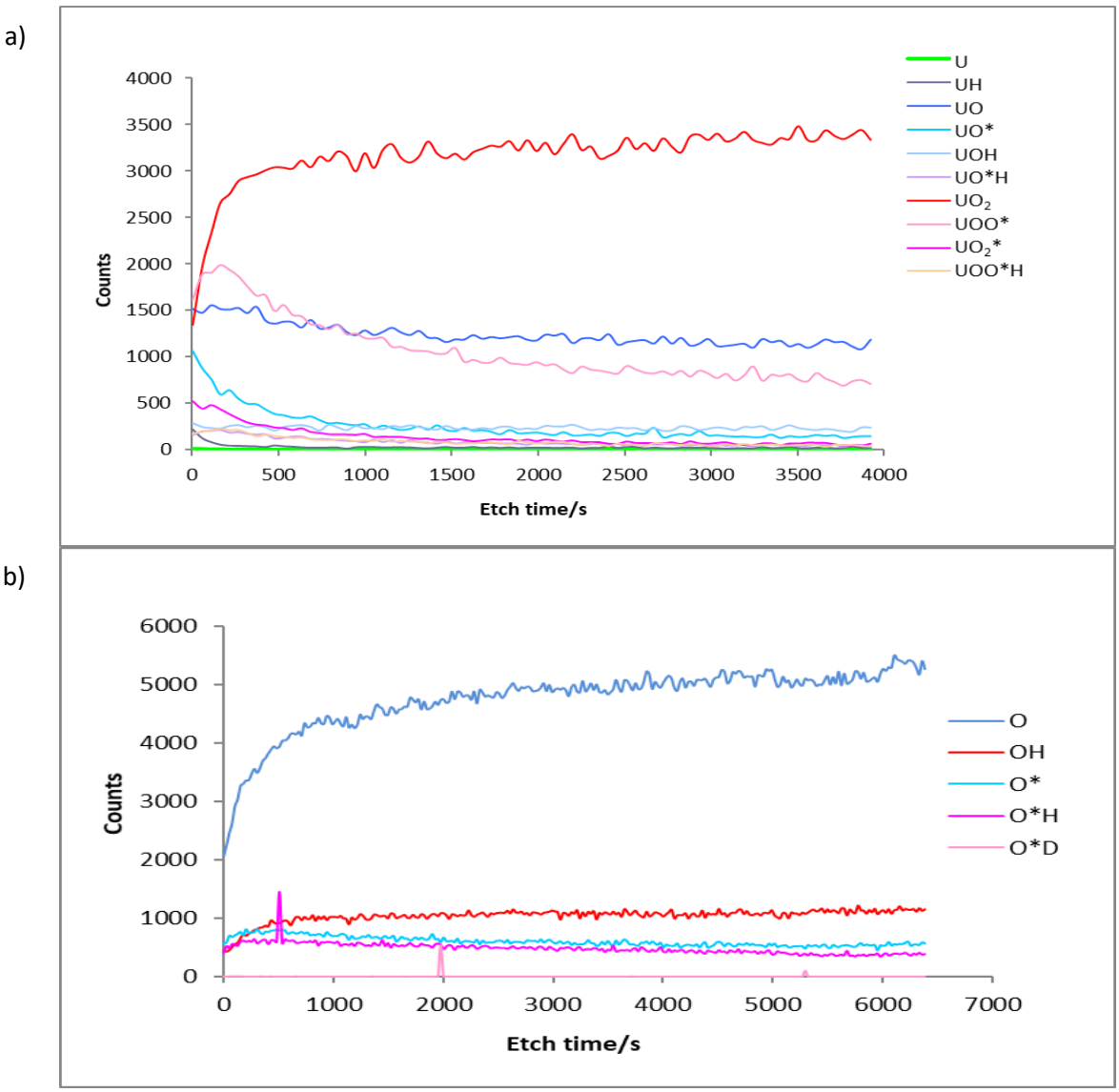

Figure 6.34 Depth profiles of UNb3 at 45°C 30 mbar, a) positive mode profile of uranium species, b) negative mode profile of oxygen species.

a)

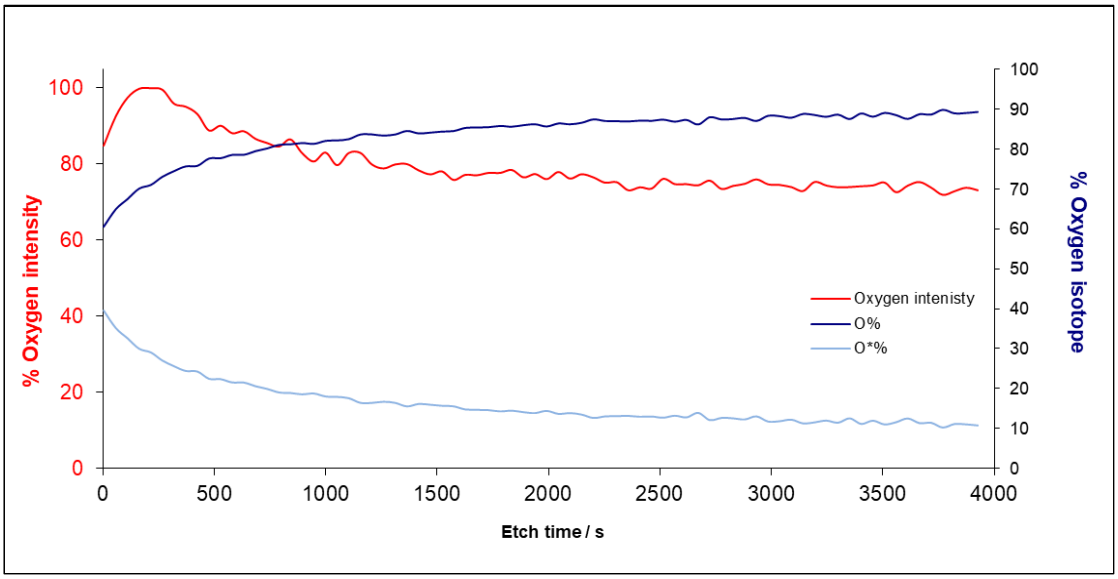

b)

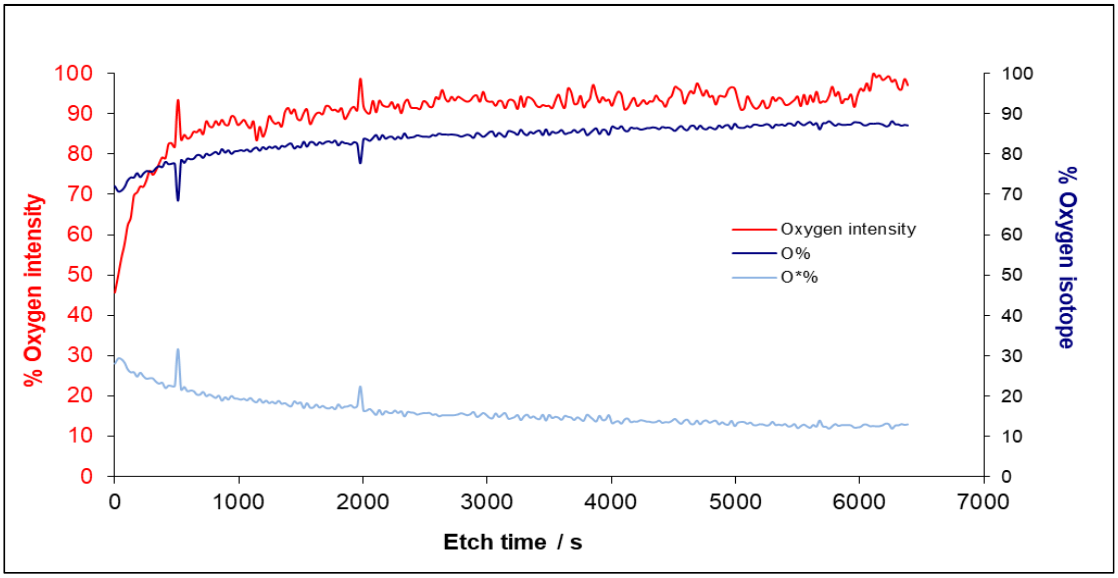

Figure 6.35 % oxide compositions calculated from the depth profiles of UNb3 at 45°C 30 mbar shown in Figure 6.34, a) % oxygen composition in positive mode, b) % oxygen composition in negative mode.

6.3.1.2 UNb6

Again, the kinetic data and SRIM have been used to determine the estimated oxide thickness and SIMS etch depths respectively. Table 6.14 and Table 6.15 contain the oxide thickness and etch depths respectively.

Table 6.14 Calculated oxide thickness values for all of the UNb6 experiments. The total time includes the exposure to both $D_2{}^{16}O$ and $H_2{}^{18}O$. This value can then be compared to the etch depths of SIMS analysis.

Temperature (°C)	Water	Exposure time (hours)	Time to grow 1 µm UO_2 (hours)	Calculated thickness of UO_2 (µm)
57.08	$D_2{}^{16}O$	10671	6984.7	1.53
	$H_2{}^{18}O$	4164	6984.7	0.6
	Total			**2.12**
44.57	$D_2{}^{16}O$	16198	11629.2	1.39
	$H_2{}^{18}O$	2817	11629.2	0.24
	Total			**1.64**
22.80	$D_2{}^{16}O$	13344	23282.5	0.57
	$H_2{}^{18}O$	3632	23282.5	0.16
	Total			**0.73**

Table 6.15 Etch depths calculated using SRIM, a sputter yield of 4.65 was used.

Temperature (°C)	Pressure (mbar)	Mode of SIMS	Depth profile (s)	Gun current (nA)	Magnification	Etch Depth (µm)
57.08	25.70	positive	14403	3.0	x5000	54.94
		negative	18021	3.0	x5000	68.74
44.57	24.83	positive - U ions	316	3.0	x3000	0.44
		positive - Nb ions	5797	3.0	x3000	8.04
		positive - both ions	3834	3.0	x3000	5.32
		negative	3035	3.0	x3000	4.21
22.80	15.30	positive	5547	3.0	x1000	0.89
		negative	3211	3.0	x1000	0.51

Figure 6.36 presents the depth profile from the UNb6 experiment conducted at 55 °C. It can be seen that the uranium oxide ion dominates the oxide. It is also evident that the oxide is very thin when compared to the base metals. In the % oxygen profiles, it can be seen that O-16 dominates (figure 6.36b).

a)

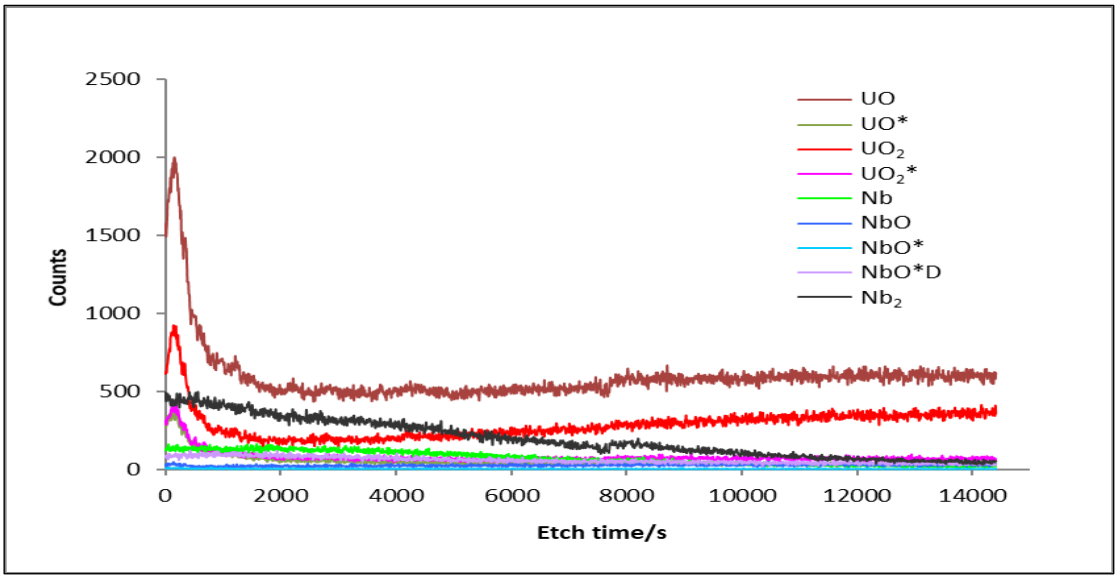

b)

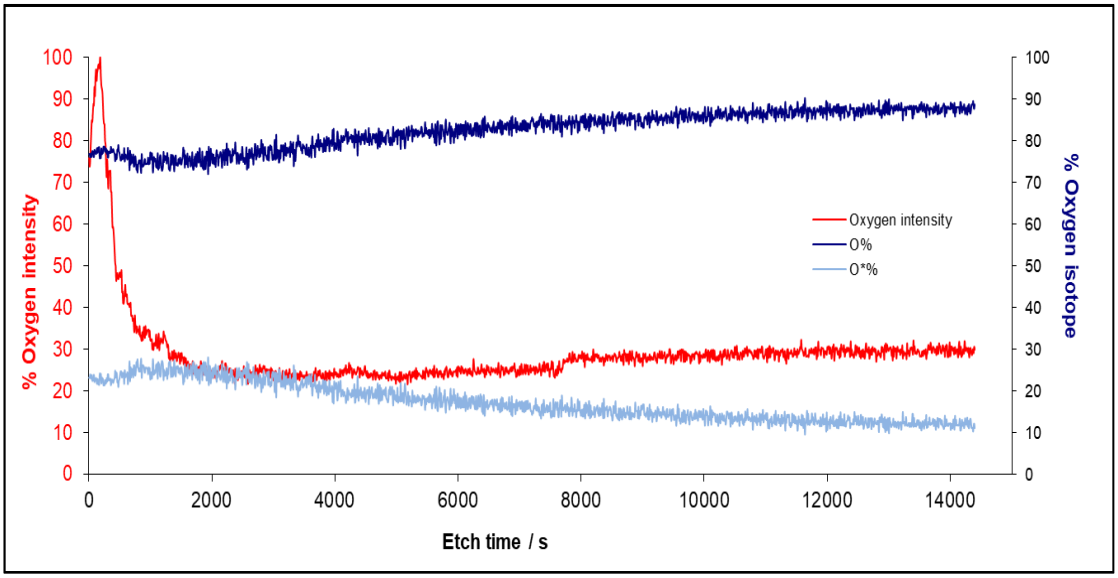

c)

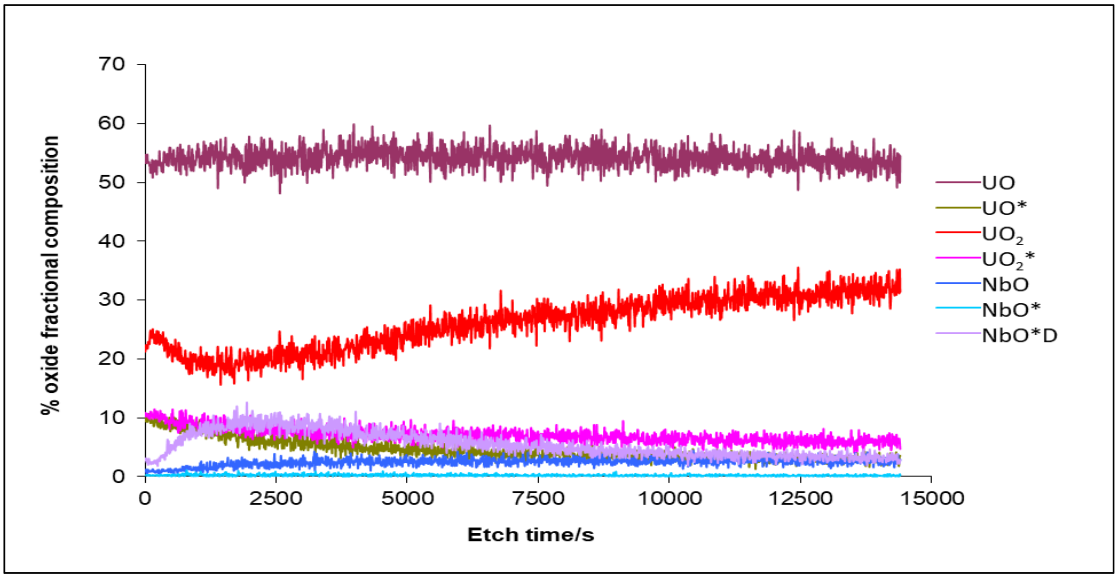

Figure 6.36 Depth profiles of UNb6 at 55 °C 30 mbar, a) positive mode profile of both uranium and niobium, b) % oxide composition for oxygen ions, c) % oxide composition for oxides of interest.

In the experiment conducted at 45 °C a depth profile of both uranium and niobium species shows an interesting result with the initial dominant species being UOH before entering niobium metal. The uranium ion remains within the background count level. When depth profiles of the individual metals (uranium and niobium) are conducted it can be seen that for niobium there is a small amount of NbO at the surface before the metal is reached (figure 6.37b) and the same is seen for uranium with UO_2 and U ions (figure 6.37c). It must be noted that these profiles are conducted on different areas on the surface; therefore, some variance in oxide thickness is to be expected.

If we compare the oxide thickness for this experiment with the corresponding base metal experiments at 45 °C it can be seen that for pure uranium an oxide thickness of 3.4 µm was estimated and for niobium a thickness of 4 µm was estimated. Both these oxides were significantly thicker than the one presented here for the alloy, demonstrating the effect alloying of niobium with uranium has on the base metal corrosion resistance.

If we compare the length of exposure of $D_2{}^{16}O$ versus $H_2{}^{18}O$ to the oxygen fraction profiles of the SIMS data (Table 6.16), it can be seen that the values are relatively similar.

Table 6.16 Comparison of % water exposure times to % oxygen ions within SIMS profiles.

		% of water vapour exposure time		**Average % oxygen within SIMS depth profiles**	
Material	**Temperature (°C)**	**$D_2{}^{16}O$**	**$H_2{}^{18}O$**	**^{16}O**	**^{18}O**
UNb3	46.41	75	25	89 (+ve mode)	11 (+ve mode)
				82 (-ve mode)	18 (-ve mode)
UNb6	57.08	72	28	80 (+ve mode)	20 (+ve mode)
				73 (-ve mode)	27 (-ve mode)
	44.57	85	15	90 (+ve mode)	10 (+ve mode)
				85 (+ve mode)	15 (+ve mode)
	22.80	79	21	79 (+ve mode)	21 (+ve mode)
				67 (-ve mode)	33 (-ve mode)

a)

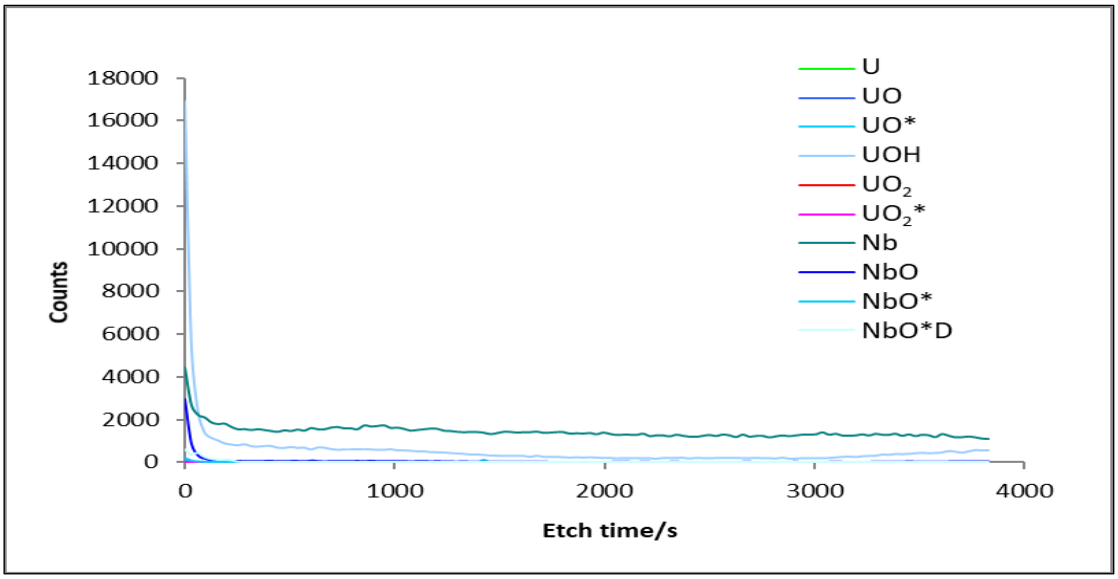

b)

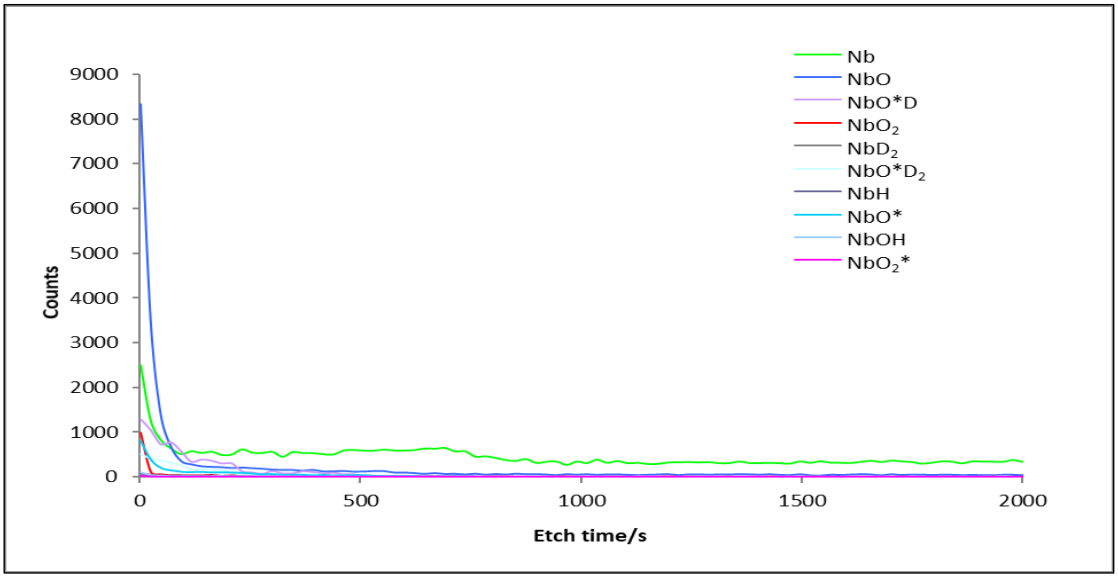

c)

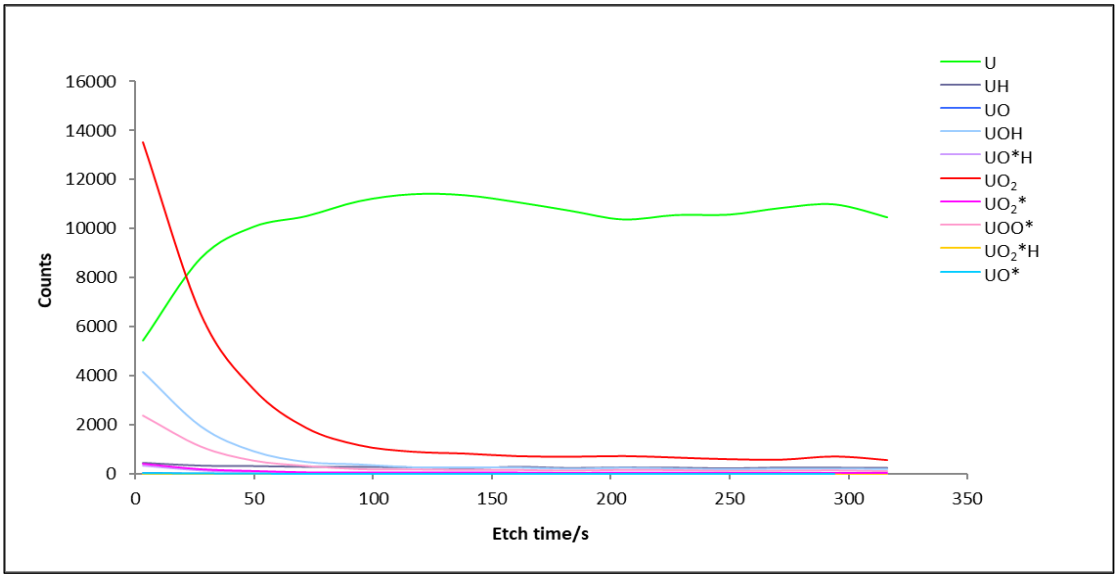

Figure 6.37 Depth profiles of UNb6 at 45 °C 30 mbar, a) positive mode profile of niobium and uranium species, b) positive mode profile of niobium species, c) positive mode profile of uranium species.

6.3.2 Analysis after exposure to water vapour plus oxygen

There were two reaction schemes investigated, $H_2{}^{18}O + {}^{16}O_2$ and $D_2{}^{16}O + {}^{18}O_2$. The use of the labelled waters and oxygen will allow isotopic analysis of the SIMS depth profiles. For pure uranium it was seen that the majority of the oxide formed from the water. For pure niobium no marked change was seen. Again, the kinetic data and SRIM have been used to determine estimated oxide thickness and SIMS etch depth respectively.

Table 6.17 and Table 6.18 contain the oxide thickness and etch depths respectively for both mixed systems. However, as the data were not recorded from the start of the experiments for both UNb3 exposures and the UNb6 $D_2{}^{16}O + {}^{18}O_2$ exposure, the exposure time (hours) will not be accurate and therefore the estimated thicknesses are likely to be considerably lower than actually seen by SIMS.

Table 6.17 Calculated oxide thickness values for the water vapour plus oxygen alloy experiments. This value can then be compared to the etch depths of SIMS analysis.

Material	Water system	Temperature (°C)	Pressure (mbar)	Exposure time (hours)	Time to grow 1 µm UO_2 (hours)	Thickness of UO_2 (µm)
UNb6	$D_2{}^{16}O + {}^{18}O_2$	57.43	90.17	1684	14369.9	0.12
	$H_2{}^{18}O + {}^{16}O_2$	59.13	55.37	4158	29724.3	0.14
UNb3	$D_2{}^{16}O + {}^{18}O_2$	59.00	85.13	800	23139.2	0.03
	$H_2{}^{18}O + {}^{16}O_2$	59.58	90.89	649	4566.9	0.14

Table 6.18 Etch depths calculated using SRIM, a sputter yield of 4.65 was used.

Material	Water system	Mode of SIMS	Depth profile (seconds)	Gun current (nA)	Magnification	Etch Depth (µm)
UNb6	$D_2{}^{16}O + {}^{18}O_2$	positive – U ions	6475	3.0	x100	0.09
		Positive – Nb ions	2142	3.0	x3000	3.35
		negative O	3910	3.0	x3000	5.42
		negative – Nb ions	3991	3.0	x100	0.06
	$H_2{}^{18}O + {}^{16}O_2$	positive	2599	3.0	X2000	1.65
		negative	5565	3.0	x1000	0.89
UNb3	$D_2{}^{16}O + {}^{18}O_2$	Positive – U ions	6197	3.0	x3000	8.60
		Positive - Nb ions	7477	3.0	x3000	10.37
		negative	3393	3.0	x3000	4.71
	$H_2{}^{18}O + {}^{16}O_2$	positive	10806	3.0	x3000	14.99

6.3.2.1 $H_2{}^{18}O + {}^{16}O_2$ system

Figure 6.38 presents a depth profile from the UNb3 experiment. It can be seen that the dominant species is uranium with some UO/UO_2 at the outermost surface followed by a significant niobium oxide component (NbO_2). This oxide structure fits with that seen previously by Younes[50]. From the % oxygen fractional composition in figure 6.38b it can be seen that the dominant oxygen species is O-16 suggesting that the majority of the oxide is formed from the oxygen; this is in contrast to what was seen for uranium. There is however some O-18 present which suggests that the oxygen from the water does play some role in the oxidation mechanism.

Figure 6.39 presents the data for the UNb6 experiment, showing positive (figure 6.39a) and negative modes (figure 6.39b). The corresponding % oxygen fraction for the negative profile is shown in Figure 6.40. From the positive depth profile (figure 6.39a) it can be seen that the uranium oxides dominate, with a small amount of niobium hydride (NbH_3) and oxide (NbO) on the surface, before the oxide-metal interface of uranium is reached. From the positive % oxygen fraction profile it can be seen the majority of the oxide is O-16, and therefore formed from the oxygen, similar to what was seen for UNb3. However, in the negative profile (figure 6.39b) both the O and O*H species dominate, with the two following the same profile as each other. The negative % oxygen fraction profile shows a change of dominating oxygen isotope which corresponds to a change from ^{16}O ion to ^{18}OH ion in the negative depth profile.

a)

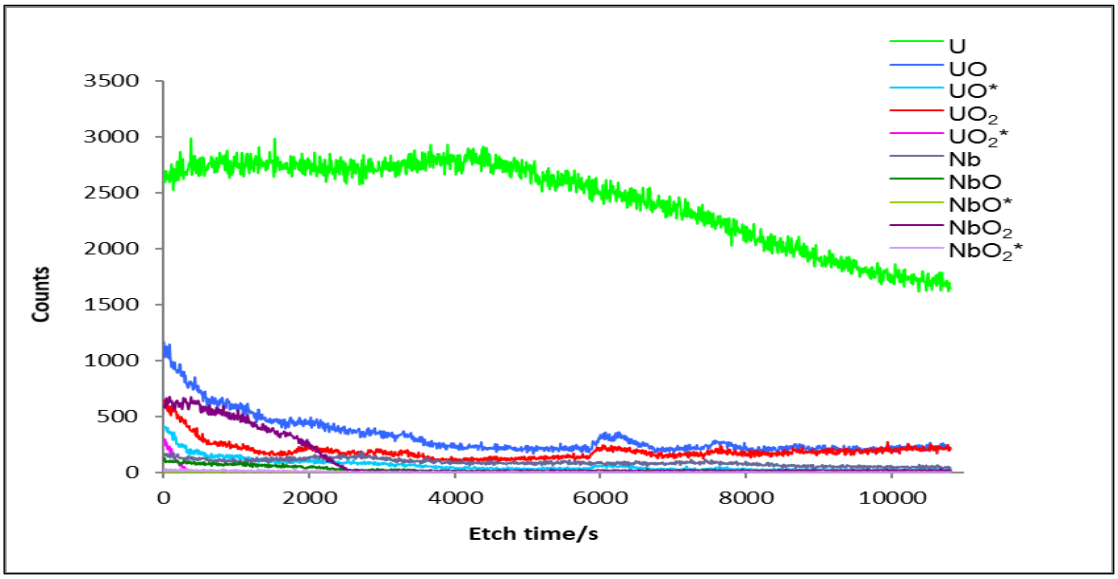

b)

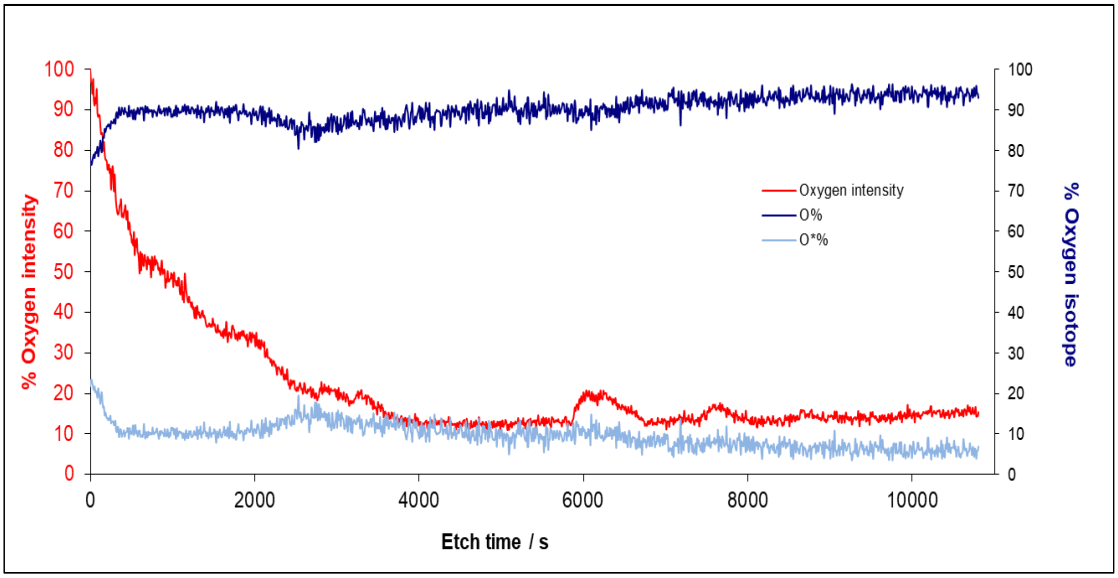

c)

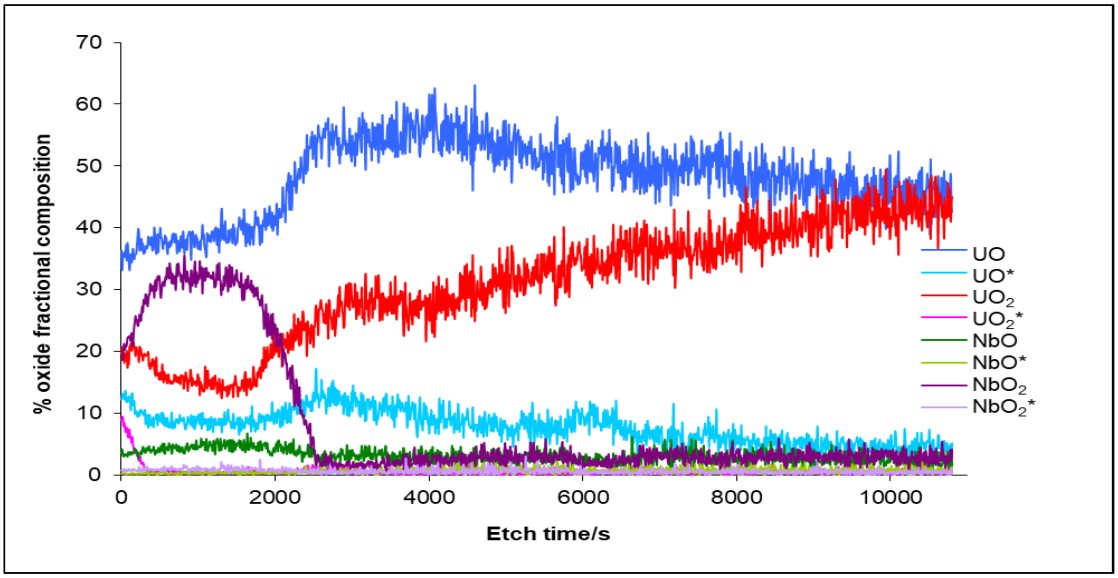

Figure 6.38 Depth profiles of UNb3 after exposure to $H_2{}^{18}O$ + $^{16}O_2$, a) positive depth profile, b) profile showing % oxygen fractions with respect to oxygen ions, c) profile presenting % oxide fractional composition with respect to molecular ions.

a)

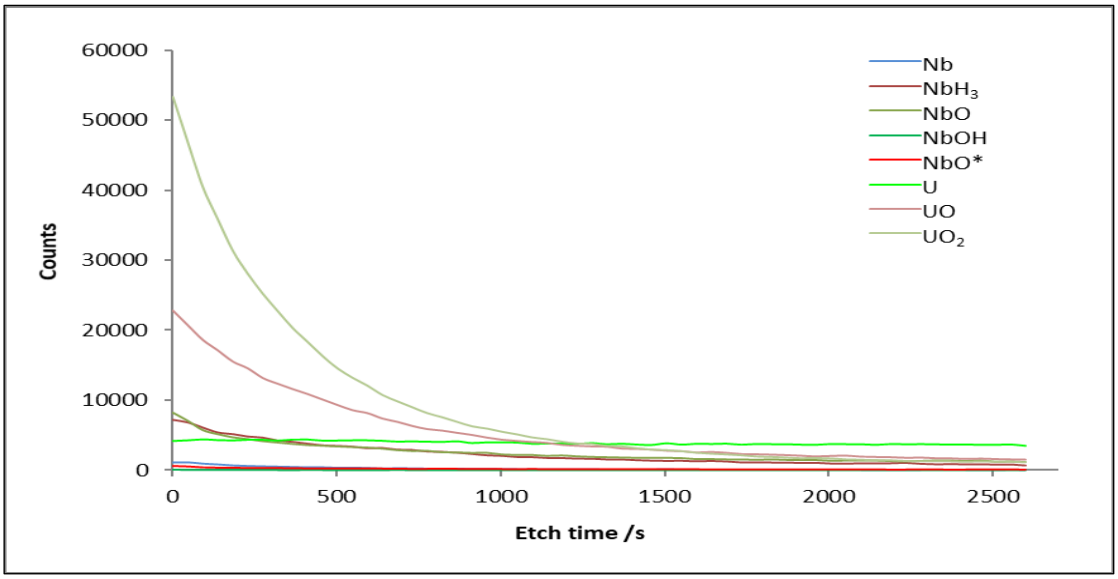

b)

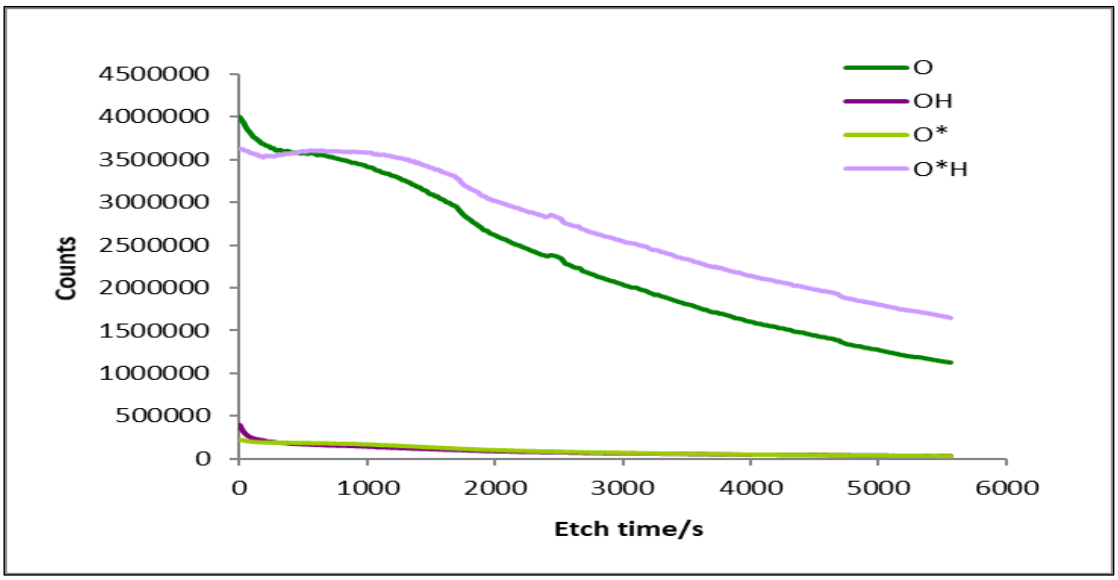

Figure 6.39 Depth profiles of UNb6 after exposure to $H_2{}^{18}O$ + $^{16}O_2$, a) positive profile, b) negative profile.

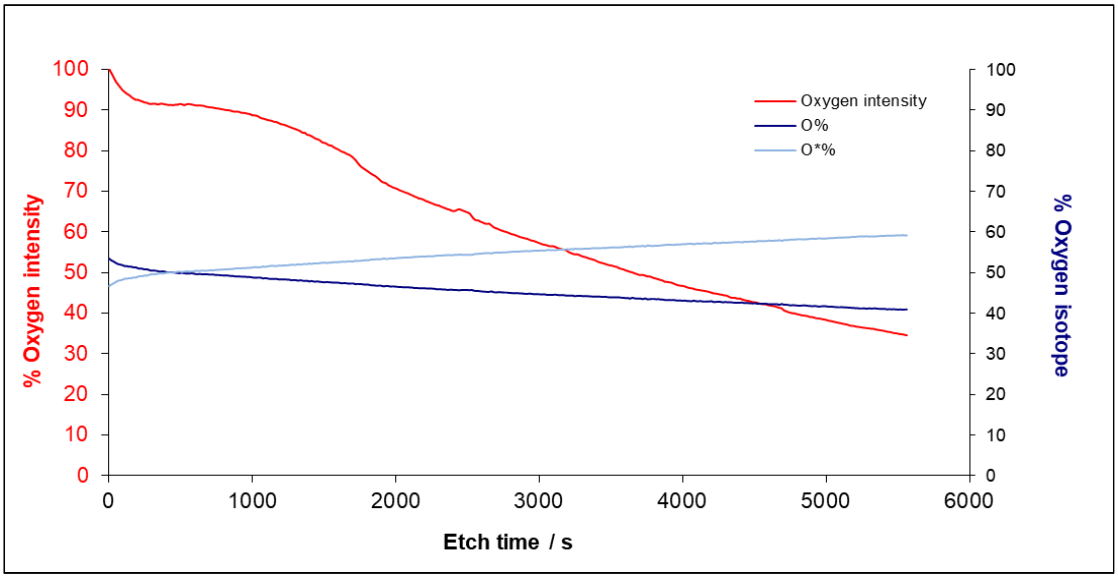

Figure 6.40 % oxygen fractions with respect to oxygen ions derived from the negative profile (figure 6.39b).

6.3.2.2 $D_2{}^{16}O + {}^{18}O_2$ system

For UNb6 the positive and negative depth profiles are shown in Figure 6.41 and Figure 6.42 respectively. Clear niobium hydride and oxide are seen at the surface, with dominant oxide being O-18 as seen in the corresponding % oxygen concentration profiles (figure 6.41b and 6.42b). For UNb3 (Figure 6.43a) there appears to be a more even distribution of the oxygen ions with both the UO_2 and the UO_2* following the same profile. This can be seen more clearly in figure 6.43b where the % oxygen fractions are presented. It can be seen that initially there is a higher percentage of O-18 within the oxide, this decreases after an etch time of~700s, with an increase in the metal ion, suggestive of the oxide-metal interface.

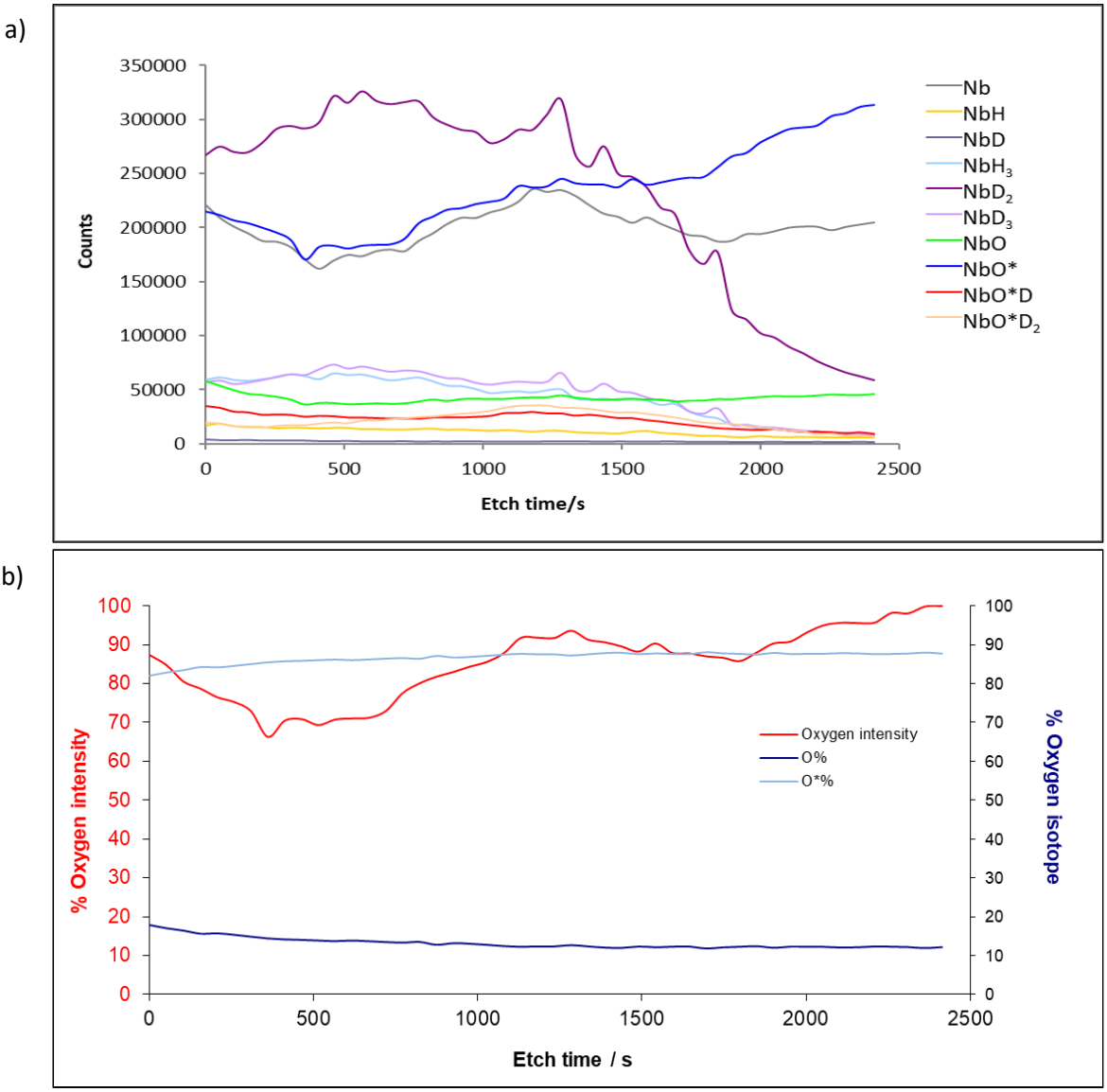

Figure 6.41 Depth profiles of UNb6 after exposure to $D_2{}^{16}O + {}^{18}O_2$, a) positive profile, b) profile showing % oxygen fractions with respect to oxygen ions.

a)

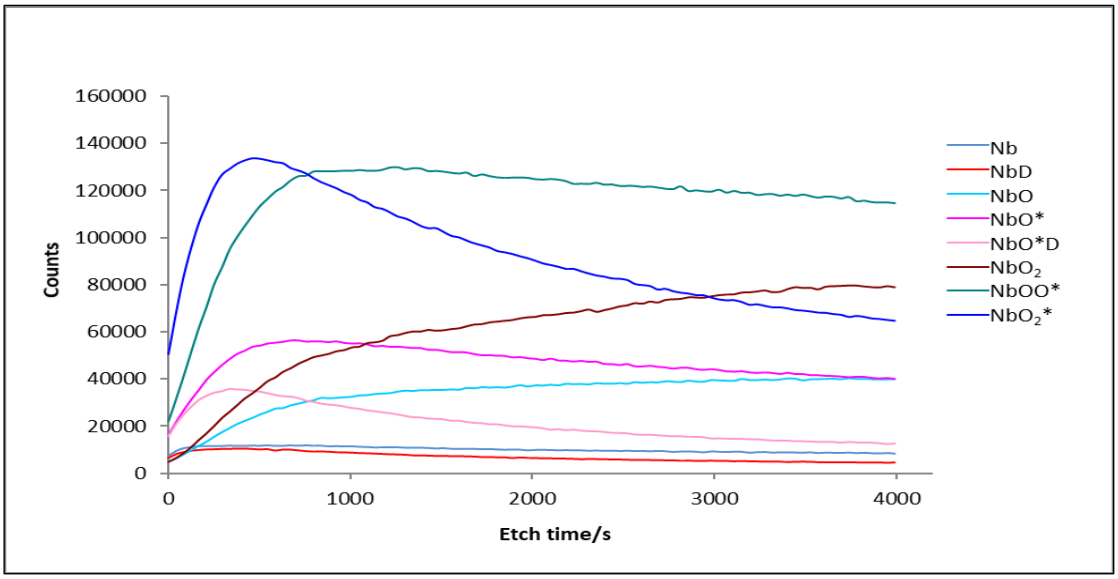

b)

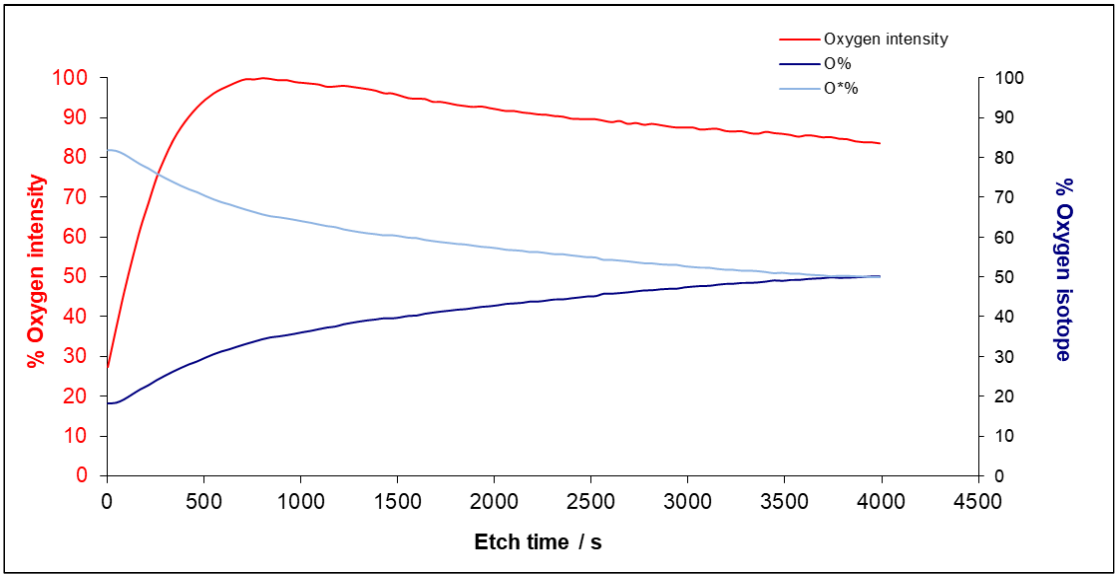

c)

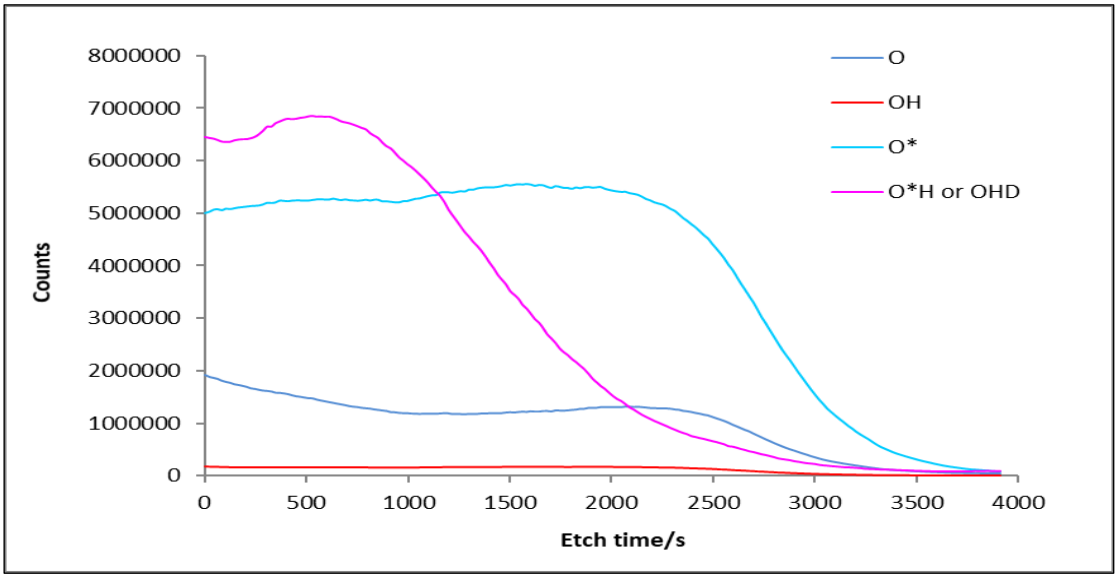

Figure 6.42 Depth profiles of UNb6 after exposure to $D_2{}^{16}O$ + $^{18}O_2$, a) negative depth profile of niobium ions, b) profile showing % oxygen fractions with respect to oxygen ions for the niobium profile, c) negative depth profile of oxygen ions.

a)

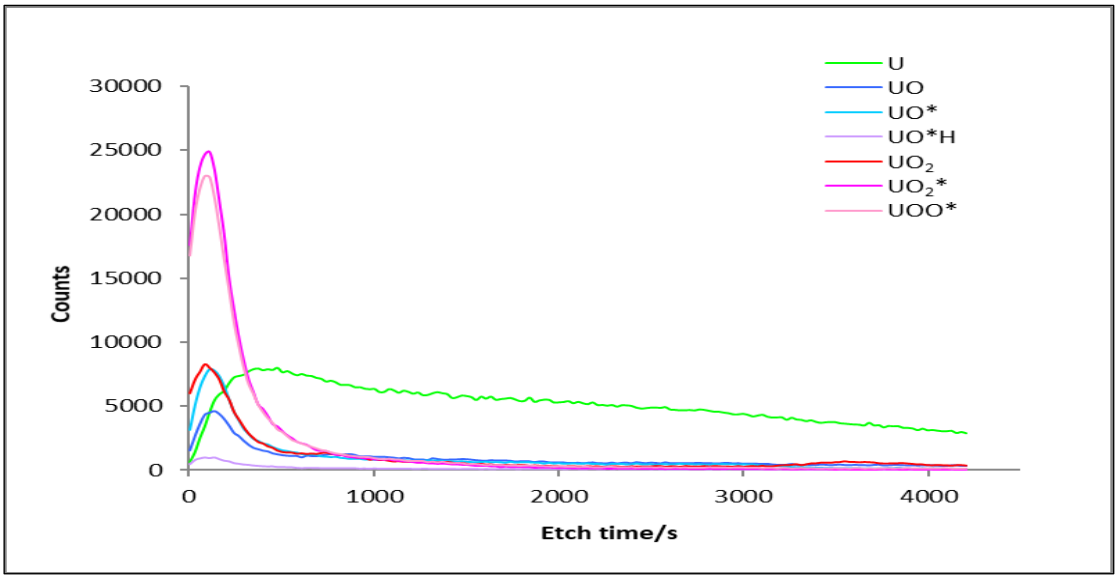

b)

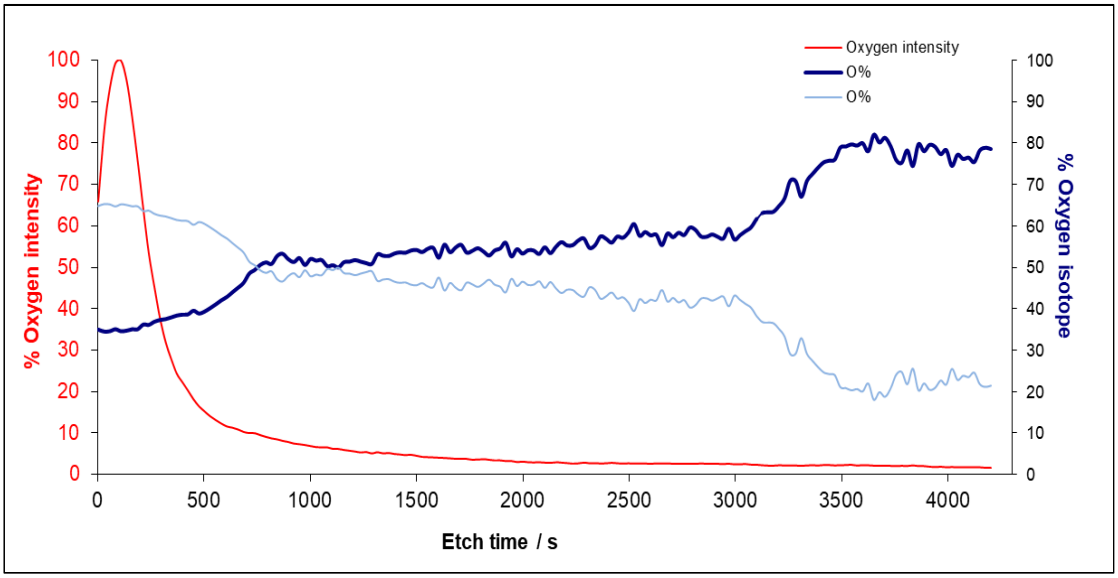

c)

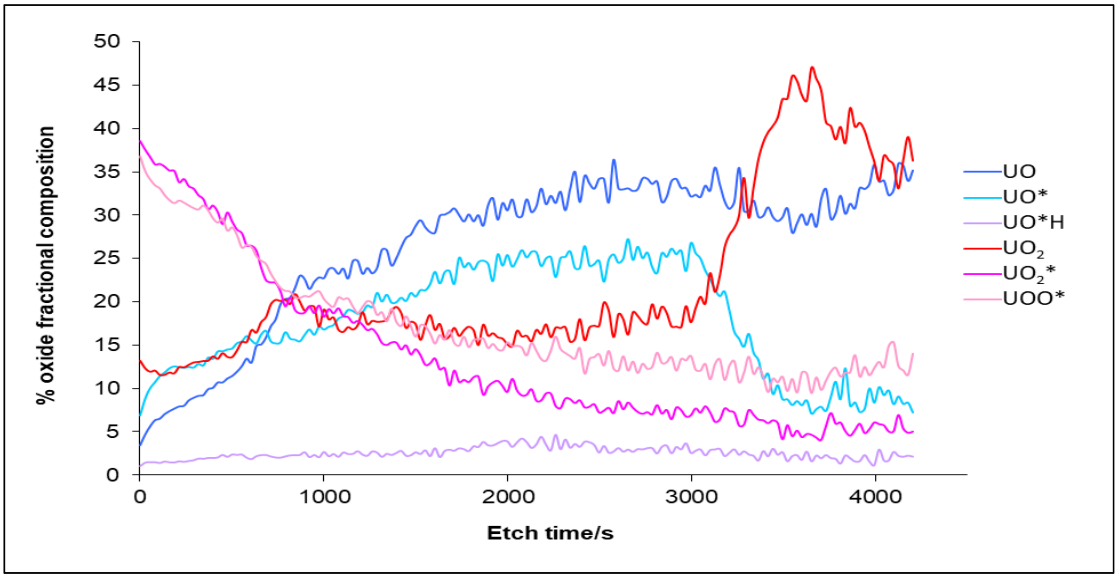

Figure 6.43 Depth profiles of UNb3 after exposure to $D_2{}^{16}O + {}^{18}O_2$, a) positive depth profile, b) profile showing % oxygen fractions with respect to oxygen ions, c) profile showing % oxygen fractions with respect to molecular ions.

6.3.3 Summary

The aim of the SIMS analysis of the alloys post water vapour exposure was to investigate the niobium participation in the oxidation mechanism and to determine the oxide structure. For the water vapour and oxygen system, SIMS analysis was used to investigate which oxidation mechanism the alloys followed, one similar to either of the base metals (uranium where the oxide formed originates from the water, or niobium where the oxide is formed from the oxygen) or a combination of the two.

Mixed oxides are once again seen, with no clear changes from O-16 to O-18, with the % contents of each agreeing with the equivalent exposure times. The oxide-metal interface was detected in the majority of the depth profiles due to the much thinner oxides on the alloys. The dominant oxide was UO_2, with a niobium oxide being seen occasionally. Niobium hydride was evident throughout the profiles.

The concept that near pure UO_2 might constitute the uppermost oxide, means in terms of catalytic splitting of water (after absorption) there should be no difference compared to pure uranium corrosion. The corrosion behaviour must therefore be controlled by processes occurring within the oxide layer. Some of the data presented here provides good evidence that Nb is controlling the corrosion behaviour.

In the isotopically-labelled water vapour plus oxygen reactions, mixtures of the species were determined in the resulting oxides. This suggests that both the water and oxygen were involved in corrosion. This is unsurprising since uranium and niobium show highly different oxidation mechanisms for both the water vapour and the water vapour plus oxygen reaction. Therefore, for the alloy system, it is likely the alloy may adopt a combination of the two.

6.4 APT analysis

Uranium-niobium systems have been studied in atom probe before. Beverini and Edmonds[1] studied U-6 wt.% Nb alloys using one-dimensional atom probe in 1989, showing two phase separation methods, segregation potentially due to spinodal decomposition at temperatures below 400 °C and a strengthening due to Nb-rich precipitates at higher temperatures.

Clarke[83] reported a change in niobium concentration in a U-13% Nb alloy with ageing. After quenching the alloy had uniform Nb concentration as detected in a LEAP instrument, but following ageing at 300°C regions of up to 35% niobium segregation was observed. Ageing at 200 °C showed no such segregation. The samples were stored under methanol to prevent air exposure, so the effects of oxidation were not significant in this study.

The current study utilises APT to investigate uranium-niobium alloys with differing weight fractions of niobium content – 3 and 6 wt.%. The samples were exposed to moist air for an hour or D_2O water vapour for two hours before being prepared for APT analysis via the FIB method. From the kinetics, it is expected that only a small amount of oxidation will have occurred. It is both the structure of this oxide and the structure of the bulk that are of interest. EDX of the alloys showed some niobium-rich regions on the surface for the UNb3 alloy but a homogenous bulk, while the UNb6 showed less enrichment at the surface but with a clear niobium rich region beneath the surface.

6.4.1 UNb3

Figure 6.44 displays an atom map for an UNb3 tip after exposure to air for one hour. The atom map displays a banded structure of uranium oxide (yellow) intermixed with regions containing both uranium (green) and niobium (blue). Figure 6.45 displays ion maps highlighting the locations of each of the key ions (uranium, niobium and uranium oxide). There was minimal niobium oxide detected in the tip.

Figure 6.46 is a 1D concentration profile along the z-axis and shows all of the ions remain relatively constant throughout. This banded structure is very different to what seen for pure uranium, where there was a clear oxide formed at the surface followed by a small layer of hydride before bulk metal was seen. This intermixed oxide-metal system clearly demonstrates the effect of alloying niobium to uranium, preventing a coherent oxide layer from being formed. The tip fractured after 100 nm and therefore it is unknown if the tip would eventually reach an oxide-metal interface and if the bulk would be a homogenous solid solution of uranium and niobium.

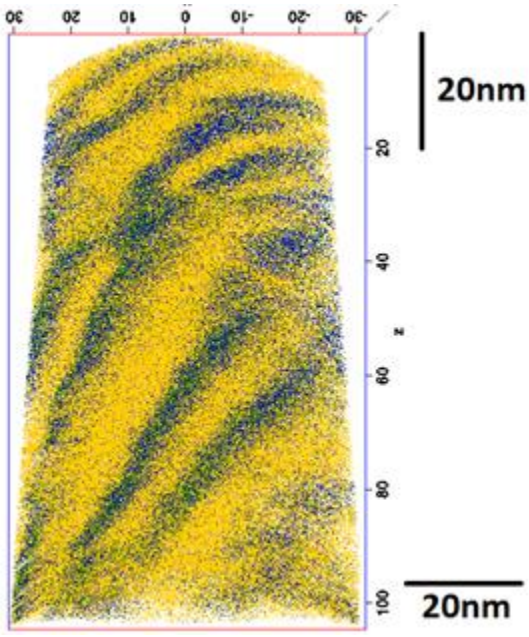

Figure 6.44 Atom map of UNb3 after exposure to air.

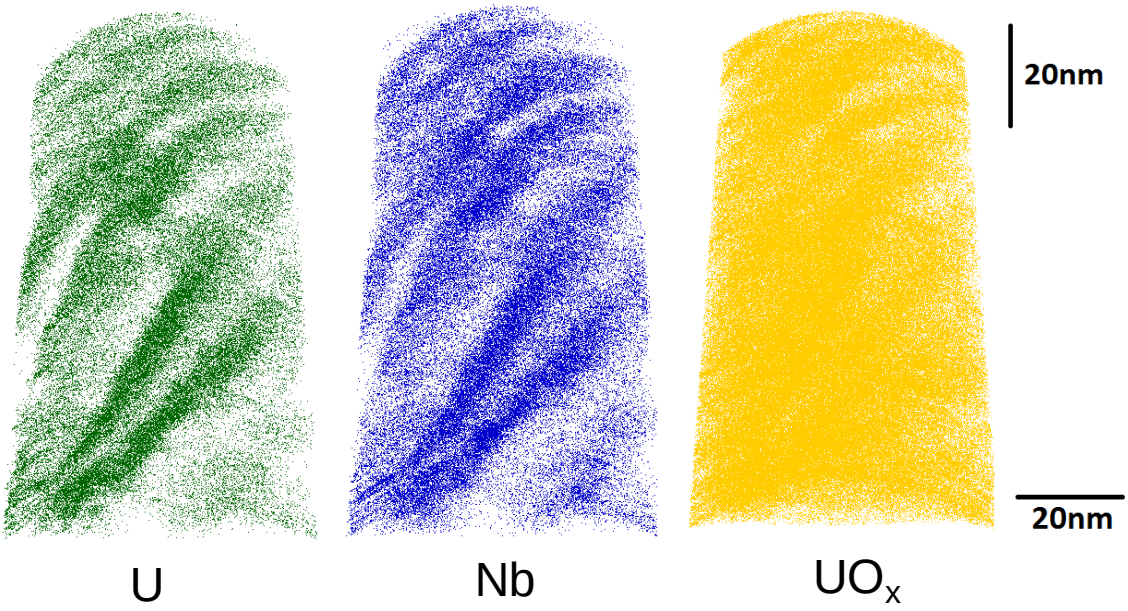

Figure 6.45 Individual ion maps of UNb3 tip from figure 6.44, uranium (green), uranium oxide (yellow) and niobium (blue).

The structure of the UNb3 alloy is similar to what has previously been seen in 9Cr steel and has been deemed a breakaway oxidation structure[84,85]. This is where there are layers/bands containing varying weights of the alloy constituents, i.e. rich and depleted regions as seen here for niobium.

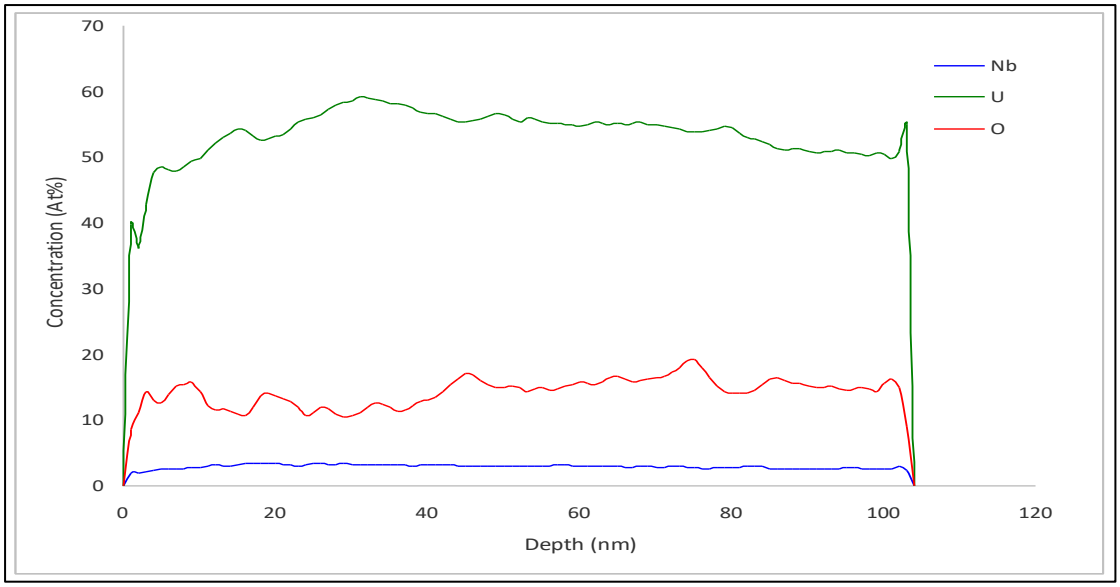

Figure 6.46 1D profile along the z-axis of the atom map from figure 6.44, highlighting the uranium, niobium and oxygen atomic ions.

Figure 6.47 and 6.48 display an atom map for another UNb3 tip prepared from the same liftout of material. It can be seen that the atom map displays a structure different to that seen in figure 6.44. The oxide is predominantly on the apex of the tip with much larger niobium rich regions (blue in figure 6.48) in the bulk. There is also some niobium oxide detected beneath the niobium oxide (lilac atoms in figure 6.48) which was not seen in the first UNb3 sample.

For the second UNb3 tip where niobium rich regions appear more clearly it can be seen from the 1D profile that niobium is present at the surface alongside the oxygen. This is expected as it was seen in the atom map (figure 6.48) that NbO is present at the surface. For the tip shown in figure 6.44, no niobium oxide was detected and therefore niobium was depleted at the surface. From the 1D profile (figure 6.49) it can also be seen that the niobium rich regions found in figure 6.47 are only slightly enriched (~15 at%) but either side of the regions the niobium concentration is consistent with the expected (~7 at%).

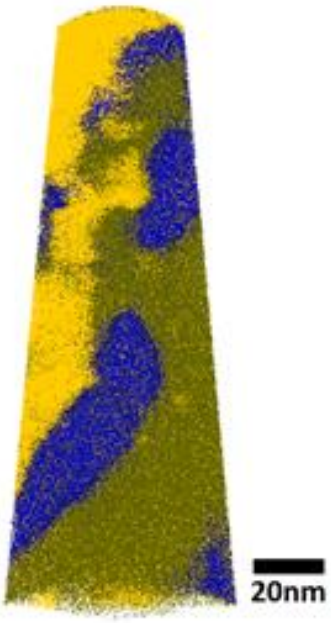

Figure 6.47 Atom map of UNb3 after exposure to air.

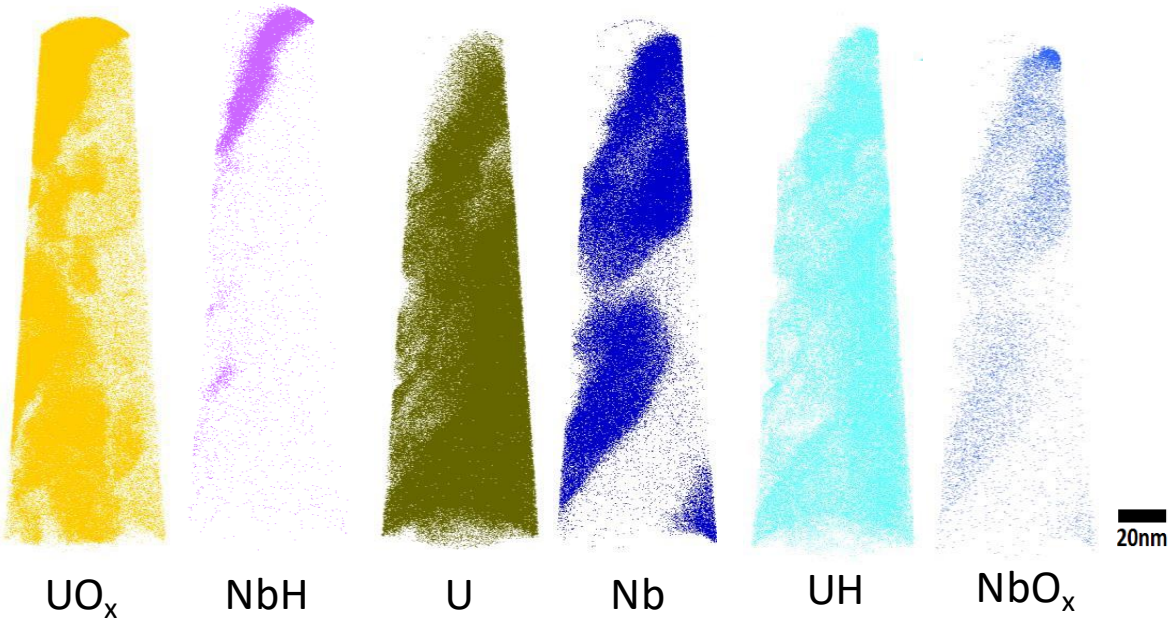

Figure 6.48 Individual ion maps of UNb3 tip from figure 6.47, uranium oxide (yellow), niobium oxide (lilac), uranium (green), niobium (blue), uranium hydride (cyan) and niobium hydride (light blue).

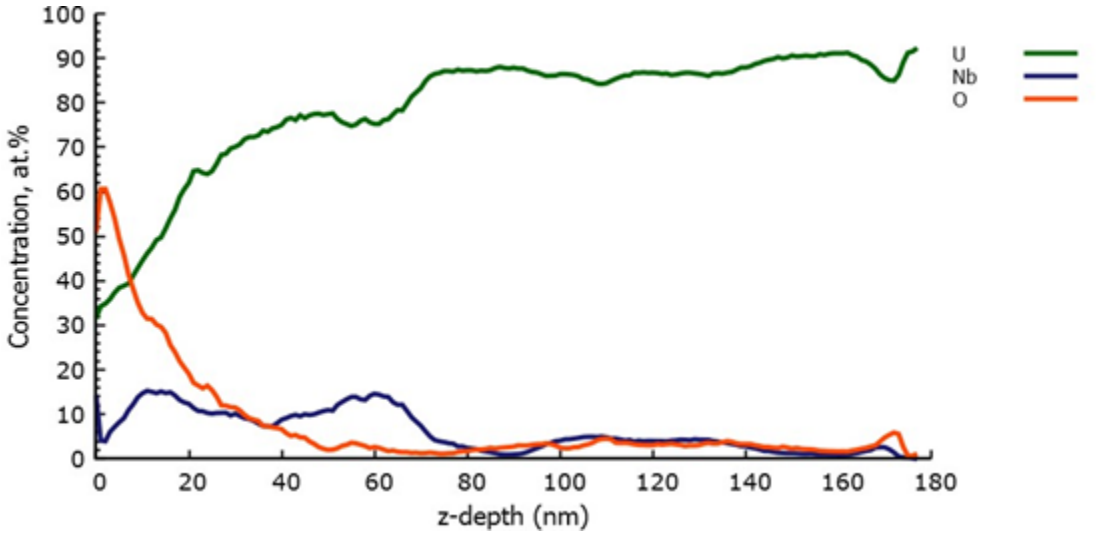

Figure 6.49 1D profile along the z-axis of the atom map from figure 6.47, highlighting the uranium, niobium and oxygen atomic ions.

Looking at the EDX analysis in section 6.1 there were clear niobium-rich regions seen on the UNb3 surface however they were distributed randomly. The presence of these niobium-rich and therefore depleted regions would affect the alloy's oxidation, with regions rich in niobium reacting at a slower rate than those depleted (as has been seen in kinetic analysis, with niobium reacting slower than both uranium and the alloys). It is therefore possible that when carrying out the liftout and thus preparation required for atom probe analysis on the UNb3 coupon, the liftout was across one of these niobium-rich regions, meaning that one tip contained niobium-rich regions at the surface while the other did not. If this is the case then it could be anticipated that a liftout of material would have regions more oxidised than others (figure 6.50).

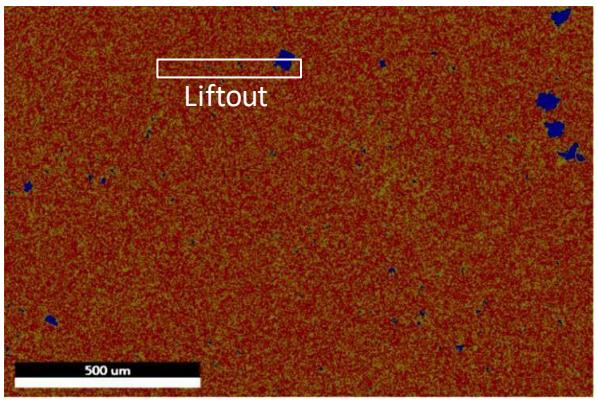

Figure 6.50 Phase map of corroded UNb3 surface with niobium-rich regions shown in blue. The rectangle shows a possible liftout region that would produce atom probe tips with varied oxide structures.

In the experiments where UNb3 coupon was exposed to D_2O water vapour for two hours, the resulting atom probe maps (figures 6.51 and 6.52), are very different to the sample exposed to air, and bear a resemblance to the uranium atom probe data in section 4.4. There is a uranium oxide at the top of the tip but the rest of the atom map is made up of a mixture of uranium and niobium, i.e. homogeneous alloy. This is the expected result for an UNb3 alloy. The main oxide is approximately 30 nm thick, with some incidental oxidation on the side of the tip also present; if this is compared to the pure uranium D_2O exposed data where the oxide was ~50 nm it can be seen that the alloy has demonstrated reduced (slower) oxidation.

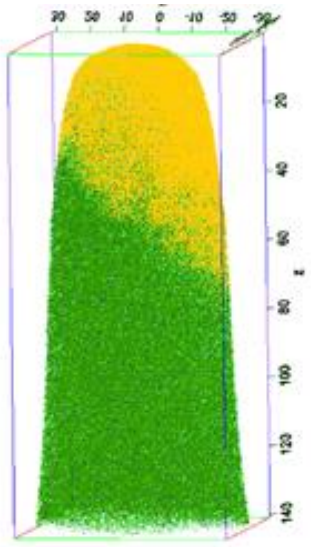

Figure 6.51 Atom map of UNb3 tip after D_2O water vapour exposure

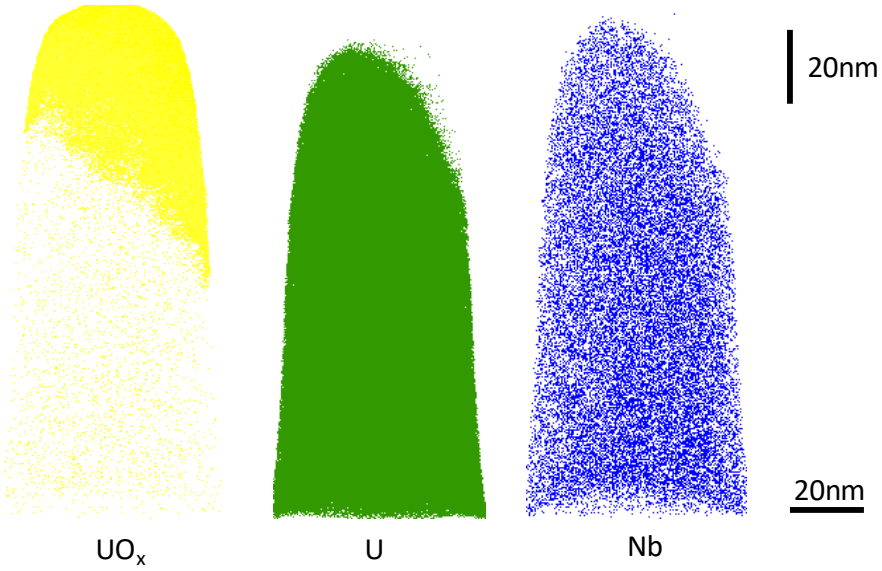

Figure 6.52 Atom map displaying individual relevant ions, UO_x (yellow), uranium (green) and niobium (blue).

Figure 6.53 displays a 1D concentration profile along the z-axis of the UNb3 tip from figure 6.51. It can be seen that after the initial uranium oxide the bulk contains a homogenous mixture of uranium and niobium, with the concentration of niobium remaining constant throughout with no niobium rich regions.

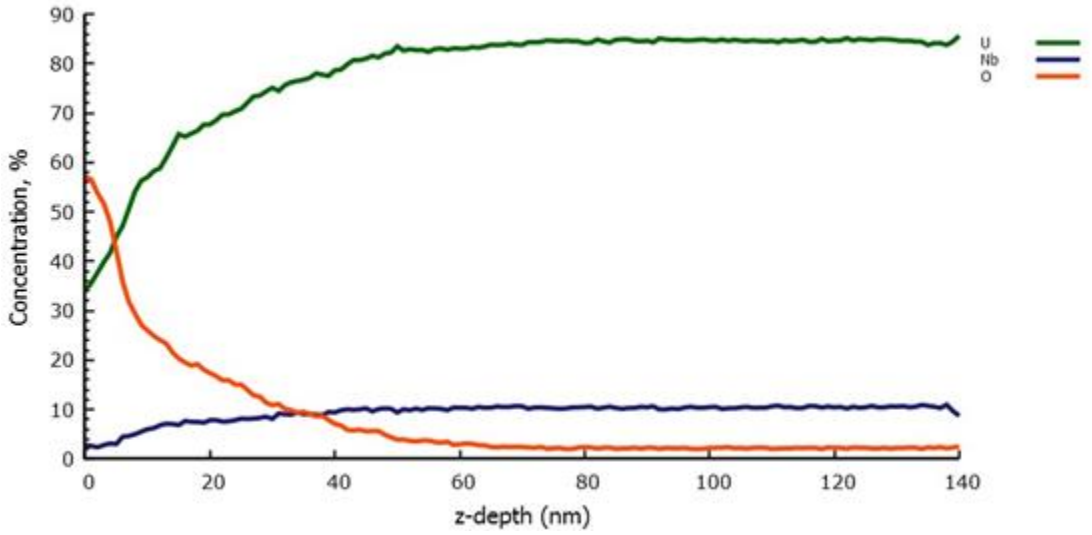

Figure 6.53 1D profile along the z-axis of the atom map from figure 6.51, highlighting the uranium, niobium and oxygen atomic ions.

6.4.2 UNb6

In the U-Nb alloys with a higher niobium content of 6 wt.%, a more continuous niobium phase was observed near the surface. Figure 6.54 shows an atom map of one such example, together with an SEM image taken prior to atom probe analysis. Although the surface of the tip has a rough 'cauliflower' appearance due to an extended oxidation period, it is possible to observe several features in the SEM image that also appear in the atom probe map. This is visible in the oxide structure but also most significantly the two niobium features – one small precipitate in the upper left of both images marked A, and a continuous niobium phase across the bottom of the dataset, marked in B. The diagonal interface between the Nb- and U-rich regions is particularly noticeable in the SEM image.

a)

b)

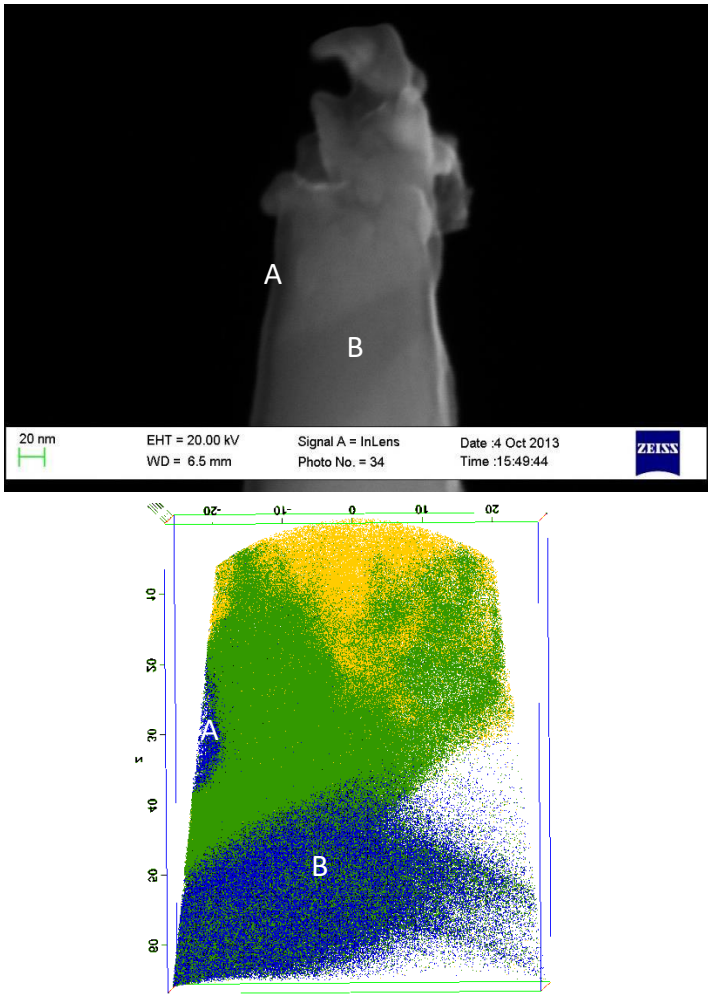

Figure 6.54 (a) SEM image of a UNb6 tip prior to analysis using the atom probe, (b) atom map of the same tip. Isosurfaces show the location of regions of high Nb (blue), U (green) and UOx (yellow) content. The niobium-rich regions are labelled A and B.

In the uranium-rich region, there is very little Nb content. Below the initial oxide cap, the green region in the atom probe map consisted of approximately 97% uranium, with small quantities of UO and UH, and just 0.1 at.% Nb. The niobium phase had a very different composition, with niobium levels around 60 at.% in the large of the two regions. The interface between these two zones was sharp, with the transition occurring within 5 nm, as illustrated in the two proxigrams in Figure 6.55. Figure 6.56 is a 1D concentration profile along the z-axis which again demonstrates the clear transition to a niobium rich region.

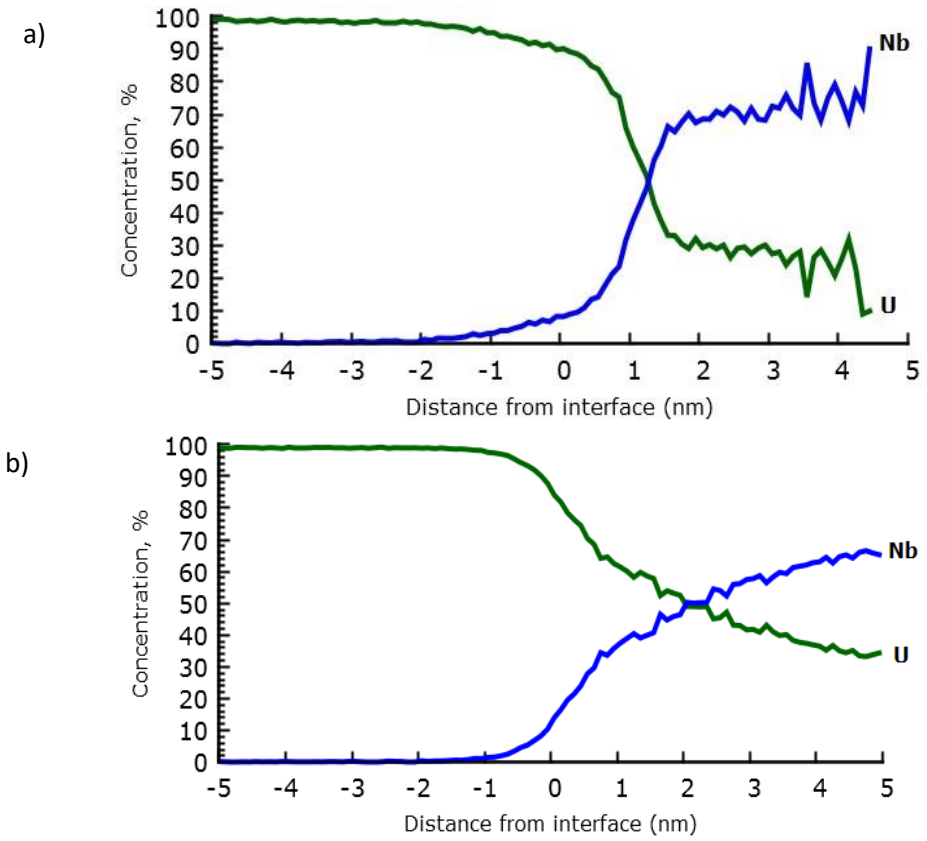

Figure 6.55 Proxigrams through the (a) smaller Nb region marked A in figure 6.54 and (b) the larger Nb phase marked B in figure 6.54.

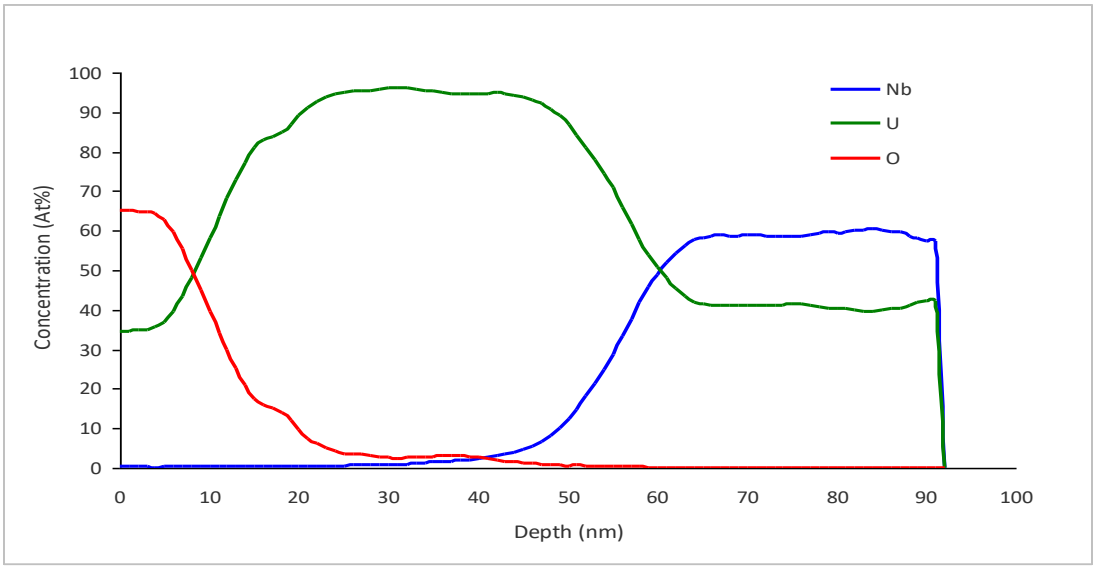

Figure 6.56 1D profile along the z-axis of the atom map from figure 6.654, highlighting the uranium, niobium and oxygen atomic ions.

Phase separation has previously been seen in aged UNb6 material[1,83] at 300 °C. It is possible that due to the age of the material used here (~30 years) it has undergone some form of decomposition resulting in a non-homogenous alloy. These regions enriched and depleted in niobium could possibly explain the kinetic results seen in section 6.2. Regions depleted in niobium would oxidise at a rate similar to that of pure uranium, i.e. significantly faster than both niobium and the alloy. Therefore, the oxidation of an alloy that displays such phases would not be expected to have an enhanced corrosion resistance and therefore it is not too surprising that the UNb6 was seen to react at a similar rate to that of the UNb3 alloy.

Clear niobium-rich and -depleted regions are again seen after exposure to D_2O. These tips were analysed to a much greater depth than the air sample in figure 6.54 and it is seen that these phases continue throughout the length of the tip up to 300 nm (figure 6.57) and up to 510 nm (figure 6.61).

Figure 6.57 shows the full atom map of an UNb6 tip highlighting the niobium bands, with the corresponding individual ion maps shown in figure 6.58. There are two clear niobium-rich regions in this tip.

A proxigram (Figure 6.59) taken from the top interface in figure 6.57 demonstrates the changes in ions across the interface, with a uranium oxide at the surface followed by a small amount of niobium oxide, then a peak in uranium and niobium hydride are seen before entering the bulk metal consisting of mainly uranium with niobium-rich bands at various intervals with depth. The niobium oxide peak appears before the uranium hydride and niobium hydride peaks suggesting a similar oxidation mechanism for the two metals occurs, possibly with the hydride reacting to form oxide as was suggested for uranium.

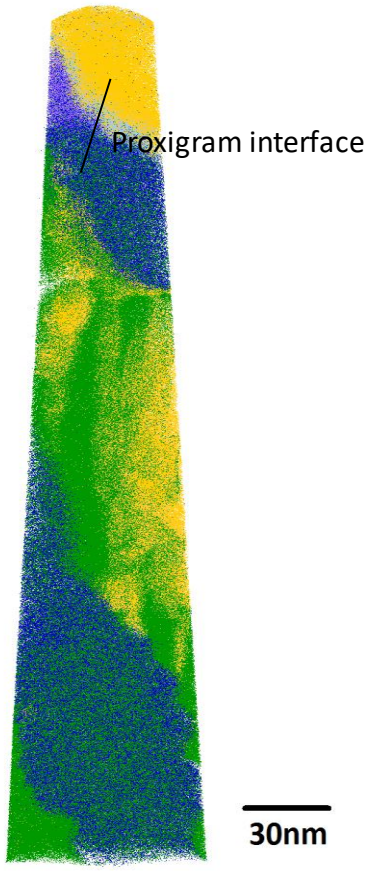

Figure 6.57 Atom map of UNb6 after D_2O water vapour exposure, showing a striped series of alternating phases.

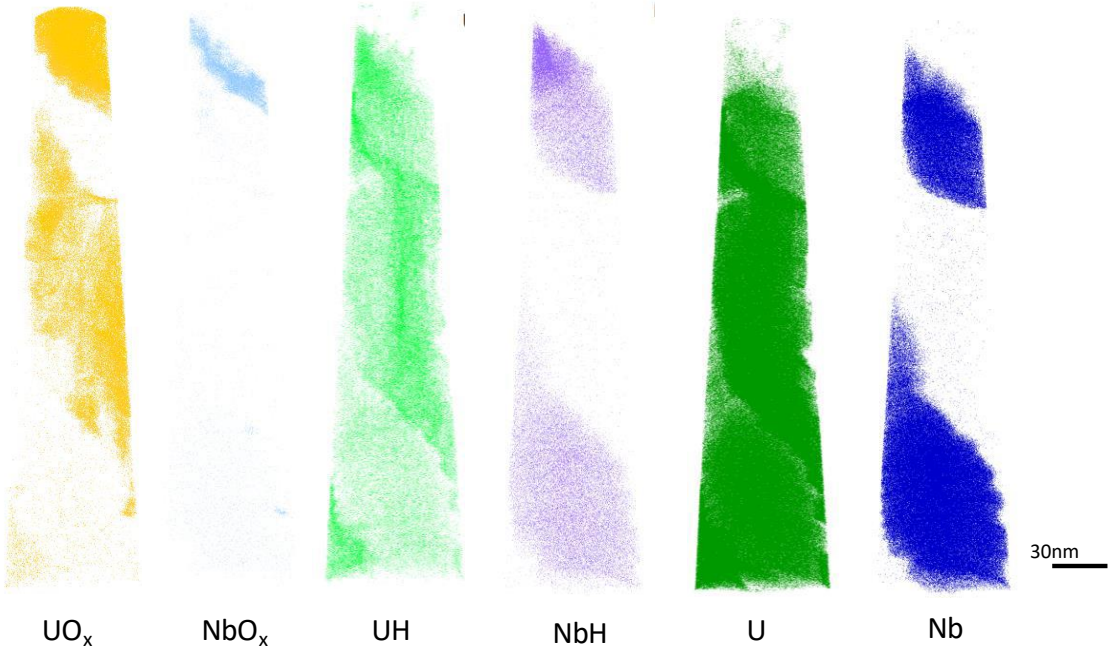

Figure 6.58 Atom map displaying individual relevant ions, UO_x (yellow), NbOx (light blue), UH (bright green), NbH (lilac), uranium (green) and niobium (blue).

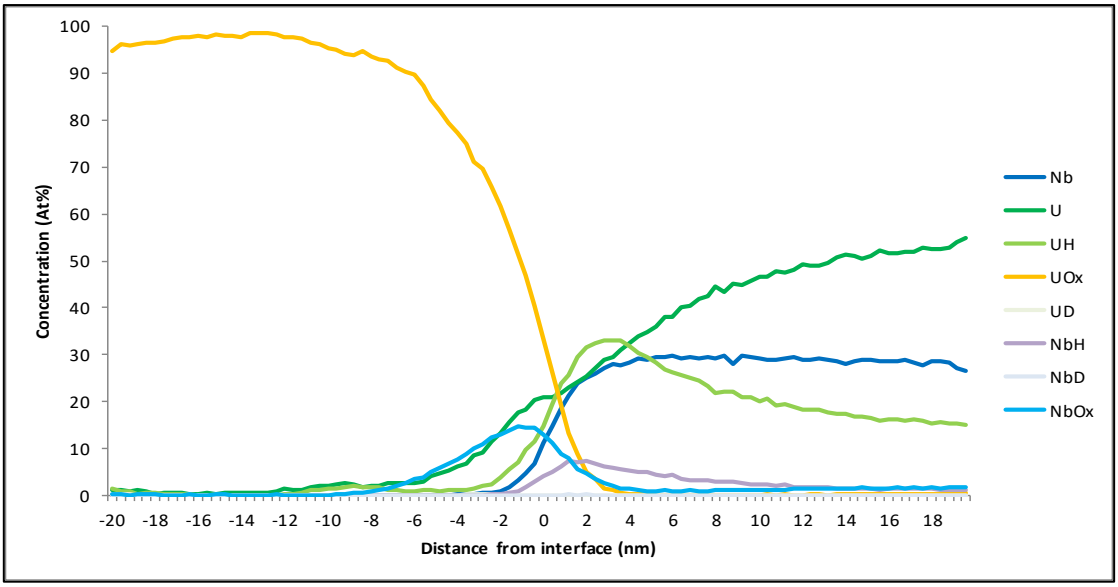

Figure 6.59 Proxigram of top interface from UNb6 atom map in figure 6.57.

Figure 6.60 displays a 1D concentration profile along the z-axis for the entire tip. It clearly shows the niobium-rich and -depleted regions within the bulk. The niobium concentration can be seen to increase to approximately 25% in the bands and then be fully depleted in the uranium regions, showing very clear phase segregation. With the UNb3 sample, the tip after D_2O exposure showed a homogenous bulk with the niobium content remaining constant at ~10%. This inhomogeneity found in the UNb6 tips is of great significance to its corrosion resistance.

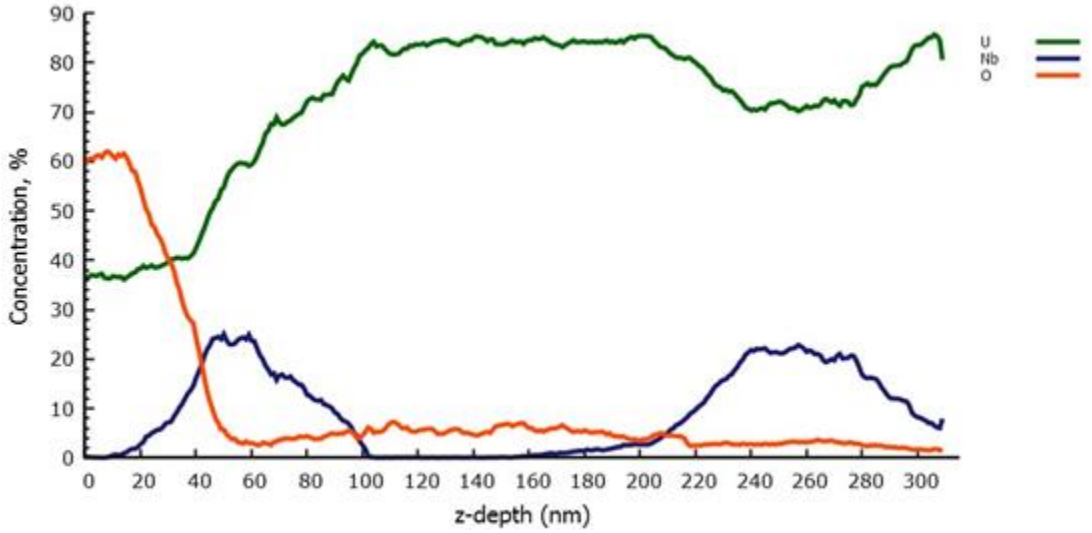

Figure 6.60 1D profile along the z-axis of the atom map from figure 6.57, highlighting the uranium, niobium and oxygen ions.

Figure 6.61 shows an atom map of a tip that was profiled to a depth of ~510 nm, with the corresponding maps of the individual ions shown in figure 6.62. The tip continues to show niobium-rich and -depleted regions which are confirmed by the 1D profile along the z-axis (figure 6.63). The niobium concentration can be seen to peak at regular intervals with depth.

Figure 6.61 Atom map of UNb6 after D_2O water vapour exposure, showing a striped series of alternating phases.

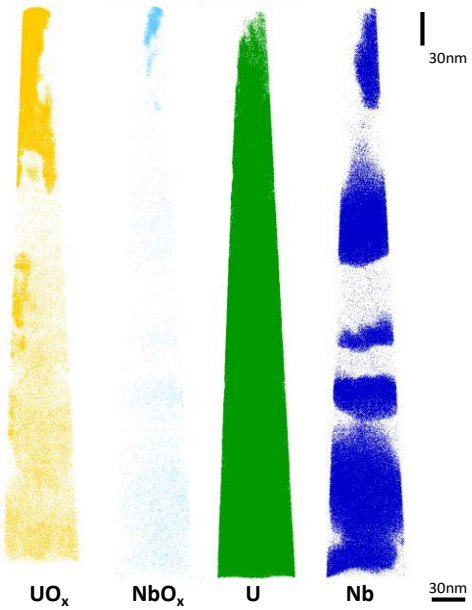

Figure 6.62 Atom map displaying individual relevant ions, UO_x (yellow), NbOx (light blue), uranium (green) and niobium (blue).

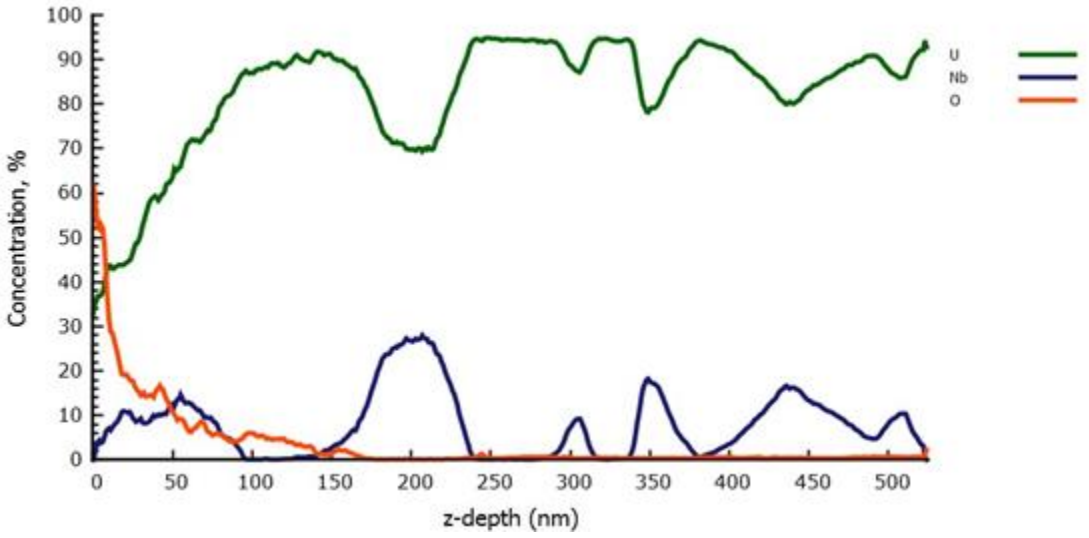

Figure 6.63 1D profile along the z-axis of the atom map from figure 6.61, highlighting the uranium, niobium and oxygen atomic ions.

The same oxide, hydride metal structure is also seen, similar to that in figure 6.57. A schematic of this structure is shown in figure 6.64 and compared to the schematics suggested for uranium and niobium.

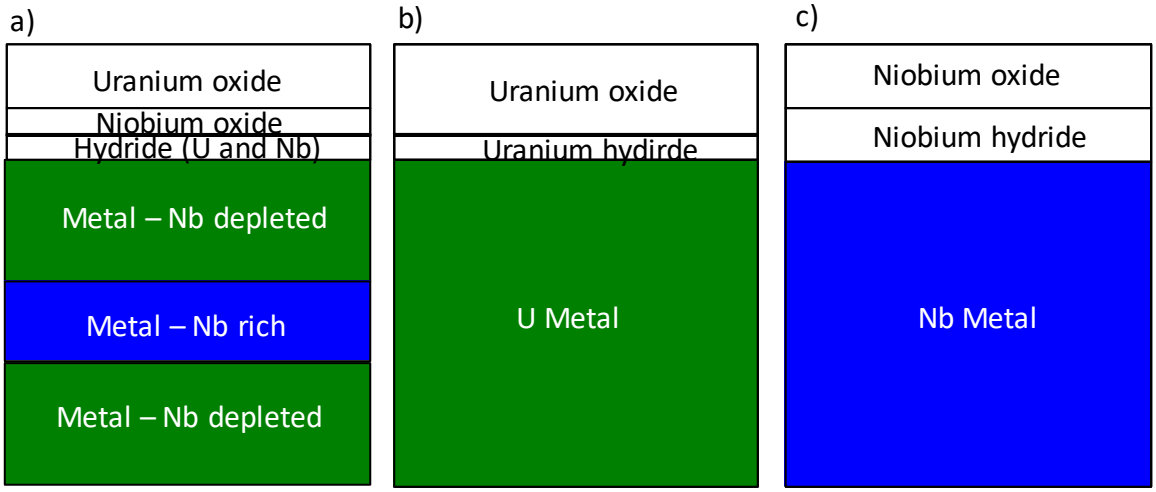

Figure 6.64 Schematics of oxide structures for (a) UNb aged phase separated alloys compared to (b) pure uranium metal and (c) pure niobium metal.

Regarding the phase separation within UNb alloy there are a number of possible ageing mechanisms including diffusional phase transformations, nucleation-and-growth reactions, spinodal reactions and martensitic phase transformations[66]. Figure 6.65 shows possible decomposition routes for a UNb6 alloy in the γ phase. To fully understand the decomposition occurring within the alloys in this study, further analysis would be required.

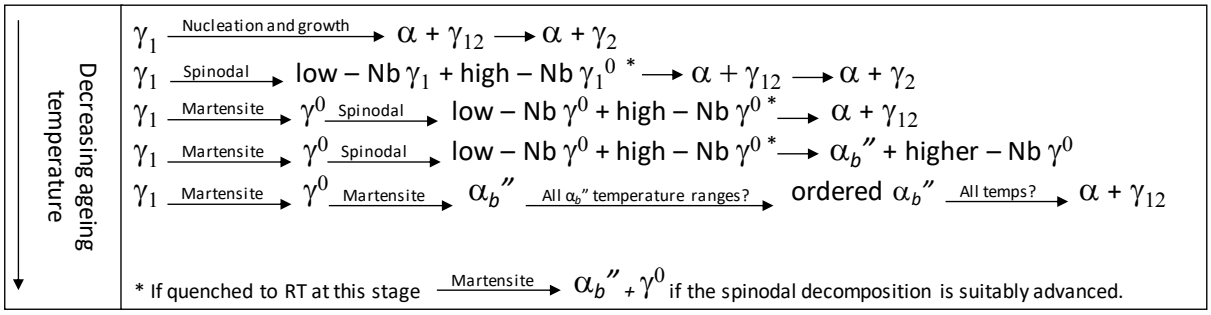

Figure 6.65 Possible decomposition routes for γ at different ageing temperatures[66]*.*

6.4.3 Summary

The atom probe analysis of UNb3 and UNb6 has provided fundamental information on the structure of these alloys that directly relates to their corrosion properties. For UNb3 the atom probe showed some phase separation on the tips exposed to air but not for the tip exposed to D_2O.

The phase separation is most likely due to ageing with the UNb6 material being significantly older than the UNb3. Any phase separation will affect the properties of the material. It has previously been shown that ageing leads to an increase in strength but a decrease in ductility and corrosion resistance. Therefore, it is likely that the observed phase separation in UNb6 is the reason for the unexpected kinetic data found in section 6.2.

Further work is required to determine the mechanism of separation whether it is spinodal decomposition, phase segregation, nucleation and growth, etc.

6.5 Chapter conclusions

For the kinetics, both alloys showed slower corrosion rates than uranium and niobium. However, UNb6 appeared to react at a faster rate than UNb3. It was postulated that ageing had led to segregation of the UNb6 which will affect its corrosion resistance. If phase separation of some form has occurred then there will be regions of niobium depletion where the material would then react as pure uranium, so much faster. The EDX analysis of a UNb6 TEM section showed a clear niobium-rich region within the bulk.

The SIMS analysis provided limited information on the oxide structure and the mechanism despite the oxide-metal interface being seen in the majority of profiles. The dominant oxide was UO_2, with a niobium oxide being seen occasionally. Niobium hydride was evident throughout the profiles. In the water vapour plus oxygen reaction, mixtures of the species were seen, suggesting both water and oxygen were involved. This is unsurprising since uranium and niobium show highly different mechanisms for both the water vapour and the water vapour plus oxygen reaction. Therefore, for the alloy system, it is likely the alloy may adopt a combination of the two.

The atom probe analysis, however, showed key information on the structure of both the oxide and the bulk metal. For UNb3 two different structures were seen after exposure to air, a banded structure with uranium oxide throughout intermixed with uranium and niobium metal, suggestive of breakaway oxidation, similar to that seen for 9Cr steel and a structure showing a more defined surface oxide followed by the bulk metal. Both tips showed some niobium-rich and -depleted regions. However, the atom probe showed a different map for the UNb3 after D_2O exposure. A tip profile similar to that seen for uranium, with a uranium oxide at the surface followed by a homogenous bulk beneath, was seen. The thickness of the oxide was significantly thinner than that seen for pure uranium, reinforcing the evidence that addition of niobium to uranium leads to enhanced corrosion resistance. The difference in the oxide structure was assigned to the liftout being taken from an area of material that contained niobium-rich and -depleted regions meaning that the material oxidised at different levels.

For UNb6 a very interesting more coarsely banded structure was identified with clear phase separation in the alloy, showing alloy regions rich and depleted in niobium. Again, there was a uranium oxide formed at the surface followed by a small amount of niobium oxide. Beneath the oxides were thin layers of uranium hydride and niobium hydride: both of these were identified by atom probe for the pure metals. This oxide, hydride then metal structure is similar to that seen for uranium and niobium, suggesting that a similar oxidation mechanism is occurring. However, for the alloys, the corresponding deuteride layer was not evident in the D_2O exposure experiment. Therefore, it is not unambiguously stated that this hydride is directly from the reaction and not from air/chamber contamination.

Beneath the hydride the sample tip then entered the bulk alloy, where instead of being a homogenous solution as expected there were bands rich in niobium with the remainder being almost pure uranium. This inhomogeneity is ascribed to slow spinodal decomposition caused by relatively low temperature thermal ageing, and is also most likely the reason for the unexpected kinetic data. The ageing mechanism is not well established, though this observed separation is of great importance as uranium niobium alloys are used for their corrosion resistance and this study has identified that over time this resistance degrades and the alloy starts to corrode at a faster rate than expected. It must however be noted that the corrosion rate was still significantly slower than that of pure uranium. However, as the material ages further, it is not presently known how this will impact the evolution of the alloy structure and thus the corrosion resistance of the alloy.

7 Chapter seven – conclusions and future work

7.1 Conclusions

The work presented in this thesis was focussed on determining the mechanism of the water vapour reaction for uranium, niobium and their alloys. The key information sought after was the diffusing species and the presence of any intermediates formed along the way (e.g. hydroxides and/or hydride), as these provide an insight into the mechanism. For the alloys, the role of the niobium and/or its oxides in the enhancement of corrosion resistance for uranium was the focus.

The study overall has provided two key pieces of information; firstly that uranium hydride is formed during the water vapour reaction and secondly that UNb6 showed clear ageing effects, with niobium-rich and depleted regions being detected.

From the atom probe analysis of uranium a clear hydride layer was detected at the oxide-metal interface. This was affirmed to be from the water vapour reaction when D_2O was used in place of air. The detection of hydroxides within the oxide helps confirm the mechanism suggested by Baker[2,3] where OH^- diffuses to the oxide-metal interface, both hydride and oxide are formed and the hydride undergoes oxidation to form new oxide as well as undergoing continual regeneration from the highly reactive atomic hydrogen. As hydride was not detected by SIMS, it suggests that the hydride layer does not continue to grow, however, the maximum thickness is not known.

For UNb6 distinct layers were seen, with a clear uranium oxide at the surface followed by uranium metal and then clear niobium-rich layers. The EDX analysis didn't show niobium-rich regions at the surface like UNb3. However, there was a clear niobium-rich region seen on the TEM section suggesting that for UNb6 the phase separation is within the bulk and not just surface related. These discrete layers suggest some form of ageing mechanism has occurred, such as phase separation, segregation or spinodal decomposition, as has been previously seen on artificially aged material. This in-homogeneity leads to a reduction in the assumed corrosion resistance of the alloy, with UNb6 and UNb3 unexpectedly corroding at similar

rates. The corrosion and oxide growth were still slower than those of pure uranium, showing that the addition of niobium continues to enhance the corrosion resistance. However, if the material continues to decompose it is possible that this enhancement may start to degrade.

The main aims of the thesis were shown as bullet points in section 1.4. For each of the materials studied there are a number of key pieces of information sought. These highlighted key points will then be referred back to in the conclusions section to determine which aims were met.

- Uranium-water vapour reaction
    - Investigate mechanism of the reaction
        - Determine diffusing species – aim met
        - Determine if any hydride is formed – aim met
- Niobium-water vapour reaction
    - Investigate the rate kinetics of the reaction
        - Pressure and temperature dependencies – aim met
        - How addition of oxygen effects the rate kinetics – aim met
    - Investigate the mechanism of the reaction
        - Determine diffusing species – aim not met, further work required
        - Determine oxide structure – aim not met, further work required
- UNb alloy-water vapour reaction
    - Investigate the rate kinetics of the reaction
        - Temperature dependencies – aim met
        - How addition of oxygen effects the rate kinetics – aim met
    - Investigate the mechanism of the reaction
        - Determine diffusing species – aim not met, further work required
        - Determine oxide structure – aim partially met, further work required
        - Determine niobium distribution within the alloy – aim partially met, further work required
        - Mechanism for enhanced resistance – aim not met, further work required

7.2 Future work

There are a few areas where further work would enable additional mechanistic information on the water vapour reaction to be determined.

Firstly, shorter water vapour experiments would allow the initial oxidation to be investigated using SIMS. The oxides formed during this study were too thick to provide conclusive data from the isotopic SIMS depth profiling. The corrosion in water vapour could be investigated at short intervals, possibly with multiple water changes to build a picture of the initial oxidation and to provide further mechanistic information.

Secondly, further atom probe analysis on the uranium hydride layer are recommended. APT could be used to study increasing water/air exposures to determine what the threshold thickness of the hydride formed at the interface would be. This may also be used to look for initial precipitation of hydride in the sub-surface, whether or not small hydride sites form and if they influence later reactivity. Isotopic water and oxygen would be required for this analysis with the possibility of changing the water part way through the reaction (as per the long-term experiments).

Finally, further analysis is required on the alloy system to investigate the mechanism of the phase transformations. It is necessary to investigate ageing and when this phase separation manifests. It would also be of interest to investigate alloys of other weight percent to see if these undergo a similar phase separation and at what age. To aid in the atom probe studies of the alloys, the analysis of niobium metal using a protective platinum strip would help by providing key information on the oxidation mechanism and oxide structure of niobium.

8 References

1. Clarke AJ, Field RD, Hackenberg RE, Thoma DJ, Brown DW, Teter DF, Miller MK, Russell KF, Edmonds DV, Beverini G. Low temperature age hardening in U-13 at.% Nb: An assessment of chemical redistribution mechanisms. *J Nucl Mater*. 2009;393:282-291.

2. Baker MM, Less LN, Osman S. Uranium + water reaction part 1, kinetic products and mechanism. *Trans faraday Soc*. 1966;62:2513-2524.

3. Baker MM, Less LN, Osman S. Uranium + water reaction Part 2, effect of oxygen and other gases. *Trans Faraday Soc*. 1966;62:2525-2530.

4. Haschke JM. Corrosion of uranium in air and water vapor: consequences for environmental dispersal. *J Alloys Compd*. 1998;278:149-160.

5. Haschke JM, Allen TH, Morales La. Reactions of plutonium dioxide with water and hydrogen-oxygen mixtures: Mechanisms for corrosion of uranium and plutonium. *J Alloys Compd*. 2001;314:78-91.

6. McGillivray GW, Geeson DA, Greenwood RC. Studies of the kinetics and mechanism of the oxidation of uranium by dry and moist air A model for determining the oxidation rate over a wide range of temperatures and water vapour pressures. *J Nucl Mater*. 1994;208:81-97.

7. Tian H, Reece CE, Kelley MJ, Wang S, Plucinski L, Smith KE, Nowell MM. Surface studies of niobium chemically polished under conditions for superconducting radio frequency (SRF) cavity production. *Appl Surf Sci*. 2006;253:1236-1242.

8. Magnani NJ. *The Reaction of Uranium and Its Alloys with Wtaer Vapour at Low Temperatures*.; 1974, SciTechConnect (osti.gov/scitech) - 4258103

9. Manner WL, Lloyd JA, Paffett MT. Reexamination of the fundamental interactions of water with uranium. *J Nucl Mater*. 1999;275:37-46.

10. Fu X, Liu K, Wang X, Zhao Z, Yu Y. X-ray photoelectron spectroscopic study of the surface reaction of uranium-niobium alloy with O2. *Surf Rev Lett*. 2003;10:381-386.

11. Kelly D, Lillard JA, Manner WL, Hanrahan R, Paffett MT. Surface characterization of oxidative corrosion of U–Nb alloys. *J Vac Sci Technol A Vacuum, Surfaces, Film*. 2001;19:1959-1964.

12. Morrall P. *AWE Unpublished Data*.; 2012.

13. Fuger J, Lemire RJ, Muller RB, Nguyen-Trung Cregu C, Konings RJM, Wanner H, Grenthe I. *Chemical Thermodynamics of Uranium, Volume 1*. 1st edition. Elsevier; 1992.

14. Jacob KT, Shekhar C, Vinay M. Thermodynamic properties of niobium oxides. *J Chem Eng*. 2010;55:4854-4863.

15. Ashby MF, Jones RH. *Engineering Materials 1,* 2nd edition. Butterworth-Heinemann; 1996.

16. Wood GC. High-temperature oxidation of alloys. *Oxid Met*. 1970;2:11-57.

17. McGurk J. Atmospheric Corrosion of Alloys. *Nexia Solut 8767*. 2007.

18. Hilton BA. Review of oxidation rates of DOE spent nuclear fuel part 1:metallic fuel. *Argonne Natl Lab ANL-00/24*. 2000, SciTechConnect (osti.gov/scitech) - 37763.

19. Ritchie AG. A review of the rates of reaction of uranium with oxygen and water vapour at temperatures up to 300° C. *J Nucl Mater*. 1981;102:170-182.

20. Kondo T, Beck FH, Fontana MG. Gas-chromatographic study on kinetics of uranium oxidation in moist environments. *corrosion*. 1974;30:330-339.

21. Colmenares CA. Oxidation mechanisms and catalytic properties of the actinides. *Prog Solid State Chem*. 1984;15:257-364. doi:10.1016/0079-6786(84)90003-7.

22. Weirick L. The oxidation of uranium in low partial pressures of oxygen and water vapour at 100°C. *Sandia, SAND83-0618*. 1984, SciTechConnect (osti.gov/scitech) - 6848474

23. Allen GC, Tucker PM, Lewis RA. X-ray photoelectron spectroscopy study of the initial oxidation of uranium metal in oxygen + water-vapour mixtures. *J Chem Soc Faraday Trans 2*. 1984;80:991-1000.

24. Kondo T, Werink ED, Beck FH, Fontana MG. Gas chromatographic + gravimetric studies of uranium oxidation mechanism. *corrosion*. 1964;20:314-320.

25. Winer K, Colmenares CA, Smith RL, Wooten F. Interaction of water vapour with clean and oxygen-covered uranium surfaces. *Surf Sci*. 1987;183:67-99.

26. Cabrera N, Mott NJ. Theory of oxidation of metals. *Repts Prop Phys,*. 1948;12:163-184.

27. Argent BB, Phelps B. The oxidation of niobium-titanium and niobium-molybdenum alloys. *J Less Common Met*. 1960;2:181-190.

28. Blackburn PE. The mechanism of the niobium reaction with Water vapour and with oxygen. *J Electrochem Soc*. 1962;109:1142-1150.

29. Gulbransen EA, Andrew KF. Reactions of zirconium, titanium, columbium and tantalum with the gases oxygen, nitrogen and hydrogen at elevated temperatures. *J Electrochem Soc*. 1949;96:364-376.

30. Gulbransen EA, Andrew KF. Kinetics of the reactions of columbium and tantalum with O2, N2 and H2. *J Met*. 1950;2:586-599.

31. Inouye H. Scaling of columbium in air. *Oak Ridge, ORNL Report-1565*. 1953, SciTechConnect (osti.gov/scitech) - 4409909

32. Cathcart JV, Campbell JJ, Smith GP. The microtopography of oxide films on niobium. *J Electrochem Soc*. 1958;105:442-446.

33. Bridges DW, Fassel Jr WM. High pressure oxidation of niobium. *J Electrochem Soc*. 1956;103:326-330.

34. Klopp WD, Sims CT, Jaffee RI. Effects of alloying on the kinetics of oxidation of niobium. *Proc Second United Nations Int Conf Peac Uses At Energy,*. 1958;6:293-296.

35. Passier F, Wouters Y, Galerie A, Caillet M. Thermal oxidation of metallic niobium by water vapor. *Oxid Met*. 2001;55:153-163. doi:10.1023/A:1010385427776.

36. Kubaschewski O, Hopkins BE. Oxidation mechanisms of niobium, tantalum, molybdenum and tungsten. *J Less Common Met*. 1960;2:172-180.

37. Phelps RT, Gulbransen EA, Hickman JW. Oxide films formed on alloys at moderate tempeartuers. Electron diffraction and electron microscope study. *Ind Eng Chem,*. 1946;18:640-652.

38. Hurlen T. Oxidation of niobium. *J Inst Met*. 1961;89:273-280.

39. Brauer G, MüH. Mineral Chemistry. In: *Proceedings of IUPAC's 16th Congress,*. ; 1958:63.

40. Cox B, Johnston C. The oxidation and corrosion of niobium. *Trans AIME*. 1963;227:36-40.

41. Kai W, Huang R. The high temperature corrosion behaviour of Nb-Al alloys in a H2/H2S/H2O gas mixture. *Oxid Met*. 1997;48:439-469.

42. Sheasby JS, Smeltzer WW. Oxygen tracer studies of the oxidation of niobium. *Oxid Met*. 1981;15:215-229.

43. Sheasby JS, Wallwork GR, Smeltzer WW. The Parabolic Oxidation Kinetics of Niobium. *J Electrochem Soc*. 1966;113:1255-1257.

44. Wu AT. Investigation of oxide layer structure on niobium surface using a secondary ion mass spectrometry. *Phys C-Superconductivity Its Appl*. 2006;441:79-82.

45. Hurlen T, Kjollesdal H, Markali J, Norman N. Oxidation of niobium. *Tech Note No 1, Contract No AF61 (052)-90,*. 1959.

46. Ford DC, Cooley LD, Seidman DN. First-principles calculations of niobium hydride formation in superconducting radio-frequency cavities. *Supercond Sci Technol*. 2013;26:Article no. 95002.

47. Ford DC, Cooley LD, Seidman DN. Suppression of hydride precipitates in niobium superconducting radio-frequency cavities. *Supercond Sci Technol*. 2013;26:Article no. 105003.

48. Kim Y-J, Tao R, Klie RF, Seidman DN. Direct atomic-scale imaging of hydrogen and oxygen interstitials in pure niobium using atom-probe tomography and aberration-corrected scanning transmission electron microscopy. *ACS Nano*. 2013;7:732-739.

49. Zhang Y, Zhang X, Chen X, Weijun G, Wang X. Effect of grain size on phase stability of monoclinic U-Nb alloy during low-temperature ageing. *J Nucl Mater*. 2015;456:167-169.

50. Younes CM, Allen GC, Embong Z. Auger electron spectroscopic study of the surface oxidation of uranium–niobium alloy {U–6wt.% Nb} in a UHV environment containing primarily H2, H2O and CO. *Surf Sci*. 2007;601:3207-3214.

51. Manner WL, Lloyd JA, Hanrahan Jr. RJ, Paffett MT. An examination of the initial oxidation of uranium-base alloy (U - 14 at% Nb) by O2 and D2O using surface sensitive techniques. *Appl Phys Lett*. 1999;150:73-88.

52. Jiangrong Y, Xiaolin W, Lizhu L, Ping Z. Investigation of oxidation of a U-2.5 wt% Nb alloy in air at low temperatures: kinetic study and oxide characterization. *Surf Interface Anal*. 2008;40:299-302.

53. http://www.microscopy.ethz.ch/sem.htm.

54. Goldstein J, Newbury DE, Joy DC, Lyman CE, Echlin P, Lifshin E, Sawyer L, Michael JR. *Scanning Electron Microscopy and X-Ray Microanalysis*. 3rd edition. Springer US; 2003.

55. Reimer L. *Scanning Electron Microscopy*. Volume 45. Springer-Verlag Berlin Heidelberg; 1998.

56. http://www.ammrf.org.au/myscope/analysis/eds/.

57. http://www.ammrf.org.au/myscope/analysis/eds/quantitative/.

58. http://www.fibics.com/fib/tutorials/introduction-focused-ion-beam-systems/4/.

59. Vickerman JC, Gilmore IS. *Surface Analysis the Principal Techniques*. 2nd edition. John Wiley & Sons; 2000.

60. Larson DJ, Kelly ThF. Annual Review of Materials Research. *Annu Rev Mater Res*. 2012;42:1-

31.

61. Gault B, Vurpillot F, Vella A, Gilbert M, Menand A, Blavette D, Deconihout B. Design of a femtosecond laser assisted tomographic atom probe. *Rev Scie Instrum*. 2006;77:Article no. 43705.

62. Bunton JH, Olsen JD, Lenz DR, Kelly ThF. Advances in pulsed-laser atom probe:Instrument and specimen design for optimum performance. *Microsc Microanal*. 2007;13:418-427.

63. Thompson K, Lawrence D, Larson DJ, Olson JD, Kelly TF, Gorman B. In situ site-specific specimen preparation for atom probe tomography. *Ultramicroscopy*. 2007;107:131-139.

64. Gault B, Ringer SP, Moody MP, Cairney JM. *Atom Probe Microscopy, Springer Series in Material Science*. Springer-Verlag New York; 2012.

65. Harker RM. The influence of oxide thickness on the early stages of the massive uranium–hydrogen reaction. *J Alloys Compd*. 2006;426:106-117.

66. Ortner S. Low temperature phase transformations and hardening in a urnaium/niobium alloy. *Nexia Solut 8868*. 2007.

67. Greenspan L. Humidity fixed points of binary saturated aqueous solutions. *J Res Nat Bur Stand*. 1977;81:89-96.

68. Ziegler JF, Ziegler MD, Biersack JP. SRIM- the stopping and range of ions in matter (2010). *Nuc Inst Methods Phys Res B*. 2010;268:1818-1823.

69. Cameca. LEAP Metallurgy Applications Note. In: *LEAP Metallurgy Applications Note*. ; 2010.

70. Vurpillot F, Gault B, Geiser BP, Larson DJ. Reconstructing atom probe data: A review. *Ultramicroscopy*. 2013;132:19-30.

71. Larson DJ, Prosa TJ, Ulfig RM, Geiser BP, Kelly ThF. *Local Electrode Atom Probe Tomography: A User's Guide*. Springer-Verlag New York; 2013.

72. Martin TL, Coe C, Bagot PAJ, Morrall P, Smith GDW, Scott T, Moody M. Atomic-scale Studies of Uranium Oxidation and Corrosion by Water Vapour. *Sci Rep*. 2016;6:Article no. 25618.

73. Glascott J, Findlay I. AWE unpublished data. 2001.

74. Harker NJ. The corrosion of uranium in sealed environments containing oxygen and water vapour - University of Bristol Thesis. 2012.

75. Ritchie AG, Greenwood RC, Randles SJ. The kinetics of the uranium-oxygen-water vapour reaction between 40 and 100°c. *J Nucl Mater*. 1986;139:121-136.

76. Morrall P, Price DW, Nelson AJ, Siekhaus WJ, Nelson E, Wu KJ, Stratman M, Mclean II W. ToF-SIMS characterization of uranium hydride. *Phil Mag Lett*. 2007;87:541-547.

77. Sundell G, Thuvander M, Yatim AK, Nordin H, Andrén H-O. Direct observation of hydrogen and deuterium in oxide grain boundaries in corroded Zirconium alloys. *Corros Sci*. 2015;90:1-4.

78. Justussan WM. Transformation kinetics of gamma-phase uranium-molybdenum-niobium alloys. *J Nucl Mater*. 1961;4:37-45.

79. Sebastian JT, Seidman DN, Yoon KE, Bauer P, Reid T, Boffo C, Norem J. Atom-probe tomography analyses of niobium superconducting RF cavity materials. *Phys C*. 2006;441:70-74.

80. Yoon KE, Seidman DN, Antoine C, Bauer P. Atomic-scale chemical analyses of niobium oxide/niobium interfaces via atom probe tomography. *Appl Phys Lett*. 2008;93:Article no. 132502.

81. Sunwoo AJ, Hiromoto DS. Effects of natural aging on the tensile properties of water-quenched U-6%Nb alloy. *J Nucl Mater*. 2004;327:37-45.

82. Hughes AN, Orman S, Picton G. Environmental factors affecting the mechanical properties of uranium. *J Nucl Mater*. 1969;33:159-164.

83. Clarke AJ, Field RD, McCabe RJ, Cady CM, Hackenberg RE, Thorma DJ. EBSD and FIB/TEM examination of shape memory effect deformation structures in U–14at.% Nb. *Acta Mater*. 2008;56:2638-2648.

84. Ferreira LFR, Calvert JM, Gleave C, Lees DG, Rowlands PC. A study of the mechanism of corrosion of some ferritic steels in high-pressure carbon dioxide with the aid of oxygen-18 as a tracer III. Fe-9% Cr-1% Mo-0.26% Si. *Proc R Soc Lond A*. 1989;422:279-288.

85. Khanna AS, Rodriguez P, Gnanamoorthy JB. Oxidation kinetics, breakaway oxidation, and inversion phenomenon in 9Cr-1Mo steels. *Oxid Met*. 1986;26:171-200.